



# ARTS Theory

edited by

**Patrick Eriksson and Stefan Buehler**

October 27, 2023

ARTS Version 2.5.11 (git: 0f6c47be)

The content and usage of ARTS are not only described by this document. An overview of ARTS documentation and help features is given in *ARTS User Guide*, Section [1.2](#). For continuous reports on changes of the source code and this user guide, subscribe to the ARTS developers mailing list at <https://www.radiativetransfer.org/contact/>.

We welcome gladly comments and reports on errors in the document. Send then an e-mail to: `patrick.eriksson (at) chalmers.se` or `sbuehler (at) uni-hamburg.de`.

If you use data generated by ARTS in a scientific publication, then please mention this and cite the most appropriate of the ARTS publications that are summarized on <https://www.radiativetransfer.org/docs/>.

Copyright (C) 2000-2015

Stefan Buehler <sbuehler (at) uni-hamburg.de>

Patrick Eriksson <patrick.eriksson (at) chalmers.se>

The ARTS program is free software; you can redistribute it and/or modify it under the terms of the GNU General Public License as published by the Free Software Foundation; either version 2, or (at your option) any later version.

This program is distributed in the hope that it will be useful, but WITHOUT ANY WARRANTY; without even the implied warranty of MERCHANTABILITY or FITNESS FOR A PARTICULAR PURPOSE. See the GNU General Public License for more details.

You should have received a copy of the GNU General Public License along with the program; if not, write to the Free Software Foundation, Inc., 59 Temple Place - Suite 330, Boston, MA 02111-1307, USA.

## Contributing authors

Author/email	Main contribution(s)
Stefan Buehler <sup>a</sup> sbuehler (at) uni-hamburg.de	Editor, Chapters 2 and 3.
Cory Davis <sup>d</sup> cory.davis (at) metSERVICE.com	Chapter 10.
Claudia Emde <sup>c</sup> claudia.emde (at) dlr.de	Chapter 6.
Patrick Eriksson <sup>b</sup> patrick.eriksson (at) chalmers.se	Editor, Chapters 1, 6 and 7.
Nikolay Koulev	Section 2.1.
Thomas Kuhn	Chapters 2 and 3.
Oliver Lemke <sup>a</sup> olemke (at) core-dump.info	Latex fixes.
Christian Melsheimer <sup>c</sup> melsheimer (at) uni-bremen.de	Chapter 5.
Manfred Brath <sup>a</sup> manfred.brath (at) uni-hamburg.de	Section 2.4.

The present address is given for active contributors, while for others the address to the institute where the work was performed is given:

<sup>a</sup> Meteorological Institute, University of Hamburg, Bundesstr. 55, 20146 Hamburg, Germany.

<sup>b</sup> Department of Earth and Space Sciences, Chalmers University of Technology, SE-41296 Gothenburg, Sweden.

<sup>c</sup> Institute of Environmental Physics, University of Bremen, P.O. Box 33044, 28334 Bremen, Germany.

<sup>d</sup> Institute for Atmospheric and Environmental Science, University of Edinburgh, EH93JZ Edinburgh, Scotland, UK.



# Contents

<b>1</b>	<b>Theoretical formalism</b>	<b>1</b>
1.1	The forward model . . . . .	1
1.2	The sensor transfer matrix . . . . .	2
1.3	Weighting functions . . . . .	3
1.3.1	Basics . . . . .	3
1.3.2	Transformation between vector spaces . . . . .	3
<b>2</b>	<b>Gas absorption and scattering</b>	<b>5</b>
2.1	Line absorption . . . . .	5
2.1.1	Line functions - theory . . . . .	6
	Basic expressions . . . . .	6
	Line shapes . . . . .	6
	Partition functions . . . . .	9
2.1.2	Line functions - method . . . . .	12
	Basic data structure . . . . .	12
	Basic expressions . . . . .	13
	Line shapes . . . . .	15
	Line strengths . . . . .	17
	Line function algorithms . . . . .	18
2.1.3	Species-specific data in ARTS . . . . .	29
	Partition function data . . . . .	30
2.2	Continuum absorption . . . . .	30
2.2.1	Water vapor continuum models . . . . .	31
	The MPM93 continuum parameterization . . . . .	31
2.2.2	Oxygen continuum absorption . . . . .	33
2.2.3	Nitrogen continuum absorption . . . . .	34
2.2.4	Carbon dioxide continuum absorption . . . . .	35
2.3	Complete absorption models . . . . .	35
2.3.1	Complete water vapor models . . . . .	35
	MPM87 water vapor absorption model . . . . .	36
	MPM89 water vapor absorption model . . . . .	38
	MPM93 water vapor absorption model . . . . .	40
	CP98 water vapor absorption model . . . . .	42
	PWR98 water vapor absorption model . . . . .	43
2.3.2	Complete oxygen models . . . . .	45
	PWR93 oxygen absorption model . . . . .	45
	MPM93 oxygen absorption model . . . . .	47

2.4	Absorption cross section model . . . . .	50
2.5	Gas scattering . . . . .	53
<b>3</b>	<b>Cloud absorption</b>	<b>55</b>
3.1	Liquid water and ice particle absorption . . . . .	55
3.2	Variability and uncertainty in cloud absorption . . . . .	58
<b>4</b>	<b>Refractive index</b>	<b>61</b>
4.1	Gases . . . . .	61
4.1.1	Microwave general method ( <code>refr_index_airMicrowavesGeneral</code> )	62
4.2	Free electrons . . . . .	63
<b>5</b>	<b>Polarisation and Stokes parameters</b>	<b>65</b>
5.1	Polarisation directions . . . . .	65
5.2	Plane monochromatic waves . . . . .	66
5.3	Measuring Stokes parameters . . . . .	71
5.4	Partial polarisation . . . . .	74
5.4.1	Polarisation of Radiation in the Atmosphere . . . . .	77
5.4.2	Antenna polarisation . . . . .	77
5.5	The scattering amplitude matrix . . . . .	79
5.6	Change of the Stokes basis . . . . .	79
5.6.1	The modified Stokes vector . . . . .	80
5.6.2	Rotated modified Stokes vector . . . . .	80
<b>6</b>	<b>Basic radiative transfer theory</b>	<b>83</b>
6.1	Basic definitions . . . . .	84
6.2	Single particle scattering . . . . .	85
6.2.1	Definition of the amplitude matrix . . . . .	85
6.2.2	Phase matrix . . . . .	86
6.2.3	Extinction matrix . . . . .	86
6.2.4	Absorption vector . . . . .	87
6.2.5	Optical cross sections . . . . .	87
6.2.6	Coordinate systems . . . . .	88
6.3	Particle Ensembles . . . . .	89
6.3.1	Single scattering approximation . . . . .	90
6.4	Radiative transfer equation . . . . .	91
6.5	The $n^2$ -law of radiance . . . . .	93
6.5.1	Introduction . . . . .	93
6.5.2	Treatment in ARTS . . . . .	94
6.6	Simple solution without scattering and polarization . . . . .	94
6.7	Clear sky simulations with sun like sources . . . . .	95
6.8	Special solutions . . . . .	97
6.9	Surface emission and reflection . . . . .	98
6.9.1	The dielectric constant and the refractive index . . . . .	98
6.9.2	Relating reflectivity and emissivity . . . . .	98
6.9.3	Specular reflections . . . . .	99
6.9.4	Rough surfaces . . . . .	101

<b>7</b>	<b>Propagation paths</b>	<b>105</b>
7.1	Structure of implementation	105
7.1.1	Main functions for clear sky paths	105
7.1.2	Main functions for propagation path steps	106
7.2	Some basic geometrical relationships for 1D and 2D	106
7.3	Calculation of geometrical propagation paths	109
7.3.1	1D	109
7.3.2	2D	109
7.3.3	3D	111
	Conversion between polar and Cartesian coordinates	111
	Finding the crossing of a specified $r$ , $\alpha$ or $\beta$	112
	Finding the crossing with a pressure level	113
	A robust 3D algorithm	114
7.4	Basic treatment of refraction	116
7.4.1	1D	118
7.4.2	2D	119
7.4.3	3D	121
<b>8</b>	<b>Particle size distributions</b>	<b>123</b>
8.1	Handling of different size descriptors	123
8.2	Modified gamma particle size distributions	123
8.2.1	Native form	124
8.2.2	Moments and gamma function	124
8.2.3	Mass content	124
8.2.4	Mass content and mean size	125
8.2.5	Mass content and median size	126
8.2.6	Mass content and mean particle mass	127
8.2.7	Mass content and total number density	127
8.2.8	Avoiding numerical problems	128
<b>9</b>	<b>Scattering: The DOIT solver</b>	<b>129</b>
9.1	Radiation field	129
9.2	Vector radiative transfer equation solution	130
9.3	Scalar radiative transfer equation solution	133
9.4	Single scattering approximation	134
9.5	Sequential update	134
9.5.1	Up-looking directions	135
9.5.2	Down-looking directions	136
9.5.3	Limb directions	136
9.6	Numerical Issues	137
9.6.1	Grid optimization and interpolation	137
9.6.2	Zenith angle grid optimization	137
9.6.3	Interpolation methods	138
9.6.4	Error estimates	139

<b>10 Scattering: The Reversed Monte Carlo solver ARTS-MC</b>	<b>143</b>
10.1 Introduction . . . . .	143
10.2 Model . . . . .	145
10.2.1 Integration over the antenna response function . . . . .	145
10.2.2 The path integral . . . . .	146
10.2.3 Emission and scattering . . . . .	147
10.2.4 The scattering integral . . . . .	148
10.2.5 Applying the Mueller matrices . . . . .	148
10.2.6 Boundary contributions . . . . .	149
10.2.7 Surface reflection . . . . .	149
10.2.8 Summary . . . . .	150
10.3 Practical considerations regarding optical properties . . . . .	150
10.3.1 Particle orientation and the evolution operator . . . . .	150
10.3.2 Particle orientation and the phase matrix . . . . .	150
10.4 Variations on the ARTS-MC algorithm . . . . .	150
10.4.1 The original ARTS-MC and forcing the original pathlength sample to be within the 3D box . . . . .	150
10.4.2 1D clear sky variables and clear sky radiance look up . . . . .	150
10.4.3 MCIPA . . . . .	150
10.4.4 optical path and ice water path calculations . . . . .	150
 <b>I Bibliography and Appendices</b>	 <b>153</b>
 <b>II Index</b>	 <b>163</b>



# Chapter 1

## Theoretical formalism

In this section, a theoretical framework of the forward model is presented. The presentation follows *Rodgers* [1990], but some extensions are made, for example, the distinction between the atmospheric and sensor parts of the forward model is also discussed. After this chapter was written, C.D. Rodgers published a textbook [*Rodgers*, 2000] presenting the formalism in more detail than *Rodgers* [1990].

### 1.1 The forward model

The radiative intensity,  $I$ , at a point in the atmosphere,  $r$ , for frequency  $\nu$  and traversing in the direction,  $\psi$ , depends on a variety of physical processes and continuous variables such as the temperature profile,  $T$ :

$$I = F(\nu, r, \psi, T, \dots) \quad (1.1)$$

To detect the spectral radiation some kind of sensor, having a finite spatial and frequency resolution, is needed, and the observed spectrum becomes a vector,  $\mathbf{y}$ , instead of a continuous function. The atmospheric radiative transfer is simulated by a computer model using a limited number of parameters as input (that is, a discrete model), and the forward model,  $\mathcal{F}$ , used in practice can be expressed as

$$\mathbf{y} = \mathcal{F}(\mathbf{x}_{\mathcal{F}}, \mathbf{b}_{\mathcal{F}}) + \varepsilon(\mathbf{x}_{\varepsilon}, \mathbf{b}_{\varepsilon}) \quad (1.2)$$

where  $\mathbf{x}_{\mathcal{F}}$ ,  $\mathbf{b}_{\mathcal{F}}$ ,  $\mathbf{x}_{\varepsilon}$  and  $\mathbf{b}_{\varepsilon}$  together give a total description of both the atmospheric and sensor states, and  $\varepsilon$  is the measurement errors. The parameters are divided in such way that  $\mathbf{x}$ , the state vector, contains the parameters to be retrieved, and the remainder is given by  $\mathbf{b}$ , the model parameter vector. The total state vector is

$$\mathbf{x} = \begin{bmatrix} \mathbf{x}_{\mathcal{F}} \\ \mathbf{x}_{\varepsilon} \end{bmatrix} \quad (1.3)$$

---

#### History

110610 Outdated information was removed (Patrick Eriksson).

000306 Written by Patrick Eriksson, partly based on *Eriksson* [1999] and *Eriksson et al.* [2002].

and the total model parameter vector is

$$\mathbf{b} = \begin{bmatrix} \mathbf{b}_{\mathcal{F}} \\ \mathbf{b}_{\varepsilon} \end{bmatrix} \quad (1.4)$$

The actual forward model consists of either empirically determined relationships, or numerical counterparts of the physical relationships needed to describe the radiative transfer and sensor effects. The forward model described here is mainly of the latter type, but some parts are more based on empirical investigations, such as the parameterisations of continuum absorption.

Both for the theoretical formalism and the practical implementation, it is suitable to make a separation of the forward model into two main sections, a first part describing the atmospheric radiative transfer for pencil beam (infinite spatial resolution) monochromatic (infinite frequency resolution) signals,

$$\mathbf{i} = \mathcal{F}_r(\mathbf{x}_r, \mathbf{b}_r) \quad (1.5)$$

and a second part modelling sensor characteristics,

$$\mathbf{y} = \mathcal{F}_s(\mathbf{i}, \mathbf{x}_s, \mathbf{b}_s) + \varepsilon(\mathbf{x}_{\varepsilon}, \mathbf{b}_{\varepsilon}) \quad (1.6)$$

where  $\mathbf{i}$  is the vector holding the spectral values for the considered set of frequencies and viewing angles ( $\mathbf{i}^i = I(\nu^i, \psi^i, \dots)$ , where  $i$  is the vector index), and  $\mathbf{x}_{\mathcal{F}}$  and  $\mathbf{b}_{\mathcal{F}}$  are separated correspondingly, that is,  $\mathbf{x}_{\mathcal{F}}^T = [\mathbf{x}_r^T, \mathbf{x}_s^T]$  and  $\mathbf{b}_{\mathcal{F}}^T = [\mathbf{b}_r^T, \mathbf{b}_s^T]$ . The vectors  $\mathbf{x}$  and  $\mathbf{b}$  can now be expressed as

$$\mathbf{x} = \begin{bmatrix} \mathbf{x}_r \\ \mathbf{x}_s \\ \mathbf{x}_{\varepsilon} \end{bmatrix} \quad (1.7)$$

and

$$\mathbf{b} = \begin{bmatrix} \mathbf{b}_r \\ \mathbf{b}_s \\ \mathbf{b}_{\varepsilon} \end{bmatrix}, \quad (1.8)$$

respectively. The subscripts of  $\mathbf{x}$  and  $\mathbf{b}$  are below omitted as the distinction should be clear by the context.

## 1.2 The sensor transfer matrix

The modelling of the different sensor parts can be described by a number of analytical expressions that together makes the basis for the sensor model. These expressions are throughout linear operations and it is possible, as suggested in *Eriksson et al. [2002]*, to implement the sensor model as a straightforward matrix multiplication:

$$\mathbf{y} = \mathbf{H}\mathbf{i} + \varepsilon \quad (1.9)$$

where  $\mathbf{H}$  is here denoted as the sensor transfer matrix. Expressions to determine  $\mathbf{H}$  are given by *Eriksson et al. [2006]*.

The matrix  $\mathbf{H}$  can further incorporate effects of a data reduction and the total transfer matrix is then

$$\mathbf{H} = \mathbf{H}_d \mathbf{H}_s \quad (1.10)$$

as

$$\mathbf{y} = \mathbf{H}_d \mathbf{y}' = \mathbf{H}_d (\mathbf{H}_s \mathbf{i} + \varepsilon') = \mathbf{H} \mathbf{i} + \varepsilon \quad (1.11)$$

where  $\mathbf{H}_d$  is the data reduction matrix,  $\mathbf{H}_s$  the sensor matrix, and  $\mathbf{y}'$  and  $\varepsilon'$  are the measurement vector and the measurement errors, respectively, before data reduction.

## 1.3 Weighting functions

### 1.3.1 Basics

A weighting function is the partial derivative of the spectrum vector  $\mathbf{y}$  with respect to some variable used by the forward model. As the input of the forward model is divided between  $\mathbf{x}$  or  $\mathbf{b}$ , the weighting functions are divided correspondingly between two matrices, the state weighting function matrix

$$\mathbf{K}_x = \frac{\partial \mathbf{y}}{\partial \mathbf{x}} \quad (1.12)$$

and the model parameter weighting function matrix

$$\mathbf{K}_b = \frac{\partial \mathbf{y}}{\partial \mathbf{b}} \quad (1.13)$$

For the practical calculations of the weighting functions, it is important to note that the atmospheric and sensor parts can be separated. For example, if  $\mathbf{x}$  only hold atmospheric and spectroscopic variables,  $\mathbf{K}_x$  can be expressed as

$$\mathbf{K}_x = \frac{\partial \mathbf{y}}{\partial \mathbf{i}} \frac{\partial \mathbf{i}}{\partial \mathbf{x}} = \mathbf{H} \frac{\partial \mathbf{i}}{\partial \mathbf{x}} \quad (1.14)$$

This equation shows that the new parts needed to calculate atmospheric weighting functions, are functions giving  $\partial \mathbf{i} / \partial \mathbf{x}$  where  $\mathbf{x}$  can represent the vertical profile of a species, atmospheric temperatures, spectroscopic data etc.

### 1.3.2 Transformation between vector spaces

It could be of interest to transform a weighting function matrix from one vector space to another<sup>1</sup>. The new vector,  $\mathbf{x}'$ , is here assumed to be of length  $n$  ( $\mathbf{x}' \in \mathbf{R}^{n \times 1}$ ), while the original vector,  $\mathbf{x}$  is of length  $p$  ( $\mathbf{x} \in \mathbf{R}^{p \times 1}$ ). The relationship between the two vector spaces is described by a transformation matrix  $\mathbf{B}$ :

$$\mathbf{x} = \mathbf{B} \mathbf{x}' \quad (1.15)$$

where  $\mathbf{B} \in \mathbf{R}^{p \times n}$ . For example, if  $\mathbf{x}'$  is assumed to be piecewise linear, then the columns of  $\mathbf{B}$  contain tent functions, that is, a function that are 1 at the point of interest and decreases

<sup>1</sup>This subject is also discussed in *Rodgers* [2000], published after writing this.

linearly down to zero at the neighbouring points. The matrix can also hold a reduced set of eigenvectors.

The weighting function matrix corresponding to  $\mathbf{x}'$  is

$$\mathbf{K}_{\mathbf{x}'} = \frac{\partial \mathbf{y}}{\partial \mathbf{x}'} \quad (1.16)$$

This matrix is related to the weighting function matrix of  $\mathbf{x}$  (Eq. 1.12) as

$$\mathbf{K}_{\mathbf{x}'} = \frac{\partial \mathbf{y}}{\partial \mathbf{x}} \frac{\partial \mathbf{x}}{\partial \mathbf{x}'} = \frac{\partial \mathbf{y}}{\partial \mathbf{x}} \mathbf{B} = \mathbf{K}_{\mathbf{x}} \mathbf{B} \quad (1.17)$$

Note that

$$\mathbf{K}_{\mathbf{x}'} \mathbf{x}' = \mathbf{K}_{\mathbf{x}} \mathbf{B} \mathbf{x}' = \mathbf{K}_{\mathbf{x}} \mathbf{x} \quad (1.18)$$

However, it should be noted that this relationship only holds for those  $\mathbf{x}$  that can be represented perfectly by some  $\mathbf{x}'$  (or vice versa), that is,  $\mathbf{x} = \mathbf{B} \mathbf{x}'$ , and not for all combinations of  $\mathbf{x}$  and  $\mathbf{x}'$ .

If  $\mathbf{x}'$  is the vector to be retrieved, we have that [Rodgers, 1990]

$$\hat{\mathbf{x}}' = \mathcal{I}(\mathbf{y}, \mathbf{c}) = \mathcal{T}(\mathbf{x}, \mathbf{b}, \mathbf{c}) \quad (1.19)$$

where  $\mathcal{I}$  and  $\mathcal{T}$  are the inverse and transfer model, respectively.

The contribution function matrix is accordingly

$$\mathbf{D}_{\mathbf{y}} = \frac{\partial \hat{\mathbf{x}}'}{\partial \mathbf{y}} \quad (1.20)$$

that is,  $\mathbf{D}_{\mathbf{y}}$  corresponds to  $\mathbf{K}_{\mathbf{x}'}$ , not  $\mathbf{K}_{\mathbf{x}}$ .

We have now two possible averaging kernel matrices

$$\mathbf{A}_{\mathbf{x}} = \frac{\partial \hat{\mathbf{x}}'}{\partial \mathbf{x}} = \frac{\partial \hat{\mathbf{x}}'}{\partial \mathbf{y}} \frac{\partial \mathbf{y}}{\partial \mathbf{x}} = \mathbf{D}_{\mathbf{y}} \mathbf{K}_{\mathbf{x}} \quad (1.21)$$

$$\mathbf{A}_{\mathbf{x}'} = \frac{\partial \hat{\mathbf{x}}'}{\partial \mathbf{x}'} = \frac{\partial \hat{\mathbf{x}}'}{\partial \mathbf{y}} \frac{\partial \mathbf{y}}{\partial \mathbf{x}} \frac{\partial \mathbf{x}}{\partial \mathbf{x}'} = \mathbf{D}_{\mathbf{y}} \mathbf{K}_{\mathbf{x}'} = \mathbf{A}_{\mathbf{x}} \mathbf{B} \quad (1.22)$$

where  $\mathbf{A}_{\mathbf{x}} \in \mathbf{R}^{p \times n}$  and  $\mathbf{A}_{\mathbf{x}'} \in \mathbf{R}^{p \times p}$ , that is, only  $\mathbf{A}_{\mathbf{x}'}$  is square. If  $p > n$ ,  $\mathbf{A}_{\mathbf{x}}$  gives more detailed information about the shape of the averaging kernels than the standard matrix ( $\mathbf{A}_{\mathbf{x}'}$ ). If the retrieval grid used is coarse, it could be the case that  $\mathbf{A}_{\mathbf{x}'}$  will not resolve all the oscillations of the averaging kernels, as shown in Eriksson [1999, Figure 11].

## Chapter 2

# Gas absorption and scattering

This chapter contains theoretical background and scientific details for gas absorption calculations in ARTS. A more practical overview, with focus on how to set up calculations, is given in *ARTS User Guide*, Chapter 6.

Gas absorption generally consists of a superposition of spectral lines and continua. Depending on the gas species, the continua either have a real physical meaning, or they are more or less empirical corrections for deficits in the explicit line-by-line calculation. In the latter case the magnitude of the continuum term will depend strongly on the exact setup of the line-by-line calculation. Combining continua and line-by-line calculation therefore requires expertise.

This chapter is structured in three main parts: Line absorption, continuum absorption, and complete absorption models. It should be noted that the three topics are tightly related. In particular, complete absorption models will normally include a line part and a continuum part. Some absorption models, notably those by Rosenkranz and Liebe will show up under both continua and complete absorption models. The continuum section then treats specifically the continuum parameterization of these model, the complete absorption model section puts more focus on the line part and the model as a whole.

Each of the main parts first introduces the theoretical background to the topic, then presents aspects of the specific implementation in ARTS.

## 2.1 Line absorption

This section will first go over the theory of line-by-line absorption. It will then switch to the method of how this theory is implemented into ARTS.

---

### History

- |            |  |
|------------|--|
| 2021-11-22 | Added gas scattering, Manfred Brath.                               |
| 2012-09-21 | Added pressure broadening and shift documentation, Stefan Buehler. |
| 2011-07-05 | Revised for ARTS2 by Stefan Buehler.                               |
| 2001-11-21 | Continuum absorption part written, Thomas Kuhn.                    |
| 2001-10-05 | Line absorption part written, Nikolay Koulev.                      |

### 2.1.1 Line functions - theory

We will introduce here the main concepts concerning line absorption. The aim is to give some overview and show some key equations, not to give a full treatment of the theory. To really understand line absorption, you should refer to one of the cited books, or some other book on spectroscopy.

#### Basic expressions

An absorption line is described by the corresponding absorption coefficient as a function of frequency  $\alpha(\nu)$ , which can be written as [Goody and Yung, 1989]:

$$\alpha(\nu) = nS(T)F(\nu) \quad (2.1)$$

where  $S(T)$  is called the line strength,  $T$  is the temperature,  $F(\nu)$  is called the line shape function, and  $n$  is the number density of the absorber. The line shape function is normalized as:

$$\int F(\nu) d\nu = 1 \quad (2.2)$$

As absorption is additive, the total absorption coefficient is derived by adding up the absorption contributions of all spectral lines of all molecular species.

#### Line shapes

So far, there exists no complete analytical function that accurately describes the line shape in all atmospheric conditions and for all frequencies. But for most cases very accurate approximations are available. Which approximation is appropriate depends mostly on the atmospheric pressure, and on whether the frequencies of interest are close to the line center, or far out in the line wing.

There are three phenomena which contribute to the line shape. These are, in increasing order of importance, the finite lifetime of an excited state in an isolated molecule, the thermal movement of the gas molecules, and their collisions with each other. They result in corresponding effects to the line shape: natural broadening, Doppler, and pressure broadening. Of these, the first one is completely negligible compared to the other two for typical atmospheric conditions. Nevertheless, we will pay a special attention to the natural broadening because its implications are of a conceptual importance for the broadening processes.

The spectral line shape can be derived in the case of natural broadening from basic physical considerations and a well-known Fourier transform theorem from the time to the frequency domain [Thorne *et al.*, 1999]. If we consider classically the spontaneous decay of the excited state of a two-level system in the absence of external radiation, then the population  $n$  of the upper level decreases according to

$$\frac{dn(t)}{dt} = -A n(t) \quad (2.3)$$

where  $A$  is Einstein A coefficient. This equation can also be interpreted as the rate of the spontaneously emitted photons because of decay. The integral form of this relation is

$$n(t) = n(0) e^{-At} = n(0) e^{-t/\tau} \quad (2.4)$$

where  $\tau$  is the mean lifetime of the excited state. Thus, the number of spontaneously emitted photons and in this way the flux of the emitted radiation then will be proportional to  $n$ . Therefore we can write for the flux  $L$  that

$$L(t) = L(0) e^{-t/\tau} = L(0) e^{-\gamma t} \quad (2.5)$$

By the afore mentioned theorem, multiplying in the time domain by  $e^{-\gamma t}$  is equivalent to convolving in the frequency domain with a function  $1/[\nu^2 - (\gamma/4\pi)^2]$ . Accordingly, the line profile of a spectral line at frequency  $\nu_0$  as a normalized line shape function will be, as defined in *Thorne et al.* [1999],

$$F(\nu) = \frac{1}{\pi} \frac{\gamma/4\pi}{(\nu - \nu_0)^2 + (\gamma/4\pi)^2} \quad (2.6)$$

This gives a bell-shaped profile and the function itself is called Lorentzian. The dependence on the position of the line is apparent through  $\nu_0$ , that is why some authors prefer to denote the function by  $F(\nu, \nu_0)$ . The result is important because of two major reasons. Firstly, without the natural broadening the line would be the delta function  $\delta(\nu - \nu_0)$ , as pointed out in *Bernath* [1995]. So the spontaneous decay of the excited state is responsible for the finite width and the certain shape of the line shape function. Secondly, the Lorentzian type of function comes significantly into play when explaining some of the other broadening effects or the complete picture of the broadened line [*Thorne et al.*, 1999].

The second effect, Doppler broadening, is important for the upper stratosphere and mesosphere for microwave frequencies. The line shape follows the velocity distribution of the gas molecules or atoms. Under the conditions of thermodynamic equilibrium, we have a probability distribution for the relative velocity  $u$  between the gas molecule and the observer of Maxwell type

$$p(u) = \sqrt{\frac{m}{2\pi kT}} \exp \left[ -\frac{mu^2}{2kT} \right] \quad (2.7)$$

where  $m$  is the mass of the molecule. Using then the formula for the Doppler shift for the non-relativistic region  $\nu - \nu_0 = \nu_0 u / c$ , one can easily derive the line shape function [*Bernath*, 1995],

$$F_D(\nu) = \frac{1}{\gamma_D \sqrt{\pi}} \exp \left[ -\left( \frac{\nu - \nu_0}{\gamma_D} \right)^2 \right] \quad (2.8)$$

where the quantity  $\gamma_D$  is called Doppler line width and equals

$$\gamma_D = \frac{\nu_0}{c} \sqrt{\frac{2kT}{m}} \quad (2.9)$$

In contrast to the line shape function for the natural broadening, the Doppler broadening leads to a Gaussian line shape function  $F_D(\nu)$ . The Doppler line width  $\gamma_D$  is so defined that it is equal to the half width at half of the maximum (HWHM) of the line shape function. A similar notation is used for all other width parameters  $\gamma_{xy}$  below.

The third broadening mechanism is pressure broadening. It is the most complicated broadening mechanism, and still subject to theoretical and experimental research. So far, there is no way to derive the exact shape of a pressure-broadened line from first principles, at least not for the far wing region. The various approximations, which are therefore used,

are immanently limited to the certain line regions they deal with. The most popular among these approximations is the *impact approximation* which postulates that the duration of the collisions of the gas molecules or atoms is very small compared to the average time between the collisions. Due to the Fourier-pair relationship between time and frequency, the line shape that follows from the impact approximation can only be expected to be accurate near the line center, not in the far wings of the line.

Lorentz was the first to achieve a result exploiting the impact approximation, the Lorentz line shape function:

$$F_L(\nu) = \frac{\gamma_L}{\pi} \frac{1}{(\nu - \nu_0)^2 + \gamma_L^2} \quad (2.10)$$

where  $\gamma_L$  is the Lorentz line width [Thorne *et al.*, 1999]. As one can see, the result Eq. 2.10 is pretty similar to Eq. 2.6 but the specific line parameters  $\gamma$  and  $\gamma_L$  make them differ significantly in the corresponding frequency regions of interest. For atmospheric pressures  $\gamma_L$  is much greater and because of that, of experimental significance in contrast to  $\gamma$ .

Elaborating the model of Lorentz, van Vleck and Weisskopf made a correction to it [Van Vleck and Weisskopf, 1945], particularly for the microwave region:

$$F_{VW}(\nu) = \left(\frac{\nu}{\nu_0}\right)^2 \frac{\gamma_L}{\pi} \left[ \frac{1}{(\nu - \nu_0)^2 + \gamma_L^2} + \frac{1}{(\nu + \nu_0)^2 + \gamma_L^2} \right] \quad (2.11)$$

which can be reduced to a Lorentzian for  $(\nu - \nu_0) \ll \nu_0$  and  $0 \ll \nu_0$ . Except for the additional factor  $(\nu/\nu_0)^2$ ,  $F_{VW}$  can be regarded as the sum of two  $F_L$  lines, one with its center frequency at  $\nu_0$ , the other at  $-\nu_0$ .

The van Vleck and Huber lineshape [Van Vleck and Huber, 1977] is similar to Eq. 2.11, except for the factor  $(\nu/\nu_0)^2$  which is replaced by  $[\nu \tanh(h\nu/2kT)/\nu_0 \tanh(h\nu_0/2kT)]$ , with  $k$  the Boltzmann constant,  $h$  the Planck constant, and  $T$  the atmospheric temperature (the denominator is actually a consequence of the line strength definition in the spectroscopic catalogs). The lineshape Eq. 2.11 with this factor can be used for the entire frequency range, since the microwave approximation:  $\tanh(x) = x$ , that leads to the factor  $(\nu/\nu_0)^2$ , is not made.

The combined picture of a simultaneously Doppler and pressure broadened line is the next step of the approximations development. The line shape function has to be approximated in this case by the Voigt line shape function

$$F_{Voigt}(\nu, \nu_0) = \int F_L(\nu, \nu') F_D(\nu', \nu_0) d\nu' \quad (2.12)$$

though there's no strict justification for its use - the two processes are assumed to act independently, which in reality is not the fact. The integral in Eq. 2.12 can not be computed analytically, so certain approximation algorithms must be used.

Another possibility would be the combination of the last two equations Eq. 2.11 and Eq. 2.12. The respective result then will be

$$F_S = \left(\frac{\nu}{\nu_0}\right)^2 [F_{Voigt}(\nu, \nu_0) + F_{Voigt}(\nu, -\nu_0)] \quad (2.13)$$

The advantage of such a model is that it behaves like a van Vleck-Weisskopf line shape function in the high pressure limit and like a Voigt one in the low pressure limit. There is one important caveat to the equation Eq. 2.13: it has to be made sure that the algorithm



that is used to compute the Voigt function really produces a Lorentz line in the high pressure limit. Another point of significance is the demand that the model yields meaningful results far from the line center, since the line center from the “mirror” line at  $-\nu_0$  is situated approximately  $2\nu_0$  away from the frequency  $\nu_0$  of computation. We explicitly verified that the algorithms of *Drayson* [1976], *Oliveiro and Longbothum* [1977], and *Kuntz and Höpfner* [1999] satisfy both requirements, while this was found to be not true for some other algorithms commonly used for Voigt-shape computation. In particular, it is not true for the Hui-Armstrong-Wray Formula, as defined in *Hui et al.* [1978] and in Equation 2.60 of *Rosenkranz* [1993]. Provided the condition above is fulfilled, the  $F_S$  line shape gives a smooth transition from high tropospheric pressures to low stratospheric ones, and should be valid near the line centers throughout the microwave region. With a Van Vleck and Huber forefactor instead of the Van Vleck and Weisskopf forefactor, it should be valid throughout the thermal infrared spectral range, but there the mirror line at negative frequency is negligible anyway, because it is so far away.

Further refinement to line shape models include speed-dependent Voigt profiles and the Hartmann-Tran profile. We will not go into them here because any theoretical description we offer at this point would not do them justice (FIXME).

### Partition functions

Partition functions are needed to compute the temperature dependence of the line intensities in local thermodynamic equilibrium. They are related to the molecular energy states and their statistical distribution during the radiation process.

In any case of spectroscopic interest the free molecules of a gas are not optically thick at all frequencies, so the radiation energy is not represented by blackbody radiation. The most common assumption made, which is sufficient in the case of tropospheric and low stratospheric research, is the *local thermodynamic equilibrium* or *LTE*. According to it, it's possible to find a common temperature, which may vary from place to place, that fits the Boltzmann energy population distribution and the Maxwell velocities distribution. This practically means, that under *LTE* the collisional processes must be of greater importance than radiative ones. In other words, an excited state must have a higher probability of de-excitation by collision than by spontaneous radiation. This is the important factor which makes natural broadening differ quantitatively so much from the pressure (collisional) one, though both are described qualitatively almost identically by Lorentzian line shape functions.

According to the Maxwell-Boltzmann distribution law, in *LTE* the total number of gas particles (molecules and atoms)  $N_n$  in a state  $E_n$  is given by

$$N_n = N_0 \frac{g_n}{g_0} e^{-E_n/kT} \quad (2.14)$$

where  $N_0$  is particle number in the ground state, and  $g_n, g_0$  are the statistical weights (degeneracies) of the  $n$ -state and the ground state [*Gordy and Cook*, 1970]. Thus the total particle number  $N$  is given by

$$N = \frac{N_0}{g_0} \sum_{n=0}^{\infty} g_n e^{-E_n/kT} = \frac{N_0}{g_0} Q(T) \quad (2.15)$$

The quantity  $Q(T)$  is the *partition function* of the gas, which generally speaking describes the energy states distribution of the gas molecules and atoms.

The values of  $S(T)$  at reference temperature  $T_0$  of Equation 2.1 are contained in spectroscopic databases (more on this below). The conversion to different temperatures in local thermodynamic equilibrium is done by

$$S(T) = S(T_0) \frac{Q(T_0)}{Q(T)} \frac{e^{-E_f/kT} - e^{-E_i/kT}}{e^{-E_f/kT_0} - e^{-E_i/kT_0}} \quad (2.16)$$

given the energies  $E_f$  and  $E_i$  of the two levels between which the transition occurs as well as the partition function  $Q(T)$  [Rothman *et al.*, 1998]. The databases contain the lower state energy  $E_l$  tabulated along with the  $S$  and the transition frequency  $\nu$ , so that the upper state energy can be computed by  $E_u = E_l + h\nu$ . Partition functions for the different molecular species are commonly available along with the spectroscopic databases, given in the form of tabulated values for a set temperatures (e.g., for JPL catalogue) or through some computer code (e.g., the TIPS program coming with the HITRAN catalogue). For non-local thermodynamic equilibrium calculations, please see the end of this subsection.

The partition function for a perfect gas molecule can be represented by the product of the *translational* and the *internal* partition functions, as defined in Herzberg [1945],

$$Q = Q_{tr} Q_{int} \quad (2.17)$$

bearing in mind that the respective energies, translational and internal, are independent of each other. The first quantity  $Q_{tr}$  accounts for the distribution of the translational energy of the gas molecules and atoms - it takes into account that the translational velocities of the molecules and atoms fulfill the Maxwell distribution. However, for Equation 2.16, the quantity we are interested in is the *internal* partition function (or the *total internal partition function*) because the transitions between the discrete internal energy states are responsible for the absorption or emittance of radiation. Accordingly  $Q_{int}$  describes the distribution of energy among the internal energy states of the gas molecules and atoms.

The internal partition function for free gaseous molecules is a function of the electronic, the vibrational, the rotational, and the nuclear spin states. An approximation is used in Gordy and Cook [1970] in order to display the individual contributions explicitly

$$Q_{int} = Q_e Q_v Q_r Q_n \quad (2.18)$$

and thus the interaction between these various states is neglected. For practically all polyatomic molecules the excited electronic states are entirely negligible to those of the ground states, i.e.  $Q_e = 1$ . Only for the very few polyatomic molecules with a multiplet ground state ( $NO_2$ ,  $ClO_2$ , and free radicals) the electronic contribution has to be considered.

If we neglect the anharmonicities, the vibrational partition function, with vibrational energy levels measured with respect to the ground state for the *harmonic oscillator*, is according to Herzberg [1945]

$$Q_v = \left( \sum_{\nu_1} e^{-\nu_1 h \omega_1 / kT} \right) \left( \sum_{\nu_2} e^{-\nu_2 h \omega_2 / kT} \right) \dots \quad (2.19)$$

where  $\nu_1, \nu_2, \dots$ , the vibrational quantum numbers, can each have the values 0, 1, 2, ... and  $\omega_1, \omega_2, \dots$  are the frequencies of the fundamental modes of vibration. The summation is taken over all values of  $\nu_1, \nu_2, \dots$ , and each fundamental mode is counted separately. This result is valid for non-degenerate vibrations. If we use the simple expression for geometric progression

$$\sum_{\nu_i} e^{-\nu_i h \omega_i / kT} = \frac{1}{1 - e^{-h \omega_i / kT}} \quad (2.20)$$

and the degeneracies  $d_1, d_2, \dots$  of the fundamental modes, we get finally for the vibrational partition function

$$Q_v = \left(1 - e^{h\omega_1/kT}\right)^{-d_1} \left(1 - e^{h\omega_2/kT}\right)^{-d_2} \dots \quad (2.21)$$

The rotational partition function looks differently for the different symmetry types of molecules. For diatomic and linear polyatomic molecules with no center of symmetry the corresponding expression is, as defined in *Gordy and Cook* [1970]

$$\begin{aligned} Q_r &= \sum_{J=0}^{\infty} (2J+1) e^{-hBJ(J+1)/kT} \\ &= \frac{kT}{hB} + \frac{1}{3} + \frac{1}{15} \frac{hB}{kT} + \frac{4}{315} \left(\frac{hB}{kT}\right)^2 + \dots \\ &\cong \frac{kT}{hB} \end{aligned} \quad (2.22)$$

For *rigid symmetric*-, *asymmetric*-, and *spherical top* molecules there are also other factors to be taken into consideration, such as the spatial structure of the molecules, nuclear spin, inversion and internal rotation. The general expression in the case of a *rigid symmetric*- top molecule according to *Herzberg* [1945] is

$$Q_r = \frac{1}{\sigma} \sum_{J=0}^{\infty} \sum_{K=-J}^J (2J+1) e^{-h[BJ(J+1) + (A-B)K^2]/kT} \quad (2.23)$$

where  $\sigma$  is a measure of the degree of symmetry. The usual symmetric top has  $C_3$  or  $C_{3v}$  symmetry, therefore  $\sigma = 3$ . To a good approximation, the summation above can be expressed as in *Gordy and Cook* [1970]

$$Q_r = \frac{1}{\sigma} \left[ \left( \frac{\pi}{B^2 A} \right) \left( \frac{kT}{h} \right)^3 \right]^{1/2} = \frac{5.34 \times 10^6}{\sigma} \left( \frac{T^3}{B^2 A} \right)^{1/2} \quad (2.24)$$

For an *asymmetric top* the formula would then be

$$Q_r = \frac{5.34 \times 10^6}{\sigma} \left( \frac{T^3}{ABC} \right)^{1/2} \quad (2.25)$$

and for a *spherical top*, using the current notation of *Gordy and Cook* [1970] in the respective expression in *Herzberg* [1945],

$$Q_r = \frac{5.34 \times 10^6}{\sigma} \left( \frac{T^3}{A^3} \right)^{1/2}. \quad (2.26)$$

For *non-local thermodynamic equilibrium, NLTE*, the partitioning is no longer as simple as described above. Yet there exist techniques to emulate the above behavior for limited use-cases. One such simplification is to assume that only the vibrational energy state's level distribution can be described by purely changing the vibrational energy state's temperature in Equation 2.21. This essentially rewrites it as

$$Q_v^{(N)} = Q_v \left( \frac{1 - e^{h\omega_N/kT_N}}{1 - e^{h\omega_N/kT}} \right)^{-d_N}, \quad (2.27)$$

where  $T_N$  is the pseudo-temperature of the  $N$ :th level. This set of equations describe LTE when  $T_N = T$

Generally in NLTE one might be better off using a more pure approach of computing the energy level distributions. This yields that the rate of absorption, replacing  $S(T)$  in Equation 2.1 as the absorption strength coefficient, is

$$k = \frac{h\nu_0}{4\pi} \frac{A_{21}c^2}{2h\nu_0^3} \left( \frac{g_2}{g_1} r_1 - r_2 \right). \quad (2.28)$$

Note that here  $r_1$  and  $r_2$  is the ratio of absorbers in state 1 and 2 respectively. To retain the system equilibrium, it is important that state 2 emits an equal rate of photons as is absorbed. This yields an emission coefficient of

$$e = \frac{h\nu_0}{4\pi} A_{21} r_2. \quad (2.29)$$

This set of equations describes LTE when  $e/B(T) \equiv k$ , where  $B(T)$  is the Planck black-body emission function at the atmospheric temperature.

### 2.1.2 Line functions - method

The line shape model employed in internal calculations is closely coupled to the data structure the user can send into the code. There have therefore been many iterations of the ARTS absorption line data format. The newest format is described here. We refer to the newest version as the ARTSCAT-6 format. Older ARTSCAT(s) are still supported but by reading only. You have stored a modern version of the ARTSCAT if the main class is called `AbsorptionLines`. Legacy catalogs used to have the user manually set several parameters about their calculations in external catalogs. Now these parameters are set to the catalog instead so that if you save and reload your catalog, the same calculations as was done before is performed on a line-by-line basis. This section will look through the basis of the line shape calculations and explain the consequences various `AbsorptionLines`-settings have on the final result. These settings are easily extensible so please return here to keep up-to-date whenever you discover or add a new option to the line shape model.

#### Basic data structure

The basic structure of the latest ARTS absorption line catalog is to group as many global variables together as possible for the lines of a single isotopologue. The global variables are introduced in table 2.1 and are meant to either describe the basis of the data or to influence the computations by selecting the algorithm invoked.

Each individual line in the catalog has their parameters described in table 2.2. Note that it is possible to set up calculations that cannot work with specialized methods because of the two changeable parameters. For instance, you cannot perform pressure broadening calculations if you do not define at least the speed-independent pressure broadening coefficients as one of your relevant line shape parameters. Other issues can arise if you do not provide defined  $J$ -quantum numbers for when you want to perform Zeeman calculations. There are very few safety measures in place to deal with these issues because it is difficult to know whether a decision is intentional (for e.g., testing) or by mistake.

Keys for AbsorptionLines		
Key	Description	Example(s)
nlines	Number of available lines	Any integer
species	The isotopologue	H2O-161; O2-67
cutofftype	Type of line cutoff	None; ByLine; ByBand
mirroringtype	How to mirror the line	None; Lorentz; Same
populationtype	How to compute the strength	LTE; NLTE
normalizationtype	How to normalize the line	None; VVH; VVW
lineshapetype	Line shape method	VP; DP; HTP
T0	Reference temperature	Any float
cutofffreq	Cutoff frequency	Any float
linemixinglimit	Line mixing pressure limit	Any float; -1
localquanta	Local quantum numbers	J N; ""
upperglobalquanta	Upper global quantum numbers	J 1/2 S 1; ""
lowerglobalquanta	Lower global quantum numbers	v1 1
broadeningspecies	Line shape broadening species	SELF AIR; SELF O2 N2
temperaturemodes	Line shape temperature models	G0 T1 T1 D0 T5 T5

Table 2.1: Global line parameters. Single line parameters can be found in table 2.2. Especially important here are each of the 5 keys used to describe a type of calculations. These are the keys whose names end in “type”. These have been given their own tables 2.3 for line shape, 2.6 for cutoff, 2.7 for normalization, 2.8 for mirroring, and 2.9 for population distribution. Some important notes about this format. There exist a defined set of quantum numbers. You can only set numbers from these. Line mixing is inactive and all line mixing parameters are set to zero if the limit is positive and the pressure level is below this limit. The broadening species must have SELF first and AIR last to include self- and/or air-broadening. These keys are not required, and you must not have all species of the atmosphere defined either. The other broadening species can be any species that is available in ARTS general calculations but isotopologue are ignored. The temperature models are discussed in table 2.5.

### Basic expressions

The generic function in use for each individual line’s cross-section can now be presented as

$$\sigma = S(\cdots) (1 - iY + G) F(\cdots), \quad (2.30)$$

where  $S(\cdots)$  is the line strength,  $Y$  is the first order line mixing coefficient,  $G$  is the second order line mixing strength-adjusting coefficient, and  $F(\cdots)$  is the line shape model with undefined inputs. The input to  $F(\cdots)$  in part depends on the selection of line shape type, which can be seen in table 2.3, and in part to the single line data. Note the differences to Equation 2.1 is mostly the separation of the line mixing coefficients and the lack of the total number density. This change is done for efficiency and to help keep the code structure easy.

The only somewhat special input to the calculations of  $F(\cdots)$  of equation 2.30 is the Zeeman splitting. To compute the Zeeman splitting, where

$$\nu_z = \frac{\mu_B}{h} (g_{z1} M_1 - g_{z2} M_2) ||\vec{B}||, \quad (2.31)$$

where  $\mu_B$  is the Bohr magneton,  $h$  is the Planck constant,  $||\vec{B}||$  is the magnitude of the

Variables for individual lines		
Variable(s)	Description	Unit(s)
$\nu_0$	Line central (reference) frequency	Hz
$I_0$	Line strength at reference temperature	m <sup>2</sup> /Hz
$E_0$	Lower state (reference) energy	J
$g_1$	Lower statistical weight	-
$g_2$	Upper statistical weight	-
$A_{21}$	Einstein coefficient	1/s
$g_{z1}$	Lower state Zeeman splitting coefficient	-
$g_{z2}$	Upper state Zeeman splitting coefficient	-
Many different	Relevant line shape parameter coefficients	Hz/Pa; Hz/Pa <sup>2</sup> ;-
Many different	Relevant local quantum numbers	-

Table 2.2: Single line parameters. Global parameters can be found in table 2.1. The first 8 are floating point values. The relevant line shape parameters are also floating point values and there are 4 floating points per temperature model, even if said model requires fewer to perform its calculations. The relevant local quantum numbers are ratios — examples that work are 1 and 1/2 — and there is two numbers per quantum number defined in the local quantum number list. Note the special ratio 0/0 is considered as an undefined rational. If you need a quantum number but it is undefined in the catalog format you load into ARTS, then undefined behavior can ensue. The line shape parameter coefficients are described in table 2.5. A value is considered relevant if it has been given a key. The storage of these values are species first and then the tags as seen in table 2.4. The local quantum numbers of each line are ordered so that the lower state numbers are given before the upper state numbers.

Keys available for <code>lineshapetype</code>		
Key	Name	$F(\dots)$ -parameters (Eq. 2.30)
DP	Doppler profile	$\Gamma_D, \nu, \nu_0, \nu_z$
LP	Lorentz profile	$\Gamma_0, \Delta_0, \nu, \nu_0, \nu_z, \delta\nu$
VP	Voigt profile	$\Gamma_D, \Gamma_0, \Delta_0, \nu, \nu_0, \nu_z, \delta\nu$
SDVP	Speed-dependent VP	$\Gamma_D, \Gamma_0, \Delta_0, \Gamma_2, \Delta_2, \nu, \nu_0, \nu_z$
HTP	Hartman-Tran profile	$\Gamma_D, \Gamma_0, \Delta_0, \Gamma_2, \Delta_2, \eta, \nu_{VC}, \nu, \nu_0, \nu_z$

Table 2.3: Type of line profile solvers and their relevant parameters, where  $\Gamma_D$  is the Doppler broadening divided by  $\sqrt{\ln 2}$  (for practical reasons),  $\nu$  is the frequency,  $\nu_0$  is the central frequency,  $\nu_z$  is the Zeeman splitting,  $\Gamma_0$  is the speed-independent pressure broadening,  $\Delta_0$  is the speed-independent pressure broadening frequency shift,  $\delta\nu$  is the second order line mixing frequency shifting,  $\Gamma_2$  is the speed-dependent pressure broadening,  $\Delta_2$  is the speed-dependent pressure broadening frequency shift,  $\eta$  is the correlation factor, and  $\nu_{VC}$  is the the frequency of velocity-changing collisions.

magnetic field strength, and  $M \in [-J, -J + 1, \dots, J - 1, J]$ , where  $J$  is the rotational quantum number. Note that physics demands that  $J \geq 0$ , that  $|J_1 - J_2| \in [0, 1]$ , and that  $|M_1 - M_2| \in [0, 1]$ .

### Line shapes

The ellipsis arguments of  $F(\dots)$  depends in part on the `temperaturemodes` `AbsorptionLines` key. The relevant line shape parameter coefficients of table 2.2 are available as overview of the different parameters and their parameter keys in table 2.4 and the method to compute a single species single parameter is seen in table 2.5.

Keys available for model parameters in <code>temperaturemodes</code>		
Key	Variable	Description
G0	$\Gamma_0$	The speed-independent pressure broadening half-width
D0	$\Delta_0$	The speed-independent pressure broadening frequency shift
G2	$\Gamma_2$	The speed-dependent pressure broadening half-width
D2	$\Delta_2$	The speed-dependent pressure broadening frequency shift
ETA	$\eta$	The correlation parameter
FVC	$\nu_{VC}$	The the frequency of velocity-changing collisions
Y	$Y$	The the first order line mixing coefficient
G	$G$	The the second order line mixing strength-adjusting coefficient
DV	$\delta\nu$	The second order line mixing frequency shifting

Table 2.4: The model parameters of pressure broadening schemes in ARTS. These are the 9 values going into the line shape model  $F(\dots)$  that can be set from the catalog itself. The way these are computed depends on the selected temperature model as seen in table 2.5.

Keys available for temperature models in <code>temperaturemodes</code>		
Key	Parameters	Equation(s)
None		$X = 0$
T0	$x_0$	$X = x_0$
T1	$x_0, x_1, T_0, T$	$X = x_0 \left(\frac{T_0}{T}\right)^{x_1}$
T2	$x_0, x_1, x_2, T_0, T$	$X = x_0 \left(\frac{T_0}{T}\right)^{x_1} \left(1 + x_2 \log\left(\frac{T}{T_0}\right)\right)$
T3	$x_0, x_1, T_0, T$	$X = x_0 + x_1 (T - T_0)$
T4	$x_0, x_1, x_2, T_0, T$	$X = \left(x_0 + x_1 \left[\frac{T_0}{T} - 1\right]\right) \left(\frac{T_0}{T}\right)^{x_2}$
T5	$x_0, x_1, T_0, T$	$X = x_0 \left(\frac{T_0}{T}\right)^{1.5x_1 + 0.25}$
DPL	$x_0, x_1, x_2, x_3, T_0, T$	$X = x_0 \left(\frac{T_0}{T}\right)^{x_1} + x_2 \left(\frac{T_0}{T}\right)^{x_3}$
LM_AER	$x_0, x_1, x_2, x_3, T$	$X = x_0 + (T - 200) \frac{x_1 - x_0}{50} \quad \forall T < 250,$ $X = x_1 + (T - 250) \frac{x_2 - x_1}{46} \quad \forall 250 \leq T \leq 296, \text{ or}$ $X = x_2 + (T - 296) \frac{x_3 - x_2}{44} \quad \forall T > 296$

Table 2.5: The temperature models available for the model parameters. Multi-line equations are conditional.

The model parameters depend on several species. To therefore align them to the atmosphere the following expression is applied

$$X(T) = \frac{r_{\text{H}_2\text{O}} X_{\text{H}_2\text{O}}(T) + r_{\text{O}_2} X_{\text{O}_2}(T) + r_{\text{O}_3} X_{\text{O}_3}(T) + \dots + r_{\text{N}_2} X_{\text{N}_2}(T)}{r_{\text{H}_2\text{O}} + r_{\text{O}_2} + r_{\text{O}_3} + \dots + r_{\text{N}_2}} \quad (2.32)$$



where  $r$  indicates the ratio of the sub-indexed species at the path point, and the  $X(T)$  gives the value for the model parameter of the sub-indexed species. If air-broadening is present, the normalization step does not occur. However, note that in the somewhat odd scenario that air broadening is present but the sum of the ratio of the other species is above 1, then air broadening will act with a negative sign to still normalize the output. The above expression is scaled by the local pressure for most of the variables available in table 2.4. The three exceptions are  $\delta\nu$  and  $G$ , which are scaled by pressure-squared, and  $\eta$ , which is not scaled by the pressure at all.

There exist three additional features dealing with the use of equation 2.30. These are the cutoff frequency, the normalization factor, and 0-frequency mirroring.

The cutoff frequency can be found in table 2.6. When cutoff of the line shape model is desired, the output line shape model changes by

$$F_c(\dots) = F(\nu, \dots) - F(\nu_c, \dots), \quad (2.33)$$

where  $\nu_c$  is the cutoff frequency found in table 2.6.

Keys available for <code>cutofftype</code>	
Key	Cutoff frequency for the line
None	$\nu_c = \infty$
ByLine	$\nu_c = \nu_{c,0} + \nu_0$
ByBand	$\nu_c = \nu_{c,0}$

Table 2.6: Cutoff types, where  $\nu_{c,0}$  is the cutoff frequency from the global values and  $\nu_0$  the single line frequency. The cutoff calculations means that the entire line shape is computed once more at the indicated frequency and the result is removed from the individual line absorption profile.

When normalization factor is active, equation 2.30 is altered by using

$$F_n(\dots) = NF(\dots), \quad (2.34)$$

where  $N$  can be found in table 2.7.

Keys available for <code>normalizationtype</code>		
Key	Name	Normalization factor
None		$N = 1$
VVH	Van Vleck and Huber	$N = \frac{\nu}{\nu_0} \frac{\tanh\left(\frac{h\nu}{2kT}\right)}{\tanh\left(\frac{h\nu_0}{2kT}\right)}$
VVW	Van Vleck and Weiskopf	$N = \frac{\nu^2}{\nu_0^2}$
RQ	Rosenkranz quadratic	$N = \frac{\nu}{\nu_0} \frac{h\nu}{2kT} \frac{1}{\sinh\left(\frac{h\nu_0}{2kT}\right)}$

Table 2.7: Normalization types, where  $h$  is Planck's constant,  $\nu$  is the frequency,  $k$  is Boltzmann's constant,  $T$  is the temperature, and  $\nu_0$  is the central frequency. These factors are applied on a line-by-line basis.

Finally, if 0-frequency mirroring is applied, equation 2.30 is altered by using

$$F_m(\dots) = F(\nu_0, \dots) + F(-\nu_0, \dots), \quad (2.35)$$



where  $F(-\nu_0, \dots)$  is computed as described in table 2.8.

The three of the line shape altering equations can be combined together. If all three are active, equation 2.30 will read

$$\sigma = S(1 - iY + G) N [F(\nu, \nu_0) + F(\nu, -\nu_0) - F(\nu_c, \nu_0) - F(\nu_c, -\nu_0)], \quad (2.36)$$

where the ellipsis in  $F(\dots)$  and  $S(\dots)$  have been dropped due to lack of page space. We leave it to the reader to figure out the less complicated combinations. Note that the “None” option that exist for all of these three are not computed but the effect is instead ignored entirely to not risk introducing numerical bugs.

Keys available for <code>mirroringtype</code>	
Key	Description
None	There is no mirroring
Lorentz	There is a line at $-\nu_0$ treated as pure Lorentz profile
Same	There is a line at $-\nu_0$ treated the same as the line at $\nu_0$
Manual	This line should have a manual copy at $-\nu_0$ in the line catalog

Table 2.8: Mirroring type. Will perform computations as if there is a line at the negative central frequency.

### Line strengths

The last global key is the population types, `populationtype` of `AbsorptionLines`. These are found in table 2.9. They affect the computations of  $S(\dots)$  of equation 2.30. If the line level distribution is considered in local thermodynamic equilibrium, then

$$S_{LTE} = I_0 \frac{1 - e^{-h\nu_0/kT}}{1 - e^{-h\nu_0/kT_0}} e^{E_0(T-T_0)/kTT_0} \frac{Q(T_0)}{Q(T)}, \quad (2.37)$$

where  $Q(T)$  is the partition function at the given temperature. If only the vibrational level distribution is considered offset from local thermodynamic equilibrium, then

$$S_{Vib-NLTE}^{(abs)} = S_{LTE} \frac{e^{E_1(T-T_1)/kTT_1} - e^{E_2(T-T_2)/kTT_2} e^{-h\nu_0/kT}}{1 - e^{-h\nu_0/kT}}, \quad (2.38)$$

where  $E_1$  is the vibrational energy of the lower vibrational level,  $E_2$  is the vibrational energy of the upper vibrational level,  $T_1$  is the vibrational temperature of the Boltzmann distribution of the lower vibrational level, and  $T_2$  is the vibrational temperature of the Boltzmann distribution of the upper vibrational level. Note that as  $T_1$  and  $T_2$  approach  $T$ , the NLTE expression goes away. Finally, if the population type is considered to not be similar at all to the distribution by kinetic collisions, then the equation becomes

$$S_{NLTE}^{(abs)} = \frac{h\nu_0}{4\pi} \left( \frac{g_2}{g_1} r_1 - r_2 \right) A_{21} \left/ \frac{2h\nu_0^3}{c^2} \right., \quad (2.39)$$

where  $r_1$  is the lower state relative distribution, and  $r_2$  is the upper state relative distribution. In both the NLTE cases we have added the superscript of “(abs)” to indicate that we are separating absorption and source cross-sections when dealing with NLTE. We do this since the atmospheric emission and absorption no longer leads to a simple Planck function,

but must be considered different. The additional emission factor for the vibrational NLTE becomes

$$S_{Vib-NLTE}^{(src)} = e^{E_2(T-T_2)/kTT_2} S_{LTE} - S_{Vib-NLTE}^{(abs)}. \quad (2.40)$$

and

$$S_{NLTE}^{(src)} = \frac{h\nu_0}{4\pi} A_{21} r_2 \left/ \frac{2h\nu_0^3/c^2}{\exp(h\nu_0/kT) - 1} \right. - S_{NLTE}^{(abs)} \quad (2.41)$$

for the respective types. Note that we consider this an additional factor so that it is possible to mix different population types in all calculations. In the LTE case you would then simply not add anything to the source terms. Note that a special input method exist for all of the NLTE values. They are not considered part of the standard line catalog inputs. To match the NLTE values to the level, the isotopologue, and quantum numbers must be used to match the line catalog.

Keys available for <code>populationtype</code>	
Key	Description
LTE	The line is treated as if in local thermodynamic equilibrium
NLTE-VibrationalTemperatures	The line is in non-local thermodynamic equilibrium but can be described by vibrational temperature distributions
NLTE	The line is in non-local thermodynamic equilibrium entirety

Table 2.9: Population types. The total strength of the line is computed from the upper and lower population densities. This key determines how it is computed. Note that the two NLTE keys will require more information to be fed into ARTS to match the energy levels to the required distribution.

To both the NLTE and LTE line strengths, an additional Zeeman term will apply if the Zeeman effect is considered. This term is

$$S_z = S(\dots) \begin{pmatrix} J_1 & 1 & J_2 \\ M_1 & M_2 - M_1 & -M_2 \end{pmatrix} \begin{pmatrix} J_1 & 1 & J_2 \\ M_1 & M_2 - M_1 & -M_2 \end{pmatrix} C, \quad (2.42)$$

where  $C$  is 1.5 if  $M_2 \equiv M_1$  or 0.75 otherwise, and  $(:::)$  are Wigner symbols. Note that all combinations of  $M$  and  $J$  are automatically computed in ARTS and checked against the sum of unity.

### Line function algorithms

This subsection will go over systematically the various algorithms that are invoked to compute each stage of the equations we have been presenting so far. Note that the order of computations are to always set the line shape functions first.

### Doppler line shape (`lineshapetype` is DP)

The Doppler line shape algorithm is just as simple as its equations in the theory section implies

$$F(\Gamma_D, \nu, \nu_0, \nu_z) = \frac{1}{\sqrt{\pi}\Gamma_D} e^{-x^2}, \quad (2.43)$$

where

$$x = \frac{\nu - \nu_0 - \nu_z}{\Gamma_D} \quad (2.44)$$

The only non-zero derivatives considered are for frequency, temperature, and line center. We do not have an algorithm that returns the phase of the line shape for the Doppler algorithm so the magnetic derivative is ignored. This might change in the future. The forward calculations are still mostly good for a quick overview, which is the main use of the Doppler line shape anyways. The frequency derivative is found as

$$\frac{\partial}{\partial \nu} F(\Gamma_D, \nu, \nu_0, \nu_z) = -\frac{2x}{\Gamma_D} F(\Gamma_D, \nu, \nu_0, \nu_z). \quad (2.45)$$

The temperature derivative is found as

$$\frac{\partial}{\partial T} F(\Gamma_D, \nu, \nu_0, \nu_z) = -\frac{\nu_0}{\Gamma_D} \frac{\partial \Gamma_D}{\partial T} [2x^2 F(\Gamma_D, \nu, \nu_0, \nu_z) + F(\Gamma_D, \nu, \nu_0, \nu_z)]. \quad (2.46)$$

The line center derivative is found as

$$\frac{\partial}{\partial \nu_0} F(\Gamma_D, \nu, \nu_0, \nu_z) = -\frac{2x^2}{\nu_0} F(\Gamma_D, \nu, \nu_0, \nu_z) + \left( \frac{1}{\Gamma_D} - \frac{1}{\nu_0} \right) 2x F(\Gamma_D, \nu, \nu_0, \nu_z). \quad (2.47)$$

### **Lorentz line shape (lineshapetype is LP)**

The Lorentz line shape algorithm is handled in complex numbers contrary to the theory section. This allows line mixing. The function is

$$F(\Gamma_0, \Delta_0, \nu, \nu_0, \nu_z, \delta\nu) = \frac{1}{z}, \quad (2.48)$$

where

$$z = \pi\Gamma_0 + i\pi(\nu_0 + \Delta_0 + \nu_z + \delta\nu - \nu). \quad (2.49)$$

The relevant derivatives are for the temperature, the frequency, the line center, the pressure broadening parameters  $\Gamma_0$  and  $\Delta_0$ , the magnetic field strength, and for the volume mixing ratio. Each of these will look fairly similar, so a helper variable is set up as

$$\Delta_F = -\pi [F(\Gamma_0, \Delta_0, \nu, \nu_0, \nu_z, \delta\nu)]^2. \quad (2.50)$$

The temperature derivative is found as

$$\frac{\partial}{\partial T} F(\Gamma_0, \Delta_0, \nu, \nu_0, \nu_z, \delta\nu) = \left( \frac{\partial \Gamma_0}{\partial T} + i \frac{\partial \Delta_0}{\partial T} + i \frac{\partial \delta\nu}{\partial T} \right) \Delta_F. \quad (2.51)$$

The frequency derivative is found as

$$\frac{\partial}{\partial \nu} F(\Gamma_0, \Delta_0, \nu, \nu_0, \nu_z, \delta\nu) = -i \Delta_F. \quad (2.52)$$

The line center derivative is found as

$$\frac{\partial}{\partial \nu_0} F(\Gamma_0, \Delta_0, \nu, \nu_0, \nu_z, \delta\nu) = i\Delta_F. \quad (2.53)$$

The  $\Gamma_0$  derivative is found as

$$\frac{\partial}{\partial \Gamma_0} F(\Gamma_0, \Delta_0, \nu, \nu_0, \nu_z, \delta\nu) = \Delta_F. \quad (2.54)$$

The  $\Delta_0$  derivative is found as

$$\frac{\partial}{\partial \Delta_0} F(\Gamma_0, \Delta_0, \nu, \nu_0, \nu_z, \delta\nu) = i\Delta_F. \quad (2.55)$$

The magnetic field strength derivative is found as

$$\frac{\partial}{\partial \|\vec{B}\|} F(\Gamma_0, \Delta_0, \nu, \nu_0, \nu_z, \delta\nu) = i \frac{\mu_B}{h} (g_{z1} M_1 - g_{z2} M_2) \Delta_F. \quad (2.56)$$

The volume mixing ratio derivative is found as

$$\frac{\partial}{\partial r} F(\Gamma_0, \Delta_0, \nu, \nu_0, \nu_z, \delta\nu) = \left( \frac{\partial \Gamma_0}{\partial r} + i \frac{\partial \Delta_0}{\partial r} + i \frac{\partial \delta\nu}{\partial r} \right) \Delta_F. \quad (2.57)$$

#### **Voigt line shape (lineshapetype is VP)**

The Voigt line shape profile also handles complex numbers contrary to the theory. The Voigt profile is computed using an external Faddeeva function package developed by *Za-ghloul and Ali* [2012] and implemented into C++ by Steven G. Johnson. The Voigt profile is

$$F(\Gamma_D, \Gamma_0, \Delta_0, \nu, \nu_0, \nu_z, \delta\nu) = \frac{w(z)}{\sqrt{\pi}\Gamma_D}, \quad (2.58)$$

where  $w(z)$  is the Faddeeva function and

$$z = \frac{\nu - \nu_0 - \nu_z - \Delta_0 - \delta\nu + i\Gamma_0}{\Gamma_D}. \quad (2.59)$$

The derivatives that matter to the Voigt algorithm are the same as those that matters for the Lorentz algorithm. Many of these derivatives will look very similar so a helper variable is set up as

$$\Delta_F = \frac{2i}{\pi\Gamma_D} - 2zF(\Gamma_D, \Gamma_0, \Delta_0, \nu, \nu_0, \nu_z, \delta\nu). \quad (2.60)$$

One problem presenting these derivatives is that many of the expression consist of three or more sub-expressions. For the remaining part of this algorithm please read  $F$  as the computed Voigt profile. The frequency derivative is

$$\frac{\partial}{\partial \nu} F = \frac{1}{\Gamma_D} \Delta_F. \quad (2.61)$$

The temperature derivative is

$$\frac{\partial}{\partial T} F = \frac{1}{\Gamma_D} \left( i \frac{\partial \Gamma_0}{\partial T} - \frac{\partial \Delta_0}{\partial T} - \frac{\partial \delta\nu}{\partial T} \right) \Delta_F - \frac{\partial \Gamma_D}{\partial T} \frac{1}{\Gamma_D} [F + z\Delta_F]. \quad (2.62)$$

The line center derivative is

$$\frac{\partial}{\partial \nu_0} F = -\frac{F}{\nu_0} - \frac{\Delta_F}{\Gamma_D} - \frac{z \Delta_F}{\nu_0} \quad (2.63)$$

The  $\Gamma_0$  derivative is

$$\frac{\partial}{\partial \Gamma_0} F = i \frac{\Delta_F}{\Gamma_D}. \quad (2.64)$$

The  $\Delta_0$  derivative is

$$\frac{\partial}{\partial \Delta_0} F = -\frac{\Delta_F}{\Gamma_D}. \quad (2.65)$$

The magnetic field strength derivative is

$$\frac{\partial}{\partial \|\vec{B}\|} F = -\frac{\mu_B}{h} (g_{z1} M_1 - g_{z2} M_2) \frac{\Delta_F}{\Gamma_D}. \quad (2.66)$$

The volume mixing ratio derivative is

$$\frac{\partial}{\partial r} F = \frac{1}{\Gamma_D} \left( i \frac{\partial \Gamma_0}{\partial r} - \frac{\partial \Delta_0}{\partial r} - \frac{\partial \delta \nu}{\partial r} \right) \Delta_F. \quad (2.67)$$

### Hartmann-Tran line shape (lineshapetype is SDVP or HTP)

The algorithm from the original paper by *Tran et al. [2013]*. This algorithm is chained and conditioned because the main algorithm reach many mathematical limits. One of these limits is the speed dependent Voigt line shape. There is still limited experience in the ARTS development community for applications of this type of line shape so many small bugs might be present and not rooted out.

The main HTP expression that holds in all cases is

$$F(\Gamma_D, \Gamma_0, \Delta_0, \Gamma_2, \Delta_2, \eta, \nu_{VC}, \nu, \nu_0, \nu_z, \delta \nu) = \quad (2.68)$$

$$F = \frac{1}{\pi} \frac{A}{[(C_0 - 3C_2/2)\eta - \nu_{VC}]A + \eta C_2 B + 1}$$

where

$$C_0 = \Gamma_0 - i\Delta_0 \quad (2.69)$$

and

$$C_2 = \Gamma_2 - i\Delta_2. \quad (2.70)$$

Now it will soon get complicated by branching out depending on values. Before going into the conditional branches, these are constant in all of the expressions that will follow

$$y = \left( \frac{1}{2 \sqrt{\ln 2} (1 - \eta) C_2 / \Gamma_D} \right)^2, \quad (2.71)$$

and

$$x = \frac{(1 - \eta) (C_0 - 3C_2/2) + \nu_{VC} + i\nu - i\nu_0 - i\nu_z}{(1 - \eta) C_2}. \quad (2.72)$$

Normally, that is if all numbers are reasonable large and normal,

$$A = \sqrt{\pi} \frac{\sqrt{\ln 2}}{\Gamma_D} [w(iz_1) - w(iz_2)] \quad (2.73)$$

and

$$B = \frac{\sqrt{\pi} [(1 - z_1^2) w(iz_1) - (1 - z_2^2) w(iz_2)] / 2\sqrt{y} - 1}{(1 - \eta) C_2}, \quad (2.74)$$

where  $z_1 = \sqrt{x+y} - \sqrt{y}$  and  $z_2 = \sqrt{x+y} + \sqrt{y}$ . This is marked as case 1 below for the description of the derivatives.

If  $|y| \leq 10^{-15}|x|$  but all other numbers are reasonably large and normal, then if  $|\sqrt{x}| \leq 4000$

$$A = \frac{2\sqrt{\pi}}{(1 - \eta) C_2} \left( \frac{1}{\sqrt{\pi}} - z_b w(iz_b) \right) \quad (2.75)$$

and

$$B = \frac{2\sqrt{\pi} [(1 - x - 2y) (1/\sqrt{\pi} - z_b w(iz_b)) + z_1 w(iz_1)] - 1}{(1 - \eta) C_2}, \quad (2.76)$$

where  $z_1 = \sqrt{x+y}$  and  $z_b = \sqrt{x}$ . This is marked as case 2.1 below for the description of the derivatives. Still if  $|y| \leq 1e-15|x|$  but all other numbers are reasonably large and normal, then if  $|\sqrt{x}| > 4000$

$$A = \frac{1/x - 3/2x^2}{(1 - \eta) C_2} \quad (2.77)$$

and

$$B = \frac{(1 - x - 2y) (1/x - 3/2x^2) + 2\sqrt{\pi} z_1 w(iz_1) - 1}{(1 - \eta) C_2}, \quad (2.78)$$

with  $z_1 = \sqrt{x+y}$ . This is marked as case 2.2 below for the description of the derivatives.

If  $|x| \leq 3 \times 10^{-8}|y|$  and the other numbers are normal then

$$A = \sqrt{\pi} \frac{\sqrt{\ln 2}}{\Gamma_D} [w(iz_1) - w(iz_2)] \quad (2.79)$$

and

$$B = \frac{\sqrt{\pi} [(1 - z_1^2) w(iz_1) - (1 - z_2^2) w(iz_2)] / 2\sqrt{y} - 1}{(1 - \eta) C_2}, \quad (2.80)$$

with  $z_1 = \sqrt{\ln 2} [i\nu - i\nu_0 - i\nu_z + (1 - \eta) (C_0 - 3C_2/2) + \nu_{VC}] / \Gamma_D$  and  $z_2 = \sqrt{x+y} + \sqrt{y}$ . This is marked as case 3 below for the description of the derivatives.

Lastly, if  $(1 - \eta) C_2 \equiv 0$ , then

$$A = \sqrt{\pi} \frac{\sqrt{\ln 2}}{\Gamma_D} w(iz_1) \quad (2.81)$$

with  $z_1 = \sqrt{\ln 2} [i\nu - i\nu_0 - i\nu_z + (1 - \eta)(C_0 - 3C_2/2) + \nu_{VC}] / \Gamma_D$ . If  $|z_1| \leq 4000$  then

$$B = \sqrt{\pi} \frac{\sqrt{\ln 2}}{\Gamma_D} \left[ (1 - z_1^2) w(iz_1) + \frac{z_1}{\sqrt{\pi}} \right] \quad (2.82)$$

otherwise if  $|z_1| > 4000$

$$B = \frac{\sqrt{\ln 2}}{\Gamma_D} \left[ \sqrt{\pi} w(iz_1) + \frac{1}{2z_1} - \frac{3}{4z_1^3} \right]. \quad (2.83)$$

These are marked as case 4.1 and 4.2, respectively, below for the description of the derivatives.

The main derivative of HTP still follows from the main expression and will look like this beast of an equation

$$\begin{aligned} \frac{\partial}{\partial t} F = & \frac{\frac{\partial A}{\partial t} / \pi \{[(C_0 - 3C_2/2)\eta - \nu_{VC}]A + \eta C_2 B + 1\} -}{\left[ (C_0 - 3C_2/2) \frac{\partial \eta}{\partial t} + \left( \frac{\partial C_0}{\partial t} - 3 \frac{\partial C_2}{\partial t} / 2 \right) \eta - \frac{\partial \nu_{VC}}{\partial t} \right] A +} \\ & \eta C_2 \frac{\partial B}{\partial t} \Big\} A / \pi \{[(C_0 - 3C_2/2)\eta - \nu_{VC}]A + \eta C_2 B + 1\}^2, \end{aligned} \quad (2.84)$$

where  $t$  represents an arbitrary variable. The derivatives that matter to the HTP algorithm are the same as those that matters for the Lorentz algorithm, with the addition of the 4 additional pressure broadening variables. Note that for many of these, several of the inputs to the above will be zero.

Going over the four generic variables defined before the branching above,

$$\begin{aligned} \frac{\partial}{\partial T} C_0 &= \frac{\partial \Gamma_0}{\partial T} - i \frac{\partial \Delta_0}{\partial T} \\ \frac{\partial}{\partial r} C_0 &= \frac{\partial \Gamma_0}{\partial r} - i \frac{\partial \Delta_0}{\partial r} \\ \frac{\partial}{\partial \Gamma_0} C_0 &= 1 \\ \frac{\partial}{\partial \Delta_0} C_0 &= -i \\ \frac{\partial}{\partial t} C_0 &= 0, \end{aligned} \quad (2.85)$$

where  $t$  is from now on any other derivative than those previously defined in an expression. Likewise,

$$\begin{aligned} \frac{\partial}{\partial T} C_2 &= \frac{\partial \Gamma_2}{\partial T} - i \frac{\partial \Delta_2}{\partial T} \\ \frac{\partial}{\partial r} C_2 &= \frac{\partial \Gamma_2}{\partial r} - i \frac{\partial \Delta_2}{\partial r} \\ \frac{\partial}{\partial \Gamma_2} C_2 &= 1 \\ \frac{\partial}{\partial \Delta_2} C_2 &= -i \\ \frac{\partial}{\partial t} C_2 &= 0. \end{aligned} \quad (2.86)$$

For the two constant expressions,

$$\frac{\partial}{\partial t} y = -2 \left[ \frac{1}{\Gamma_D} \frac{\partial \Gamma_D}{\partial t} + \left( \frac{\partial \eta}{\partial t} C_2 + (1 - \eta) \frac{\partial C_2}{\partial t} \right) / (1 - \eta) C_2 \right] y, \quad (2.87)$$

and

$$\begin{aligned}
\frac{\partial}{\partial \|\vec{B}\|} x &= -\frac{i\mu_B(g_{z1}M_1 - g_{z2}M_2)/h}{(1-\eta)C_2} \\
\frac{\partial}{\partial \nu_0} x &= -\frac{i}{(1-\eta)C_2} \\
\frac{\partial}{\partial \nu} x &= -\frac{i}{(1-\eta)C_2} \\
\frac{\partial}{\partial t} x &= \frac{\frac{\partial \nu_{VC}}{\partial t} - (C_0 - 3C_2/2) \frac{\partial \eta}{\partial t} + (1-\eta) \left( \frac{\partial C_0}{\partial t} - 3 \frac{\partial C_2}{\partial t} / 2 \right)}{(1-\eta)C_2} - \frac{(1-\eta) \frac{\partial C_2}{\partial t} - \frac{\partial \eta}{\partial t} C_2}{(1-\eta)C_2} x.
\end{aligned} \tag{2.88}$$

Before branching, this replacement will be used throughout the expressions

$$\Delta_{w(iz)} = -2 \left[ \frac{1}{\sqrt{\pi}} - zw(iz) \right] \frac{\partial z}{\partial t}. \tag{2.89}$$

In case 1,

$$\frac{\partial}{\partial t} A = \sqrt{\pi} \left[ (w(iz_1) - w(iz_2)) \frac{\sqrt{\ln 2}}{\Gamma_D} \frac{\partial \Gamma_D}{\partial t} + (\Delta_{w(iz_1)} - \Delta_{w(iz_2)}) \frac{\sqrt{\ln 2}}{\Gamma_D} \right], \tag{2.90}$$

and

$$\begin{aligned}
\frac{\partial}{\partial t} B &= \frac{\frac{\sqrt{\pi}[(z_1^2-1)w(iz_1) - (z_2^2-1)w(iz_2)] \frac{\partial y}{\partial t} + 4\sqrt{y^3}(1-\eta)C_2}{\sqrt{\pi}[-(z_1^2-1)\Delta_{w(iz_1)} + (z_2^2-1)\Delta_{w(iz_2)} - 2w(iz_1)z_1 \frac{\partial z_1}{\partial t} + 2w(iz_2)z_2 \frac{\partial z_2}{\partial t}]} + \frac{[ \sqrt{\pi}(z_1^2-1)w(iz_1) - \sqrt{\pi}(z_2^2-1)w(iz_2) + 2\sqrt{y} ] \left[ (1-\eta) \frac{\partial C_2}{\partial t} - \frac{\partial \eta}{\partial t} C_2 \right]}{2\sqrt{y}[(1-\eta)C_2]^2}}{2\sqrt{y}(1-\eta)C_2} + \tag{2.91}
\end{aligned}$$

The remaining derivatives for case 1 are, for completeness,

$$\frac{\partial}{\partial t} z_1 = -\frac{\partial y}{\partial t} / 2\sqrt{y} + \left( \frac{\partial x}{\partial t} + \frac{\partial y}{\partial t} \right) / 2\sqrt{x+y} \tag{2.92}$$

and

$$\frac{\partial}{\partial t} z_2 = \frac{\partial y}{\partial t} / 2\sqrt{y} + \left( \frac{\partial x}{\partial t} + \frac{\partial y}{\partial t} \right) / 2\sqrt{x+y}. \tag{2.93}$$

In case 2.1,

$$\frac{\partial}{\partial t} A = \frac{-\sqrt{\pi} \left[ w(iz_b) \frac{\partial x}{\partial t} + 2x \Delta_{w(iz_b)} \right]}{\sqrt{x}(1-\eta)C_2} + \frac{2(\sqrt{\pi}w(iz_b)\sqrt{x}-1) \left[ (1-\eta) \frac{\partial C_2}{\partial t} - \frac{\partial \eta}{\partial t} C_2 \right]}{[(1-\eta)C_2]^2}, \tag{2.94}$$

and

$$\begin{aligned}
\frac{\partial}{\partial t} B &= \frac{\frac{-[2(\sqrt{\pi}w(iz_b)\sqrt{x}-1)(x+2y-1) + 2\sqrt{\pi}\sqrt{x+y}w(iz_1)-1] \left[ (1-\eta) \frac{\partial C_2}{\partial t} - \frac{\partial \eta}{\partial t} C_2 \right]}{[(1-\eta)C_2]^2} + \frac{2[(\sqrt{\pi}w(iz_b)\sqrt{x}-1) \left( \frac{\partial x}{\partial t} + 2 \frac{\partial y}{\partial t} \right) \sqrt{\pi}\sqrt{x+y} \Delta_{w(iz_1)}]}{(1-\eta)C_2}}{\sqrt{x} + \sqrt{\pi} \left( w(iz_b) \frac{\partial x}{\partial t} + 2x \Delta_{w(iz_b)} \right) (x+2y-1)} + \frac{\sqrt{\pi} \left( \frac{\partial x}{\partial t} + \frac{\partial y}{\partial t} \right) w(iz_1)}{\sqrt{x+y}(1-\eta)C_2}, \tag{2.95}
\end{aligned}$$

with

$$\frac{\partial}{\partial t} z_b = \frac{\partial x}{\partial t} / 2\sqrt{x}. \tag{2.96}$$



In case 2.2,

$$\frac{\partial}{\partial t} A = \frac{(3-x)(1-\eta)C_2 \frac{\partial x}{\partial t} - (x-3/2)x \left[ (1-\eta) \frac{\partial C_2}{\partial t} - \frac{\partial \eta}{\partial t} C_2 \right]}{x^3 [(1-\eta)C_2]^2} \quad (2.97)$$

and

$$\begin{aligned} \frac{\partial}{\partial t} B = & \frac{\left[ (-2\sqrt{\pi}\sqrt{x+y}w(iz_1)+1)x^2+(x-3/2)(x+2y-1) \right] \left[ (1-\eta) \frac{\partial C_2}{\partial t} - \frac{\partial \eta}{\partial t} C_2 \right]}{x^2 [(1-\eta)C_2]^2} + \\ & \frac{(x-3)(x+2y-1) \frac{\partial x}{\partial t} - (x-3/2) \left( \frac{\partial x}{\partial t} + 2 \frac{\partial y}{\partial t} \right) x}{x^3 (1-\eta)C_2} + \\ & \frac{\sqrt{\pi} [2(x+y)\Delta_{w(iz_1)} + (\frac{\partial x}{\partial t} + \frac{\partial y}{\partial t})w(iz_1)]}{\sqrt{x+y}(1-\eta)C_2}. \end{aligned} \quad (2.98)$$

In both case 2.1 and 2.2,

$$\frac{\partial}{\partial t} z_1 = \left[ \frac{\partial x}{\partial t} + \frac{\partial y}{\partial t} \right] / 2\sqrt{x+y}. \quad (2.99)$$

In case 3,

$$\frac{\partial}{\partial t} A = \sqrt{\pi} \left[ (w(iz_1) - w(iz_2)) \frac{\sqrt{\ln 2}}{\Gamma_D} \frac{\partial \Gamma_D}{\partial t} + (\Delta_{w(iz_1)} - \Delta_{w(iz_2)}) \frac{\sqrt{\ln 2}}{\Gamma_D} \right] \quad (2.100)$$

and

$$\begin{aligned} \frac{\partial}{\partial t} B = & \frac{\sqrt{\pi} [(z_1^2-1)w(iz_1) - (z_2^2-1)w(iz_2)] \frac{\partial y}{\partial t}}{4\sqrt{y^3}(1-\eta)C_2} + \\ & \frac{\sqrt{\pi} 2 [-(z_1^2-1)\Delta_{w(iz_1)} + (z_2^2-1)\Delta_{w(iz_2)} - 2w(iz_1)z_1 \frac{\partial z_1}{\partial t} + 2w(iz_2)z_2 \frac{\partial z_2}{\partial t}]}{4\sqrt{y}(1-\eta)C_2} + \\ & \frac{[\sqrt{\pi}(z_1^2-1)w(iz_1) - \sqrt{\pi}(z_2^2-1)w(iz_2) + 2\sqrt{y}] \left[ (1-\eta) \frac{\partial C_2}{\partial t} - \frac{\partial \eta}{\partial t} C_2 \right]}{2\sqrt{y} [(1-\eta)C_2]^2}, \end{aligned} \quad (2.101)$$

with

$$\begin{aligned} \frac{\partial}{\partial \|B\|} z_1 &= -i\sqrt{\ln 2} i\mu_B (g_{z_1} M_1 - g_{z_2} M_2) / h\Gamma_D \\ \frac{\partial}{\partial \nu_0} z_1 &= -i \sqrt{\ln 2} / \Gamma_D \\ \frac{\partial}{\partial \nu} z_1 &= i \sqrt{\ln 2} / \Gamma_D \\ \frac{\partial}{\partial t} z_1 &= [i\nu - i\nu_0 - i\nu_z + (1-\eta)(C_0 - 3C_2/2) + \nu_{VC}] \frac{\sqrt{\ln 2}}{\Gamma_D} \frac{\partial \Gamma_D}{\partial t} + \\ & \frac{\sqrt{\ln 2}}{\Gamma_D} \left[ (1-\eta) \left( \frac{\partial C_0}{\partial t} - 3 \frac{\partial C_2}{\partial t} / 2 \right) - \frac{\partial \eta}{\partial t} (C_0 - 3C_2/2) + \frac{\partial \nu_{VC}}{\partial t} \right] \end{aligned} \quad (2.102)$$

and

$$\frac{\partial}{\partial t} z_2 = \frac{\partial y}{\partial t} / 2\sqrt{y} + \left( \frac{\partial x}{\partial t} + \frac{\partial y}{\partial t} \right) / 2\sqrt{x+y}. \quad (2.103)$$

In both case 4.1 and case 4.2,

$$\frac{\partial}{\partial t} A = \sqrt{\pi} \left( w(iz_1) \frac{\sqrt{\ln 2}}{\Gamma_D} \frac{\partial \Gamma_D}{\partial t} + \frac{\sqrt{\ln 2}}{\Gamma_D} \Delta_{w(iz_1)} \right). \quad (2.104)$$

For case 4.1,

$$\frac{\partial}{\partial t} B = - \left\{ \sqrt{\pi} \left[ (z_1^2 - 1) \Delta_{w(iz_1)} + 2w(iz_1) z_1 \frac{\partial z_1}{\partial t} \right] - \frac{\partial z_1}{\partial t} \right\} \frac{\sqrt{\ln 2}}{\Gamma_D} - \left[ \sqrt{\pi} (z_1^2 - 1) w(iz_1) - z_1 \right] \frac{\sqrt{\ln 2}}{\Gamma_D} \frac{\partial \Gamma_D}{\partial t} \quad (2.105)$$

and for case 4.2,

$$\frac{\partial}{\partial t} B = \left( \sqrt{\pi} w(iz_1) z_1^3 + z_1^2/2 - 3/4 \right) \frac{\sqrt{\ln 2}}{\Gamma_D} \frac{\partial \Gamma_D}{\partial t} / z_1^3 + \left( \sqrt{\pi} z_1^4 \Delta_{w(iz_1)} - z_1^2/2 \frac{\partial z_1}{\partial t} + 9 \frac{\partial z_1}{\partial t} / 4 \right) \frac{\sqrt{\ln 2}}{\Gamma_D} / z_1^4 \quad (2.106)$$

with

$$\begin{aligned} \frac{\partial}{\partial ||\vec{B}||} z_1 &= -i \sqrt{\ln 2} i \mu_B (g_{z_1} M_1 - g_{z_2} M_2) / h \Gamma_D \\ \frac{\partial}{\partial \nu_0} z_1 &= -i \sqrt{\ln 2} / \Gamma_D \\ \frac{\partial}{\partial \nu} z_1 &= i \sqrt{\ln 2} / \Gamma_D \\ \frac{\partial}{\partial t} z_1 &= [i\nu - i\nu_0 - i\nu_z + (1 - \eta) (C_0 - 3C_2/2) + \nu_{VC}] \frac{\sqrt{\ln 2}}{\Gamma_D} \frac{\partial \Gamma_D}{\partial t} + \frac{\sqrt{\ln 2}}{\Gamma_D} \left[ (1 - \eta) \left( \frac{\partial C_0}{\partial t} - 3 \frac{\partial C_2}{\partial t} / 2 \right) - \frac{\partial \eta}{\partial t} (C_0 - 3C_2/2) + \frac{\partial \nu_{VC}}{\partial t} \right]. \end{aligned} \quad (2.107)$$

#### Van Vleck and Huber normalization (normalizationtype is VVH)

The van Vleck and Huber algorithm modifies the line shape calculations. It computes

$$N = \frac{\nu \tanh(h\nu/2kT)}{\nu_0 \tanh(h\nu_0/2kT)}, \quad (2.108)$$

It adds its own derivatives in the form of temperature, frequency, and line center. The derivatives are

$$\begin{aligned} \frac{\partial}{\partial T} [NF] &= -\frac{h}{2kT^2} \left\{ \left[ \nu_0 \tanh\left(\frac{h\nu_0}{2kT}\right) - \frac{\nu_0}{\tanh(h\nu_0/2kT)} \right] N \right. \\ &\quad \left. \nu_0 \tanh\left(\frac{h\nu_0}{2kT}\right) N^2 + \frac{\nu N}{\tanh(h\nu/2kT)} \right\} F + N \frac{\partial F}{\partial T} \\ \frac{\partial}{\partial \nu} [NF] &= \left\{ \frac{1}{\nu} + \frac{h}{2kT} \left[ \frac{1}{\tanh(h\nu/2kT)} - \tanh\left(\frac{h\nu}{2kT}\right) \right] \right\} NF + N \frac{\partial F}{\partial \nu} \\ \frac{\partial}{\partial \nu} [NF] &= \left\{ \frac{1}{\nu_0} + \frac{h}{2kT} \left[ \tanh\left(\frac{h\nu_0}{2kT}\right) - \frac{1}{\tanh(h\nu_0/2kT)} \right] \right\} NF + N \frac{\partial F}{\partial \nu_0} \\ \frac{\partial}{\partial t} [NF] &= N \frac{\partial F}{\partial t}, \end{aligned} \quad (2.109)$$

where  $F$  and  $[\partial F/\partial T; \partial F/\partial \nu; \partial F/\partial \nu_0; \partial F/\partial t]$  are set in a line shape algorithm.

#### Van Vleck and Weiskopf normalization (normalizationtype is VVW)

The van Vleck and Weiskopf algorithm modifies the line shape calculations. It computes

$$N = \frac{\nu^2}{\nu_0^2}, \quad (2.110)$$

meaning it adds frequency and line center derivatives. The derivatives are

$$\begin{aligned} \frac{\partial}{\partial \nu} [NF] &= \frac{2}{\nu} NF + N \frac{\partial F}{\partial \nu} \\ \frac{\partial}{\partial \nu_0} [NF] &= -\frac{2}{\nu_0} NF + N \frac{\partial F}{\partial \nu_0} \\ \frac{\partial}{\partial t} [NF] &= N \frac{\partial F}{\partial \nu_0} \end{aligned} \quad (2.111)$$

where  $F$  and  $[\partial F/\partial \nu; \partial F/\partial \nu_0; \partial F/\partial t]$  are set in a line shape algorithm.

**Rosenkranz quadratic normalization (normalizationtype is RQ)**

The Rosenkranz quadratic algorithm modifies the line shape calculations. It computes

$$N = \frac{\nu^2}{h\nu_0 \sinh(h\nu_0/2kT)/2kT}, \quad (2.112)$$

meaning it adds the same derivatives as the van Vleck and Huber methods. The derivatives are

$$\begin{aligned} \frac{\partial}{\partial T} [NF] &= -\frac{kT - h\nu_0/2 \tanh(h\nu_0/2kT)}{kT^2} NF + N \frac{\partial F}{\partial T} \\ \frac{\partial}{\partial \nu} [NF] &= \frac{2}{\nu} NF + N \frac{\partial F}{\partial \nu} \\ \frac{\partial}{\partial \nu_0} [NF] &= \left[ -\frac{1}{\nu_0} - h/2kT \tanh(h\nu_0/2kT) \right] NF + N \frac{\partial F}{\partial \nu_0} \\ \frac{\partial}{\partial t} [NF] &= N \frac{\partial F}{\partial t}, \end{aligned} \quad (2.113)$$

where  $F$  and  $[\partial F/\partial T; \partial F/\partial \nu; \partial F/\partial \nu_0; \partial F/\partial t]$  are set in a line shape algorithm.

**LTE line strength (populationtype is LTE)**

The main equation of the LTE line strength is

$$S_{LTE} = I_0 \frac{1 - e^{-h\nu_0/kT}}{1 - e^{-h\nu_0/kT_0}} e^{E_0(T-T_0)/kTT_0} \frac{Q(T_0)}{Q(T)}. \quad (2.114)$$

It adds its own derivatives in the form of temperature, line strength, and line center. The derivatives are

$$\begin{aligned} \frac{\partial}{\partial T} [SNF]_{LTE} &= S \left( \frac{NF}{kT^2} \left[ E_0 - \frac{h\nu_0 e^{-h\nu_0/kT}}{1 - e^{-h\nu_0/kT}} \right] - \frac{NF}{Q(T)} \frac{\partial Q(T)}{\partial T} + \frac{\partial [NF]}{\partial T} \right) \\ \frac{\partial}{\partial I_0} [SNF]_{LTE} &= \frac{SNF}{I_0} \\ \frac{\partial}{\partial \nu_0} [SNF]_{LTE} &= S \left( \frac{-hNF}{(1 - e^{-h\nu_0/kT})} \left[ \frac{e^{-h\nu_0/kT_0}}{kT_0} - \frac{e^{-h\nu_0/kT}}{kT} \right] + \frac{\partial [NF]}{\partial \nu_0} \right) \\ \frac{\partial}{\partial t} [SNF]_{LTE} &= S \frac{\partial}{\partial t} [NF]. \end{aligned} \quad (2.115)$$

Note that  $NF$  is here assumed set by one of the normalization functions. If no normalization function is used, this is considered equivalent to  $N := 1$ . Note that  $S = S_{LTE}$ . All source ratios are set to zero by this algorithm.

**NLTE line strength with vibrational temperatures (populationtype is NLTE-VibrationalTemperatures)**

The main equation of the NLTE line strength with vibrational temperatures is

$$S_{Vib-NLTE}^{(abs)} = S_{LTE} \frac{e^{E_1(T-T_1)/kTT_1} - e^{E_2(T-T_2)/kTT_2} e^{-h\nu_0/kT}}{1 - e^{-h\nu_0/kT}}. \quad (2.116)$$

It adds its own derivatives in the form of temperature, line strength, line center, and the

vibrational temperatures. The derivatives are

$$\begin{aligned}
\frac{\partial}{\partial T} [SNF]^{(abs)} &= \frac{S}{S_{LTE}} \frac{\partial}{\partial T} [SNF]_{LTE} - SNF \left[ \frac{(h\nu_0)^2 e^{-\frac{h\nu_0}{kT}} (e^{E_1(T-T_1)/kTT_1} - e^{E_2(T-T_2)/kTT_2})}{kT^2 (e^{-h\nu_0/kT} - 1)^2} - \right. \\
&\quad \left. \frac{h\nu_0 (E_1 e^{E_1(T-T_1)/kTT_1} - E_2 e^{-\frac{h\nu_0}{kT}} e^{E_2(T-T_2)/kTT_2})}{kT^2 (e^{-h\nu_0/kT} - 1)} \right] \\
\frac{\partial}{\partial I_0} [SNF]^{(abs)} &= \frac{SNF}{I_0} \\
\frac{\partial}{\partial \nu_0} [SNF]^{(abs)} &= \frac{S}{S_{LTE}} \frac{\partial}{\partial \nu_0} [SNF]_{LTE} - \frac{h e^{-h\nu_0/kT} (e^{E_1(T-T_1)/kTT_1} - e^{E_2(T-T_2)/kTT_2})}{kT^2 (e^{-h\nu_0/kT} - 1)^2} S_{LTE} NF \\
\frac{\partial}{\partial T_1} [SNF]^{(abs)} &= \frac{E_1 e^{E_1(T-T_1)/kTT_1}}{e^{E_1(T-T_1)/kTT_1} - e^{E_2(T-T_2)/kTT_2} e^{-h\nu_0/kT}} \frac{1}{kT_1^2} SNF \\
\frac{\partial}{\partial T_2} [SNF]^{(abs)} &= \frac{E_2 e^{E_2(T-T_1)/kTT_2} e^{-h\nu_0/kT}}{e^{E_2(T-T_1)/kTT_1} - e^{E_2(T-T_2)/kTT_2} e^{-h\nu_0/kT}} \frac{1}{kT_2^2} SNF \\
\frac{\partial}{\partial t} [SNF]^{(abs)} &= S \frac{\partial}{\partial t} [NF] \\
\frac{\partial}{\partial t} [SNF]^{(abs)} &= S \frac{\partial}{\partial t} [NF].
\end{aligned} \tag{2.117}$$

Note that  $NF$  is here assumed set by one of the normalization functions. If no normalization function is used, this is considered equivalent to  $N := 1$ . Note that  $S = S_{Vib-NLTE}^{(abs)}$  and that  $S_{LTE}$  is as computed in another algorithm. Since the atmosphere is not locally thermodynamically stable, the source function differs from the emission function by some small amount following

$$S_{Vib-NLTE}^{(src)} = S_{LTE} e^{E_2(T-T_2)/kTT_2}. \tag{2.118}$$

and the following derivatives are the pure derivatives

$$\begin{aligned}
\frac{\partial}{\partial T} [SNF]^{(src)} &= \frac{S}{S_{LTE}} \frac{\partial}{\partial T} [SNF]_{LTE} - S \frac{E_2}{kT^2} NF \\
\frac{\partial}{\partial I_0} [SNF]^{(src)} &= \frac{SNF}{I_0} \\
\frac{\partial}{\partial \nu_0} [SNF]^{(src)} &= \frac{S}{S_{LTE}} \frac{\partial}{\partial \nu_0} [SNF]_{LTE} \\
\frac{\partial}{\partial T_1} [SNF]^{(src)} &= 0 \\
\frac{\partial}{\partial T_2} [SNF]^{(src)} &= S \frac{E_2}{kT_2^2} NF \\
\frac{\partial}{\partial t} [SNF]^{(src)} &= S \frac{\partial}{\partial t} [NF],
\end{aligned} \tag{2.119}$$

where  $S := S_{Vib-NLTE}^{(src)}$ . Note that we consider all of this as an 'additional' source in our algorithms. So the values that are returned by internal algorithms are always the difference between source and absorption and not the independent source.

Lastly, please remember that even though we output the temperature derivative of this function, this does not make much sense since a change in the atmosphere and signal of course means that also the  $T_1$  and  $T_2$  values change. So be careful using this algorithm.

### NLTE line strength with ratios (populationtype is NLTE)

The main equation here is that

$$S_{NLTE}^{(abs)} = \frac{h\nu_0}{4\pi} \left( \frac{g_2}{g_1} r_1 - r_2 \right) A_{21} / \frac{2h\nu_0^3}{c^2}, \tag{2.120}$$

and the following derivatives

$$\begin{aligned}
\frac{\partial}{\partial T} [SNF]^{(abs)} &= S \frac{\partial}{\partial T} [NF] \\
\frac{\partial}{\partial \nu_0} [SNF]^{(abs)} &= S \frac{\partial}{\partial \nu_0} [NF] + \frac{h(g_2 r_1 / g_1 - r_2)}{4\pi} \frac{A_{21}}{2h\nu_0^3/c^2} NF - \frac{3}{\nu_0} SNF \\
\frac{\partial}{\partial r_1} [SNF]^{(abs)} &= -\frac{h\nu_0}{4\pi} \frac{A_{21}}{2h\nu_0^3/c^2} NF \\
\frac{\partial}{\partial r_2} [SNF]^{(abs)} &= \frac{h\nu_0}{4\pi} \frac{g_2}{g_1} \frac{A_{21}}{2h\nu_0^3/c^2} NF, \\
\frac{\partial}{\partial t} [SNF]^{(abs)} &= S \frac{\partial}{\partial t} [NF],
\end{aligned} \tag{2.121}$$

where  $S := S_{NLTE}^{(abs)}$ . The source is

$$S_{NLTE}^{(src)} = \frac{h\nu_0}{4\pi} r_2 \left( e^{h\nu_0/kT} - 1 \right) A_{21} \left/ \frac{2h\nu_0^3}{c^2} \right. \tag{2.122}$$

with the following derivatives

$$\begin{aligned}
\frac{\partial}{\partial T} [SNF]^{(src)} &= S \frac{\partial}{\partial T} [NF] + NF \frac{h^2 \nu_0^2}{4\pi} r_2 e^{h\nu_0/kT} A_{21} \left/ kT^2 \frac{2h\nu_0^3}{c^2} \right. \\
\frac{\partial}{\partial \nu_0} [SNF]^{(src)} &= S \frac{\partial}{\partial \nu_0} [NF] + \frac{h}{4\pi} r_2 A_{21} \frac{e^{h\nu_0/kT} - 1}{2h\nu_0^3/c^2} NF + \\
&\quad \left( \frac{he^{h\nu_0/kT}}{2kTh\nu_0^3/c^2} - \frac{3}{\nu_0} \frac{e^{h\nu_0/kT} - 1}{e^{h\nu_0/kT} - 1} \right) \frac{h\nu_0}{4\pi} r_2 A_{21} NF \\
\frac{\partial}{\partial r_1} [SNF]^{(src)} &= 0 \\
\frac{\partial}{\partial r_2} [SNF]^{(src)} &= \frac{SNF}{r_2} \\
\frac{\partial}{\partial t} [SNF]^{(src)} &= S \frac{\partial}{\partial t} [NF],
\end{aligned} \tag{2.123}$$

where  $S := S_{NLTE}^{(src)}$ .

### 2.1.3 Species-specific data in ARTS

A line absorption species in ARTS is a particular isotopologue of a particular molecule. Quantities such as the molecular mass and the isotopologue ratio are specific and constant for each species. Here is a list of all species-specific information that is needed:

- Isotopologue name
- Isotopologue mass
- Partition function data
- Isotopologue ratio

The isotopologue name and isotopologue mass data is stored in `isotopolgues.h`, and the partition function data is compiled into ARTS during the course of a normal build. To work with external definitions of species data, we maintain (currently) two files `hitran_species.cc` and `jpl_species.cc`. These keep track of all HITRAN and JPL specific data, respectively, required to translate these data-bases into ARTS formats. Isotopologue ratios must be input by the user during the course of running ARTS. As a convenience that should mostly work on Earth, we provide `isotopologue_ratiosInitFromBuiltin`, which is guaranteed to provide some value to all valid isotopologue in ARTS.

*Buehler et al. [2005]* contains an explicit list of species that were implemented at the time of writing of that article. We do not include such a list here, because it is hard to maintain. Instead, we directly refer the user to check for the implemented species directly in file `isotopolgues.h`. There, also the different sources of data are documented.

### Partition function data

ARTS uses linear interpolation from larger datasets or polynomials to approximate partition functions.

The consistency of partition function data from different sources, and the impact of partition function errors on sub-millimeter wave limb sounder retrievals, was studied in detail in *Verdes et al.* [2005]. The partition function data collection in ARTS is based on that study but updated by the latest total partition functions from *Gamache et al.* [2021].

In general, the data in general are derived from the following sources:

**TIPS:** Default.

**JPL:** Only species (including individual isotopologues) not covered by TIPS.

**Agnes Perrin:** Personal communication, only for species BrO.

The TIPS program is developed and maintained by B. Gamache. In conjunction with HITRAN it is the suggested way to derive the partition functions and is part of the HITRAN distributions. More recent versions might be available via B. Gamache's website ([http://faculty.uml.edu/robert\\_gamache/](http://faculty.uml.edu/robert_gamache/), 'Software and Data' section). TIPS covers all molecular species and isotopologues found in the respective version of the HITRAN database. Often it includes some more species than HITRAN, and extensions for other species (e.g., species of astrophysical interest) can be derived from the Gamache website.

Earlier versions of TIPS (until at least 1997) provided 3rd order polynomial coefficients, which were then used in ARTS. Newer versions (from at latest 2003) provide partition functions for a specific molecule and isotopologue at a specific temperature, and tabulated values can be obtained through successive runs of the program. Polynomial coefficients then need to be derived by a fit to the TIPS output.

The coefficients for the few species which are not covered in TIPS are calculated from JPL values. The JPL catalogue has a different way to calculate the partition function. It provides the partition function at a set of specific temperatures: 300, 225, 150, 75, 37.5, 18.75, 9.375 K. An interpolation scheme is given for values inbetween: the partition functions are assumed to be proportional to  $T^{1.5}$  for non-linear molecules (degrees of freedom: 3) and proportional to  $T$  for linear molecules (degrees of freedom 2). From these data polynomial coefficients are derived in the same way as from TIPS output: first, partition functions are tabulated on a 1K-step grid, then a least-square fit over  $T = 150 - 300$  K is performed.

The partition function data for BrO were provided by Agnes Perrin, Orsay, France.

The temperature range used for deriving the polynomial fit was judged to be representative of the range of temperatures occurring in the Earth atmosphere. For calculations in planetary atmospheres it might be advantageous being able to use other data, e.g. such derived for temperatures prevailing there. We are exploring options to allow for that (e.g., read data from include files as done for isotopologue ratios, or replacement of parameterized partition functions by directly calculated ones through embedding TIPS and the JPL scheme in ARTS).

## 2.2 Continuum absorption

As pointed out above, some molecules show beside the resonant line absorption also non-resonant continuum absorption. The main qualitative difference is the smooth dependence

on frequency of the non-resonant absorption part in contrast to the resonant absorption part who shows strong local maxima and minima.

The implemented continuum absorption modules are connected with water vapor ( $\text{H}_2\text{O}$ ), oxygen ( $\text{O}_2$ ), nitrogen ( $\text{N}_2$ ), and carbon dioxide ( $\text{CO}_2$ ). Since these molecules have various permanent electric or magnetic multipoles, the physical explanations for the continuum absorption is different for each of these molecules.

Water Vapor has a strong electric dipole moment and posses therefore a wealth of rotational transitions in the microwave up to the submillimeter range. One explanation for the  $\text{H}_2\text{O}$ -continuum absorption is the inadequate formulation of the far wings of a spectral line, since the usually employed *Van Vleck and Weisskopf* [1945] line shape is according to its derivation only valid in the near wing zone. Other explanations are (see *Rosenkranz* [1993] for details) far wing contribution from far-infrared water vapor lines, collision induced absorption (CIA), and water polymer absorption. At present one can not definitively decide which of these possibilities is the correct one, probably all of them play a more or less important role, depending on the frequency range.

Oxygen is special, because it has no permanent electric dipole moment, but a permanent magnetic dipole moment. The aligned spins of the two valence electrons gives a  $^3\Sigma$  ground state of molecular oxygen. Due to the selection rules for magnetic dipole transitions, transitions with resonance frequency equal to zero are allowed. Such transitions have a characteristic Debye line shape function.

The homonuclear nitrogen molecule has in lowest order an electric quadrupole moment of modest magnitude. For the frequency range below 1 THz the collision induced rotation absorption band [*Goody and Yung*, 1989] is of most importance. The band center is around 3 THz and at 1 THz the band strength is approximately 1/6 of the maximum value (see Figure 5.2 of *Goody and Yung* [1989]). The electric field of the quadrupole moment of one molecule induces a dipole moment in the second molecule. This allows rotational transitions according to the electric quadrupole selection rules,  $|\Delta J| = 0, 2$  (see *Rosenkranz* [1993] for details).

In a similar way, carbon dioxide also exhibits a collision induced absorption band (maximum around 1.5 THz, Figure 5.10 of *Goody and Yung* [1989]). Characteristic for collision induced absorption is the dependency on the square of the molecular density.

### 2.2.1 Water vapor continuum models

As shown by *Liebe and Layton* [1987], *Rosenkranz* [1998], and *Ma and Tipping* [1990], the water vapor continuum absorption can be well described by

$$\alpha_c = \nu^2 \cdot \Theta^3 \cdot (C_{\text{H}_2\text{O}}^0 \cdot P_{\text{H}_2\text{O}}^2 \cdot \Theta^{n_s} + C_d^0 \cdot P_{\text{H}_2\text{O}} \cdot P_d \cdot \Theta^{n_d}) \quad (2.124)$$

where  $\Theta = 300 \text{ K}/T$ , and the microwave approximation ( $h\nu \ll k_B T$ ) of the radiation field term is already applied. The adjustment of Eq. 2.124 to the data is performed through the parameter set  $C_{\text{H}_2\text{O}}^0$ ,  $n_s$ ,  $C_d^0$ , and  $n_d$ . Table 2.10 gives some commonly used continuum parameter sets.

#### The MPM93 continuum parameterization

In the MPM93 model [*Liebe et al.*, 1993], the water vapor continuum is treated as a pseudo-line located in the far infrared around 2 THz. The pseudo-line continuum has therefore not

model	$C_{\text{H}_2\text{O}}^0$ [dB/km hPa <sup>2</sup> GHz <sup>2</sup> ]	$n_s$ [1]	$C_d^0$ [dB/km hPa <sup>2</sup> GHz <sup>2</sup> ]	$n_d$ [1]	ref.
MPM87	$6.50 \cdot 10^{-8}$	7.5	$0.206 \cdot 10^{-8}$	0.0	<i>Liebe and Layton [1987]</i>
MPM89	$6.50 \cdot 10^{-8}$	7.3	$0.206 \cdot 10^{-8}$	0.0	<i>Liebe [1989]</i>
CP98	$8.04 \cdot 10^{-8}$	7.5	$0.254 \cdot 10^{-8}$	0.0	<i>Cruz Pol et al. [1998]</i>
PWR98	$7.80 \cdot 10^{-8}$	4.5	$0.236 \cdot 10^{-8}$	0.0	<i>Rosenkranz [1998]</i>
MPM93*	$7.73 \cdot 10^{-8}$	4.55	$0.253 \cdot 10^{-8}$	1.55	<i>Liebe et al. [1993]</i>

Table 2.10: Values of commonly used continuum parameter sets. The last line (MPM93\*) represents an approximation of the pseudo-line continuum of MPM93 in the form of Eq. 2.124.

four but seven parameters, the pseudo-line center frequency ( $\nu^*$ ) and the six pseudo-line parameters ( $b_1^*, \dots, b_6^*$ ):

$$\alpha_c^{\text{MPM93}} = 0.1820 \cdot \frac{b_1^*}{\nu^*} \cdot P_{\text{H}_2\text{O}} \cdot \Theta^{3.5} \cdot \exp(b_2^* \cdot (1 - \Theta)) \cdot \nu^2 \cdot F_c(\nu, \nu_k) \quad (2.125)$$

$$F_c(\nu, \nu_k) = \left[ \frac{\gamma_c}{(\nu^* + \nu)^2 + \gamma_c^2} + \frac{\gamma_c}{(\nu^* - \nu)^2 + \gamma_c^2} \right] \quad (2.126)$$

$$\gamma_c = b_3^* \cdot \left( b_4^* \cdot P_{\text{H}_2\text{O}} \cdot \Theta^{b_6^*} + P_d \cdot \Theta^{b_5^*} \right) \quad (2.127)$$

Table 2.11 lists the values of this continuum parameter set. It is remarkable that all these parameters are much larger compared to the physical water vapor line parameters of the same model. The only exception is  $b_2^*$ , the parameter which governs the exponential temperature behavior of the line strength. The magnitude of the pseudo-line width is shown for four

$\nu^*$ [GHz]	$b_1^*$ [kHz hPa]	$b_2^*$ [1]	$b_3^*$ [MHz hPa]	$b_4^*$ [1]	$b_5^*$ [1]	$b_6^*$ [1]
1780.000	2230.000	0.952	17.620	30.50	2.00	5.00

Table 2.11: List of the MPM93 pseudo-line water vapor continuum parameters.

different cases in Table 2.12.

	contribution		total
	H <sub>2</sub> O–H <sub>2</sub> O	H <sub>2</sub> O–air	
$\gamma_c(200 \text{ K})$	40.8 GHz	80.4 GHz	121.2 GHz
$\gamma_c(300 \text{ K})$	5.4 GHz	23.0 GHz	28.4 GHz

Table 2.12: Magnitude of the line width of the pseudo-line of the continuum term in MPM93. Assumed is a total pressure of 1000 hPa and a water vapor partial pressure of 10 hPa.

This change of continuum parameterization makes it difficult to compare MPM93 with the models which use Eq. (2.124). However, with respect to microwave frequencies, the line shape function,  $F_c(\nu)$ , can be approximated since the magnitude of the pseudo-line



width is much smaller compared to the distance between microwave frequencies and  $\nu^*$ , as shown for four different cases in Table 2.12:

$$F_c(\nu, \nu_k) \approx 2 \cdot \frac{\gamma_c}{\nu_c^2} \quad (2.128)$$

Inserting Eq. (2.128) into Eq. (2.125) gives a quadratic frequency dependence of the MPM93 continuum, similar to the continuum parameterization expressed in Eq. (2.124). By additionally approximating the temperature dependence to the simple form

$$\begin{aligned} n_s \cdot \ln(\Theta) &= \ln\left(\Theta^{3.5} \cdot e^{b_2^* \cdot (1-\Theta)}\right) \\ n_s &= 3.5 + b_2^* \cdot \frac{1-\Theta}{\ln(\Theta)} \\ n_s &\approx 3.5 - b_2^* = 2.55 \quad \text{with } \ln(\Theta) \approx (\Theta - 1) \end{aligned} \quad (2.129)$$

one can rearrange the pseudo-line continuum to fit Eq. (2.124) (denoted by MPM93\*). The so deduced continuum parameter set is given in Table 2.10.

The MPM93\* continuum parameters  $C_{\text{H}_2\text{O}}^0$  and  $C_d^0$  are 20 % and 15 % larger, respectively, than in the case of MPM87/MPM89. Large discrepancies exist for the temperature exponents  $n_s$  and  $n_d$  between MPM93\* and earlier model versions. The exponent  $n_s$  is in MPM93\* only 60 % of the corresponding value in MPM89 and the temperature dependence of the H<sub>2</sub>O-air term is significant larger than for earlier MPM versions. This reduction of  $n_s$  is mainly due to additional measurements considered in MPM93 [Becker and Autler, 1946; Godon et al., 1992], while the continuum parameters in MPM87/MPM89 are determined by a single laboratory measurement at 138 GHz.

### 2.2.2 Oxygen continuum absorption

As pointed out by Van Vleck [1987], the standard theory for non-resonant absorption is that of Debye (see also Townes and Schawlow [1955]). The Debye line shape is obtained from the VVW line shape function by the limiting case  $\nu_k \rightarrow 0$ . Both, Liebe et al. [1993] and Rosenkranz [1993] adopted the Debye theory for their models. The only difference is the formulation of the line broadening, where the influence of water vapor is treated slightly different:

$$\alpha_c = C \cdot P_d \cdot \Theta^2 \cdot \frac{\nu^2 \cdot \gamma}{\nu^2 + \gamma^2} \quad (2.130)$$

$$\gamma = w \cdot (P_d \cdot \Theta^{0.8} + 1.1 \cdot P_{\text{H}_2\text{O}} \cdot \Theta) \quad : \text{ Rosenkranz} \quad (2.131)$$

$$\gamma = w \cdot P_{\text{tot}} \cdot \Theta^{0.8} \quad : \text{ MPM93} \quad (2.132)$$

where  $P_d$  denotes the dry air partial pressure ( $P_d = P_{\text{tot}} - P_{\text{H}_2\text{O}}$ ). The value for the strength is  $C = 2.56 \cdot 10^{-20} \text{ 1/(m Pa Hz)}$  in the case of the Rosenkranz model and  $C = 2.57 \cdot 10^{-20} \text{ 1/(m Pa Hz)}$  in the case of the MPM93 model. The MPM93 value for  $C$  is therefore about 0.4 % larger than in the Rosenkranz model. Since the volume mixing ratio of oxygen in dry air is constant in the lower Earth atmosphere (0.20946 [Goody, 1995]), both models incorporate the oxygen  $VMR$  ( $VMR_{\text{O}_2}$ ) in the constant  $C$ . In the arts model

the separation between the oxygen  $VMR$  and the constant  $C$  is explicitly done. In this case follows:

$$C = 0.20946 \cdot \hat{C} \quad (2.133)$$

$$\hat{C} = 1.22 \cdot 10^{-19} [1/(\text{m Hz Pa})] \quad : \text{Rosenkranz} \quad (2.134)$$

$$\hat{C} = 1.23 \cdot 10^{-19} [1/(\text{m Hz Pa})] \quad : \text{MPM93} \quad (2.135)$$

The width parameter  $w$  is in both models the same,  $w = 5.6 \cdot 10^3 \text{ Hz/Pa}$ . If we define the width  $\gamma$  in a more general way like

$$\gamma = w \cdot (A \cdot P_d \cdot \Theta^{n_d} + B \cdot P_{\text{H}_2\text{O}} \cdot \Theta^{n_w}) \quad (2.136)$$

we can fit both models, the Rosenkranz and the MPM93 model, into the same parameterization with ( $A = 1$ ,  $B = 1.1$ ,  $n_d = 0.8$ ,  $n_w = 1.0$ ) for the Rosenkranz model and ( $A = 1.0$ ,  $B = 1.0$ ,  $n_d = 0.8$ ,  $n_w = 0.8$ ) for MPM93.

The oxygen continuum absorption term is proportional to the collision frequency of a single oxygen molecule with other air molecules and thus proportional to the dry air pressure<sup>1</sup>.

### 2.2.3 Nitrogen continuum absorption

Since molecular nitrogen has in its unperturbed state no electric or magnetic dipole moment (but an electric quadrupole moment), it shows no rotational spectral signature in the microwave region. Regardless of this, nitrogen absorbs radiation in this frequency range due to collision induced absorption (CIA). Far-infrared roto-translational band structures from free-free interactions give rise to far wing absorption below 1 THz.

Different parameterizations of this absorption term for the frequency range below 1 THz are available *Rosenkranz* [1993]; *Liebe et al.* [1993]; *Borysow and Frommhold* [1986]. Common to all these models is the quadratic dependency on  $\text{N}_2$  partial pressure which is a direct consequence of the underlying CIA processes involved. The simplest model is given by *Rosenkranz* [1993], which uses the same parameterization as for the water vapor continuum, described in Equation 2.124:

$$\alpha_c = C \cdot \nu^{n_\nu} \cdot \Theta^{n_T} \cdot P_{\text{N}_2}^{n_p} \quad (2.137)$$

with  $C = 4.56 \cdot 10^{-13} \text{ dB}/(\text{km hPa}^2 \text{ GHz}^2)$ ,  $n_\nu = 2$ ,  $n_T = 3.55$ , and  $n_p = 2$ , respectively. The laboratory data set for the determination of  $C$  is mainly from *Dagg et al.* [1975, 1978] around 70 and 140 GHz, respectively.

The MPM models has compared with Equation 2.137 an additional frequency dependent term which leads to the following expression

$$\alpha_c = \hat{C} \cdot (1.0 - 1.2 \cdot 10^{-5} \cdot \nu^{1.5}) \cdot \nu^2 \cdot \Theta^{3.5} \cdot P_d^2 \quad : \text{MPM89} \quad (2.138)$$

$$\alpha_c = \hat{C} \cdot \frac{\nu^2}{(1.0 + a \cdot \nu^{n_\nu})} \cdot \Theta^{3.5} \cdot P_d^2 \quad : \text{MPM93} \quad (2.139)$$

where the parameter is  $\hat{C} = 2.55 \cdot 10^{-13} \text{ dB}/(\text{km hPa}^2 \text{ GHz}^2)$ ,  $a = 1.9 \cdot 10^{-5} \text{ GHz}^{-n_\nu}$ , and  $n_\nu = 1.5$ . based on data from *Stankevich* [1974] and *Stone et al.* [1984]. With respect to

<sup>1</sup>The absorption due to weakly bound complexes of  $\text{O}_2\text{-X}$  with  $X = \text{H}_2\text{O}$ ,  $\text{N}_2$  is treated separately and therefore not included in this Debye formula.

the 22 GHz water vapor line, the additional frequency terms in brackets in Equations 2.138 and 2.139 are nearly unity and therefore not essential. Therefore all three parameterizations have the same frequency and temperature relationship, but the absolute magnitude is in the case of Rosenkranz 80 % higher compared with the MPM models.

The model of Borysow and Frommhold<sup>2</sup> is somewhat different since their focus is mainly on the radiative transfer in the Titan's atmosphere with the infrared interferometer spectrometer, IRIS, on board the Voyager Spacecraft. This detailed model is primarily designed to parameterize each of the roto-translational spectral lines around 200 cm<sup>-1</sup> ( $\approx$  6 THz) accurately. The analyzed data set incorporate the data source used by the Rosenkranz but is largely extended with measurements in the far-infrared.

## 2.2.4 Carbon dioxide continuum absorption

*Rosenkranz* [1993] gives a similar parameterization for the CO<sub>2</sub>-continuum absorption term as for the nitrogen continuum, with

$$\alpha_c = \nu^2 \cdot [C_s \cdot P_{\text{CO}_2}^2 \cdot \Theta^{n_s} + C_f \cdot P_{\text{CO}_2} \cdot P_{\text{N}_2} \cdot \Theta^{n_f}] \quad (2.140)$$

where the parameter values  $C_s = 3.23 \cdot 10^{-11}$  dB/(km hPa<sup>2</sup> GHz<sup>2</sup>),  $C_f = 1.18 \cdot 10^{-11}$  dB/(km hPa<sup>2</sup> GHz<sup>2</sup>),  $n_s = 5.08$ , and  $n_f = 4.7$ , respectively, are determined from laboratory measurements of *Ho et al.* [1966]; *Dagg et al.* [1975]. Since the foreign term includes only nitrogen as perturber, one can get an estimate for dry air by replacing  $P_{\text{N}_2}$  by the dry air partial pressure in Equation 2.140. Because nitrogen is usually a more efficient perturber than oxygen, this estimation can be regarded as an upper limit. Concerning the Earth's atmosphere, the foreign broadening term is more interesting since the carbon dioxide partial pressure is only approximately 0.04 % of the nitrogen partial pressure up to 90 km.

## 2.3 Complete absorption models

The MPM absorption model of Liebe and coworkers consists of modules for water vapor and oxygen absorption. The Rosenkranz (PWR98) absorption model include also H<sub>2</sub>O and O<sub>2</sub> while the Cruz-Pol et al. (CP98) absorption models include absorption due to water vapor. Additionally the CP98 model has a strongly reduced parameter set for the H<sub>2</sub>O-line absorption since it is especially intended for the range around the 22 GHz water line. The MPM and R98 are valid from the microwave up to the submillimeter frequency range (1-1000 GHz).

Implemented in ARTS are the following modules of the above mentioned models:

species	model
H <sub>2</sub> O	MPM87, MPM89, MPM93, PWR98, CP98
O <sub>2</sub>	MPM93, PWR98

### 2.3.1 Complete water vapor models

In ARTS several complete water vapor absorption models are implemented and can easily be used. Implemented models are the versions MPM87 [*Liebe and Layton, 1987*], MPM89 [*Liebe, 1989*], and MPM93 [*Liebe et al., 1993*] of the Liebe Millimeter-wave Propagation

<sup>2</sup>the source code of this model can be downloaded from the home page of A. Borysow:  
<http://www.astro.ku.dk/~aborysow/>

Model and additionally the models of Cruz-Pol et al. (CP98) [*Cruz Pol et al., 1998*] and P. W. Rosenkranz (PWR98) [*Rosenkranz, 1998*]. MPM and PWR98 are especially designed for fast absorption calculations in the frequency range of 1-1000 GHz while the CP98 model is a reduced model for a narrow frequency band around the 22 GHz H<sub>2</sub>O-line (especially used by ground-based radiometers).

The total water vapor absorption ( $\alpha_{\text{tot}}$ ) is in all the stated models described by a line absorption ( $\alpha_{\ell}$ ) term and a continuum absorption ( $\alpha_c$ ) term:

$$\alpha_{\text{tot}} = \alpha_{\ell} + \alpha_c \quad (2.141)$$

The main differences between the different models is the line shape used for  $\alpha_{\ell}$  and the formulation of  $\alpha_c$ .

It has to be emphasized that,  $\alpha_{\ell}$  and  $\alpha_c$  of different models are not necessarily compatible and should therefore not be interchanged between different models.

### MPM87 water vapor absorption model

This version, which is described in *Liebe and Layton [1987]* and follows the general line of the MPM model to divide the total water vapor absorption,  $\alpha_{\text{tot}}^{\text{MPM87}}$ , into a spectral line term,  $\alpha_{\ell}^{\text{MPM87}}$ , and a continuum term not attributed to spectral lines,  $\alpha_c^{\text{MPM87}}$ :

$$\alpha_{\text{tot}}^{\text{MPM87}} = \alpha_{\ell}^{\text{MPM87}} + \alpha_c^{\text{MPM87}} \quad \text{dB/km} \quad (2.142)$$

**Water vapor line absorption:** The MPM87 [*Liebe and Layton, 1987*] water vapor line catalog consists of 30 lines from 22 GHz up to 988 GHz. The center frequencies and parameter values are listed in Table 2.13. To describe the line absorption, a set of three parameters ( $b_{1,k}$  and  $b_{3,k}$ ) per line are used: two for the line strength and one for the line width. The total line absorption coefficient (in units of dB/km) is the sum over all individual line absorption coefficients<sup>3</sup>:

$$\alpha_{\ell}^{\text{MPM87}} = 0.1820 \cdot \nu \cdot \sum_k S_k(T) \cdot F(\nu, \nu_k) \quad \text{dB/km} \quad (2.143)$$

where  $S_k(T)$  is the line intensity described by the parameterization

$$S_k(T) = b_{1,k} \cdot P_{\text{H}_2\text{O}} \cdot \Theta^{3.5} \cdot \exp(b_{2,k} \cdot [1 - \Theta]) \quad \text{kHz} \quad (2.144)$$

with  $\nu_k$  as the line center frequency,  $P_{\text{H}_2\text{O}}$  the water vapor partial pressure and  $\Theta = 300 \text{ K}/T$ .

The line shape function,  $F(\nu, \nu_k)$ , in Eq. (2.143) is the standard Van Vleck-Weisskopf (VW) function, given by:

$$F(\nu, \nu_k) = \left( \frac{\nu}{\nu_k} \right) \cdot \left[ \frac{\gamma_k}{(\nu - \nu_k)^2 + \gamma_k^2} + \frac{\gamma_k}{(\nu + \nu_k)^2 + \gamma_k^2} \right] \quad (2.145)$$

$$(2.146)$$

<sup>3</sup>The factor  $0.1820 \cdot 10^6$  is equal to  $(4\pi/c) \cdot 10 \log(e)$  (the term  $(4\pi/c)$  comes from the definition of the absorption coefficient in terms of the dielectric constant and the term  $10 \log(e)$  is due to the definition of the Decibel.) The velocity of light is defined as  $c = 2.9979 \cdot 10^{-4} \text{ km GHz}$ . The factor  $10^6$  is incorporated into the line strength and does therefore not appear in the pre-factor.

The pressure broadened line width,  $\gamma_k$ , is calculated with the single parameter  $b_{3,k}$  in the following way:

$$\gamma_k = b_{3,k} \cdot (4.80 \cdot P_{\text{H}_2\text{O}} \cdot \Theta^{1.1} + P_d \cdot \Theta^{0.6}) \quad \text{GHz} \quad (2.147)$$

where  $P_d$  is the partial pressure of dry air ( $P_d = P_{\text{tot}} - P_{\text{H}_2\text{O}}$ ). The parameterizations of  $S_k(T)$  and  $\gamma_k$  are already in use for the early version of MPM81 [Liebe, 1981].

$k$	$\nu_k$ [GHz]	$b_{1,k}$ [ $\frac{\text{kHz}}{\text{kPa}}$ ]	$b_{2,k}$ [1]	$b_{3,k}$ [ $\frac{\text{GHz}}{\text{kPa}}$ ]
1	22.235080	0.1090	2.143	$27.84 \cdot 10^{-3}$
2	67.813960	0.0011	8.730	$27.60 \cdot 10^{-3}$
3	119.995940	0.0007	8.347	$27.00 \cdot 10^{-3}$
4	183.310117	2.3000	0.653	$31.64 \cdot 10^{-3}$
5	321.225644	0.0464	6.156	$21.40 \cdot 10^{-3}$
6	325.152919	1.5400	1.515	$29.70 \cdot 10^{-3}$
7	336.187000	0.0010	9.802	$26.50 \cdot 10^{-3}$
8	380.197372	11.9000	1.018	$30.36 \cdot 10^{-3}$
9	390.134508	0.0044	7.318	$19.00 \cdot 10^{-3}$
10	437.346667	0.0637	5.015	$13.70 \cdot 10^{-3}$
11	439.150812	0.9210	3.561	$16.40 \cdot 10^{-3}$
12	443.018295	0.1940	5.015	$14.40 \cdot 10^{-3}$
13	448.001075	10.6000	1.370	$23.80 \cdot 10^{-3}$
14	470.888947	0.3300	3.561	$18.20 \cdot 10^{-3}$
15	474.689127	1.2800	2.342	$19.80 \cdot 10^{-3}$
16	488.491133	0.2530	2.814	$24.90 \cdot 10^{-3}$
17	503.568532	0.0374	6.693	$11.50 \cdot 10^{-3}$
18	504.482692	0.0125	6.693	$11.90 \cdot 10^{-3}$
19	556.936002	510.0000	0.114	$30.00 \cdot 10^{-3}$
20	620.700807	5.0900	2.150	$22.30 \cdot 10^{-3}$
21	658.006500	0.2740	7.767	$30.00 \cdot 10^{-3}$
22	752.033227	250.0000	0.336	$28.60 \cdot 10^{-3}$
23	841.073593	0.0130	8.113	$14.10 \cdot 10^{-3}$
24	859.865000	0.1330	7.989	$28.60 \cdot 10^{-3}$
25	899.407000	0.0550	7.845	$28.60 \cdot 10^{-3}$
26	902.555000	0.0380	8.360	$26.40 \cdot 10^{-3}$
27	906.205524	0.1830	5.039	$23.40 \cdot 10^{-3}$
28	916.171582	8.5600	1.369	$25.30 \cdot 10^{-3}$
29	970.315022	9.1600	1.842	$24.00 \cdot 10^{-3}$
30	987.926764	138.0000	0.178	$28.60 \cdot 10^{-3}$

Table 2.13: List of H<sub>2</sub>O spectral lines and their spectroscopic parameters (H<sub>2</sub>O-air mixture) for the MPM87 model [Liebe and Layton, 1987].

**Water vapor continuum absorption:** The water vapor continuum absorption coefficient in MPM87,  $\alpha_c^{\text{MPM87}}$ , is determined from laboratory measurements at 137.8 GHz by Liebe and Layton covering the following parameter range:

temperature 282-316 K  
 relative humidity 0-95 %  
 dry air pressure 0 - 160 kPa

The mathematical expression of  $\alpha_c^{\text{MPM87}}$  is derived from the far wing approximation of the line absorption and is expressed as follows

$$\alpha_c^{\text{MPM87}} = \nu^2 \cdot P_{\text{H}_2\text{O}} \cdot (C_{\text{H}_2\text{O}}^0 \cdot P_{\text{H}_2\text{O}} \cdot \Theta^{n_s} + C_d^0 \cdot P_d \cdot \Theta^{n_f}), \quad (2.148)$$

with the continuum parameter set  $C_{\text{H}_2\text{O}}^0$ ,  $C_d^0$ ,  $n_s$ , and  $n_f$ . The determined values of the continuum parameters are:

$$C_{\text{H}_2\text{O}}^0 = 6.496 \cdot 10^{-6} \text{ (dB/km) / (hPa} \cdot \text{GHz)}^2$$

$$n_s = 10.5$$

$$C_d^0 = 0.206 \cdot 10^{-6} \text{ (dB/km) / (hPa} \cdot \text{GHz)}^2$$

$$n_d = 3.0$$

#### MPM89 water vapor absorption model

MPM89 is described in *Liebe* [1989] and follows the general line of the MPM model to devide the total water vapor absorption,  $\alpha_{\text{tot}}^{\text{MPM89}}$ , into a spectral line term,  $\alpha_{\ell}^{\text{MPM89}}$ , and a continuum term not attributed to spectral lines,  $\alpha_c^{\text{MPM89}}$ :

$$\alpha_{\text{tot}}^{\text{MPM89}} = \alpha_{\ell}^{\text{MPM89}} + \alpha_c^{\text{MPM89}} \quad \text{dB/km} \quad (2.149)$$

All the absorption coefficients are calculated in units of dB/km.

**Water vapor line absorption:** The MPM89 water vapor line catalog consists of the same 30 lines like MPM87 from 22 GHz up to 988 GHz. The center frequencies and parameter values are listed in Table 2.14. To describe the line absorption, a set of six parameters ( $b_{1,k}$  and  $b_{6,k}$ ) per line are used: two for the line strength and four for the line width. The total line absorption coefficient (in units of dB/km) is the sum over all individual line absorption coefficients:

$$\alpha_{\ell}^{\text{MPM89}} = 0.1820 \cdot \nu \cdot \sum_k S_k(T) \cdot F(\nu, \nu_k) \quad \text{dB/km} \quad (2.150)$$

where  $S_k(T)$  is the line intensity described by the parameterization

$$S_k(T) = b_{1,k} \cdot P_{\text{H}_2\text{O}} \cdot \Theta^{3.5} \cdot \exp(b_{2,k} \cdot [1 - \Theta]) \quad \text{kHz} \quad (2.151)$$

whit  $\nu_k$  as the line center frequency,  $P_{\text{H}_2\text{O}}$  the water vapor partial pressure and  $\Theta = 300 \text{ K}/T$ .

The line shape function,  $F(\nu, \nu_k)$ , in Eq. (2.150) is the standard Van Vleck-Weisskopf (VW) function, given by

$$F(\nu, \nu_k) = \left( \frac{\nu}{\nu_k} \right) \cdot \left[ \frac{\gamma_k}{(\nu - \nu_k)^2 + \gamma_k^2} + \frac{\gamma_k}{(\nu + \nu_k)^2 + \gamma_k^2} \right] \quad (2.152)$$

where the pressure broadened line width,  $\gamma_k$ , is calculated as

$$\gamma_k = b_{3,k} \cdot (b_{5,k} \cdot P_{\text{H}_2\text{O}} \cdot \Theta^{b_{6,k}} + P_d \cdot \Theta^{b_{4,k}}) \cdot 10^{-3} \quad \text{GHz} \quad (2.153)$$

with  $P_d = P_{\text{tot}} - P_{\text{H}_2\text{O}}$  as the dry air partial pressure. The only difference between MPM87 and MPM89 with respect to the line absorption is the parameterization of the pressure broadened line width,  $\gamma_k$ , which is calculated with the four parameters  $b_{3,k}$  to  $b_{6,k}$  in the case of MPM89 whereas in MPM87 a single parameter ( $b_{3,k}$ ) is used (see Eq. (2.147)).

$k$	$\nu_k$ [GHz]	$b_{1,k}$ [ $\frac{\text{kHz}}{\text{kPa}}$ ]	$b_{2,k}$ [1]	$b_{3,k}$ [ $\frac{\text{MHz}}{\text{kPa}}$ ]	$b_{4,k}$ [1]	$b_{5,k}$ [1]	$b_{6,k}$ [1]
1	22.235080	0.1090	2.143	28.11	0.69	4.80	1.00
2	67.813960	0.0011	8.735	28.58	0.69	4.93	0.82
3	119.995940	0.0007	8.356	29.48	0.70	4.78	0.79
4	183.310074	2.3000	0.668	28.13	0.64	5.30	0.85
5	321.225644	0.0464	6.181	23.03	0.67	4.69	0.54
6	325.152919	1.5400	1.540	27.83	0.68	4.85	0.74
7	336.187000	0.0010	9.829	26.93	0.69	4.74	0.61
8	380.197372	11.9000	1.048	28.73	0.69	5.38	0.84
9	390.134508	0.0044	7.350	21.52	0.63	4.81	0.55
10	437.346667	0.0637	5.050	18.45	0.60	4.23	0.48
11	439.150812	0.9210	3.596	21.00	0.63	4.29	0.52
12	443.018295	0.1940	5.050	18.60	0.60	4.23	0.50
13	448.001075	10.6000	1.405	26.32	0.66	4.84	0.67
14	470.888947	0.3300	3.599	21.52	0.66	4.57	0.65
15	474.689127	1.2800	2.381	23.55	0.65	4.65	0.64
16	488.491133	0.2530	2.853	26.02	0.69	5.04	0.72
17	503.568532	0.0374	6.733	16.12	0.61	3.98	0.43
18	504.482692	0.0125	6.733	16.12	0.61	4.01	0.45
19	556.936002	510.0000	0.159	32.10	0.69	4.11	1.00
20	620.700807	5.0900	2.200	24.38	0.71	4.68	0.68
21	658.006500	0.2740	7.820	32.10	0.69	4.14	1.00
22	752.033227	250.0000	0.396	30.60	0.68	4.09	0.84
23	841.073593	0.0130	8.180	15.90	0.33	5.76	0.45
24	859.865000	0.1330	7.989	30.60	0.68	4.09	0.84
25	899.407000	0.0550	7.917	29.85	0.68	4.53	0.90
26	902.555000	0.0380	8.432	28.65	0.70	5.10	0.95
27	906.205524	0.1830	5.111	24.08	0.70	4.70	0.53
28	916.171582	8.5600	1.442	26.70	0.70	4.78	0.78
29	970.315022	9.1600	1.920	25.50	0.64	4.94	0.67
30	987.926764	138.0000	0.258	29.85	0.68	4.55	0.90

Table 2.14: List of  $\text{H}_2\text{O}$  spectral lines and their spectroscopic parameters ( $\text{H}_2\text{O}$ -air mixture) for the MPM89 model [*Liebe, 1989*].

**Water vapor continuum absorption:** The MPM89 continuum absorption coefficients in,  $\alpha_c^{\text{MPM89}}$ , are identical as those in MPM87 (see Sec. 2.3.1 for details):

$$\alpha_c^{\text{MPM89}} = \nu^2 \cdot P_{\text{H}_2\text{O}} \cdot (C_{\text{H}_2\text{O}}^0 \cdot P_{\text{H}_2\text{O}} \cdot \Theta^{\text{ns}} + C_d^0 \cdot P_d \cdot \Theta^{\text{nf}}), \quad (2.154)$$

with

$$C_{\text{H}_2\text{O}}^{\text{O}} = 6.496 \cdot 10^{-6} \text{ (dB/km) / (hPa} \cdot \text{GHz)}^2$$

$$n_{\text{S}} = 10.5$$

$$C_{\text{d}}^{\text{O}} = 0.206 \cdot 10^{-6} \text{ (dB/km) / (hPa} \cdot \text{GHz)}^2$$

$$n_{\text{d}} = 3.0$$

### MPM93 water vapor absorption model

This version, which is described in *Liebe et al.* [1993] and follows the general line of the MPM model to divide the total water vapor absorption,  $\alpha_{\text{tot}}^{\text{MPM93}}$ , into a spectral line term,  $\alpha_{\ell}^{\text{MPM93}}$ , and a continuum term not attributed to spectral lines,  $\alpha_{\text{c}}^{\text{MPM93}}$ :

$$\alpha_{\text{tot}}^{\text{MPM93}} = \alpha_{\ell}^{\text{MPM93}} + \alpha_{\text{c}}^{\text{MPM93}} \quad \text{dB/km} \quad (2.155)$$

The continuum absorption is parameterized like a resonant spectral line of  $\text{H}_2\text{O}$ , a so-called pseudo-line. This is a fundamental change in the parameterization of the water vapor continuum in respect to all older versions of MPM, which makes it quite complicate to compare the different versions, especially to distinguish a self- and foreign broadening term in the continuum.

**Water vapor line absorption:** The water vapor line spectrum of MPM93 [*Liebe et al.*, 1993] consists of 34 lines below 1 THz (four more than in MPM89 and MPM87). To describe the MPM93 water vapor line absorption, a set of six parameters ( $b_{1,k}$  and  $b_{6,k}$ ) per line are used: two for the line strength and four for the line width. The total line absorption coefficient (in units of dB/km) is the sum over all individual line absorption coefficients:

$$\alpha_{\ell}^{\text{MPM93}} = 0.1820 \cdot \nu \cdot \sum_k S_k(T) \cdot F(\nu, \nu_k) \quad \text{dB/km} \quad (2.156)$$

where  $S_k(T)$  is the line intensity described by the parameterization

$$S_k(T) = b_{1,k} \cdot P_{\text{H}_2\text{O}} \cdot \Theta^{3.5} \cdot \exp(b_{2,k} \cdot [1 - \Theta]) \quad \text{kHz} \quad (2.157)$$

with  $\nu_k$  as the line center frequency,  $P_{\text{H}_2\text{O}}$  the water vapor partial pressure and  $\Theta = 300 \text{ K}/T$ .

The line shape function,  $F(\nu, \nu_k)$ , in Eq. (2.143) is the standard Van Vleck-Weisskopf (VW) function, given by:

$$F(\nu, \nu_k) = \left( \frac{\nu}{\nu_k} \right) \cdot \left[ \frac{\gamma_k}{(\nu - \nu_k)^2 + \gamma_k^2} + \frac{\gamma_k}{(\nu + \nu_k)^2 + \gamma_k^2} \right] \quad (2.158)$$

$$(2.159)$$

The pressure broadened line width,  $\gamma_k$ , is calculated with the single parameter  $b_{3,k}$  in the following way:

$$\gamma_k = b_{3,k} \cdot (b_{4,k} \cdot P_{\text{H}_2\text{O}} \cdot \Theta^{b_{6,k}} + P_{\text{d}} \cdot \Theta^{b_{5,k}}) \cdot 10^{-3} \quad \text{GHz} \quad (2.160)$$

where  $P_{\text{d}}$  is the partial pressure of dry air ( $P_{\text{d}} = P_{\text{tot}} - P_{\text{H}_2\text{O}}$ ).



The parameterizations of  $S_k(T)$  was already in use for the early version of MPM81 [Liebe, 1981]. The expression for  $\gamma_k$  is the same as in MPM89. The main difference between MPM93 and MPM89 concerning the water vapor line absorption is the updated line catalog.

$k$	$\nu_k$ [GHz]	$b_{1,k}$ [ $\frac{\text{kHz}}{\text{hPa}}$ ]	$b_{2,k}$ [1]	$b_{3,k}$ [ $\frac{\text{MHz}}{\text{hPa}}$ ]	$b_{4,k}$ [1]	$b_{5,k}$ [1]	$b_{6,k}$ [1]
1	22.235080	0.01130	2.143	2.811	4.80	0.69	1.00
2	67.803960	0.00012	8.735	2.858	4.93	0.69	0.82
3	119.995940	0.00008	8.356	2.948	4.78	0.70	0.79
4	183.310091	0.24200	0.668	3.050	5.30	0.64	0.85
5	321.225644	0.00483	6.181	2.303	4.69	0.67	0.54
6	325.152919	0.14990	1.540	2.783	4.85	0.68	0.74
7	336.222601	0.00011	9.829	2.693	4.74	0.69	0.61
8	380.197372	1.15200	1.048	2.873	5.38	0.54	0.89
9	390.134508	0.00046	7.350	2.152	4.81	0.63	0.55
10	437.346667	0.00650	5.050	1.845	4.23	0.60	0.48
11	439.150812	0.09218	3.596	2.100	4.29	0.63	0.52
12	443.018295	0.01976	5.050	1.860	4.23	0.60	0.50
13	448.001075	1.03200	1.405	2.632	4.84	0.66	0.67
14	470.888947	0.03297	3.599	2.152	4.57	0.66	0.65
15	474.689127	0.12620	2.381	2.355	4.65	0.65	0.64
16	488.491133	0.02520	2.853	2.602	5.04	0.69	0.72
17	503.568532	0.00390	6.733	1.612	3.98	0.61	0.43
18	504.482692	0.00130	6.733	1.612	4.01	0.61	0.45
19 <sup>+</sup>	547.676440	0.97010	0.114	2.600	4.50	0.70	1.00
20 <sup>+</sup>	552.020960	1.47700	0.114	2.600	4.50	0.70	1.00
21	556.936002	48.74000	0.159	3.210	4.11	0.69	1.00
22	620.700807	0.50120	2.200	2.438	4.68	0.71	0.68
23 <sup>+</sup>	645.866155	0.00713	8.580	1.800	4.00	0.60	0.50
24	658.005280	0.03022	7.820	3.210	4.14	0.69	1.00
25	752.033227	23.96000	0.396	3.060	4.09	0.68	0.84
26	841.053973	0.00140	8.180	1.590	5.76	0.33	0.45
27	859.962313	0.01472	7.989	3.060	4.09	0.68	0.84
28	899.306675	0.00605	7.917	2.985	4.53	0.68	0.90
29	902.616173	0.00426	8.432	2.865	5.10	0.70	0.95
30	906.207325	0.01876	5.111	2.408	4.70	0.70	0.53
31	916.171582	0.83400	1.442	2.670	4.78	0.70	0.78
32 <sup>+</sup>	923.118427	0.00869	10.220	2.900	5.00	0.70	0.80
33	970.315022	0.89720	1.920	2.550	4.94	0.64	0.67
34	987.926764	13.21000	0.258	2.985	4.55	0.68	0.90
	$\nu^*$ [GHz]	$b_1^*$ [ $\frac{\text{kHz}}{\text{hPa}}$ ]	$b_2^*$ [1]	$b_3^*$ [ $\frac{\text{MHz}}{\text{hPa}}$ ]	$b_4^*$ [1]	$b_5^*$ [1]	$b_6^*$ [1]

---

1780.000000	2230.00000	0.952	17.620	30.50	2.00	5.00
-------------	------------	-------	--------	-------	------	------

---

Table 2.15: List of used H<sub>2</sub>O spectral lines and their spectroscopic coefficients of H<sub>2</sub>O in air for the MPM93 model [Liebe *et al.*, 1993]. The last separated line is the unphysical pseudo-line used in MPM93. The lines which are marked with a “+” were not in the MPM87/MPM89 line catalog.

**The MPM93 continuum parameterization:** In the MPM93 version the water vapor continuum is parameterized as an ordinary spectral line (Eqs. (2.157, 2.158)). The parameters of this continuum “pseudo-line” ( $\nu^*$ ,  $b_1^*$ ,  $b_2^*$ ,  $b_3^*$ ,  $b_4^*$ ,  $b_5^*$ ,  $b_6^*$ ) are given in Table 2.15. More details about this continuum parameterization and its microwave approximation can be found in Section 2.2.1 of this guide.

### CP98 water vapor absorption model

**Line absorption** component [Cruz Pol *et al.*, 1998] for the water vapor line absorption is based on MPM87 with the main difference that the line catalog consists of only a single line at  $\nu_o = 22$  GHz. The contributions from the other lines is put into the water vapor continuum module. The line absorption is therefore very quickly calculated (in units of Np/km) according to the formula

$$\alpha_\ell^{\text{CP98}} = 0.0419 \cdot S_0(T) \cdot F(\nu, \nu_k) \quad (2.161)$$

with

$$\begin{aligned} S_0(T) &= 0.0109 \cdot C_L \cdot P_{\text{H}_2\text{O}} \cdot \nu_0 \cdot \Theta^{3.5} \cdot \exp(2.143 \cdot [1 - \Theta]) \\ \gamma &= 0.002784 \cdot C_W \cdot (P_d \cdot \Theta^{0.6} + 4.8 \cdot P_{\text{H}_2\text{O}} \cdot \Theta^{1.1}) \end{aligned} \quad (2.162)$$

where  $P_{\text{H}_2\text{O}}$  and  $P_d$  are the partial pressure of water vapor and dry air in units of hPa, respectively and the Van Vleck-Weisskopf line shape,  $F(\nu, \nu_k)$ . The numbers correspond to the line parameters from MPM87 for this special line and the factors  $C_L$  and  $C_W$  are adjustable scaling factors to match the model with the measurements. Setting the scaling factors to  $C_L=1.00$  and  $C_W=1.00$  leads to the same results as for MPM87. According to the parameter estimation of Cruz–Pol *et al.* best agreement between data and model is obtained with  $C_L = 1.0639 \pm 0.016$  and  $C_W = 1.0658 \pm 0.0096$ . The correlation between these two scaling factors was found to be negligible, as can be seen from Table 2.16.

The main reason why the Cruz-Pol model (CP98) considers only one line lies in the fact that CP98 is especially designed for the data analysis in the 20-31.4 GHz region. The determination of the scaling factors was performed with ground based radiometer data in the frequency range of from different locations<sup>4</sup> in the USA.

**Water vapor continuum absorption:** The CP98 model uses the same water vapor continuum parameterization as MPM87, just scaled with an empirical factor,  $C_C$ , determined from the above mentioned data:

$$\alpha_c^{\text{CP98}} = C_C \cdot \alpha_c^{\text{MPM87}} \quad (2.163)$$

---

<sup>4</sup>The data were recorded at San Diego, California (11. December 1991) and West Palm Beach, Florida (8.-21. March 1992)

	$C_L$	$C_W$	$C_C$	$C_X$
value	1.0639	1.0658	1.2369	1.0739
std. dev.	0.016	0.0096	0.155	0.252
correlation				
$C_L$	1	-0.085	0.045	-0.048
$C_W$	-0.085	1	-0.513	0.485
$C_C$	0.045	-0.513	1	-0.989
$C_X$	-0.048	0.485	-0.989	1

Table 2.16: Scaling parameter values with standard deviation and correlation coefficients according to [Cruz Pol et al., 1998]. The scaling parameters are  $C_L$ :22 GHz line strength,  $C_W$ :22 GHz line width,  $C_C$ :H<sub>2</sub>O-continuum, and  $C_X$ :O<sub>2</sub>-absorption.  $C_X$  scales the entire oxygen absorption, the continuum as well as the line absorption. The Cruz-Pol et al. model uses the Rosenkranz [1993] oxygen absorption model.

The scaling factor  $C_C$ , as given in Table 2.16, gives a 23.69 % increased continuum absorption compared with MPM87 (see Table 2.10 for a comparison of the parameter values). But one has to keep in mind that  $C_C$  has a high correlation with the scaling factor of the oxygen absorption,  $C_X$ , since these two components could not be completely distinguished in the data. Therefore the value of 23.69 % has a standard deviation of 15.5 % and is not so reliable than  $C_L$  and  $C_W$ .

### PWR98 water vapor absorption model

The water vapor continuum formulation of Rosenkranz [1998] is a re-investigation of the existing models MPM87/MPM89, MPM93, and CKD\_2.1 especially for the frequency region below 1-1000 GHz. in the context of the available laboratory and atmospheric data [Bauer et al., 1989, 1993, 1995; Becker and Autler, 1946; English et al., 1994; Godon et al., 1992; Liebe, 1984; Liebe and Layton, 1987; Westwater et al., 1980].

Rosenkranz adopted the structure of MPM89 for his improved model (R98). However, some important differences exist compared with MPM89:

- the water vapor line catalogs are different
- the R98 uses the Van Vleck–Weisskopf line shape function with cutoff and MPM89 without cutoff

**Water vapor line absorption:** The local line absorption is defined as

$$\begin{aligned}
 \alpha_{\ell}^{\text{R98}} &= N_{\text{H}_2\text{O}} \cdot \sum_k S_k(T) \cdot F_c(\nu, \nu_k) \\
 &= N_{\text{H}_2\text{O}} \cdot \sum_k S_k(T) \cdot \left( \frac{\nu}{\nu_k} \right)^2 \cdot [f_c(\nu, +\nu_k) + f_c(\nu, -\nu_k)] \text{ Np/km} \quad (2.164)
 \end{aligned}$$

where  $N_{\text{H}_2\text{O}}$  is the number density of water molecules,  $\nu$  the frequency and  $S$  the line intensity, calculated from the HITRAN92 data base Rothman et al. [1992]. Considered for this re-investigation are 15 lines with a frequency lower than 1 THz as listed in Table 2.17.

The line shape function  $F_c(\nu, \nu_k)$  has a cutoff frequency,  $\nu_{\text{cutoff}}$ , and a baseline subtraction similar to the CKD model [Clough et al., 1989]. The introduction of a cutoff frequency

has two advantages: (1) the cutoff avoids applying the line shape to distant frequencies where the line form is theoretically not well understood and (2) the cutoff also establishes a limit to the summation in Eq. (2.164) where lines far away from the cutoff limit do not contribute to the sum. The Rosenkranz formulation uses the same value for the cutoff frequency as the CKD model:

$$\nu_{\text{cutoff}} = 750 \text{ GHz} \quad (2.165)$$

The explicit mathematical form of the line shape function is defined in such a way that in the limit  $\nu_{\text{cutoff}} \rightarrow \infty$  the combination of Eq. (2.164) with the line shape function would be equivalent to a Van Vleck–Weisskopf [*Van Vleck and Weisskopf, 1945*] line shape:

$$f_c(\nu, \pm \nu_k) = \begin{cases} \frac{\gamma_k}{\pi} \left\{ \frac{1}{(\nu \mp \nu_k)^2 + \gamma_k^2} - \frac{1}{\nu_{\text{cutoff}}^2 + \gamma_k^2} \right\} & : |\nu \pm \nu_k| < \nu_{\text{cutoff}} \\ 0 & : |\nu \pm \nu_k| \geq \nu_{\text{cutoff}} \end{cases} \quad (2.166)$$

$\nu_k$  is the line center frequency and  $\gamma_k$  the line half width, which is calculated according to

$$\gamma_k = w_{s,k} \cdot P_{\text{H}_2\text{O}} \cdot \Theta^{n_s} + w_{f,k} \cdot P_d \cdot \Theta^{n_f} \quad \text{GHz} \quad (2.167)$$

with  $P_{\text{H}_2\text{O}}$  and  $P_d$  as the partial pressure of water vapor and of dry air, respectively. The line depending parameters  $w_{s,k}$ ,  $n_s$ ,  $w_{f,k}$ , and  $n_f$  are listed in Table 2.17 and the dimensionless parameter  $\Theta$  is defined as  $\Theta = 300 \text{ K}/T$ .

Because of the structural similarity to MPM89, the line broadening parameters differ only in minor respects from the values used therein (only the parameters  $x_{s,1}$ ,  $w_{f,2}$  and  $w_{s,2}$  are significantly different).

index	$\nu_k$	$w_{f,k}$	$n_f$	$w_{s,k}$	$n_s$
k	[GHz]	[GHz/kPa]	[1]	[GHz/kPa]	[1]
1	22.2351	0.00281	0.69	0.01349	0.61
2	183.3101	0.00281	0.64	0.01491	0.85
3	321.2256	0.00230	0.67	0.01080	0.54
4	325.1529	0.00278	0.68	0.01350	0.74
5	380.1974	0.00287	0.54	0.01541	0.89
6	439.1508	0.00210	0.63	0.00900	0.52
7	443.0183	0.00186	0.60	0.00788	0.50
8	448.0011	0.00263	0.66	0.01275	0.67
9	470.8890	0.00215	0.66	0.00983	0.65
10	474.6891	0.00236	0.65	0.01095	0.64
11	488.4911	0.00260	0.69	0.01313	0.72
12	556.9360	0.00321	0.69	0.01320	1.00
13	620.7008	0.00244	0.71	0.01140	0.68
14	752.0332	0.00306	0.68	0.01253	0.84
15	916.1712	0.00267	0.70	0.01275	0.78

Table 2.17: Line parameters of the Rosenkranz absorption model (PWR98) (values taken from *Rosenkranz [1998]*).

**Water vapor continuum absorption:** The continuum absorption in R98 has the same functional dependence on frequency, pressure, and temperature like in MPM87/MPM89 (see Sec. 2.3.1 for details):

$$\alpha_c^{R98} = \nu^2 \cdot P_{H_2O} \cdot (C_{H_2O}^O \cdot P_{H_2O} \cdot \Theta^{n_s} + C_d^O \cdot P_d \cdot \Theta^{n_f}) \quad (2.168)$$

with

$$C_{H_2O}^O = 7.80 \cdot 10^{-8} \text{ (dB/km) / (hPa} \cdot \text{GHz)}^2$$

$$n_s = 7.5$$

$$C_d^O = 0.236 \cdot 10^{-8} \text{ (dB/km) / (hPa} \cdot \text{GHz)}^2$$

$$n_d = 3.0$$

The main difference to the MPM versions are the values of these parameters, since Rosenkranz used additional data to fit his set of parameters. A second point is the cut-off in the line shape of the line absorption calculation. Since this cutoff decreases the line absorption in the window regions, the continuum absorption tends to compensate this decrease to get the same total absorption as without cutoff. This effects mainly the parameters  $C_{H_2O}^O$  and  $C_d^O$  but has also an influence in the temperature dependence and therefore on  $n_s$  and  $n_d$ .

### 2.3.2 Complete oxygen models

Since the Maxwell equations are symmetric in the electric and magnetic fields, electric as well as magnetic dipole transitions are both possible although magnetic dipoles are in general some orders of magnitudes weaker and therefore not relevant in atmospheric radiative transfer models. An exception to this is the complex around 60 GHz of the paramagnetic oxygen magnetic dipole transitions. This bulk of lines arise due to the fact that for rotational quantum numbers  $K > 1$  the allowed transitions  $\Delta J = \pm 1$  have an energy gap of approximately 60 GHz.

The most frequently used absorption model for this absorption effect is that of Liebe, Rosenkranz, and Hufford [*Liebe et al.*, 1992] (also reported in *Rosenkranz* [1993] with a slightly different parameterization).

For oxygen – like for water vapor – the total absorption ( $\alpha_{tot}$ ) is modelled as the line absorption ( $\alpha_\ell$ ) plus a continuum absorption ( $\alpha_c$ ):

$$\alpha_{tot} = \alpha_\ell + \alpha_c \quad (2.169)$$

It has to be emphasized that,  $\alpha_\ell$  and  $\alpha_c$  of different models are not necessarily compatible and should therefore not be interchanged.

#### PWR93 oxygen absorption model

**Resonant oxygen absorption** The oxygen absorption model of Rosenkranz is described in *Rosenkranz* [1993]. It is based on the investigations made by Liebe, Rosenkranz, and Hufford [*Liebe et al.*, 1992]. The FORTRAN77 computer program of Rosenkranz for the O<sub>2</sub> absorption calculation can be downloaded via anonymous ftp from mesa.mit.edu/phil/lbl\_rt.

The oxygen line catalog has 40 lines from which 33 lines build the complex around 60 GHz. The parameterization of the line absorption,  $\alpha_\ell^{\text{R98}}$ , is:

$$\alpha_\ell^{\text{R98}} = \frac{n_{\text{O}_2}}{\pi} \cdot \sum_{k=1}^{40} S_k(T) \cdot F(\nu, \nu_k) \quad (2.170)$$

line intensity:

$$S_k(T) = S_k(300 \text{ K}) / \exp(b_k \cdot \Theta) \quad (2.171)$$

line shape function:

$$F(\nu, \nu_k) = \left( \frac{\nu}{\nu_k} \right)^2 \cdot \left[ \frac{\Gamma_k + (\nu - \nu_k) \cdot Y_k}{(\nu - \nu_k)^2 + \Gamma_k^2} + \frac{\Gamma_k - (\nu + \nu_k) \cdot Y_k}{(\nu + \nu_k)^2 + \Gamma_k^2} \right]$$

line width:

$$\Gamma_k = w_k \cdot (P_d \cdot \Theta^{0.8} + 1.1 \cdot P_{\text{H}_2\text{O}} \cdot \Theta) \quad (2.172)$$

line coupling:

$$Y_k = P_{\text{air}} \cdot \Theta^{0.8} \cdot [y_k + (\Theta - 1) \cdot v_k]$$

number density of  $\text{O}_2$ :

$$n_{\text{O}_2} = (0.20946 \cdot P_{\text{air}}) / (k_B \cdot T)$$

where  $S_k(300 \text{ K})$  denotes the reference line intensity at  $T=300 \text{ K}$  and the exponential term approximates the exact partition function. All model parameters (see Refs. *Rosenkranz* [1993] and *Liebe et al.* [1992] for the laboratory measurements and the fitting parameters) are tabulated in Table 2.18.

index $k$	$\nu_k$ [GHz]	$S_k(300 \text{ K})$ [cm <sup>2</sup> Hz]	$b_k$ [1]	$w_k$ [ $\frac{\text{MHz}}{\text{hPa}}$ ]	$y_k$ [ $\frac{10^{-3}}{\text{hPa}}$ ]	$v_k$ [ $\frac{10^{-3}}{\text{hPa}}$ ]
1	118.7503	.2936 · 10 <sup>-14</sup>	.009	1.63	-0.0233	0.0079
2	56.2648	.8079 · 10 <sup>-15</sup>	.015	1.646	0.2408	-0.0978
3	62.4863	.2480 · 10 <sup>-14</sup>	.083	1.468	-0.3486	0.0844
4	58.4466	.2228 · 10 <sup>-14</sup>	.084	1.449	0.5227	-0.1273
5	60.3061	.3351 · 10 <sup>-14</sup>	.212	1.382	-0.5430	0.0699
6	59.5910	.3292 · 10 <sup>-14</sup>	.212	1.360	0.5877	-0.0776
7	59.1642	.3721 · 10 <sup>-14</sup>	.391	1.319	-0.3970	0.2309
8	60.4348	.3891 · 10 <sup>-14</sup>	.391	1.297	0.3237	-0.2825
9	58.3239	.3640 · 10 <sup>-14</sup>	.626	1.266	-0.1348	0.0436
10	61.1506	.4005 · 10 <sup>-14</sup>	.626	1.248	0.0311	-0.0584
11	57.6125	.3227 · 10 <sup>-14</sup>	.915	1.221	0.0725	0.6056
12	61.8002	.3715 · 10 <sup>-14</sup>	.915	1.207	-0.1663	-0.6619
13	56.9682	.2627 · 10 <sup>-14</sup>	1.260	1.181	0.2832	0.6451
14	62.4112	.3156 · 10 <sup>-14</sup>	1.260	1.171	-0.3629	-0.6759
15	56.3634	.1982 · 10 <sup>-14</sup>	1.660	1.144	0.3970	0.6547
16	62.9980	.2477 · 10 <sup>-14</sup>	1.665	1.139	-0.4599	-0.6675
17	55.7838	.1391 · 10 <sup>-14</sup>	2.119	1.110	0.4695	0.6135
18	63.5685	.1808 · 10 <sup>-14</sup>	2.115	1.108	-0.5199	-0.6139
19	55.2214	.9124 · 10 <sup>-15</sup>	2.624	1.079	0.5187	0.2952
20	64.1278	.1230 · 10 <sup>-14</sup>	2.625	1.078	-0.5597	-0.2895

Table 2.18: (continued on next page)

index	$\nu_k$	$S_k(300\text{ K})$	$b_k$	$w_k$	$y_k$	$v_k$
21	54.6712	$.5603 \cdot 10^{-15}$	3.194	1.05	0.5903	0.2654
22	64.6789	$.7842 \cdot 10^{-15}$	3.194	1.05	-0.6246	-0.2590
23	54.1300	$.3228 \cdot 10^{-15}$	3.814	1.02	0.6656	0.3750
24	65.2241	$.4689 \cdot 10^{-15}$	3.814	1.02	-0.6942	-0.3680
25	53.5957	$.1748 \cdot 10^{-15}$	4.484	1.00	0.7086	0.5085
26	65.7648	$.2632 \cdot 10^{-15}$	4.484	1.00	-0.7325	-0.5002
27	53.0669	$.8898 \cdot 10^{-16}$	5.224	.97	0.7348	0.6206
28	66.3021	$.1389 \cdot 10^{-15}$	5.224	.97	-0.7546	-0.6091
29	52.5424	$.4264 \cdot 10^{-16}$	6.004	.94	0.7702	0.6526
30	66.8368	$.6899 \cdot 10^{-16}$	6.004	.94	-0.7864	-0.6393
31	52.0214	$.1924 \cdot 10^{-16}$	6.844	.92	0.8083	0.6640
32	67.3696	$.3229 \cdot 10^{-16}$	6.844	.92	-0.8210	-0.6475
33	51.5034	$.8191 \cdot 10^{-17}$	7.744	.89	0.8439	0.6729
34	67.9009	$.1423 \cdot 10^{-16}$	7.744	.89	-0.8529	-0.6545
35	368.4984	$.6460 \cdot 10^{-15}$	.048	1.92	0.0000	0.0000
36	424.7631	$.7047 \cdot 10^{-14}$	.044	1.92	0.0000	0.0000
37	487.2494	$.3011 \cdot 10^{-14}$	.049	1.92	0.0000	0.0000
38	715.3932	$.1826 \cdot 10^{-14}$	.145	1.81	0.0000	0.0000
39	773.8397	$.1152 \cdot 10^{-13}$	.141	1.81	0.0000	0.0000
40	834.1453	$.3971 \cdot 10^{-14}$	.145	1.81	0.0000	0.0000

Table 2.18: List of O<sub>2</sub> spectral lines of the Rosenkranz absorption model [Rosenkranz, 1993].

**Oxygen continuum absorption:** As pointed out by Van Vleck [Van Vleck, 1987], the standard theory for non-resonant absorption is that of Debye (see also Ref. Townes and Schawlow [1955]). The Debye line shape is obtained from the VVW line shape function by the limiting case  $\nu_k \rightarrow 0$ . Rosenkranz [Rosenkranz, 1993] adopt the Debye theory for his models:

$$\alpha_c = C \cdot P_d \cdot \Theta^2 \cdot \frac{\nu^2 \cdot \gamma}{\nu^2 + \gamma^2} \quad (2.173)$$

$$\gamma = w \cdot (P_d \cdot \Theta^{0.8} + 1.1 \cdot P_{\text{H}_2\text{O}} \cdot \Theta) \quad (2.174)$$

The values for the parameters are  $C = 1.11 \cdot 10^{-5}$  dB/km/(hPa GHz) and  $w = 5.6 \cdot 10^{-4}$  GHz/hPa, respectively. This absorption term is proportional to the collision frequency of a single oxygen molecule and thus proportional to the dry air pressure<sup>5</sup>.

### MPM93 oxygen absorption model

**Oxygen line absorption:** The oxygen line catalog has 44 lines from which 37 lines build the complex around 60 GHz [Liebe et al., 1993]. The parameterization of the line absorp-

<sup>5</sup>The absorption due to weakly bound complexes of O<sub>2</sub>-X with X = H<sub>2</sub>O, N<sub>2</sub> is treated separately and therefore not included in this Debye formula.

tion,  $\alpha_\ell^{\text{MPM}}$ , is (in units of dB/km):

$$\alpha_\ell^{\text{MPM}} = 0.1820 \cdot \nu^2 \cdot \sum_{k=1}^{44} S_k(T) \cdot F(\nu, \nu_k) \quad \text{dB/km} \quad (2.175)$$

with

line intensity:

$$S_k(T) = \frac{a_{1,k}}{\nu_k} \cdot P_d \cdot \Theta^3 \cdot \exp[a_{2,k} \cdot (1 - \Theta)] \quad (2.176)$$

line shape function:

$$F(\nu, \nu_k) = \left[ \frac{\gamma_k + (\nu - \nu_k) \cdot \delta_k}{(\nu - \nu_k)^2 + \gamma_k^2} + \frac{\gamma_k - (\nu + \nu_k) \cdot \delta_k}{(\nu + \nu_k)^2 + \gamma_k^2} \right]$$

line width:

$$\gamma_k = a_{3,k} \cdot 10^{-3} \cdot (P_d \cdot \Theta^{a_{4,k}} + 1.10 \cdot P_{\text{H}_2\text{O}} \cdot \Theta) \quad (2.177)$$

line coupling:

$$\delta_k = P_{\text{air}} \cdot \Theta^{0.8} \cdot [a_{5,k} + \Theta \cdot a_{6,k}]$$

where  $a_{1-5,k}$  are the fitted parameters due to laboratory measurements [*Liebe et al., 1992*]. All model parameters are tabulated in Table 2.19. One has to note that in the MPM93 code is a threshold value for  $\alpha_\ell^{\text{MPM}}$  implemented:

$$\alpha_\ell^{\text{MPM}} = \begin{cases} \alpha_\ell^{\text{MPM}} & : \alpha_\ell^{\text{MPM}} > 0 \\ 0 & : \alpha_\ell^{\text{MPM}} < 0 \end{cases} \quad (2.178)$$

Therefore the oxygen absorption in the wings of the strong O<sub>2</sub>-lines is remarkably higher than in the R93 model.

index $k$	$\nu_k$ [GHz]	$a_{1,k}$ [ $\frac{\text{kHz}}{\text{hPa}}$ ]	$a_{2,k}$ [1]	$a_{3,k}$ [ $\frac{\text{MHz}}{\text{hPa}}$ ]	$a_{4,k}$ [1]	$a_{5,k}$ [ $\frac{10^3}{\text{hPa}}$ ]	$a_{6,k}$ [ $\frac{10^3}{\text{hPa}}$ ]
1	50.474238	0.094	9.694	0.890	0.0	0.240	0.790
2	50.987749	0.246	8.694	0.910	0.0	0.220	0.780
3	51.503350	0.608	7.744	0.940	0.0	0.197	0.774
4	52.021410	1.414	6.844	0.970	0.0	0.166	0.764
5	52.542394	3.102	6.004	0.990	0.0	0.136	0.751
6	53.066907	6.410	5.224	1.020	0.0	0.131	0.714
7	53.595749	12.470	4.484	1.050	0.0	0.230	0.584
8	54.130000	22.800	3.814	1.070	0.0	0.335	0.431
9	54.671159	39.180	3.194	1.100	0.0	0.374	0.305
10	55.221367	63.160	2.624	1.130	0.0	0.258	0.339
11	55.783802	95.350	2.119	1.170	0.0	-0.166	0.705
12	56.264775	54.890	0.015	1.730	0.0	0.390	-0.113
13	56.363389	134.400	1.660	1.200	0.0	-0.297	0.753
14	56.968206	176.300	1.260	1.240	0.0	-0.416	0.742
15	57.612484	214.100	0.915	1.280	0.0	-0.613	0.697
16	58.323877	238.600	0.626	1.330	0.0	-0.205	0.051
17	58.446590	145.700	0.084	1.520	0.0	0.748	-0.146
18	59.164207	240.400	0.391	1.390	0.0	-0.722	0.266

Table 2.19: (continued on next page)



index	$\nu_k$	$a_{1,k}$	$a_{2,k}$	$a_{3,k}$	$a_{4,k}$	$a_{5,k}$	$a_{6,k}$
19	59.590983	211.200	0.212	1.430	0.0	0.765	-0.090
20	60.306061	212.400	0.212	1.450	0.0	-0.705	0.081
21	60.434776	246.100	0.391	1.360	0.0	0.697	-0.324
22	61.150560	250.400	0.626	1.310	0.0	0.104	-0.067
23	61.800154	229.800	0.915	1.270	0.0	0.570	-0.761
24	62.411215	193.300	1.260	1.230	0.0	0.360	-0.777
25	62.486260	151.700	0.083	1.540	0.0	-0.498	0.097
26	62.997977	150.300	1.665	1.200	0.0	0.239	-0.768
27	63.568518	108.700	2.115	1.170	0.0	0.108	-0.706
28	64.127767	73.350	2.620	1.130	0.0	-0.311	-0.332
29	64.678903	46.350	3.195	1.100	0.0	-0.421	-0.298
30	65.224071	27.480	3.815	1.070	0.0	-0.375	-0.423
31	65.764772	15.300	4.485	1.050	0.0	-0.267	-0.575
32	66.302091	8.009	5.225	1.020	0.0	-0.168	-0.700
33	66.836830	3.946	6.005	0.990	0.0	-0.169	-0.735
34	67.369598	1.832	6.845	0.970	0.0	-0.200	-0.744
35	67.900867	0.801	7.745	0.940	0.0	-0.228	-0.753
36	68.431005	0.330	8.695	0.920	0.0	-0.240	-0.760
37	68.960311	0.128	9.695	0.900	0.0	-0.250	-0.765
38	118.750343	94.500	0.009	1.630	0.0	-0.036	0.009
39	368.498350	6.790	0.049	1.920	0.6	0.000	0.000
40	424.763124	63.800	0.044	1.930	0.6	0.000	0.000
41	487.249370	23.500	0.049	1.920	0.6	0.000	0.000
42	715.393150	9.960	0.145	1.810	0.6	0.000	0.000
43	773.839675	67.100	0.130	1.820	0.6	0.000	0.000
44	834.145330	18.000	0.147	1.810	0.6	0.000	0.000

Table 2.19: List of O<sub>2</sub> spectral lines of the MPM93 absorption model [*Liebe et al.*, 1993].

**Oxygen continuum absorption:** As pointed out by Van Vleck [*Van Vleck*, 1987], the standard theory for non-resonant absorption is that of Debye (see also Ref. *Townes and Schawlow* [1955]). The Debye line shape is obtained from the VVW line shape function by the limiting case  $\nu_k \rightarrow 0$ . *Liebe et al.* [1993] adopt the Debye theory for his model:

$$\begin{aligned}\alpha_c &= C \cdot P_d \cdot \Theta^2 \cdot \frac{\nu^2 \cdot \gamma}{\nu^2 + \gamma^2} \\ \gamma &= w \cdot P_{\text{tot}} \cdot \Theta^{0.8}\end{aligned}\tag{2.179}$$

The values for the parameters are  $C = 1.11 \cdot 10^{-5}$  dB/km/(hPa GHz) and  $w = 5.6 \cdot 10^{-4}$  GHz/hPa, respectively. This absorption term is proportional to the collision frequency of a single oxygen molecule and thus proportional to the dry air pressure<sup>6</sup>.

<sup>6</sup>The absorption due to weakly bound complexes of O<sub>2</sub>-X with X = H<sub>2</sub>O, N<sub>2</sub> is treated separately and therefore not included in this Debye formula.

## 2.4 Absorption cross section model

Many heavy polyatomic molecules possess spectra that are too dense and complex to compute line-by-line. Instead measured absorption cross-sections are used. The 2016 edition of HITRAN (high-resolution transmission molecular absorption database) draws on such compilations, and complements them with numerous individual measurements from the literature, in order to provide measured absorption cross-sections for numerous gas molecules. These HITRAN cross-section data are described in detail in *Gordon et al. [2017]*. For each molecular absorption species, there are data in one or more spectral bands, and for each spectral band, there can be data at several different pressures and several different temperatures.

The basic idea is to set up a simple model for the pressure and temperature dependence of the absorption species, and then apply a global fit to all the available laboratory spectra for a given species.

The HITRAN cross-section data are very diverse in their spectral resolution, and in pressure  $p$  and temperature  $T$  coverage, as discussed in detail in *Kochanov et al. [2019]*. For example, there are species that have high  $p / T$  resolution data in a specific spectral range and only coarse  $p / T$  resolution data outside that range. Frequency resolution also varies considerably in different parts of the spectrum. Before the fit, the input data have to be harmonised with respect to their frequency grids. The highest spectral resolution of the set of observations of a species is used as the reference resolution. The observations with coarser frequency resolution are linearly interpolated onto this resolution. Some molecular species have a very high resolution for a small spectral range, and coarse resolution or no data elsewhere. Therefore, the data are split into bands of different spectral resolution. Table 2.20 and 2.21 list the implemented species, their bands, and for each band the  $p / T$  limits of the laboratory data and the polynomial orders in  $p$  and  $T$  that were adopted.

Since the number of observations at different temperatures and pressures varies over the spectral range, the fitting model is selected for each frequency individually, as summarised in Table 2.22. Explicitly, for a given species and at a given frequency  $\nu$ , the observed cross-section  $\sigma(\nu, T, p)$  is fitted in temperature  $T$  and pressure  $p$  by an up to 2nd order polynomial:

$$\sigma(\nu, T, p) = c_{00}(\nu) + c_{10}(\nu)x + c_{01}(\nu)y + c_{20}(\nu)x^2 \quad (2.180)$$

with

$$x = \frac{T}{T_0}, \quad (2.181)$$

and

$$y = \frac{p}{p_0}, \quad (2.182)$$

using a least squares fit. The variables  $T_0 = 1$  K and  $p_0 = 1$  Pa are constant factors to remove the units of  $T$  and  $p$ . The coefficients  $c_{ij}$  and the cross-section  $\sigma(\nu)$  are defined in units of  $[\text{m}^2]$ .

The fitting process includes a simple outlier detection algorithm.

1. Fit the data using all given data at frequency  $f$ .
2. Estimate the residuals between fit and data.

Table 2.20: Considered cross section species together with spectral, pressure and temperature limits and with  $O_{p,T}$  the maximum polynomial order of the pressure/temperature dependency of the band. (First half)

species	band	$\tilde{\nu}_{min}$ [cm <sup>-1</sup> ]	$\tilde{\nu}_{max}$ [cm <sup>-1</sup> ]	$\delta\tilde{\nu}$ [cm <sup>-1</sup> ]	$p_{min}$ [hPa]	$p_{max}$ [hPa]	$T_{min}$ [K]	$T_{max}$ [K]	$O_p$	$O_T$
CFC11	0	570	810	0.060	1013.25	1013.25	278.10	323.10	0	1
	1	810	880	0.003	10.00	1013.25	190.00	323.10	1	2
	2	880	1050	0.060	1013.25	1013.25	278.10	323.10	0	1
	3	1050	1120	0.003	10.00	1013.25	190.00	323.10	1	2
	4	1120	6500	0.060	1013.25	1013.25	278.10	323.10	0	1
CFC12	0	800	1270	0.001	10.00	1014.58	189.50	296.30	1	2
CFC113	0	600	1250	0.015	0.00	1013.25	203.00	323.10	1	2
	1	1250	5000	0.060	1013.25	1013.25	278.10	323.10	0	1
CFC114	0	600	815	0.060	1013.25	1013.25	278.10	323.10	0	1
	1	815	860	0.015	0.00	1013.25	203.00	323.10	1	2
	2	860	870	0.060	1013.25	1013.25	278.10	323.10	0	1
	3	870	960	0.015	0.00	1013.25	203.00	323.10	1	2
	4	960	1030	0.060	1013.25	1013.25	278.10	323.10	0	1
	5	1030	1067	0.015	0.00	1013.25	203.00	323.10	1	2
	6	1067	1095	0.060	1013.25	1013.25	278.10	323.10	0	1
	7	1095	1285	0.015	0.00	1013.25	203.00	323.10	1	2
CFC115	8	1285	5000	0.060	1013.25	1013.25	278.10	323.10	0	1
	0	955	1015	0.015	0.00	0.00	203.00	293.00	0	2
	1	1110	1145	0.015	0.00	0.00	203.00	293.00	0	2
	2	1167	1260	0.015	0.00	0.00	203.00	293.00	0	2
HCFC22	0	730	1380	0.001	0.00	1019.38	181.00	297.00	1	2
HCFC141b	0	550	560	0.060	1013.25	1013.25	278.10	323.10	0	1
	1	560	3100	0.008	0.00	1013.25	223.00	323.10	1	2
	2	3100	6500	0.060	1013.25	1013.25	278.10	323.10	0	1
HCFC142b	0	600	650	0.060	1013.25	1013.25	278.10	323.10	0	1
	1	650	1500	0.008	0.00	1013.25	223.00	323.10	1	2
	2	1500	6500	0.060	1013.25	1013.25	278.10	323.10	0	1
HFC23	0	950	1500	0.001	30.66	1016.45	187.60	294.40	1	2
HFC32	0	400	450	0.120	933.26	933.26	296.00	296.00	0	0
	1	450	630	0.017	0.00	1013.25	253.00	323.10	1	1
	2	630	995	0.060	933.26	1013.25	278.10	323.10	0	1
	3	995	1236	0.015	0.00	1013.25	203.00	323.10	1	2
	4	1236	1385	0.060	933.26	1013.25	278.10	323.10	0	1
	5	1385	1475	0.015	0.00	1013.25	203.00	323.10	1	2
HFC125	6	1475	6500	0.060	1013.25	1013.25	278.10	323.10	0	1
	0	495	495	0.048	0.00	0.00	253.00	253.00	0	0
	1	495	499	0.048	0.00	799.93	203.00	273.00	0	1
	2	499	1504	0.048	0.00	1013.25	203.00	323.10	1	2
HFC134a	3	1504	6500	0.060	1013.25	1013.25	278.10	323.10	0	1
	0	75	590	0.017	0.00	0.00	253.00	253.00	0	0
	1	600	750	0.015	0.00	0.00	253.00	253.00	0	0
HFC143a	2	750	1600	0.001	0.00	1014.32	190.00	296.00	1	2
	0	500	550	0.060	1013.25	1013.25	278.10	323.10	0	1
	1	550	3500	0.008	0.00	1013.25	203.00	323.10	1	2
HFC152a	2	3500	6500	0.060	1013.25	1013.25	278.10	323.10	0	1
	0	525	830	0.060	1013.25	1013.25	278.10	323.10	0	1
	1	830	840	0.010	0.00	1013.25	253.00	323.10	1	1
	2	840	995	0.009	0.00	1013.25	253.00	323.10	1	1
	3	995	1050	0.010	0.00	1013.25	253.00	323.10	1	1
	4	1050	1205	0.009	0.00	1013.25	253.00	323.10	1	1
	5	1205	1320	0.010	0.00	1013.25	253.00	323.10	1	1
	6	1320	1490	0.009	0.00	1013.25	253.00	323.10	1	1
HFC227ea	7	1490	1500	0.010	0.00	1013.25	253.00	323.10	1	1
	8	1500	6500	0.060	1013.25	1013.25	278.10	323.10	0	1
	0	400	500	0.121	933.26	933.26	296.00	296.00	0	0
	1	500	6500	0.060	933.26	1013.25	278.10	323.10	0	1
HFC236fa	0	350	1500	0.120	933.26	933.26	296.00	296.00	0	0
HFC245fa	0	640	1500	0.241	933.26	933.26	296.00	296.00	0	0
HFC365mfc	0	600	2000	0.060	933.26	933.26	296.00	296.00	0	0

Table 2.21: Considered cross section species together with spectral, pressure and temperature limits and with  $O_{p,T}$  the maximum polynomial order of the pressure/temperature dependency of the band. (Second half)

species	band	$\tilde{\nu}_{min}$ [cm <sup>-1</sup> ]	$\tilde{\nu}_{max}$ [cm <sup>-1</sup> ]	$\delta\tilde{\nu}$ [cm <sup>-1</sup> ]	$p_{min}$ [hPa]	$p_{max}$ [hPa]	$T_{min}$ [K]	$T_{max}$ [K]	$O_p$	$O_T$
HFC4310mee	0	500	550	0.060	1013.25	1013.25	278.10	323.10	0	1
	1	550	3500	0.030	0.00	1013.25	278.10	340.00	1	1
	2	3500	6500	0.060	1013.25	1013.25	278.10	323.10	0	1
CH3CCl3	0	500	6500	0.060	1013.25	1013.25	278.10	323.10	0	1
CCl4	0	700	860	0.001	10.00	1013.25	207.90	296.70	1	2
CH2Cl2	0	600	6500	0.060	1013.25	1013.25	278.10	323.10	0	1
CHCl3	0	580	725	0.060	1013.25	1013.25	278.10	323.10	0	1
	1	725	805	0.048	0.00	1013.25	253.00	323.10	1	1
	2	805	7200	0.060	1013.25	1013.25	278.10	323.10	0	1
Halon1211	0	600	6500	0.060	1013.25	1013.25	278.10	323.10	0	1
Halon1301	0	510	6500	0.060	1013.25	1013.25	278.10	323.10	0	1
Halon2402	0	550	6500	0.060	1013.25	1013.25	278.10	323.10	0	1
NF3	0	600	6500	0.060	1013.25	1013.25	278.10	323.10	0	1
SF6	0	560	925	0.060	1013.25	1013.25	278.10	323.10	0	1
	1	925	955	0.005	26.93	1013.52	180.00	323.10	1	2
	2	955	6500	0.060	1013.25	1013.25	278.10	323.10	0	1
SO2F2	0	500	6500	0.060	1013.25	1013.25	278.10	323.10	0	1
CF4	0	570	1250	0.060	1013.25	1013.25	278.10	323.10	0	1
	1	1250	1290	0.003	10.05	1014.58	180.40	323.10	1	2
	2	1290	6500	0.060	1013.25	1013.25	278.10	323.10	0	1
C2F6	0	500	680	0.060	1013.25	1013.25	278.10	323.10	0	1
	1	680	750	0.015	0.00	1013.25	253.00	323.10	1	1
	2	750	1061	0.060	1013.25	1013.25	278.10	323.10	0	1
	3	1061	1165	0.003	0.00	1013.65	180.60	323.10	1	2
	4	1165	1170	0.060	1013.25	1013.25	278.10	323.10	0	1
	5	1170	1220	0.030	0.00	1013.25	253.00	323.10	1	1
	6	1220	1285	0.003	0.00	1013.65	180.60	323.10	1	2
	7	1285	1380	0.030	0.00	1013.25	253.00	323.10	1	1
	8	1380	6500	0.060	1013.25	1013.25	278.10	323.10	0	1
C3F8	0	600	6500	0.060	1013.25	1013.25	278.10	323.10	0	1
cC4F8	0	550	555	0.061	1013.25	1013.25	278.10	323.10	0	1
	1	555	590	0.015	0.00	1013.25	253.00	323.10	1	1
	2	590	900	0.060	1013.25	1013.25	278.10	323.10	0	1
	3	900	1460	0.015	0.00	1013.25	253.00	323.10	1	1
	4	1460	6500	0.060	1013.25	1013.25	278.10	323.10	0	1
C4F10	0	500	6500	0.060	1013.25	1013.25	278.10	323.10	0	1
C5F12	0	500	700	0.060	1013.25	1013.25	278.10	323.10	0	0
	1	700	1400	0.012	0.00	1013.25	278.10	323.10	0	1
	2	1400	6500	0.060	1013.25	1013.25	278.10	323.10	0	0
C6F14	0	700	1400	0.012	0.00	0.00	297.00	297.00	0	0
C8F18	0	700	1400	0.012	0.00	0.00	297.00	297.00	0	0

3. Fit the data excluding all data points with residuals  $> 1.5 \sigma_{data}$  in which  $\sigma_{data}$  is the standard deviation of the data at given frequency

Table 2.22: Fitting conditions for the cross-section fit. Variables  $x$  and  $y$  are defined according to Equations 2.181 and 2.182. Column ‘min. obs.’ states the minimum required number of observations (laboratory cross-section spectra at different  $p/T$  conditions). The last two columns state the required range in  $p$  and  $T$ , respectively.

fit model	$N_{T,min}$	$N_{p,min}$	$N_{min}$	$\max(p) - \min(p) \geq$	$\max(T) - \min(T) \geq$
$c_{00} + c_{10}x + c_{01}y + c_{20}x^2$	5	2	6	800 hPa	80 K
$c_{00} + c_{10}x + c_{01}y$	2	2	4	800 hPa	40 K
$c_{00} + c_{10}x + c_{20}x^2$	5	1	5	0 hPa	80 K
$c_{00} + c_{10}x$	3	1	3	0 hPa	40 K
$c_{00} + c_{01}y$	1	3	3	800 hPa	0 K
$c_{00}$	1	1	1	0 hPa	0 K

Negative absorption cross sections can occur, when using the fit outside the limited temperature and pressure range. These ranges are defined by the minimum and maximum pressure and temperature of the set of observations for the given species ( $p_{min}$ ,  $p_{max}$ ,  $T_{min}$ ,  $T_{max}$ ). Within the range of atmospheric conditions, the negative values occur only at the noise level of the absorption spectra. Therefore, negative absorption cross sections are simply set to zero. To avoid a positive bias due to the removal of negative values, the spectrum is scaled afterwards so that the integral over the spectrum of the specific band does not change.

## 2.5 Gas scattering

This sections contains theoretical background and scientific details for gas scattering calculations in ARTS. By gas scattering is meant the scattering of electromagnetic radiation with atoms and molecules. Here, we consider only elastic scattering in the case that the wavelength  $\lambda$  is much greater than the spatial dimension  $D$  of the molecule/atom

$$\lambda \gg \pi D \quad (2.183)$$

also known as Rayleigh scattering. Non-elastic scattering processes like Raman or Compton scattering are not considered.

In Earth related optical radiative transfer, Rayleigh scattering is modelled from mixture models based on classical electrodynamics e. g. *Bodhaine et al. [1999]*<sup>7</sup>, *Tomasi et al. [2005]* or *Eberhard [2010]*. In astrophysical related radiative transfer Rayleigh scattering is also modelled from quantum theory [*Fisák, J. et al., 2016*]. For the quantum theory of Rayleigh scattering, see for example *Long [2002]* or *Vinogradov et al. [2021]*. For now, the quantum mechanical treatment of Rayleigh scattering is beyond our scope. Therefore we stick to the classical way.

Following *Tomasi et al. [2005]* for the scattering coefficient  $\beta$  generally holds

$$\beta(\lambda, z) = N(z) \sigma(\lambda, z) \quad (2.184)$$

<sup>7</sup>*Bodhaine et al. [1999]* for example is used in LibRadTran (<http://www.libradtran.org/doc/libRadtran.pdf>, 27/01/2021)

with  $N(z)$  the total number density of molecules and atoms,  $\lambda$  the wavelength and  $z$  the altitude and  $\sigma$  the scattering cross section.

$$\sigma(\lambda, z) = \frac{24\pi^3 \left( n(\lambda, z)^2 - 1 \right)^2}{\lambda^4 N(z)^2 \left( n(\lambda, z)^2 + 2 \right)^2} F(\lambda, z) \quad (2.185)$$

$n(\lambda, z)$  is the refractive index for wavelength  $\lambda$  at altitude  $z$ . Depending on the actual model for the refractive index, the refractive index is a function of pressure  $p$ , temperature  $T$ , wavelength, atmospheric gas composition  $vmr_1, \dots, vmr_M$

$$\Rightarrow n(\lambda, z) = n(\lambda, p, T, vmr_1, \dots, vmr_M) . \quad (2.186)$$

$F(\lambda, z)$  is known as the King factor for the depolarization of air.

$$F(\lambda, z) = \frac{\sum vmr_i(z) F_i(\lambda)}{\sum vmr_i(z)} \quad (2.187)$$

Basically, this means that not only the scattering coefficient  $\beta$  depends on pressure  $p$ , temperature  $T$ , wavelength  $\lambda$  and atmospheric gas compositions  $vmr_i$  but also the scattering cross section. This is different to the scattering handling of solid and liquid matter. For solid and liquid matter the scattering cross sections are independent of pressure, but for the scattering at atoms and molecules this does not hold. Furthermore for the case of gas scattering the normalized phase matrix is in good approximation frequency independent, whereas for the scattering at solid and liquid matter it is not.

For the case of gas scattering the molecules and atoms are assumed to be randomly oriented. In that case the normalized Rayleigh scattering phase matrix for a spherical object *Mishchenko et al. [2002]* is

$$P = \frac{3}{4} \begin{pmatrix} 1 + \cos^2 \Theta & -\sin^2 \Theta & 0 & 0 \\ -\sin^2 \Theta & 1 + \cos^2 \Theta & 0 & 0 \\ 0 & 0 & 2 \cos \Theta & 0 \\ 0 & 0 & 0 & 2 \cos \Theta \end{pmatrix} \quad (2.188)$$

Furthermore, the Rayleigh scattering cross section for air in the visible part of the spectrum can be approximated using a fitted version [*Stamnes et al., 2017*] of the numerical results of [*Bates, 1984*].

$$\sigma_{ray, xsec} = 10^{-28} \lambda^{-4} \sum_{i=0}^3 a_i \lambda^{-2i} \quad [\text{cm}^2] \quad (2.189)$$

with the wavelength  $\lambda$  in  $[\mu\text{m}]$ . The coefficients are

$$\begin{aligned} a_0 &= 3.9729066 \\ a_1 &= 4.6547659 \cdot 10^{-2} \\ a_2 &= 4.5055995 \cdot 10^{-4} \\ a_3 &= 2.3229848 \cdot 10^{-5} . \end{aligned}$$

The formula is accurate to 0.3% for wavelengths between  $0.205\ \mu\text{m}$  and  $1.05\ \mu\text{m}$ . The Rayleigh scattering coefficient is

$$\sigma_{ray} = N\sigma_{ray,xsec} = \frac{p}{Tk_b}\sigma_{ray,xsec} \quad (2.190)$$

with  $N$  the number density of molecules, pressure  $p$ , temperature  $T$  and the Boltzmann constant  $k_B$ .





## Chapter 3

# Cloud absorption

So far only absorption due to air was described. However further, larger particles like hydrometeors (i.e., liquid water and ice particles in the air, either suspended or precipitating), aerosols, dust, haze and the like can have a noticeable effect on the radiative transfer through the atmosphere, too. To treat these particles, one normally sets up a calculation with scattering, which needs input optical properties such as the phase matrix. Several chapters, both in *ARTS User Guide* and here in *ARTS Theory*, deal with such scattering simulations.

This short chapter is not related to the scattering parts in ARTS. Instead, it describes some functions that handle only the absorption by particles, not the scattering. They may be useful in some special cases. Practically, they work exactly as the continuum and complete gas absorption models, just the ‘VMR’ is interpreted as a condensate amount.

Note that it is also possible to only use particles with complete optical property data in the non-scattering context, only considering their absorption effects and neglecting the scattering. This is described in *ARTS User Guide*, Section 6.5.9.

### 3.1 Liquid water and ice particle absorption

The MPM93 model provides beside the absorption model of air also an absorption model for suspended liquid water droplets and ice particles [*Liebe et al.*, 1989, 1991; *Hufford*, 1991; *Liebe et al.*, 1993]. The model is applicable for the Rayleigh regime, for which the relation  $r < 0.05 \cdot \lambda$  holds where  $r$  is the particle radius and  $\lambda$  is the wavelength<sup>1</sup>, e. g. for a frequency of around 22 GHz this means  $r < 500 \mu\text{m}$ . Considering *Salby* [1996], this criterium is – except for cirrus – nearly for every aerosol and cloud class satisfied. But one has to bear in mind that these values have a wide range of variability, for example, *Salby* [1996] states that the mean particle radius for stratus, cumulus, and nimbus clouds can be in the range of 10-1000  $\mu\text{m}$  and that the particle radius distribution is highly unsymmetric.

With respect to the imaginary part of the complex refractivity, a unified parameterization of liquid and ice particle absorption is formulated in MPM93:

$$\begin{aligned}\alpha &= 0.1820 \cdot \nu \cdot N'' && \text{dB/km} \\ N'' &= \frac{3}{2} \cdot \frac{w}{m} \cdot \text{Im}[(\epsilon_r - 1)/(\epsilon_r + 2)] \\ N'' &= \frac{3}{2} \cdot \frac{w}{m} \cdot \left[ \frac{3 \cdot \epsilon_r''}{(\epsilon_r' + 2)^2 + (\epsilon_r'')^2} \right]\end{aligned}\tag{3.1}$$

---

<sup>1</sup>See *Brussaard and Watson* [1995], page 81, for details.

where  $w$  is the liquid water ( $0.0 < LWC < 5.0 \text{ g/m}^3$ ) or ice mass ( $0.0 IWC < 1.0 \text{ g/m}^3$ ) content and  $m$  is the water or ice bulk density ( $\rho_{l,i}=1.0 \text{ g/cm}^3$  and  $0.916 \text{ g/cm}^3$ , respectively). The difference between liquid water and ice absorption is put in the expressions for the complex permittivities (i. e. the relative dielectric constant),  $\epsilon_r = \epsilon'_r + i \cdot \epsilon''_r$ , which depend on frequency and temperature.

• Complex permittivity for suspended liquid water droplets:

$$\begin{aligned}\epsilon'_r &= \epsilon_o - \nu^2 \cdot \left[ \frac{\epsilon_o - \epsilon_1}{\nu^2 + \gamma_1^2} + \frac{\epsilon_1 - \epsilon_2}{\nu^2 + \gamma_2^2} \right] \\ \epsilon''_r &= \nu \cdot \left[ \gamma_1 \cdot \frac{\epsilon_o - \epsilon_1}{\nu^2 + \gamma_1^2} + \gamma_2 \cdot \frac{\epsilon_1 - \epsilon_2}{\nu^2 + \gamma_2^2} \right] \\ \epsilon_o &= 77.66 + 103.3 \cdot (\Theta - 1)\end{aligned}\tag{3.2}$$

$$\begin{aligned}\epsilon_1 &= 0.0671 \cdot \epsilon_o \\ \epsilon_2 &= 3.52 \\ \gamma_1 &= 20.20 - 146 \cdot (\Theta - 1) + 316 \cdot (\Theta - 1)^2 \text{ GHz} \\ \gamma_2 &= 39.8 \cdot \gamma_1 \text{ GHz} \\ \Theta &= 300 \text{ K} / T\end{aligned}\tag{3.3}$$

• Complex permittivity for ice crystals:

$$\begin{aligned}\epsilon'_r &= 3.15 \\ \epsilon''_r &= \frac{a}{\nu} + b \cdot \nu \\ a &= (\Theta - 0.1871) \cdot \exp(17.0 - 22.1 \cdot \Theta)\end{aligned}\tag{3.4}$$

$$\begin{aligned}b &= \left[ \left( \frac{0.233}{1 - 0.993/\Theta} \right)^2 + \frac{6.33}{\Theta} - 1.31 \right] \cdot 10^{-5} \\ \Theta &= 300 \text{ K} / T\end{aligned}\tag{3.5}$$

The absorption is directly proportional to the liquid or ice water content  $LWC/IWC$  and inversely proportional to the density of a single liquid ice particle  $\rho_{l,i}$ . Like the mean particle radius, the liquid and ice water content have a high variability. Table 3.1 reflects this variability by summarizing different literature values for several cloud types. Additional uncertainty of this absorption term comes from two sides: (1) the difference to the Rayleigh approximation of the order of 1-6% as reported in *Li et al. [1997]* and (2) from the fit of the complex permittivity. Since  $\epsilon(\nu, T)$  was fitted to measurements which were mostly performed above  $0^\circ\text{C}$ , the extrapolated values for  $T < 0^\circ\text{C}$  for super-cooled clouds are not well established. For example in *Liebe et al. [1991]* itself two different parameterizations for the so called primary relaxation frequency ( $\gamma_1$  in Equation 3.2) are given, one polynomial in  $\Theta$  as presented in Equation 3.2) and an exponential function derived from theory. Although the polynomial describes the selected data better than the exponential function, this might not be true for temperatures well below  $0^\circ\text{C}$ . The difference in  $\gamma_1$  according to these two approaches can be more than 2 GHz for very low temperatures [*Lipton et al., 1999*]. The resulting consequences from this discrepancy for the absorption calculation at three microwave frequencies are shown in Figure 3.1. A more detailed discussion about this source of uncertainty is given in Section 3.2.

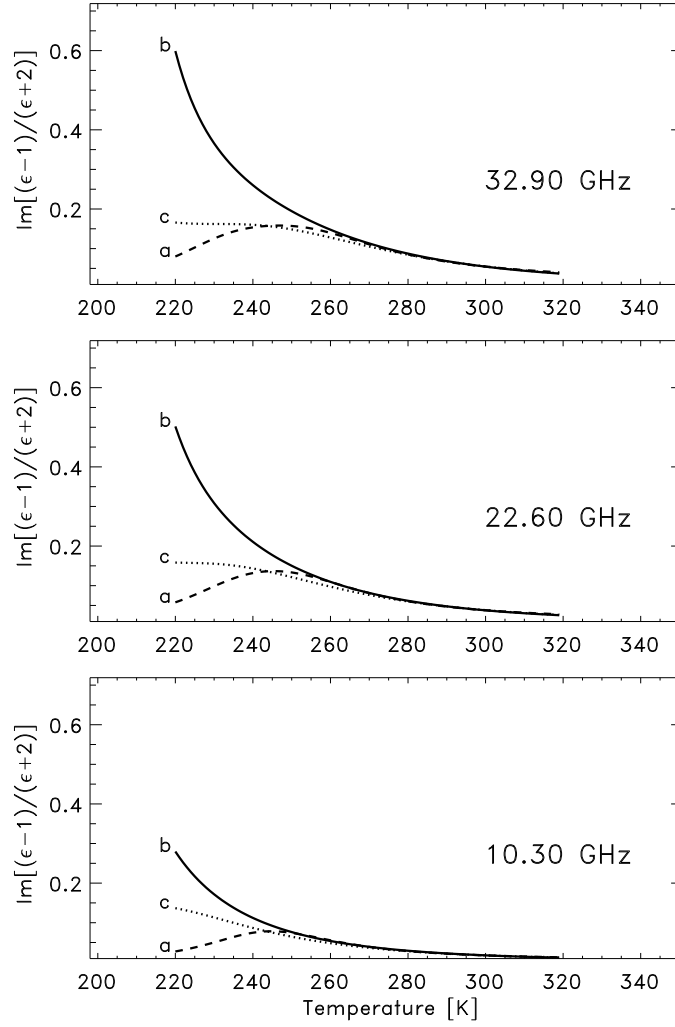


Figure 3.1: Comparison of the imaginary part of the expression  $(\epsilon_r - 1)/(\epsilon_r + 2)$  for liquid water at the three frequencies of 32.9, 22.6, and 10.3 GHz. Plotted are the two common models of *Liebe et al.* [1991] (a) and *Ray* [1972] (b). The Ray parameterization is calculated with the F77 program of W. Wiscombe, NASA, GSFC, take from [ftp://climate.gsfc.nasa.gov/pub/wiscombe/Refrac\\_Index/WATER/](ftp://climate.gsfc.nasa.gov/pub/wiscombe/Refrac_Index/WATER/). Additionally the *Liebe et al.* [1991] parameterization (c) with the alternative expression for the first relaxation frequency,  $\gamma_1 = 20.1 \cdot \exp[7.88 \cdot (1 - \Theta)]$ , is plotted.

liquid water content ( $LWC$ )			
cloud	class	(g/m <sup>3</sup> )	reference
stratus	St	0.15	<i>Salby [1996]</i>
		0.09-0.9	<i>Seinfeld and Pandis [1998]</i>
		0.28-0.3	<i>Hess et al. [1998]</i>
		0.29	<i>Kneizys et al. [1996]</i>
nimbostratus	Ns	0.4	<i>Salby [1996]</i>
		0.65	<i>Kneizys et al. [1996]</i>
		0.05-0.3	<i>Berton [2000]</i>
altostratus	As	<0.01-0.2	<i>Seinfeld and Pandis [1998]</i>
		0.41	<i>Kneizys et al. [1996]</i>
		0.1-1	<i>Berton [2000]</i>
stratocumulus	Sc	0.3	<i>Salby [1996]</i>
		<0.1-0.7	<i>Seinfeld and Pandis [1998]</i>
		0.15	<i>Kneizys et al. [1996]</i>
		<0.5	<i>Pawlowska et al. [2000]</i>
cumulus	Cu	0.05-1	<i>Berton [2000]</i>
		0.5	<i>Salby [1996]</i>
		0.26-0.44	<i>Hess et al. [1998]</i>
		1.00	<i>Kneizys et al. [1996]</i>
cumulonimbus	Cb	2.5	<i>Salby [1996]</i>
		0.1-2	<i>Berton [2000]</i>
cumulus congestus	Cg	0.1-3.2	<i>Berton [2000]</i>
FIRE-ACE	-	<0.7	<i>Shupe et al. [2000]</i>

ice water content ( $IWC$ )			
cloud	class	(g/m <sup>3</sup> )	reference
cirrus	Ci	0.025	<i>Salby [1996]</i>
		0.00193-0.0260	<i>Hess et al. [1998]</i>
		$3.128 \cdot 10^{-4}$ -0.06405	<i>Kneizys et al. [1996]</i>
		0.15-0.3	<i>Larsen et al. [1998]</i>
		<0.1	<i>Berton [2000]</i>
cirrostratus	Cs	0.2	<i>Salby [1996]</i>
		0.05-2	<i>Berton [2000]</i>

Table 3.1: Stated values for the liquid and ice water content of several cloud classes from different sources.

### 3.2 Variability and uncertainty in cloud absorption

In the case of clouds three sources of uncertainties can be considered at first sight: (1) validity of the Rayleigh approximation (2) the parameterization of the relative dielectric constants ( $\epsilon_r$ ) of water and ice in the microwave region, and (3) the statistical and climatological variability of the cloud liquid water and ice content.

As it was stated above (Section 3.1) the Rayleigh approximation is valid for particle sizes  $< 500 \mu\text{m}$ . Figure 3.2 shows a particle size distribution for water clouds and ice clouds (cirrus) from the OPAC model [*Hess et al., 1998*]. According to this model only

cirrus clouds will have particles of size larger than  $500\ \mu\text{m}$ . Nevertheless one has to keep in mind that the variability of the particle size can be very high so that at certain conditions some cloud types (most probable is the cumulonimbus) a non-negligible large particle concentration can occur.

The uncertainty in the relative dielectric constant of water (see e. g. *Lipton et al.* [1999]) is largest below the freezing temperature, since only a few measurements at  $-4^\circ\text{C}$  contributed to the parameterization of  $\epsilon_r$  in *Liebe et al.* [1991], which in turn is used in the cloud liquid water absorption model of MPM93. Figure 3.1 shows a comparison of *Liebe et al.* [1991] and *Ray* [1972]<sup>2</sup> parameterizations for the temperature dependence of the expression  $\text{Im}[(\epsilon_r - 1)/(\epsilon_r + 2)]$ , which is in the Rayleigh approximation one of the relevant terms in the absorption calculation (see Equation 3.1). Additionally the same calculations with the alternative expression of the first relaxation frequency,  $\gamma_1$ , as stated in Equation 2b of *Liebe et al.* [1991] is shown. The three versions give comparable results for temperatures warmer than 260 K but show significant differences for temperatures below 240 K. However, an uncertainty estimation of  $\text{Im}[(\epsilon_r - 1)/(\epsilon_r + 2)]$  is due to the lack of measurements not easy, but it will certainly increase with decreasing temperature.

The largest variability of the involved quantities of cloud absorption is the liquid and ice water content ( $LWC$  and  $IWC$ ) of the clouds (see Table 3.1). Even within a single cloud the  $LWC$  ( $IWC$ ) changes with altitude and the distance from the cloud center as can be seen for example in Figure 10 of *Ludlam and Mason* [1957] and in the model study of *Costa et al.* [2000].

---

<sup>2</sup>The calculations for this parameterization are performed with the computer code of W. Wiscombe, NASA, GSFC ([ftp://climate.gsfc.nasa.gov/pub/wiscombe/Refrac\\_Index/WATER/](ftp://climate.gsfc.nasa.gov/pub/wiscombe/Refrac_Index/WATER/)) For the microwave frequency range this program uses the *Ray* [1972] temperature parameterization.

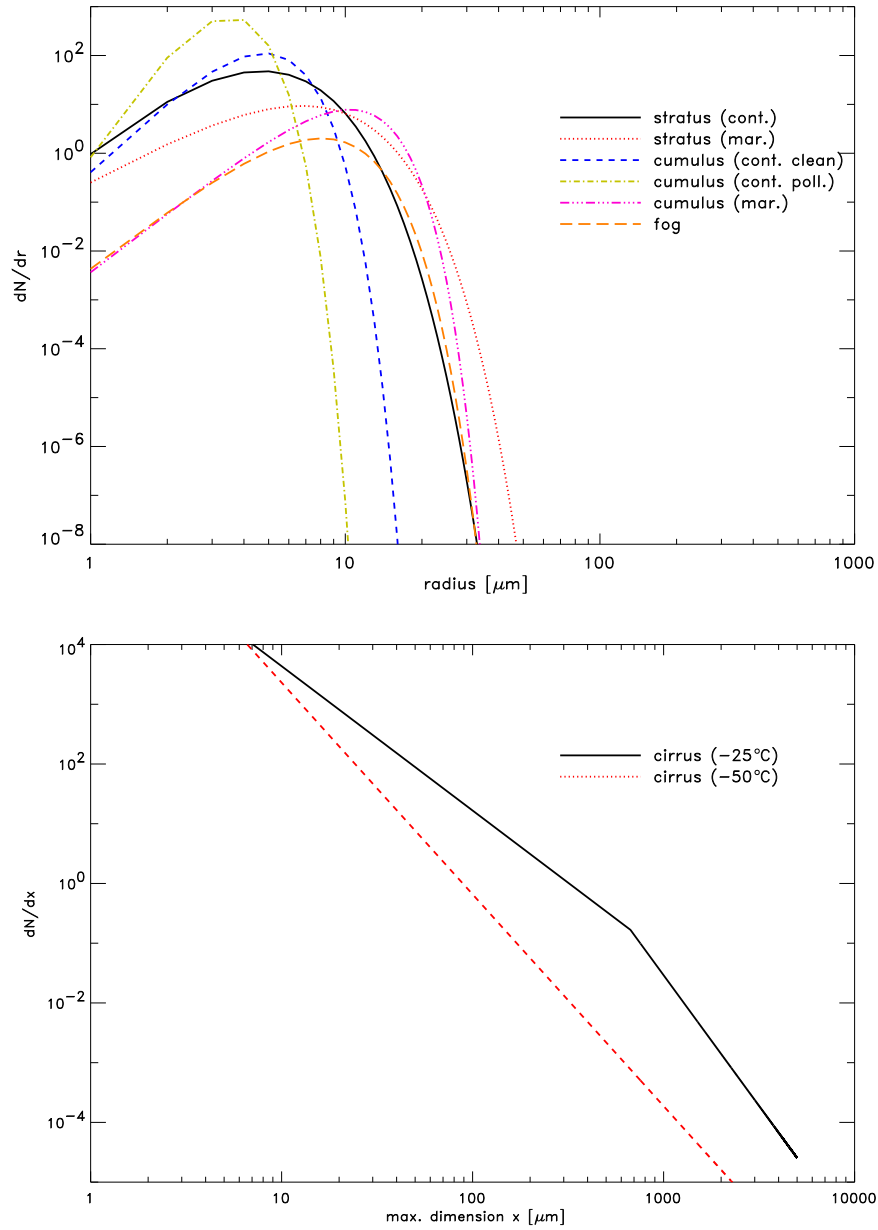


Figure 3.2: Cloud particle size distributions according to Equations 3a and 3c and the microphysical properties are from the Tables 1a and 1b of the OPAC model [Hess *et al.*, 1998]. For the liquid water clouds (upper plot) a modified gamma distribution is assumed whereas for the ice clouds (lower plot) exponential functions are taken.

## Chapter 4

# Refractive index

Refractive index describes several effects of matter on propagation of electromagnetic waves. Refractive index is basically a complex quantity. However, in this chapter it is restricted to its real part, neglecting the imaginary part, which describes absorption. Effects the real part of the refractive index describes particularly include changes of the propagation speed of electromagnetic waves, which leads to a delay of the signal, as well as a change of the propagation direction, a bending of the propagation path. The latter is commonly called refraction.

Several components in the atmosphere contribute to refraction, hence to the refractive index: the gas mixture (“air”), solid and liquid constituents (clouds, precipitation, aerosols), and electrons. Refractivity ( $N$ ) describes the deviation of the refractive index of a medium  $n$  from the vacuum refractive index ( $n_{\text{vacuum}} = 1$ ):  $N = n - 1$ . Contributions of the different components to refractivity are additive. One distinguishes between monochromatic and group refractive index, which differ in case of dispersion leading to diverging propagation paths at different frequencies. **FIXME: That needs to be more specific.**

### 4.1 Gases

According to *Newell and Baird* [1965], the refractivity  $N$ , i.e., the deviation of the refractive index  $n$  from 1.0 ( $N = n - 1$ ), of a gas can be assumed to be proportional to its density. *Newell and Baird* [1965] give no validity range for this assumption, but at least *Stratton* [1968] assumes that it is valid even for the relatively high densities in the Venusian atmosphere. We have not investigated whether this assumption may break down at some point in the Jupiter atmosphere.

If we accept the assumption of refractivity scaling with gas density, then the problem of parameterizing the refractivity can be separated into two sub-problems: (a) determining the refractivity index for reference conditions (reference pressure  $p$  and temperature  $T$ ), and (b) deciding which gas law to use to scale it to other conditions. The total refractivity is then simply the sum of all partial refractivities, in other words

$$N = N_{\text{ref},1} \frac{n_1}{n_{\text{ref},1}} + N_{\text{ref},2} \frac{n_2}{n_{\text{ref},2}} + \dots \quad (4.1)$$

---

#### History

130802 Started based on AUG chapter and ESA-planetary TN1 (Jana Mendrok).

where  $N$  is the total refractivity,  $N_{\text{ref},i}$  is the partial refractivity for gas  $i$  at reference conditions,  $n_i$  is the partial density, and  $n_{\text{ref},i}$  is the reference density.

Different solutions have been proposed, where approaches specific for Earth atmosphere commonly are empirical parameterisations. Below we describe the background and formulas applied for the different methods implemented in ARTS.

#### 4.1.1 Microwave general method (`refr_index_airMicrowavesGeneral`)

Apart from presenting a basic approach, *Newell and Baird* [1965] also provide a thorough study of both refractivity of different gases for reference conditions and which gas law to use to scale those to other conditions. They present laboratory refractivity measurements for dry CO<sub>2</sub>-free air, argon, carbon dioxide, helium, hydrogen, nitrogen, and oxygen covering the most relevant gases (probably apart from water vapor) in planetary atmospheres. The actual refractivity values of *Newell and Baird* [1965] are stated in the paper abstract and are not repeated here. The conditions for the reported refractivity values are  $T = 0^\circ\text{C}$  and  $p = 760$  Torr. The measurements are for a frequency of 47.7 GHz. Out of the reference refractivities provided by *Newell and Baird* [1965], we apply those of N<sub>2</sub>, O<sub>2</sub>, CO<sub>2</sub>, H<sub>2</sub>, and He in this algorithm.

*Newell and Baird* [1965] also address the question which gas law to use to scale the measurements to other  $p/T$  conditions, choosing different approaches depending on the specific gas in question. While the more complicated gas laws they suggest can be expected to be more accurate in the relatively narrow range of  $p/T$  conditions considered by *Newell and Baird* [1965], it is not easy to assess how well they will hold outside the range for which they were originally derived. We therefore simply use the ideal gas law, as given in Equation 7 of *Newell and Baird* [1965] for all gases. This results in the simple parameterization

$$N = \frac{273.15 \text{ K}}{760 \text{ Torr}} \left[ N_{\text{ref},1} \frac{p_1}{T} + N_{\text{ref},2} \frac{p_2}{T} + \dots \right] \quad (4.2)$$

where  $N(T, p)$  is the total refractivity, the first factor reflects the reference conditions for the *Newell and Baird* [1965] data,  $N_{\text{ref},i}$  are the partial refractivities as reported in the abstract of their article,  $p_i$  are the partial pressures, and  $T$  is temperature.

In addition to reference refractivities of the five species given by *Newell and Baird* [1965], we have derived an equivalent value for H<sub>2</sub>O from the H<sub>2</sub>O contribution of the parametrization for microwave refractivity in Earth (`refr_index_airMicrowavesEarth`) with parameters of the expression taken from *Bevis et al.* [1994] and a reference temperature of  $T_0 = 273.15$  K. Using the ideal gas law reduces temperature dependence to inverse proportionality, whereas the microwave Earth parameterization also carries an inverse quadratic dependence. This causes notable deviations from H<sub>2</sub>O refractivity as given by the microwave Earth parameterization when temperature is not close to the reference temperature applied. However, the deviations are significantly smaller than when refraction by H<sub>2</sub>O is not explicitly accounted for.

Hence, the above formulas can currently be used with up to six contributing gas species (N<sub>2</sub>, O<sub>2</sub>, CO<sub>2</sub>, H<sub>2</sub>, and He as well as H<sub>2</sub>O). To account for contributions from further gases (i.e., when volume mixing ratios of these six do not add up to 1), the calculated refractivity from those five gases is normalised to a volume mixing ratio of 1. By adding reference refractive index data from further species – as done for water vapor –, the method can easily be extended and made more complete.



## 4.2 Free electrons

Free electrons, as exist in the ionosphere, will affect propagating radio waves in several ways. Free electrons will have an impact of the propagation speed of radio waves, hence a signal can be delayed and refracted.

An electromagnetic wave passing through a plasma (such as the ionosphere) will drive electrons to oscillate and re-radiating the wave frequency. This is the basic reason of the contribution of electrons to the refractive index. An important variable is the plasma frequency,  $\nu_p$ :

$$\omega_p = \sqrt{\frac{Ne^2}{\epsilon_0 m}}, \quad (4.3)$$

where  $\omega_p = 2\pi\nu_p$ ,  $N$  is the electron density,  $e$  is the charge of an electron,  $\epsilon_0$  is the permittivity of free space, and  $m$  is the mass of an electron. For example, for the Earth's ionosphere  $\nu_p \approx 9$  MHz. Waves having a frequency below  $\nu_p$  are reflected by a plasma.

Neglecting influences of any magnetic field, the refractive index of a plasma is [e.g. *Rybicki and Lightman, 1979*]

$$n = \sqrt{1 - \frac{\omega_p^2}{\omega^2}} = \sqrt{1 - \frac{Ne^2}{\epsilon_0 m \omega^2}}, \quad (4.4)$$

where  $\omega$  is the angular frequency ( $\omega = 2\pi\nu$ ). This refractive index is less than unity (phase velocity is greater than the speed of light), but is approaching unity with increasing frequency. The group velocity is [*Rybicki and Lightman, 1979*]

$$v_g = c \sqrt{1 - \frac{Ne^2}{\epsilon_0 m \omega^2}} \quad (4.5)$$

which is clearly less than the speed of light. The energy (or information) of a signal propagating through the ionosphere travels with the group velocity, and the group speed refractive index ( $n_g = \frac{c}{v_g}$ ) is

$$n_g = \left(1 - \frac{Ne^2}{\epsilon_0 m \omega^2}\right)^{-1/2}. \quad (4.6)$$

Equations 4.4 and 4.6 are implemented in `refr_index_airFreeElectrons`. The method demands that the radiative transfer frequency is at least twice the plasma frequency.



## Chapter 5

# Polarisation and Stokes parameters

The present version of ARTS implements the radiative transfer equation in tensor form, i.e., for the 4 components of the Stokes vector, not just for its first component, the intensity or radiance. This means that the model can include polarisation dependence in absorption or scattering processes. It is therefore necessary to give some details on the polarisation of radiation, the definition of the Stokes parameters, and the definition of antenna polarisation.

This section could need to be revised. At least there is an inconsistency regarding the V-element between this section and what is written elsewhere. In this section V is said to be right-hand minus left-hand circular polarisation, while elsewhere it is the opposite.

### 5.1 Polarisation directions

Electromagnetic waves in homogeneous, isotropic media are transverse waves, i.e., their oscillating electric and magnetic fields are in a plane perpendicular to the propagation direction. The choice of two basis vectors – we shall call them polarisation directions here – that span that transverse plane is arbitrary; often they are called “horizontal” and “vertical” and correspond to some horizontal and vertical direction of the particular setting. Nevertheless, what is meant by horizontal/vertical, or parallel/perpendicular, is purely a matter of definition.

Here, we stick to the system called laboratory frame or fixed frame, used by *Mishchenko et al.* [2002]: We use a coordinate system where the  $z$ -axis points toward local zenith. We denote the propagation direction of radiation by a unit vector  $\mathbf{n} = \mathbf{k}/k$ , where  $k$  is the wave number.  $\mathbf{n}$  is given by two angles, the zenith angle  $\theta$ , i.e., the angle between  $\mathbf{n}$  and the  $z$ -axis, and the azimuth angle  $\phi$ , i.e., the angle between the projection of  $\mathbf{n}$  into the  $xy$ -plane and the  $x$ -axis:

$$\mathbf{n} = \begin{pmatrix} \cos \phi \sin \theta \\ \sin \phi \sin \theta \\ \cos \theta \end{pmatrix} \quad (5.1)$$

Then we define the polarisation directions by the partial derivatives of  $\mathbf{n}$  with respect to  $\theta$

---

#### History

040524 Section on scattering matrices added by Patrick Eriksson.

040426 Created and written by Christian Melsheimer.

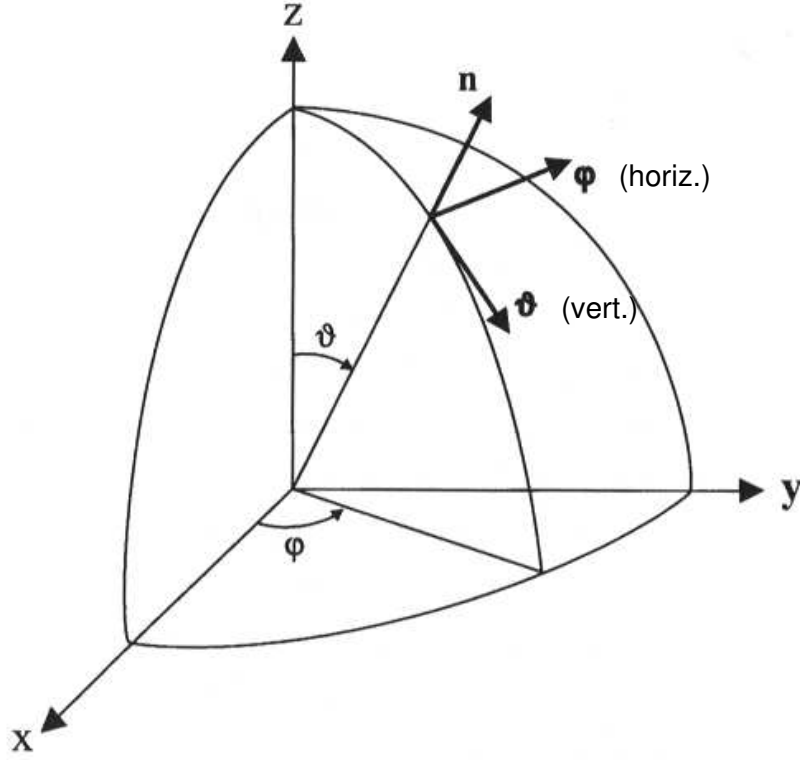


**Figure 1** Laboratory coordinate system.

Figure 5.1: The definition of the polarisation directions, adapted from *Mishchenko et al. [2002]*

and  $\phi$ . We shall call them  $\theta$ -direction (also: vertical) and  $\phi$ -direction (also: horizontal), respectively, see Figure 5.1. Their unit basis vectors are

$$\mathbf{e}_\theta = \mathbf{e}_v = \frac{\partial \mathbf{n}}{\partial \theta} / \left\| \frac{\partial \mathbf{n}}{\partial \theta} \right\| = \begin{pmatrix} \cos \phi \cos \theta \\ \sin \phi \cos \theta \\ -\sin \theta \end{pmatrix} \quad (5.2)$$

$$\mathbf{e}_\phi = \mathbf{e}_h = \frac{\partial \mathbf{n}}{\partial \phi} / \left\| \frac{\partial \mathbf{n}}{\partial \phi} \right\| = \begin{pmatrix} -\sin \phi \\ \cos \phi \\ 0 \end{pmatrix} \quad (5.3)$$

The vectors  $\mathbf{n}$ ,  $\mathbf{e}_\theta$  ( $=\mathbf{e}_v$ ),  $\mathbf{e}_\phi$  ( $=\mathbf{e}_h$ ) are mutually orthogonal and define (in the mentioned order) a right-handed system, i.e.,  $(\mathbf{n} \times \mathbf{e}_\theta) \cdot \mathbf{e}_\phi = 1$  and the same for all cyclic permutations.

## 5.2 Plane monochromatic waves

Plane monochromatic electromagnetic waves are commonly written in the form

$$\mathbf{E}(\mathbf{x}, t) = \begin{bmatrix} E_v \\ E_h \end{bmatrix} e^{i(\mathbf{k}\mathbf{x} - \omega t)} = (E_v \mathbf{e}_v + E_h \mathbf{e}_h) e^{i(\mathbf{k}\mathbf{x} - \omega t)} \quad (5.4)$$

where  $\mathbf{E}$  is the electric field vector, the subscripts  $v$  and  $h$  denote the components with vertical and horizontal polarisation, respectively.  $E_v$  and  $E_h$ , the amplitudes, are complex numbers,  $\mathbf{k}$  and  $\omega$  are the wavenumber vector and the angular frequency, respectively, of the plane wave, and the unit vectors  $\mathbf{e}_v = (1, 0)^T$ ,  $\mathbf{e}_h = (0, 1)^T$ . It is always implicitly understood that the actual, physical, electric field is the real part of the above expression. Rewriting the complex amplitudes  $E_v$  and  $E_h$  using real, non-negative amplitudes  $a_v$  and  $a_h$ , and phases  $\delta_v$  and  $\delta_h$ ,

$$E_v = a_v e^{i\delta_v}, E_h = a_h e^{i\delta_h} \quad (5.5)$$

the actual electric field vector  $\tilde{\mathbf{E}}$  is

$$\tilde{\mathbf{E}}(\mathbf{x}, t) = \text{Re}[\mathbf{E}(\mathbf{x}, t)] = \begin{bmatrix} a_v \cdot \cos(\mathbf{k}\mathbf{x} - \omega t + \delta_v) \\ a_h \cdot \cos(\mathbf{k}\mathbf{x} - \omega t + \delta_h) \end{bmatrix} \quad (5.6)$$

In general, instruments do not measure the electric or magnetic field vectors of an electromagnetic wave, but rather the time-averaged intensity, i.e., the energy flux,  $F$ . This is the time-averaged Poynting vector (which, in turn, is proportional to the square of the electric field), thus:

$$\begin{aligned} F &= \sqrt{\frac{\epsilon}{\mu}} \overline{(\tilde{\mathbf{E}}(\mathbf{x}, t))^2} \\ &= \sqrt{\frac{\epsilon}{\mu}} \left( \overline{a_v^2 \cos^2(\mathbf{k}\mathbf{x} - \omega t + \delta_v)} + \overline{a_h^2 \cos^2(\mathbf{k}\mathbf{x} - \omega t + \delta_h)} \right) \end{aligned} \quad (5.7)$$

The overline denotes the time average which for cosine squares is 1/2, thus:

$$F = \frac{1}{2} \sqrt{\frac{\epsilon}{\mu}} (a_v^2 + a_h^2) \quad (5.8)$$

Taking into account that for plane, monochromatic waves the time average always results in a factor  $\frac{1}{2}$ , we can also directly write the intensity using the electric field vector in complex notation (Equation 5.4).

$$\begin{aligned} F &= \frac{1}{2} \sqrt{\frac{\epsilon}{\mu}} \mathbf{E}(\mathbf{x}, t) \cdot \mathbf{E}^*(\mathbf{x}, t) \\ &= \frac{1}{2} \sqrt{\frac{\epsilon}{\mu}} (E_v E_v^* + E_h E_h^*) \end{aligned} \quad (5.9)$$

where the asterisk denotes complex conjugation.

In addition to the flux, three more intensity quantities are defined as in the following equations. They are called *Stokes parameters*:

$$I = \frac{1}{2} \sqrt{\frac{\epsilon}{\mu}} (E_v E_v^* + E_h E_h^*) \quad (5.10)$$

$$Q = \frac{1}{2} \sqrt{\frac{\epsilon}{\mu}} (E_v E_v^* - E_h E_h^*) \quad (5.11)$$

$$U = -\frac{1}{2} \sqrt{\frac{\epsilon}{\mu}} (E_v E_h^* + E_h E_v^*) \quad (5.12)$$

$$V = i \frac{1}{2} \sqrt{\frac{\epsilon}{\mu}} (E_h E_v^* - E_v E_h^*) \quad (5.13)$$

Written as a row or column vector,  $(I, Q, U, V)$  is called *Stokes vector*. Note that sometimes,  $S_0, S_1, S_2, S_3$  is used instead of  $I, Q, U, V$ . Using the amplitude/phase notation

from Equation 5.5, we can rewrite the Stokes parameters as

$$I = \frac{1}{2} \sqrt{\frac{\epsilon}{\mu}} (a_v^2 + a_h^2) \quad (5.14)$$

$$Q = \frac{1}{2} \sqrt{\frac{\epsilon}{\mu}} (a_v^2 - a_h^2) \quad (5.15)$$

$$U = -\sqrt{\frac{\epsilon}{\mu}} a_v a_h \cos(\delta_v - \delta_h) \quad (5.16)$$

$$V = -\sqrt{\frac{\epsilon}{\mu}} a_v a_h \sin(\delta_v - \delta_h) \quad (5.17)$$

The Stokes parameters fully characterise the electromagnetic wave and therefore contain the same information as the electric field vector (except for one absolute phase). Since instruments generally measure intensities (fluxes), describing electromagnetic radiation by the Stokes parameters is more practical than describing it by the electric (or magnetic) field vector. Furthermore, the Stokes parameters are always real numbers. Note that the Stokes parameters are sometimes defined with different signs of  $Q$ ,  $U$ , or  $V$  (the definitions and signs used here are based on *Mishchenko et al.* [2000]). Moreover, their normalisation may vary. In particular, the Stokes parameters can be normalised to represent radiance or irradiance (instead of intensity), which is usually done in radiative transfer contexts.

In order to understand what the Stokes parameters mean, we have to go back to the electric field vector and see what polarisation state it describes. To do so, we look at the curve that the tip of the physical electric field vector  $\tilde{\mathbf{E}}$  describes with time at a fixed position  $\mathbf{x}_0$ :

$$\tilde{E}_v(t) = a_v \cos(\Delta_v - \omega t) \quad (5.18)$$

$$\tilde{E}_h(t) = a_h \cos(\Delta_h - \omega t) \quad (5.19)$$

where  $\Delta_{v,h} = \mathbf{kx}_0 + \delta_{v,h}$ . To see that this is an ellipse, we first split the cosines using the addition theorem:

$$\tilde{E}_v(t) = a_v \cos \Delta_v \cos(\omega t) + a_v \sin \Delta_v \sin(\omega t) \quad (5.20)$$

$$\tilde{E}_h(t) = a_h \cos \Delta_h \cos(\omega t) + a_h \sin \Delta_h \sin(\omega t) \quad (5.21)$$

In order to have the tip of  $\tilde{\mathbf{E}}$  describe an ellipse with semi-major axis  $a_0 \cos \beta$  and semi-minor axis  $a_0 \sin \beta$ , where  $a_0^2 = a_v^2 + a_h^2$ , it should have the following form

$$\tilde{E}_v(t) = a_0 \sin \beta \cos(\omega t) \quad (5.22)$$

$$\tilde{E}_h(t) = a_0 \cos \beta \sin(\omega t) \quad (5.23)$$

Here  $\beta$  must be between  $-45^\circ$  and  $45^\circ$ : the tip of the vector  $\tilde{\mathbf{E}}$  describes a circle for  $\beta = \pm 45^\circ$  (circular polarisation), oscillates along the  $h$ -axis for  $\beta = 0$  (linear polarisation) and else describes an ellipse (cf. Figure 5.2). The sense of rotation is counterclockwise for positive  $\beta$  (corresponding to left-circular or left-elliptic polarisation) and clockwise for negative  $\beta$  (corresponding to right-circular or right-elliptic polarisation). Since  $|\tan \beta|$  is the ratio of the semi-minor and semi-major axes of the ellipse (the ellipticity),  $\beta$  is called the ellipticity angle. Note that the semi-major axis is oriented along the positive  $h$ -axis. To have the major axis of the ellipse enclose an arbitrary angle  $\zeta$  ( $0 \leq \zeta < 180^\circ$ ) with the  $h$ -axis, we apply a rotation matrix and get the equation for an ellipse with arbitrary shape (ellipticity) and orientation (cf. Figure 5.3):

$$\tilde{E}_v(t) = a_0 (\sin \beta \cos(\omega t) \cos \zeta + \cos \beta \sin(\omega t) \sin \zeta) \quad (5.24)$$

$$\tilde{E}_h(t) = a_0 (-\sin \beta \cos(\omega t) \sin \zeta + \cos \beta \sin(\omega t) \cos \zeta) \quad (5.25)$$

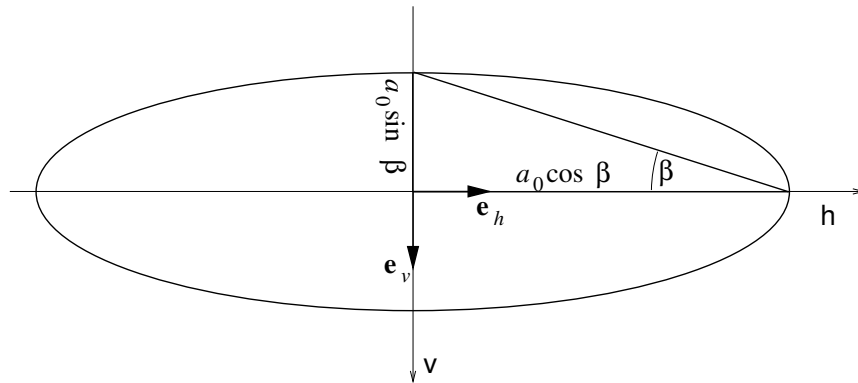


Figure 5.2: The ellipse that the electric field vector describes with time, with the major axis oriented along the  $h$ -axis.

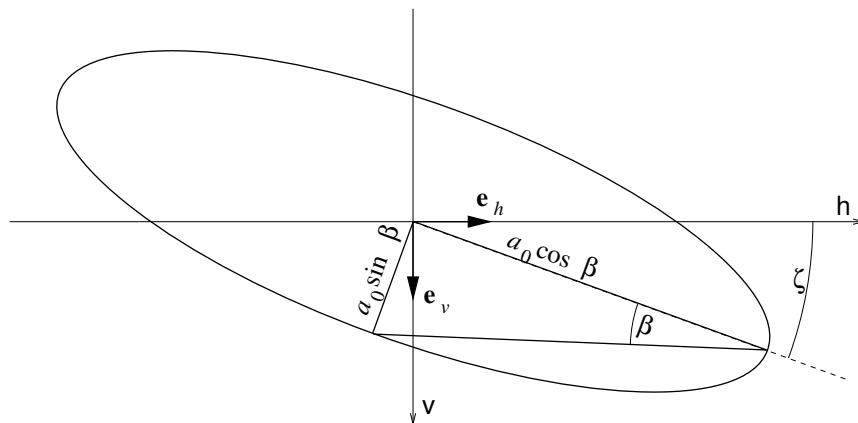


Figure 5.3: The ellipse that the electric field vector describes with time, with the major axis oriented arbitrarily.

With these definitions, horizontal polarisation corresponds to  $\beta = 0^\circ$  and  $\zeta = 0^\circ$ ; vertical polarisation to  $\beta = 0^\circ$  and  $\zeta = 90^\circ$ ; left-circular to  $\beta = 45^\circ$  and any value of  $\zeta$ ; right-circular to  $\beta = -45^\circ$  and any value of  $\zeta$ .

Now we want to establish a direct connection between the parameters  $\beta$  and  $\zeta$  describing the shape (ellipticity) and orientation of the polarisation ellipse on the one hand, and the amplitudes  $a_v$  and  $a_h$  and phases  $\delta_v$  and  $\delta_h$  of the components of the electric field vector on the other hand. Comparing the  $\sin(\omega t)$  and  $\cos(\omega t)$  terms in Equations 5.24 to 5.25 with the corresponding terms in Equations 5.20 to 5.21, we get:

$$a_v \cos \Delta_v = a_0 \sin \beta \cos \zeta \quad (5.26)$$

$$a_v \sin \Delta_v = a_0 \cos \beta \sin \zeta \quad (5.27)$$

and

$$a_h \cos \Delta_h = -a_0 \sin \beta \sin \zeta \quad (5.28)$$

$$a_h \sin \Delta_h = a_0 \cos \beta \cos \zeta \quad (5.29)$$

Multiplying Equation 5.26 with Equation 5.28, and Equation 5.27 with Equation 5.29 and adding up the results, we get

$$a_v a_h (\cos \Delta_v \cos \Delta_h + \sin \Delta_v \sin \Delta_h) = a_0^2 \sin \zeta \cos \zeta (\cos^2 \beta - \sin^2 \beta) \quad (5.30)$$

Using the addition theorems for sinusoidals and taking into account that  $\Delta_v - \Delta_h = \delta_v - \delta_h$ :

$$\frac{a_v a_h}{a_0^2} \cos(\delta_v - \delta_h) = \frac{1}{2} \sin(2\zeta) \cos(2\beta) \quad (5.31)$$

In a similar way, subtracting the product of Equation 5.27 with Equation 5.28 from the product of Equation 5.26 with Equation 5.29 and adding up the results, we get

$$-\frac{a_v a_h}{a_0^2} \sin(\delta_v - \delta_h) = \frac{1}{2} \sin(2\beta) \quad (5.32)$$

The above two equations tell us how to translate the amplitudes ( $a_v, a_h$ ) and phases ( $\delta_v, \delta_h$ ) of the vertical and horizontal component of the electric field into the orientation and shape of the ellipse that the tip of the electric field vector describes with time. We can obtain one further relation by subtracting the sum of the squares of Equation 5.28 and Equation 5.29 from the sum of the squares of Equation 5.26 and Equation 5.27:

$$a_v^2 - a_h^2 = -a_0^2 \cos(2\zeta) \cos(2\beta) \quad (5.33)$$

Finally, we use the above 3 equations (5.31, 5.32 and 5.33) to rewrite the Stokes parameters (Equations 5.14 to 5.17) as

$$I = \frac{1}{2} \sqrt{\frac{\epsilon}{\mu}} a_0^2 \quad (5.34)$$

$$Q = -\frac{1}{2} \sqrt{\frac{\epsilon}{\mu}} a_0^2 \cos(2\zeta) \cos(2\beta) \quad (5.35)$$

$$U = -\frac{1}{2} \sqrt{\frac{\epsilon}{\mu}} a_0^2 \sin(2\zeta) \cos(2\beta) \quad (5.36)$$

$$V = -\frac{1}{2} \sqrt{\frac{\epsilon}{\mu}} a_0^2 \sin(2\beta) \quad (5.37)$$



FIXME:  $\beta < 0$  is right-handed pol. (see above, consistent with Jackson and others); thus  $V > 0$ . This conflicts with Mishchenko's book (p.26).

Thus, we can get the orientation angle  $\zeta$  of the ellipse from

$$\tan(2\zeta) = \frac{U}{Q} \quad (5.38)$$

Since  $0 \leq 2\zeta < 360^\circ$ , there are 2 solutions for  $\zeta$  for a given pair  $U, Q$ . This ambiguity is resolved by looking at Equation 5.35, taking into account that  $|\beta| \leq 45^\circ$  and thus  $\cos(2\beta) \geq 0$ : The sign of  $\cos(2\zeta)$  must be the same as the sign of  $-Q$ .

We get the ellipticity angle  $\beta$  from

$$\tan(2\beta) = -\frac{V}{(Q^2 + U^2)^{1/2}} \quad (5.39)$$

$I$  is the total intensity of the radiation,  $Q$  is the difference in the intensity of the vertically and horizontally polarised components (cf. Section 5.3).  $I$  is always non-negative, and  $Q, U$ , and  $V$  are between  $+I$  and  $-I$ , since they can be expressed as a product of  $I$  with sines and/or cosines (Equations 5.35 to 5.37). Note also that the 4 Stokes parameters are not independent (for completely polarised radiation, see further Section 5.4), since the following equality applies:

$$I^2 = Q^2 + U^2 + V^2 \quad (5.40)$$

Some examples of Stokes parameters for specific polarisations are given at the end of the next section (page 74).

### 5.3 Measuring Stokes parameters

The three different ways given so far to write the Stokes parameters (Equations 5.10ff., Equations 5.14ff., Equations 5.34ff.) are not very helpful if we actually want to measure the Stokes parameters. So here we are going to rewrite them while keeping in mind that most instruments can just measure intensities of radiation.

We have seen above that the Stokes parameter  $Q$  is the difference in the intensity of the vertically and horizontally polarised components (Equations 5.11, or 5.15)

$$Q = I_v - I_h \quad (5.41)$$

where

$$I_v = \frac{1}{2} \sqrt{\frac{\epsilon}{\mu}} E_v E_v^* \quad (5.42)$$

$$I_h = \frac{1}{2} \sqrt{\frac{\epsilon}{\mu}} E_h E_h^* \quad (5.43)$$

Thus if we measure  $I_v$  and  $I_h$  using – for optical wavelengths – a polariser aligned with the  $v$ - and the  $h$ -axis, respectively, or using – for microwaves – two appropriately aligned dipole antennas, we can directly obtain  $I$  by taking their sum and  $Q$  by taking their difference.

$U$  and  $V$  can likewise be expressed as differences of intensities, but not with respect to the linear base  $\mathbf{e}_v$  and  $\mathbf{e}_h$ . We recall Equation 5.4, omitting the oscillatory term:

$$\mathbf{E} = (E_v \mathbf{e}_v + E_h \mathbf{e}_h) \quad (5.44)$$

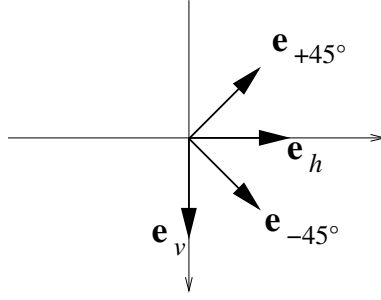


Figure 5.4: Two sets of basis vectors for the linear basis.

Now we want to write  $\mathbf{E}$  by two components along polarisation axes at  $\pm 45^\circ$  with respect to the  $h$ -axis. The basis vectors are thus (cf. Figure 5.4)

$$\mathbf{e}_{+45^\circ} = \sqrt{\frac{1}{2}} (\mathbf{e}_h - \mathbf{e}_v) \quad (5.45)$$

$$\mathbf{e}_{-45^\circ} = \sqrt{\frac{1}{2}} (\mathbf{e}_h + \mathbf{e}_v) \quad (5.46)$$

and we get the field vector in this modified linear basis:

$$\mathbf{E} = \underbrace{\sqrt{\frac{1}{2}} (E_v + E_h)}_{E_{-45^\circ}} \mathbf{e}_{-45^\circ} + \underbrace{\sqrt{\frac{1}{2}} (-E_v + E_h)}_{E_{+45^\circ}} \mathbf{e}_{+45^\circ} \quad (5.47)$$

With the definitions of intensities of the components,

$$I_{-45^\circ} = \frac{1}{2} \sqrt{\frac{\epsilon}{\mu}} E_{-45^\circ} E_{-45^\circ}^* \quad (5.48)$$

$$I_{+45^\circ} = \frac{1}{2} \sqrt{\frac{\epsilon}{\mu}} E_{+45^\circ} E_{+45^\circ}^* \quad (5.49)$$

we get for their difference:

$$\begin{aligned} I_{-45^\circ} - I_{+45^\circ} &= \frac{1}{2} \sqrt{\frac{\epsilon}{\mu}} \left[ \frac{1}{2} (E_v + E_h) (E_v^* + E_h^*) - \frac{1}{2} (-E_v + E_h) (-E_v^* + E_h^*) \right] \\ &= \frac{1}{2} \sqrt{\frac{\epsilon}{\mu}} (E_v E_h^* + E_h E_v^*) \end{aligned}$$

Therefore (cf. Equation 5.12)

$$U = I_{+45^\circ} - I_{-45^\circ} \quad (5.51)$$

Thus if we measure  $I_{+45^\circ}$  and  $I_{-45^\circ}$  using – for optical wavelengths – a polariser aligned at  $+45^\circ$  and  $-45^\circ$  with respect to the  $h$ -axis, respectively, or using – for microwaves – two appropriately aligned dipole antennas, we can directly obtain  $U$  by taking their difference.

In order to see how to measure the fourth Stokes parameter,  $V$ , we have to transform to the circular basis, i.e., express  $\mathbf{E}$  by a left-hand ( $LH$ ) and a right-hand ( $RH$ ) circularly polarised component. The relevant equations:

Basis vectors

$$\mathbf{e}_{LH} = \sqrt{\frac{1}{2}} (\mathbf{e}_v + i\mathbf{e}_h) \quad (5.52)$$

$$\mathbf{e}_{RH} = \sqrt{\frac{1}{2}} (\mathbf{e}_v - i\mathbf{e}_h) \quad (5.53)$$

Field vector in circular base

$$\mathbf{E} = \underbrace{\sqrt{\frac{1}{2}}(E_v - iE_h)}_{E_{LH}} \mathbf{e}_{LH} + \underbrace{\sqrt{\frac{1}{2}}(E_v + iE_h)}_{E_{RH}} \mathbf{e}_{RH} \quad (5.54)$$

Intensity of the components

$$I_{LH} = \frac{1}{2} \sqrt{\frac{\epsilon}{\mu}} E_{LH} E_{LH}^* \quad (5.55)$$

$$I_{RH} = \frac{1}{2} \sqrt{\frac{\epsilon}{\mu}} E_{RH} E_{RH}^* \quad (5.56)$$

Their difference

$$\begin{aligned} I_{LH} - I_{RH} &= \frac{1}{2} \sqrt{\frac{\epsilon}{\mu}} \left[ \frac{1}{2} (E_v - iE_h)(E_v^* + iE_h^*) - \frac{1}{2} (E_v + iE_h)(E_v^* - iE_h^*) \right] \\ &= i \frac{1}{2} \sqrt{\frac{\epsilon}{\mu}} (E_v E_h^* - E_h E_v^*) \end{aligned} \quad (5.57)$$

Therefore (cf. Equation 5.13):

$$V = I_{RH} - I_{LH} \quad (5.58)$$

Thus if we measure  $I_{RH}$  and  $I_{LH}$  using – for microwaves – appropriate helical beam antennas, we can directly obtain  $V$  by taking their difference. Unfortunately, for optical wavelengths, we cannot measure  $I_{RH}$  and  $I_{LH}$  directly with the help of filters like polarisers and retarders<sup>1</sup>. However, a combination of a retarder and a polarizer can be used to measure the sum of  $I$  and  $V$ :

The light first passes through a retarder that delays the phase of the horizontally polarised component by  $90^\circ$  with respect to the phase of the vertically polarised component (a quarter-wave plate). A phase delay by  $90^\circ$  can be expressed as a multiplication of the horizontal component by  $i$ , so the resulting electric field vector  $\mathbf{E}'$  is

$$\mathbf{E}' = (E_v \mathbf{e}_v + iE_h \mathbf{e}_h) \quad (5.59)$$

The light then passes through a polarizer that is aligned at  $-45^\circ$  with respect to the  $h$ -axis. This means we have to project  $\mathbf{E}'$  onto  $\mathbf{e}_{-45^\circ}$ , resulting in

$$\mathbf{E}'' = (\mathbf{E}' \cdot \mathbf{e}_{-45^\circ}) \mathbf{e}_{-45^\circ} = \sqrt{\frac{1}{2}} (E_v + iE_h) \mathbf{e}_{-45^\circ} \quad (5.60)$$

Measuring the intensity now, we get

$$\begin{aligned} I'' &= |\mathbf{E}''|^2 \\ &= \frac{1}{2} (E_v + iE_h)(E_v^* - iE_h^*) \\ &= \frac{1}{2} (|E_v|^2 + |E_h|^2 - i(E_v E_h^* - E_h E_v^*)) \\ &= \frac{1}{2} (I + V) \end{aligned} \quad (5.61)$$

Here is a summary of the Stokes parameters in terms of intensities of orthogonal components:

$$I = I_v + I_h = I_{-45^\circ} + I_{+45^\circ} = I_{RH} + I_{LH} \quad (5.62)$$

$$Q = I_v - I_h \quad (5.63)$$

$$U = I_{+45^\circ} - I_{-45^\circ} \quad (5.64)$$

$$V = I_{RH} - I_{LH} \quad (5.65)$$

<sup>1</sup> A retarder allows the phase of two orthogonal components of light to be varied with respect to each other.

We see that  $Q$  and  $U$  are both related to linear polarisation, while  $V$  is related to circular polarisation.

Here are the Stokes parameters for some standard polarisations:

polarisation	$(I, Q, U, V)$
horizontal	$(I, -I, 0, 0)$
vertical	$(I, +I, 0, 0)$
linear $\pm 45^\circ$	$(I, 0, \mp I, 0)$
right-circular	$(I, 0, 0, I)$
left-circular	$(I, 0, 0, -I)$

As mentioned, this deviates from what is written elsewhere. In other parts  $V$  is defined as to be left-hand minus right-hand circular polarisation, which appears to be consistent with *Mishchenko et al. [2002]*, see their page 23.

## 5.4 Partial polarisation

The equality  $I^2 = Q^2 + U^2 + V^2$  (Equation 5.40) is valid for the ideal case of a monochromatic plane wave that is completely polarised, i.e., where the amplitudes  $a_v$  and  $a_h$  and the phases  $\delta_v$  and  $\delta_h$  are fixed and do not vary with time. This means that the plane wave is emitted by one coherent source.

In reality, i.e., in the case of natural radiation, the amplitudes and phases fluctuate, since the radiation originates from several sources that do not emit radiation coherently, and since the emission from one source usually has very short coherence times. This means that we usually have a superposition of radiation from several incoherent sources, and that the polarisation state of the radiation from each source fluctuates as well<sup>2</sup>. Typically, such fluctuations have time scales that are longer than the period ( $2\pi/\omega$ ) of the oscillation, but that are still shorter than the integration time of the instrument that measures the radiation. Thus, the instrument measures an incoherent superposition of time averages over of the fluctuating polarisation. If the fluctuations are random for all the sources and if the different sources emit incoherently and are not in any way oriented, then there is no preferred orientation, ellipticity or handedness of the emitted radiation, which is then called unpolarised. This is the case for radiation from the sun. If the fluctuations are not completely random, the radiation is called partially polarised.

To quantify this rather heuristic argumentation, we express the above-mentioned ideas in the language of the Stokes parameters: The Stokes parameters  $I, Q, U, V$  derived from measurements result from the superposition of radiation from many sources and/or the average over emission events with individual Stokes parameters  $I_i, Q_i, U_i, V_i$ . Since the different sources and/or emission events are incoherent, the Stokes parameters – which are intensity, not amplitude quantities – can simply be added up:

$$I = \sum_i I_i, \quad Q = \sum_i Q_i, \quad U = \sum_i U_i, \quad V = \sum_i V_i \quad (5.66)$$

In the case of unpolarised radiation, i.e., when the amplitudes and phases, or equivalently, the orientation angle  $\zeta$  and the ellipticity angle  $\beta$  are random (uniformly distributed),  $Q, U,$  and  $V$  each cancel out.

<sup>2</sup>This does, of course, not apply to coherent sources like lasers or coherent radars.

The equality  $I_i^2 = Q_i^2 + U_i^2 + V_i^2$  (cf. Equation 5.40) still holds for each contribution  $i$ , but for the resulting  $I, Q, U, V$ , we have in general the inequality

$$I^2 \geq Q^2 + U^2 + V^2 \quad (5.67)$$

To prove it, we must once again go back to the amplitude/phase notation (Equations 5.14ff.), also cf. *Chandrasekhar* [1960, chap. I.15], but we shall omit the factor  $\frac{1}{2}\sqrt{\frac{\epsilon}{\mu}}$  on the right-hand sides, for the sake of better readability:

$$I = \sum_i I_i = \sum_i \left(a_v^{(i)}\right)^2 + \sum_i \left(a_h^{(i)}\right)^2 \quad (5.68)$$

$$Q = \sum_i Q_i = \sum_i \left(a_v^{(i)}\right)^2 - \sum_i \left(a_h^{(i)}\right)^2 \quad (5.69)$$

$$U = \sum_i U_i = -2 \sum_i a_v^{(i)} a_h^{(i)} \cos \delta^{(i)} \quad (5.70)$$

$$V = \sum_i V_i = 2 \sum_i a_v^{(i)} a_h^{(i)} \sin \delta^{(i)} \quad (5.71)$$

$$(5.72)$$

where  $\delta^{(i)} = \delta_v^{(i)} - \delta_h^{(i)}$ . We get

$$\begin{aligned} I^2 - Q^2 - U^2 - V^2 &= 4 \sum_i \left(a_v^{(i)}\right)^2 \sum_i \left(a_h^{(i)}\right)^2 \\ &\quad - 4 \left( \sum_i a_v^{(i)} a_h^{(i)} \cos \delta^{(i)} \right)^2 \\ &\quad - 4 \left( \sum_i a_v^{(i)} a_h^{(i)} \sin \delta^{(i)} \right)^2 \end{aligned} \quad (5.73)$$

The first term on the right-hand side can be rearranged as

$$\sum_i \left(a_v^{(i)} a_h^{(i)}\right)^2 + \sum_{\substack{i,j \\ i \neq j}} \left(a_v^{(i)} a_h^{(j)}\right)^2 \quad (5.74)$$

The other two terms can be rearranged similarly to yield:

$$\begin{aligned} & - \sum_i \left(a_v^{(i)} a_h^{(i)}\right)^2 \left[ \cos^2 \delta^{(i)} + \sin^2 \delta^{(i)} \right] \\ & - \sum_{\substack{i,j \\ i \neq j}} a_v^{(i)} a_h^{(i)} a_v^{(j)} a_h^{(j)} \left[ \cos \delta^{(i)} \cos \delta^{(j)} + \sin \delta^{(i)} \sin \delta^{(j)} \right] \end{aligned} \quad (5.75)$$

Putting this into Equation 5.73 (and dividing by 4), the sums over just  $i$  cancel and we get:

$$\begin{aligned} (I^2 - Q^2 - U^2 - V^2)/4 &= \sum_{\substack{i,j \\ i \neq j}} \left(a_v^{(i)} a_h^{(j)}\right)^2 \\ &\quad - \sum_{\substack{i,j \\ i \neq j}} a_v^{(i)} a_h^{(i)} a_v^{(j)} a_h^{(j)} \cos(\delta^{(i)} - \delta^{(j)}) \end{aligned} \quad (5.76)$$

where the cosine addition theorem was used. In the summation, we now change from  $i \neq j$  to  $i < j$ , so we have to symmetrise the first term (the second term is already symmetric with respect to  $i$  and  $j$  and therefore just gets a factor 2):

$$(I^2 - Q^2 - U^2 - V^2)/4 = \sum_{\substack{i,j \\ i < j}} \left[ \left( a_v^{(i)} a_h^{(j)} \right)^2 + \left( a_v^{(j)} a_h^{(i)} \right)^2 - 2 \left( a_v^{(i)} a_h^{(j)} \right) \left( a_v^{(j)} a_h^{(i)} \right) \cos(\delta^{(i)} - \delta^{(j)}) \right] \quad (5.77)$$

Each summand of the sum on the right-hand side is positive, since it is greater than or equal to  $(a_v^{(i)} a_h^{(j)} - a_v^{(j)} a_h^{(i)})^2$ , which completes the proof. The right-hand side vanishes only if  $\delta^{(i)} = \delta^{(j)}$  and  $a_v^{(i)}/a_h^{(i)} = a_v^{(j)}/a_h^{(j)}$  for all  $i, j$ , i.e., if the phase difference and amplitude ratio between the horizontal and vertical component of the electric field is the same for all contributions, in other words: if all contributions have the same polarisation.

For completeness, we shall now restate the definition of the Stokes component, extended to include natural radiation (i.e., including the case of partially polarised and unpolarised radiation). Instead of summing over the individual emission events, we use ensemble averages, denoted by angular brackets:

$$I = \frac{1}{2} \sqrt{\frac{\epsilon}{\mu}} \langle E_v E_v^* + E_h E_h^* \rangle \quad (5.78)$$

$$Q = \frac{1}{2} \sqrt{\frac{\epsilon}{\mu}} \langle E_v E_v^* - E_h E_h^* \rangle \quad (5.79)$$

$$U = -\frac{1}{2} \sqrt{\frac{\epsilon}{\mu}} \langle E_v E_h^* + E_h E_v^* \rangle \quad (5.80)$$

$$V = i \frac{1}{2} \sqrt{\frac{\epsilon}{\mu}} \langle E_h E_v^* - E_v E_h^* \rangle \quad (5.81)$$

Except for the ensemble average  $\langle \dots \rangle$ , the definition is identical to the one for monochromatic, plane waves (Equations 5.10 to 5.13). The same applies to the second and third definitions of the Stokes parameters (Equations 5.14 to 5.17 and Equations 5.34 to 5.37, respectively). Note that the fourth definition (Equations 5.62 to 5.65) which uses sums and differences of intensities, is equally valid for fully polarised, partially polarised and unpolarised radiation. The definition of intensities, however, has to include the ensemble average:  $I_h = \langle E_h E_h^* \rangle$  etc.

Now we can define a measure for the degree of polarisation,  $p$ , as:

$$p = \frac{\sqrt{Q^2 + U^2 + V^2}}{I} \quad (5.82)$$

For completely polarised radiation,  $Q^2 + U^2 + V^2 = I^2$ , so  $p = 1$ , and for unpolarised radiation,  $Q = U = V = 0$ , so  $p = 0$ .

Furthermore, it can be convenient to define the polarised component of radiation by

$$I_p^2 = Q^2 + U^2 + V^2 \quad (5.83)$$

and the unpolarised component as

$$I_u = I - I_p \quad (5.84)$$

Thus, partially polarised radiation, described by a Stokes vector  $(I, Q, U, V)$ , can be regarded as a superposition of completely polarised radiation described by the Stokes vector  $(I_p, Q, U, V)$  and unpolarised radiation described by the Stokes vector  $(I_u, 0, 0, 0)$ . We

see that the Stokes parameter formalism can conveniently deal with partially polarised and with unpolarised radiation, much in contrast to the formalism using the electric field (amplitude and phase).

In addition to the degree of polarisation,  $p$ , we can define measures for the circularity and the linearity of the polarisation. Recalling Equations 5.64 and 5.65, we can define the degree of linear polarisation,  $p_{lin}$ , as

$$p_{lin} = \frac{\sqrt{Q^2 + U^2}}{I} \quad (5.85)$$

and the the degree of circular polarisation,  $p_{circ}$ , as

$$p_{circ} = \frac{V}{I} \quad (5.86)$$

### 5.4.1 Polarisation of Radiation in the Atmosphere

The radiation encountered in atmospheric sounding (for which ARTS is intended) is natural radiation, coming from the sun, space (cosmic background), and/or the atmosphere and the Earth surface (thermal radiation, scattered radiation)<sup>3</sup>. Radiation from the sun is unpolarised, as already mentioned; the same applies for the cosmic background. In contrast, radiation emitted by the ground can be polarised, dependent on material, texture and direction. Radiation emitted by the atmosphere (thermal radiation) is almost unpolarised because of the random orientation of the air molecules. An exception is caused by the Zeeman effect induced in oxygen molecules by the – anisotropic – Earth's magnetic field. Scattering of radiation by oriented particles, e.g. ice particles in cirrus clouds, is sensitive to polarisation, and generally increases the degree of polarisation. Typically  $I > |Q| > |U|, |V|$ .

### 5.4.2 Antenna polarisation

Finally we want to know what an antenna of arbitrary polarisation response (antenna polarisation) measures if radiation of some other arbitrary polarisation is incident on it.

In order to clarify the concept, we first consider some trivial examples: We assume an antenna that receives only vertically polarised radiation.

- If the incident radiation is fully horizontally polarised, the antenna will measure nothing.
- If the incident radiation is fully vertically polarised, the antenna will measure the full intensity of the radiation.
- If the radiation is fully left- or right-circularly polarised, the antenna will measure half of the full intensity, for circularly polarised radiation is made up of equal portions of vertically and horizontally polarised radiation, superimposed with a phase lag of 90°.

In order to be able to describe the general case, we first have to formalise the description of the antenna polarisation. Polarised radiation is described by

1. the Jones vector, or
2. the Stokes vector, or

---

<sup>3</sup>This is not so for active sounding techniques that use a coherent source, such as lidar.

3. intensity,  $I$ , orientation angle,  $\zeta$  (i.e., the angle between the major axis of the polarisation ellipse and the horizontal polarisation direction), and ellipticity angle,  $\beta$  (see page 68).

Since the intensity of the radiation is the absolute square (the squared “length”) of the complex Jones vector, or, in other words, the first Stokes component,  $I$ , the polarisation alone is defined by

1. a normalised Jones vector, or
2. three normalised Stokes components  $Q$ ,  $U$ , and  $V$  (where  $Q^2 + U^2 + V^2 = 1$ ), or
3. the orientation angle  $\zeta$  and the ellipticity angle  $\beta$  (see Equation 5.38 to 5.39).

In the same way, the polarisation of the antenna can be described in one of three ways:

1. a normalised Jones vector

$$\mathbf{e} = \begin{bmatrix} e_v \\ e_h \end{bmatrix} \quad \text{where} \quad \mathbf{e} \cdot \mathbf{e}^* = 1 \quad (5.87)$$

(note that in the scalar product of two complex vectors, the second one has to be complex-conjugated.)

2. a normalised Stokes vector

$$\mathbf{i} = (1, q, u, v) \quad \text{where} \quad q^2 + u^2 + v^2 = 1 \quad (5.88)$$

3. the two angles  $\zeta$  and  $\beta$ . According to Equation 5.34 to 5.37, we have:

$$q = -\cos(2\zeta) \cos(2\beta) \quad (5.89)$$

$$u = -\sin(2\zeta) \cos(2\beta) \quad (5.90)$$

$$v = -\sin(2\beta) \quad (5.91)$$

Now we can calculate the intensity  $I'$  the antenna measures. In terms of the electrical fields, i.e., Jones vectors, we just have to project the Jones vector  $\mathbf{E}$  of the incident radiation onto the normalised Jones vector  $\mathbf{e}$  of the antenna,

$$\mathbf{E}' = (\mathbf{E} \cdot \mathbf{e}^*) \mathbf{e} \quad (5.92)$$

(this is in effect like passing through a polarizer) and then take its absolute square

$$I' = \frac{1}{2} \sqrt{\frac{\epsilon}{\mu}} |\mathbf{E}'|^2 = \frac{1}{2} \sqrt{\frac{\epsilon}{\mu}} |(\mathbf{E} \cdot \mathbf{e}^*)|^2 \quad (5.93)$$

With some elementary algebra (mainly using that  $\frac{1}{2} \sqrt{\frac{\epsilon}{\mu}} E_v E_v^* = (I + Q)/2$ ,  $\frac{1}{2} \sqrt{\frac{\epsilon}{\mu}} E_h E_h^* = (I - Q)/2$ ,  $\frac{1}{2} \sqrt{\frac{\epsilon}{\mu}} E_v E_h^* = -(U - iV)/2$  which follow immediately from Equation 5.10 to 5.13) this can be rewritten in terms of the of the Stokes vector  $\mathbf{I}$  of the incident radiation and the Stokes vector  $\mathbf{i}$  of the antenna. It turns out to be just a scalar product:

$$I' = \frac{1}{2} \mathbf{i} \cdot \mathbf{I} \quad (5.94)$$



## 5.5 The scattering amplitude matrix

The electric field,  $[E_v, E_h]^T$ , originating from a single scattering event of an incident electric field  $[E_v^0, E_h^0]^T$  may in the far field be written as (see further Equation 6.7)

$$\begin{bmatrix} E_v \\ E_h \end{bmatrix} = f(r) \begin{bmatrix} S_2 & S_3 \\ S_4 & S_1 \end{bmatrix} \begin{bmatrix} E_v^0 \\ E_h^0 \end{bmatrix}, \quad (5.95)$$

where  $S_j$  are the scattering amplitude functions and all distance effects are put into the function  $f(r)$ . Using Stokes based nomenclature, the equation above becomes

$$\begin{bmatrix} I \\ Q \\ U \\ V \end{bmatrix} = g(r) \mathbf{F} \begin{bmatrix} I^0 \\ Q^0 \\ U^0 \\ V^0 \end{bmatrix}, \quad (5.96)$$

where all distance effects are put into the function  $g(r)$  and the transformation matrix  $\mathbf{F}$  can be expressed as [Liou, 2002, Sec. 5.4.3].

$$\mathbf{F} = \begin{bmatrix} \frac{1}{2}(M_2+M_3+M_4+M_1) & \frac{1}{2}(M_2-M_3+M_4-M_1) & S_{23}+S_{41} & -D_{23}-D_{41} \\ \frac{1}{2}(M_2+M_3-M_4-M_1) & \frac{1}{2}(M_2-M_3-M_4+M_1) & S_{23}-S_{41} & -D_{23}+D_{41} \\ S_{24}+S_{31} & S_{24}-S_{31} & S_{21}+S_{34} & -D_{21}+D_{34} \\ D_{24}+D_{31} & D_{24}-D_{31} & D_{21}+D_{34} & S_{21}-S_{34} \end{bmatrix}. \quad (5.97)$$

The elements of  $\mathbf{F}$  are finally given by the following expressions:

$$M_k = |S_k|^2, \quad (5.98)$$

$$S_{kj} = S_{jk} = (S_j S_k^* + S_k S_j^*)/2, \quad (5.99)$$

$$-D_{kj} = D_{jk} = i(S_j S_k^* - S_k S_j^*)/2, \quad j, k = 1, 2, 3, 4. \quad (5.100)$$

Depending on the properties of the scattering event, the structure of the matrix  $\mathbf{F}$  differs. Two special cases are:

$$S_1 = S_2, \quad S_3 = S_4 = 0 \rightarrow \mathbf{F} = \begin{bmatrix} x & 0 & 0 & 0 \\ 0 & x & 0 & 0 \\ 0 & 0 & x & 0 \\ 0 & 0 & 0 & x \end{bmatrix}, \quad (5.101)$$

$$S_3 = S_4 = 0 \rightarrow \mathbf{F} = \begin{bmatrix} x & x & 0 & 0 \\ x & x & 0 & 0 \\ 0 & 0 & x & x \\ 0 & 0 & x & x \end{bmatrix}, \quad (5.102)$$

where  $x$  indicates elements deviating from 0. Many (most?) natural materials have the property that  $S_4$  is the complex conjugate of  $S_3$  ( $S_3 = S_4^*$ ) and this results in that  $\mathbf{F}$  is a symmetric matrix (in general with all element positions filled).

## 5.6 Change of the Stokes basis

In this section vector-matrix formalism is used. The standard Stokes vector is

$$\mathbf{s} = \begin{bmatrix} I \\ Q \\ U \\ V \end{bmatrix}. \quad (5.103)$$

### 5.6.1 The modified Stokes vector

There are also other definitions of the Stokes vector, such as the modified Stokes vector:

$$\mathbf{m} = \begin{bmatrix} I_v \\ I_h \\ U \\ V \end{bmatrix}. \quad (5.104)$$

A Stokes vector is converted to its modified counterpart by the matrix:

$$\mathbf{C}_m = \begin{bmatrix} 1/2 & 1/2 & 0 & 0 \\ 1/2 & -1/2 & 0 & 0 \\ 0 & 0 & 1 & 0 \\ 0 & 0 & 0 & 1 \end{bmatrix}. \quad (5.105)$$

The reversed transformation is

$$\mathbf{C}_s = \begin{bmatrix} 1 & 1 & 0 & 0 \\ 1 & -1 & 0 & 0 \\ 0 & 0 & 1 & 0 \\ 0 & 0 & 0 & 1 \end{bmatrix}. \quad (5.106)$$

A matrix operating on a Stokes vector is called a Mueller matrix. How to convert such a matrix ( $\mathbf{M}$ ) operating on a standard Stokes vector to its modified counterpart ( $\mathbf{M}_m$ ) can be understood by considering

$$\mathbf{M}_m \mathbf{m} = \mathbf{C}_m \mathbf{M} \mathbf{C}_s \mathbf{m}. \quad (5.107)$$

That is

$$\mathbf{M}_m = \mathbf{C}_m \mathbf{M} \mathbf{C}_s. \quad (5.108)$$

### 5.6.2 Rotated modified Stokes vector

In some cases it could be of interest to place  $I_h$  at the first position, or some intermediate state between pure  $I_v$  and  $I_h$ . These cases can be seen as a rotation of what is considered as the direction of vertical polarisation. The Mueller matrix for such a rotation is

$$\mathbf{L}(\alpha) = \begin{bmatrix} 1 & 0 & 0 & 0 \\ 0 & \cos(2\alpha) & \sin(2\alpha) & 0 \\ 0 & -\sin(2\alpha) & \cos(2\alpha) & 0 \\ 0 & 0 & 0 & 1 \end{bmatrix}, \quad (5.109)$$

where  $\alpha$  is the size of the rotation. That is the rotated modified Stokes vector is

$$\mathbf{r} = \mathbf{C}_m \mathbf{L}(\alpha) \mathbf{s}. \quad (5.110)$$

The extension of the conversion in Eq. 5.108 is

$$\mathbf{M}_r = \mathbf{C}_m \mathbf{L}(\alpha) \mathbf{M} \mathbf{L}(-\alpha) \mathbf{C}_s. \quad (5.111)$$

The matrix products left and right of  $\mathbf{M}$  are

$$\mathbf{C}_m \mathbf{L}(\alpha) = \begin{bmatrix} 1/2 & \cos(2\alpha)/2 & \sin(2\alpha)/2 & 0 \\ 1/2 & -\cos(2\alpha)/2 & -\sin(2\alpha)/2 & 0 \\ 0 & -\sin(2\alpha) & \cos(2\alpha) & 0 \\ 0 & 0 & 0 & 1 \end{bmatrix}, \quad (5.112)$$

and

$$\mathbf{L}(-\alpha) \mathbf{C}_s = \begin{bmatrix} 1 & 1 & 0 & 0 \\ \cos(2\alpha) & -\cos(2\alpha) & -\sin(2\alpha) & 0 \\ \sin(2\alpha) & -\sin(2\alpha) & \cos(2\alpha) & 0 \\ 0 & 0 & 0 & 1 \end{bmatrix}, \quad (5.113)$$

The relationships between the elements in  $\mathbf{s}$  and  $\mathbf{r}$  are

$$\mathbf{C}_m \mathbf{L}(\alpha) \begin{bmatrix} I \\ Q \\ U \\ V \end{bmatrix} = \frac{1}{2} \begin{bmatrix} I + \cos(2\alpha)Q + \sin(2\alpha)U \\ I - \cos(2\alpha)Q - \sin(2\alpha)U \\ 2 \sin(2\alpha)Q + 2 \cos(2\alpha)U \\ V \end{bmatrix}. \quad (5.114)$$

If  $U = 0$  the first element in  $\mathbf{r}$  can be written as

$$\mathbf{r}_I = I_v \cos^2(\alpha) + I_h \sin^2(\alpha), \quad (5.115)$$

where  $I_v$  and  $I_h$  are the radiances at vertical and horizontal polarisation, in the basis of the original Stokes vector. That is, by selecting  $\alpha = 90^\circ$ , a modified Stokes vector with  $I_h$  in the first position is effectively obtained. Further, Equation 5.115 equals the expression normally assumed to model the change in polarisation response of microwave cross-track sounders as a function of scanning angle. If the sensor measures “quasi-vertical” (the polarisation when looking just besides nadir),  $\alpha$  matches the angle between nadir and the viewing direction,  $\beta$ . If the sensor instead measures “quasi-horizontal”,  $\alpha$  should be replaced with  $90 - \beta$ .



## Chapter 6

# Basic radiative transfer theory

When dealing with atmospheric radiation a division can be made between two different wavelength ranges where the limit is found around  $5\text{ }\mu\text{m}$ , i.e. one range consists of the near IR, visible and UV regions while the second range covers thermal and far IR and microwaves. The first reason to this division is the principal sources to the radiation in the two ranges, for wavelengths shorter than  $5\text{ }\mu\text{m}$  the solar radiation is dominating while at longer wavelengths the thermal emission from the surface and the atmosphere is more important. A second reason is the importance of scattering but here it is impossible to give a fixed limit. Clouds are important scattering objects for most frequencies but at cloud free conditions scattering can in many cases be neglected for wavelengths  $> 5\text{ }\mu\text{m}$ . If the atmosphere can be assumed to be in local thermodynamic equilibrium the radiative transfer can be simplified considerably, and this is a valid assumption for the IR region and microwaves but not for e.g. UV frequencies.

The radiative transfer in the atmosphere must be adequately described in many situations, as when estimating rates of photochemical reactions, calculating radiative forcing in the atmosphere or evaluating a remote sensing observation. It is not totally straightforward to quantify the radiative transfer with good accuracy because the calculations can be very computationally demanding and many of the parameters needed are hard to determine. For example, situations when a great number of transitions or multiple scattering must be considered will cause long calculations while as a rule scattering is difficult to model because the shape and size distribution of the scattering particles are highly variable quantities.

This chapter introduces the theoretical background which is essential to develop a radiative transfer model including scattering. The theory is based on concepts of electrodynamics, starting from the Maxwell equations. An elementary book for electrodynamics is written by *Jackson* [1998]. For optics and scattering of radiation by small particles the reader may refer for instance to *van de Hulst* [1957] and *Bohren and Huffman* [1998]. The notation used in this chapter is mostly adapted from the book “Scattering, Absorption, and

---

### History

- 211122 Add Section about direct sources.
- 120924 Added discussion of the n2-law, mainly using text originally written for an ESA report by Bengt Rydberg (PE).
- 110615 Revised, and moved parts about surface from AUG (PE).
- 050224 Most text replaced by chapter 1 from Claudia Emde’s phd-thesis.
- 030305 Copied from a compendium written by Patrick Eriksson.

Emission of Light by Small Particles” by *Mishchenko et al.* [2002]. Several lengthy derivations of formulas, which are not shown in detail here, can also be found in this book. The purpose of this chapter is to provide definitions and give ideas, how these definitions can be derived using principles of electromagnetic theory. For the derivation of the radiative transfer equation an outline of the traditional phenomenological approach is given.

## 6.1 Basic definitions

From the Maxwell equations one can derive the formula for the electromagnetic field vector  $\mathbf{E}$  of a plane electromagnetic wave propagating in a homogeneous medium without sources:

$$\mathbf{E}(\mathbf{r}, t) = \mathbf{E}_0 \exp\left(-\frac{\omega}{c} m_I \hat{n} \cdot \mathbf{r}\right) \exp\left(i\frac{\omega}{c} m_R \hat{n} \cdot \mathbf{r} - i\omega t\right), \quad (6.1)$$

where  $\mathbf{E}_0$  is the amplitude of the electromagnetic wave in vacuum,  $c$  is the speed of light in vacuum,  $\omega$  is the angular frequency,  $\mathbf{r}$  is the position vector and  $\hat{n}$  is a real unit vector in the direction of propagation. The complex refractive index  $m$  is

$$m = m_R + im_I = c\sqrt{\epsilon\mu}, \quad (6.2)$$

where  $m_R$  is the non-negative real part and  $m_I$  is the non-negative imaginary part. Furthermore  $\mu$  is the permeability of the medium and  $\epsilon$  the permittivity. For a vacuum,  $m = m_R = 1$ . The imaginary part of the refractive index, if it is non-zero, determines the decay of the amplitude of the wave as it propagates through the medium, which is thus absorbing. The real part determines the phase velocity  $v = c/m_R$ . The time-averaged Poynting vector  $\mathbf{P}(\mathbf{r})$ , which describes the flow of electromagnetic energy, is defined as

$$\mathbf{P}(\mathbf{r}) = \frac{1}{2} \text{Re}(\langle \mathbf{E}(\mathbf{r}) \rangle \times \langle \mathbf{H}^*(\mathbf{r}) \rangle), \quad (6.3)$$

where  $\mathbf{H}$  is the magnetic field vector and the  $*$  denotes the complex conjugate. The Poynting vector for a homogeneous wave is given by

$$\langle \mathbf{P}(\mathbf{r}) \rangle = \frac{1}{2} \text{Re} \left( \sqrt{\frac{\epsilon}{\mu}} |\mathbf{E}_0|^2 \exp\left(-2\frac{\omega}{c} m_I \hat{n} \cdot \mathbf{r}\right) \hat{n} \right). \quad (6.4)$$

Equation 6.4 shows that the energy flows in the direction of propagation and its absolute value  $I(\mathbf{r}) = |\langle \mathbf{P}(\mathbf{r}) \rangle|$ , which is usually called intensity (or irradiance), is exponentially attenuated. Rewriting Equation 6.4 gives

$$I(\mathbf{r}) = I_0 \exp(-\alpha^p \hat{n} \cdot \mathbf{r}), \quad (6.5)$$

where  $I_0$  is the intensity for  $\mathbf{r} = \mathbf{0}$ . The absorption coefficient  $\alpha^p$  is

$$\alpha^p = 2\frac{\omega}{c} m_I = \frac{4\pi m_I}{\lambda} = \frac{4\pi m_I \nu}{c}, \quad (6.6)$$

where  $\lambda$  is the free-space wavelength and  $\nu$  the frequency. Intensity has the dimension of monochromatic flux [energy/(area  $\times$  time)].

## 6.2 Scattering, absorption and thermal emission by a single particle

A parallel monochromatic beam of electromagnetic radiation propagates in vacuum without any change in its intensity or polarization state. A small particle, which is interposed into the beam, can cause several effects:

**Absorption:** The particle converts some of the energy contained in the beam into other forms of energy.

**Elastic scattering:** Part of the incident energy is extracted from the beam and scattered into all spatial directions at the frequency of the incident beam. Scattering can change the polarization state of the radiation.

**Inelastic scattering:** As above, but the frequency is changed by the scattering. This process is neglected below.

**Extinction:** The energy of the incident beam is reduced by an amount equal to the sum of absorption and scattering.

**Dichroism:** The change of the polarization state of the beam as it passes a particle.

**Thermal emission:** If the temperature of the particle is non-zero, the particle emits radiation in all directions over a large frequency range.

The beam is an oscillating plane magnetic wave, whereas the particle can be described as an aggregation of a large number of discrete elementary electric charges. The incident wave excites the charges to oscillate with the same frequency and thereby radiate secondary electromagnetic waves. The superposition of these waves gives the total elastically scattered field.

One can also describe the particle as an object with a refractive index different from that of the surrounding medium. The presence of such an object changes the electromagnetic field that would otherwise exist in an unbounded homogeneous space. The difference of the total field in the presence of the object can be thought of as the field *scattered* by the object. The angular distribution and the polarization of the scattered field depend on the characteristics of the incident field as well as on the properties of the object as its size relative to the wavelength and its shape, composition and orientation.

### 6.2.1 Definition of the amplitude matrix

For the derivation of a relation between the incident and the scattered electric field we consider a finite scattering object in the form of a single body or a fixed aggregate embedded in an infinite homogeneous, isotropic and non-absorbing medium. We assume that the individual bodies forming the scattering object are sufficiently large that they can be characterized by optical constants appropriate to bulk matter, not to optical constants appropriate for single atoms or molecules. Solving the Maxwell equations for the internal volume, which is the interior of the scattering object, and the external volume one can derive a formula, which expresses the total electric field everywhere in space in terms of the incident field and the field inside the scattering object. Applying the far field approximation gives a relation between incident and scattered field, which is that of a spherical wave. The amplitude matrix

$\mathbf{S}(\hat{n}^{\text{sca}}, \hat{n}^{\text{inc}})$  includes this relation:

$$\begin{bmatrix} E_{\psi}^{\text{sca}}(r\hat{n}^{\text{sca}}) \\ E_{\omega}^{\text{sca}}(r\hat{n}^{\text{sca}}) \end{bmatrix} = \frac{e^{ikr}}{r} \mathbf{S}(\hat{n}^{\text{sca}}, \hat{n}^{\text{inc}}) \begin{bmatrix} E_{0\psi}^{\text{inc}} \\ E_{0\omega}^{\text{inc}} \end{bmatrix}. \quad (6.7)$$

The amplitude matrix depends on the directions of incident  $\hat{n}^{\text{inc}}$  and scattering  $\hat{n}^{\text{sca}}$  as well as on size, morphology, composition, and orientation of the scattering object with respect to the coordinate system. The distance between the origin and the observation point is denoted by  $r$  and the wave number of the external volume is denoted by  $k$ .

The amplitude matrix provides a complete description of the scattering pattern in the far field zone. The amplitude matrix explicitly depends on  $\omega^{\text{inc}}$  and  $\omega^{\text{sca}}$  even when  $\psi^{\text{inc}}$  and/or  $\psi^{\text{sca}}$  equal 0 or  $\pi$ .

### 6.2.2 Phase matrix

The phase matrix  $\mathbf{Z}$  describes the transformation of the Stokes vector of the incident wave into that of the scattered wave for scattering directions away from the incidence direction ( $\hat{n}^{\text{sca}} \neq \hat{n}^{\text{inc}}$ ),

$$\mathbf{s}^{\text{sca}}(r\hat{n}^{\text{sca}}) = \frac{1}{r^2} \mathbf{Z}(\hat{n}^{\text{sca}}, \hat{n}^{\text{inc}}) \mathbf{s}^{\text{inc}}. \quad (6.8)$$

The  $4 \times 4$  phase matrix can be written in terms of the amplitude matrix elements for single particles [Mishchenko *et al.*, 2002]. All elements of the phase matrix have the dimension of area and are real. As the amplitude matrix, the phase matrix depends on  $\omega^{\text{inc}}$  and  $\omega^{\text{sca}}$  even when  $\psi^{\text{inc}}$  and/or  $\psi^{\text{sca}}$  equal 0 or  $\pi$ . In general, all 16 elements of the phase matrix are non-zero, but they can be expressed in terms of only seven independent real numbers. Four elements result from the moduli  $|S_{ij}|$  ( $i, j = 1, 2$ ) and three from the phase-differences between  $S_{ij}$ . If the incident beam is unpolarized, i.e.,  $\mathbf{s}^{\text{inc}} = (I^{\text{inc}}, 0, 0, 0)^T$ , the scattered light generally has at least one non-zero Stokes parameter other than intensity:

$$I^{\text{sca}} = Z_{11} I^{\text{inc}}, \quad (6.9)$$

$$Q^{\text{sca}} = Z_{21} I^{\text{inc}}, \quad (6.10)$$

$$U^{\text{sca}} = Z_{31} I^{\text{inc}}, \quad (6.11)$$

$$V^{\text{sca}} = Z_{41} I^{\text{inc}}. \quad (6.12)$$

This is the phenomena is traditionally called “polarization”. The non-zero degree of polarization Equation 5.82 can be written in terms of the phase matrix elements

$$p = \frac{\sqrt{Z_{21}^2 + Z_{31}^2 + Z_{41}^2}}{Z_{11}}. \quad (6.13)$$

### 6.2.3 Extinction matrix

In the special case of the exact forward direction ( $\hat{n}^{\text{sca}} = \hat{n}^{\text{inc}}$ ) the attenuation of the incoming radiation is described by the extinction matrix  $\mathbf{K}$ . In terms of the Stokes vector we get

$$\mathbf{s}(r\hat{n}^{\text{inc}}) \Delta S = \mathbf{s}^{\text{inc}} \Delta S - \mathbf{K}(\hat{n}^{\text{inc}}) \mathbf{s}^{\text{inc}} + O(r^{-2}). \quad (6.14)$$

Here  $\Delta S$  is a surface element normal to  $\hat{n}^{\text{inc}}$ . The extinction matrix can also be expressed explicitly in terms of the amplitude matrix. It has only seven independent elements. Again the elements depend on  $\omega^{\text{inc}}$  and  $\omega^{\text{sca}}$  even when the incident wave propagates along the  $z$ -axis.



### 6.2.4 Absorption vector

The particle also emits radiation if its temperature  $T$  is above zero Kelvin. According to Kirchhoff's law of radiation the emissivity equals the absorptivity of a medium under thermodynamic equilibrium. The energetic and polarization characteristics of the emitted radiation are described by a four-component Stokes emission column vector  $\mathbf{a}(\hat{\mathbf{r}}, T, \omega)$ . The emission vector is defined in such a way that the net rate, at which the emitted energy crosses a surface element  $\Delta S$  normal to  $\hat{\mathbf{r}}$  at distance  $r$  from the particle at frequencies from  $\omega$  to  $\omega + \Delta\omega$ , is

$$W^e = \frac{1}{r^2} \mathbf{a}(\hat{\mathbf{r}}, T, \omega) B(T, \omega) \Delta S \Delta\omega, \quad (6.15)$$

where  $W^e$  is the power of the emitted radiation and  $B$  is the Planck function. In order to calculate  $\mathbf{a}$  we assume that the particle is placed inside an opaque cavity of dimensions large compared to the particle and any wavelengths under consideration. We have thermodynamic equilibrium if the cavity and the particle is maintained at the constant temperature  $T$ . The emitted radiation inside the cavity is isotropic, homogeneous, and unpolarized. We can represent this radiation as a collection of quasi-monochromatic, unpolarized, incoherent beams propagating in all directions characterized by the Planck blackbody radiation

$$B(T, \omega) \Delta S \Delta\Omega = \frac{\hbar \omega^3}{2\pi^2 v^2 \left[ \exp\left(\frac{\hbar \omega}{k_B T}\right) - 1 \right]} \Delta S \Delta\Omega, \quad (6.16)$$

where  $\Delta\Omega$  is a small solid angle about any direction,  $\hbar$  is the Planck constant divided by  $2\pi$ , and  $k_B$  is the Boltzmann constant. With respect to the  $n^2$ -law discussed below, it could be noticed that the Planck law is governed by the local phase velocity,  $v$ , [see e.g. *Thomas and Stamnes, 2002*], and not the vacuum speed.

The blackbody Stokes vector is

$$\mathbf{s}_b(T, \omega) = \begin{bmatrix} B(T, \omega) \\ 0 \\ 0 \\ 0 \end{bmatrix}. \quad (6.17)$$

For the Stokes emission vector, which we also call particle absorption vector, we can derive

$$a_i^p(\hat{\mathbf{r}}, T, \omega) = K_{i1}(\hat{\mathbf{r}}, \omega) - \int_{4\pi} d\hat{\mathbf{r}}' Z_{i1}(\hat{\mathbf{r}}, \hat{\mathbf{r}}', \omega), \quad i = 1, \dots, 4. \quad (6.18)$$

This relation is a property of the particle only, and it is valid for any particle, in thermodynamic equilibrium or non-equilibrium.

### 6.2.5 Optical cross sections

The optical cross-sections are defined as follows: The product of the scattering cross section  $C_{\text{sca}}$  and the incident monochromatic energy flux gives the total monochromatic power removed from the incident wave as a result of scattering into all directions. The product of the absorption cross section  $C_{\text{abs}}$  and the incident monochromatic energy flux gives the power which is removed from the incident wave by absorption. The extinction cross section

$C_{\text{ext}}$  is the sum of scattering and absorption cross section. One can express the extinction cross sections in terms of extinction matrix elements

$$C_{\text{ext}} = \frac{1}{I_{\text{inc}}} ( K_{11}(\hat{\mathbf{n}}^{\text{inc}})I^{\text{inc}} + K_{12}(\hat{\mathbf{n}}^{\text{inc}})Q^{\text{inc}} + \quad (6.19)$$

$$K_{13}(\hat{\mathbf{n}}^{\text{inc}})U^{\text{inc}} + K_{14}(\hat{\mathbf{n}}^{\text{inc}})V^{\text{inc}}), \quad (6.20)$$

and the scattering cross section in terms of phase matrix elements

$$C_{\text{sca}} = \frac{1}{I_{\text{inc}}} \int_{4\pi} d\hat{\mathbf{r}} ( Z_{11}(\hat{\mathbf{r}}, \hat{\mathbf{n}}^{\text{inc}})I^{\text{inc}} + Z_{12}(\hat{\mathbf{r}}, \hat{\mathbf{n}}^{\text{inc}})Q^{\text{inc}} + \quad (6.21)$$

$$Z_{13}(\hat{\mathbf{r}}, \hat{\mathbf{n}}^{\text{inc}})U^{\text{inc}} + Z_{14}(\hat{\mathbf{r}}, \hat{\mathbf{n}}^{\text{inc}})V^{\text{inc}}). \quad (6.22)$$

The absorption cross section is the difference between extinction and scattering cross section:

$$C_{\text{abs}} = C_{\text{ext}} - C_{\text{sca}}. \quad (6.23)$$

The single scattering albedo  $\omega_0$ , which is a commonly used quantity in radiative transfer theory, is defined as the ratio of the scattering and the extinction cross section:

$$\omega_0 = \frac{C_{\text{sca}}}{C_{\text{ext}}} \leq 1. \quad (6.24)$$

All cross sections are real-valued positive quantities and have the dimension of area.

The phase function is generally defined as

$$p(\hat{\mathbf{r}}, \hat{\mathbf{n}}^{\text{inc}}) = \frac{4\pi}{C_{\text{sca}}I_{\text{inc}}} ( Z_{11}(\hat{\mathbf{r}}, \hat{\mathbf{n}}^{\text{inc}})I^{\text{inc}} + Z_{12}(\hat{\mathbf{r}}, \hat{\mathbf{n}}^{\text{inc}})Q^{\text{inc}} + \quad (6.25)$$

$$Z_{13}(\hat{\mathbf{r}}, \hat{\mathbf{n}}^{\text{inc}})U^{\text{inc}} + Z_{14}(\hat{\mathbf{r}}, \hat{\mathbf{n}}^{\text{inc}})V^{\text{inc}}). \quad (6.26)$$

The phase function is dimensionless and normalized:

$$\frac{1}{4\pi} \int_{4\pi} p(\hat{\mathbf{r}}, \hat{\mathbf{n}}^{\text{inc}}) d\hat{\mathbf{r}} = 1. \quad (6.27)$$

### 6.2.6 Coordinate systems: The laboratory frame and the scattering frame

For radiative transfer calculations we need a coordinate system to describe the direction of propagation. For this purpose we use the laboratory frame, which is shown in Figure 6.1, right panel. The z-axis corresponds to the local zenith direction and the x-axis points towards the north-pole. The propagation direction is described by the local zenith angle  $\theta$  and the local azimuth angle  $\phi$ . This coordinate system is the most appropriate frame to describe the propagation direction and the polarization state of the radiation. However, in order to describe scattering of radiation by a particle or a particle ensemble, it makes sense to define another coordinate system taking into consideration the symmetries of the particle or the scattering medium, as one gets much simpler expressions for the single scattering properties. For macroscopically isotropic and mirror-symmetric scattering media it is convenient to use the scattering frame, in which the incidence direction is parallel to the z-axis and the x-axis coincides with the scattering plane, that is, the plane through the unit vectors  $\hat{\mathbf{n}}^{\text{inc}}$  and  $\hat{\mathbf{n}}^{\text{sca}}$ . The scattering frame is illustrated in Figure 6.1, left panel. For symmetry reasons the single scattering properties defined with respect to the scattering frame can only depend on the scattering angle  $\Theta$ ,

$$\Theta = \arccos(\hat{\mathbf{n}}^{\text{inc}} \cdot \hat{\mathbf{n}}^{\text{sca}}), \quad (6.28)$$

between the incident and the scattering direction.

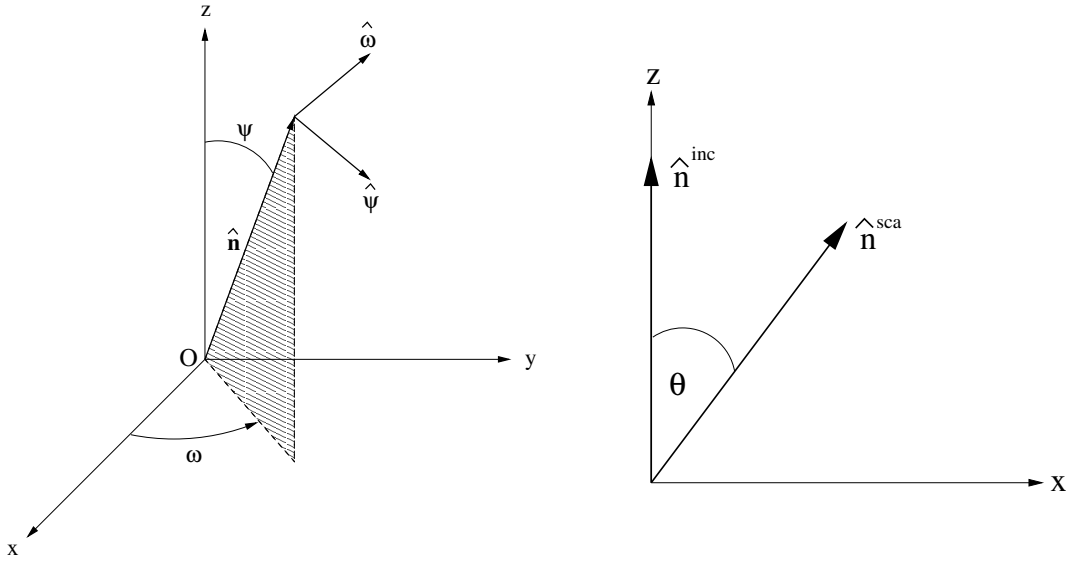


Figure 6.1: Right: Coordinate system to describe the direction of propagation and the polarization state of a plane electromagnetic wave (adapted from Mishchenko). Left: Illustration of the scattering frame. The z-axis coincides with the incident direction  $\hat{n}^{\text{inc}}$ . The scattering angle  $\Theta$  is the angle between  $\hat{n}^{\text{inc}}$  and  $\hat{n}^{\text{sca}}$ .

### 6.3 Scattering, absorption and emission by ensembles of independent particles

The formalism described in the previous chapter applies only for radiation scattered by a single body or a fixed cluster consisting of a limited number of components. In reality, one normally finds situations, where radiation is scattered by a very large group of particles forming a constantly varying spatial configuration. Clouds of ice crystals or water droplets are a good example for such a situation. A particle collection can be treated at each given moment as a fixed cluster, but as a measurement takes a finite amount of time, one measures a statistical average over a large number of different cluster realizations.

Solving the Maxwell equations for a whole cluster, like a collection of particles in a cloud, is computationally too expensive. Fortunately, particles forming a random group can often be considered as independent scatterers. This approximation is valid under the following assumptions:

1. Each particle is in the far-field zone of all other particles.
2. Scattering by the individual particles is incoherent.

As a consequence of assumption 2, the Stokes parameters of the partial waves can be added without regard to the phase. If the particle number density is sufficiently small, the single scattering approximation can be applied. The scattered field in this approach is obtained by summing up the fields generated by the individual particles in response to the external field in isolation from all other particles. If the particle positions are random, one can show, that the phase matrix, the extinction matrix and the absorption vector are obtained by summing up the respective characteristics of all constituent particles.

### 6.3.1 Single scattering approximation

We consider a volume element containing  $N$  particles. We assume that  $N$  is sufficiently small, so that the mean distance between the particles is much larger than the incident wavelength and the average particle size. Furthermore we assume that the contribution of the total scattered signal of radiation scattered more than once is negligibly small. This is equivalent to the requirement

$$\frac{N \langle C_{\text{sca}} \rangle}{l^2} \ll 1, \quad (6.29)$$

where  $\langle C_{\text{sca}} \rangle$  is the average scattering cross section per particle and  $l$  is the linear dimension of the volume element. The electric field scattered by the volume element can be written as the vector sum of the partial scattered fields scattered by the individual particles:

$$\mathbf{E}^{\text{sca}}(\mathbf{r}) = \sum_{n=1}^N \mathbf{E}_n^{\text{sca}}(\mathbf{r}). \quad (6.30)$$

As we assume single scattering the partial scattered fields are given according to Equation 6.7:

$$\begin{bmatrix} [E_n^{\text{sca}}(\mathbf{r})]_{\psi} \\ [E_n^{\text{sca}}(\mathbf{r})]_{\omega} \end{bmatrix} = \frac{e^{ikr}}{r} \mathbf{S}(\hat{\mathbf{r}}, \hat{\mathbf{n}}^{\text{inc}}) \begin{bmatrix} E_{0\psi}^{\text{inc}} \\ E_{0\omega}^{\text{inc}} \end{bmatrix}, \quad (6.31)$$

where  $\mathbf{S}$  is the total amplitude scattering matrix given by:

$$\mathbf{S}(\hat{\mathbf{r}}, \hat{\mathbf{n}}^{\text{inc}}) = \sum_{n=1}^N e^{i\Delta_n} \mathbf{S}_n(\hat{\mathbf{r}}, \hat{\mathbf{n}}^{\text{inc}}). \quad (6.32)$$

$\mathbf{S}_n(\hat{\mathbf{r}}, \hat{\mathbf{n}}^{\text{inc}})$  are the individual amplitude matrices and the phase  $\Delta_n$  is given by

$$\Delta_n = k \mathbf{r}_{\text{On}} \cdot (\hat{\mathbf{n}}^{\text{inc}} - \hat{\mathbf{r}}), \quad (6.33)$$

where the vector  $\mathbf{r}_{\text{On}}$  connects the origin of the volume element  $O$  with the  $n$ th particle origin (see Figure 6.2). Since  $\Delta_n$  vanishes in forward direction and the individual extinction matrices can be written in terms of the individual amplitude matrix elements, the total extinction matrix is given by

$$\mathbf{K} = \sum_{n=1}^N \mathbf{K}_n = N \langle \mathbf{K} \rangle, \quad (6.34)$$

where  $\langle \mathbf{K} \rangle$  is the average extinction matrix per particle. One can derive the analog equation for the phase matrix

$$\mathbf{Z} = \sum_{n=1}^N \mathbf{Z}_n = N \langle \mathbf{Z} \rangle, \quad (6.35)$$

where  $\langle \mathbf{Z} \rangle$  is the average phase matrix per particle. In almost all practical situations, radiation scattered by a collection of independent particles is incoherent, as a minimal displacement of a particle or a slight change in the scattering geometry changes the phase differences entirely. It is important to note, that the ensemble averaged phase matrix and the ensemble averaged extinction matrix have in general 16 independent elements. The relations between the matrix elements, which can be derived for single particles, do not hold for particle ensembles.

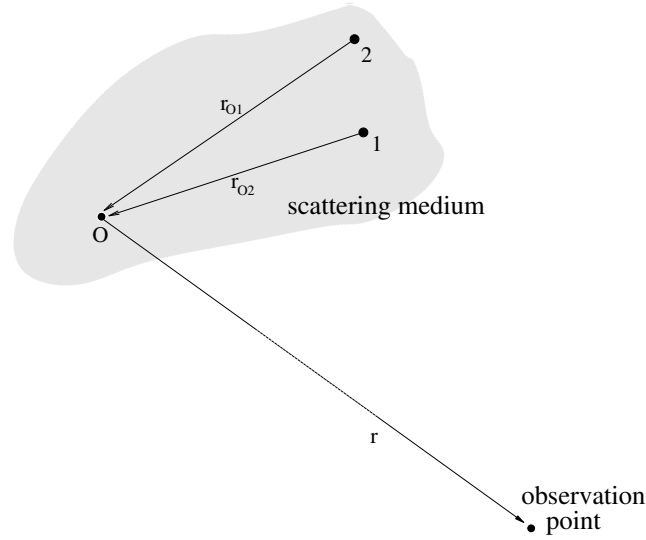


Figure 6.2: A volume element of a scattering medium consisting of a particle ensemble.  $O$  is the origin of the volume element,  $r_{O1}$  connects the origin with particle 1 and  $r_{O2}$  with particle 2. The observation point is assumed to be in the far-field zone of the volume element.

## 6.4 Phenomenological derivation of the radiative transfer equation

When the scattering medium contains a very large number of particles the single scattering approximation is no longer valid. In this case we have to take into account that each particle scatters radiation that has already been scattered by another particle. This means that the radiation leaving the medium has a significant multiple scattered component. The observation point is assumed to be in the far-field zone of each particle, but it is not necessarily in the far-field zone of the scattering medium as a whole. A traditional method in this case is to solve the radiative transfer equation. This approach still assumes, that the particles forming the scattering medium are randomly positioned and widely separated and that the extinction and the phase matrices of each volume element can be obtained by incoherently adding the respective characteristics of the constituent particles. In other words the scattering media is assumed to consist of a large number of discrete, sparsely and randomly distributed particles and is treated as continuous and locally homogeneous. Radiative transfer theory is originally a phenomenological approach based on considering the transport of energy through a medium filled with a large number of particles and ensuring energy conservation. *Mishchenko* [2002] has demonstrated that it can be derived from electromagnetic theory of multiple wave scattering in discrete random media under certain simplifying assumptions.

In the phenomenological radiative transfer theory, the concept of single scattering by individual particles is replaced by the assumption of scattering by a small homogeneous volume element. It is furthermore assumed that the result of scattering is not the transformation of a plane incident wave into a spherical scattered wave, but the transformation of the specific intensity vector, which includes the Stokes vectors from all waves contributing to the electromagnetic radiation field.

The vector radiative transfer equation (VRTE) is

$$\frac{d\mathbf{s}(\nu, \mathbf{r}, \hat{\mathbf{n}})}{ds} = -\mathbf{K}(\nu, \mathbf{r}, \hat{\mathbf{n}})\mathbf{s}(\nu, \mathbf{r}, \hat{\mathbf{n}}) + \mathbf{a}(\nu, \mathbf{r}, \hat{\mathbf{n}})B(\nu, \mathbf{r}) + \int_{4\pi} d\hat{\mathbf{n}}' \mathbf{Z}(\nu, \mathbf{r}, \hat{\mathbf{n}}, \hat{\mathbf{n}}')\mathbf{s}(\nu, \mathbf{r}, \hat{\mathbf{n}}'), \quad (6.36)$$

where  $\mathbf{s}$  is the specific intensity vector,  $\mathbf{K}$  is the total extinction matrix,  $\mathbf{a}$  is the total absorption vector,  $B$  is the Planck function and  $\mathbf{Z}$  is the total phase matrix. Furthermore  $\nu$  is the frequency of the radiation,  $ds$  is a path-length-element of the propagation path,  $\mathbf{r}$  represents the atmospheric position and  $\hat{\mathbf{n}}$  the propagation direction. Equation 6.36 is valid for monochromatic or quasi-monochromatic radiative transfer. We can use this equation for simulating microwave radiative transfer through the atmosphere, as the scattering events do not change the frequency of the radiation.

The four-component specific intensity vector  $\mathbf{s} = (I, Q, U, V)^T$  fully describes the radiation and it can directly be associated with the measurements carried out by a radiometer used for remote sensing. For the definition of the components of the specific intensity vector refer to Section 5, where the Stokes components are described.

The three terms on the right hand side of Equation 6.36 describe physical processes in an atmosphere containing different particle types and different trace gases. The first term represents the extinction of radiation traveling through the scattering medium,  $\mathbf{K}$ . For microwave radiation in cloudy atmospheres, extinction is caused by gaseous absorption, particle absorption and particle scattering. Therefore  $\mathbf{K}$  can be written as a sum of two matrices, the particle extinction matrix  $\mathbf{K}^p$  and the gaseous extinction matrix  $\mathbf{K}^g$ :

$$\mathbf{K}(\nu, \mathbf{r}, \hat{\mathbf{n}}) = \mathbf{K}^p(\nu, \mathbf{r}, \hat{\mathbf{n}}) + \mathbf{K}^g(\nu, \mathbf{r}, \hat{\mathbf{n}}). \quad (6.37)$$

The particle extinction matrix is the sum over the individual specific extinction matrices  $\mathbf{K}_i^p$  of the  $N$  different particles types contained in the scattering medium weighted by their particle number densities  $n_i^p$ :

$$\mathbf{K}^p(\nu, \mathbf{r}, \hat{\mathbf{n}}) = \sum_{i=1}^N n_i^p \mathbf{K}_i^p(\nu, \mathbf{r}, \hat{\mathbf{n}}). \quad (6.38)$$

The gaseous extinction matrix can normally be derived from the scalar gas absorption. This is because there is no polarization due to gas absorption at cloud altitudes, and the off-diagonal elements of the gaseous extinction matrix are zero. On the other hand, at very high altitudes above approximately 40 km there is polarization due to the Zeeman effect, mainly due to oxygen molecules. In addition, in the topsphere and stratosphere molecular scattering can be neglected in the microwave frequency range. Hence the coefficients on the diagonal correspond to the gas absorption coefficient:

$$\mathbf{K}_{l,m}^g(\nu, \mathbf{r}) = \alpha^g(\nu, \mathbf{r}) \quad \text{if } l = m \\ 0 \quad \text{if } l \neq m. \quad (6.39)$$

where  $\alpha^g$  is the total scalar gas absorption coefficient, which is calculated from the individual absorption coefficients of all  $M$  trace gases  $\alpha_i^g$  and their volume mixing ratios  $n_i^g$  as:

$$\alpha^g(\nu, \mathbf{r}) = \sum_{i=1}^M n_i^g \alpha_i^g(\nu, \mathbf{r}). \quad (6.40)$$

The second term in Equation 6.36 is the thermal source term. It describes thermal emission by gases and particles in the atmosphere. The absorption vector  $\mathbf{a}$  is

$$\mathbf{a}(\nu, \mathbf{r}, \hat{\mathbf{n}}) = \mathbf{a}^p(\nu, \mathbf{r}, \hat{\mathbf{n}}) + \mathbf{a}^g(\nu, \mathbf{r}, \hat{\mathbf{n}}), \quad (6.41)$$

where  $\mathbf{a}^p$  and  $\mathbf{a}^g$  are the particle absorption vector and the gas absorption vector, respectively. The particle absorption vector is a sum over the individual absorption vectors  $\mathbf{a}_i^p$ , again weighted with  $n_i^p$ :

$$\mathbf{a}^p(\nu, \mathbf{r}, \hat{\mathbf{n}}) = \sum_{i=1}^N n_i^p \mathbf{a}_i^p(\nu, \mathbf{r}, \hat{\mathbf{n}}). \quad (6.42)$$

The gas absorption vector is simply (if no Zeeman splitting)

$$\mathbf{a}^g = [\alpha^p, 0, 0, 0]^T. \quad (6.43)$$

The last term in Equation 6.36 is the scattering source term. It adds the amount of radiation which is scattered from all directions  $\hat{\mathbf{n}}'$  into the propagation direction  $\hat{\mathbf{n}}$ . The phase matrix  $\mathbf{Z}$  is the sum of the individual phase matrices  $\mathbf{Z}_i$  weighted with  $n_i^p$ :

$$\mathbf{Z}(\nu, \mathbf{r}, \hat{\mathbf{n}}) = \sum_{i=1}^N n_i^p \mathbf{Z}_i(\nu, \mathbf{r}, \hat{\mathbf{n}}). \quad (6.44)$$

The scalar radiative transfer equation (SRTE)

$$\begin{aligned} \frac{dI(\nu, \mathbf{r}, \hat{\mathbf{n}})}{ds} = & -K_{11}(\nu, \mathbf{r}, \hat{\mathbf{n}})I(\nu, \mathbf{r}, \hat{\mathbf{n}}) + a_1(\nu, \mathbf{r}, \hat{\mathbf{n}})B(\nu, \mathbf{r}) \\ & + \int_{4\pi} d\hat{\mathbf{n}}' Z_{11}(\nu, \mathbf{r}, \hat{\mathbf{n}}, \hat{\mathbf{n}}')I(\nu, \mathbf{r}, \hat{\mathbf{n}}') \end{aligned} \quad (6.45)$$

can be used presuming that the radiation field is unpolarized. This approximation is reasonable if the scattering medium consists of spherical or completely randomly oriented particles, where  $\mathbf{K}^p$  is diagonal and only the first element of  $\mathbf{a}^p$  is non-zero.

## 6.5 The $n^2$ -law of radiance

### 6.5.1 Introduction

The radiance,  $s$ , is unchanged for propagation in “free space”. The term free space implies a refractive index of unity and that extinction is zero. However, it is possible to define a slightly different quantity that is conserved also for propagation with a varying refractive index. This quantity is here denoted as,  $s_{n2}$ , and is defined as [Mobley, 1994; Mätzler and Melsheimer, 2006]:

$$s_{n2} \equiv \frac{s}{n^2}. \quad (6.46)$$

That is, for radiation propagating without extinction or any sources,  $s_{n2}$  is constant along the propagation path. This is denoted as the  $n^2$ -law for radiance. This impact of  $n$  can, for different reasons, normally be neglected. As a consequence and to keep the nomenclature simple, the  $n^2$ -law is in general ignored in the ARTS documentation.

### 6.5.2 Treatment in ARTS

As mentioned, the quantity defined by Equation 6.46 is constant for propagation without attenuation. Further, it can be shown that the radiance corresponding to some emission is independent on the refractive index along the propagation path, only the refractive indexes at the emission and measurement points matter. This is also valid with attenuation along the propagation path [Moble, 1994, Eq. 4.23]:

$$\frac{I_m}{n_m^2} = e^{-\tau} \frac{I_e}{n_e^2}, \quad (6.47)$$

where  $I_m$  is measured radiance,  $n_m$  the refractive index where the measurement is performed,  $I_e$  emitted radiance,  $n_e$  the refractive index at the emission point, and  $\tau$  is the optical thickness between the two points.

As long as LTE applies, the emission is proportional to the Planck function,  $B$  (Eq. 6.16). Hence, using an emissivity,  $\varepsilon$ , we have

$$\frac{I_e}{n_e^2} = \frac{\varepsilon B(T_e)}{n_e^2} = \varepsilon B_{n2}(T_e), \quad (6.48)$$

where  $T_e$  is the temperature of the emitting substance, and

$$B_{n2}(T_B) \equiv \frac{B(T_B)}{n^2} = \frac{2h\nu^3}{c^2(\exp(h\nu/k_b T_B) - 1)}. \quad (6.49)$$

That is, it turns out that by consistently apply  $c$  in the Planck function (instead of  $v$ ), the dependency of  $n_e$  is removed. What remains to obtain the correct radiance to output,  $I$ , is to consider the impact of  $n_m$ :

$$I = n_m^2 I', \quad (6.50)$$

where  $I'$  is the radiance calculated ignoring the  $n^2$ -law.

As discussed by Mätzler and Melsheimer [2006], it can be deduced from basic principles that the brightness temperature must be a preserved quantity, even in light of the  $n^2$ -law. This statement can also be understood from Equation 6.49. In simple terms, the brightness temperature is defined with respect to the local Planck function and the impact of refractive index variations vanishes if the radiance is measured in terms of brightness temperature.

## 6.6 Simple solution without scattering and polarization

If scattering can be neglected and the atmosphere is assumed to be in local thermodynamic equilibrium, the radiative transfer equation gets unusually simple. These assumptions will be made below and they are normally valid for the infrared region and longer wavelengths as in the microwave region. For these conditions the atmospheric absorption and emission are linked and the basic problem to determine the radiative transfer is to calculate the absorption. At the wavelengths considered rotational and vibrational transitions are the dominating absorbing processes.

The basic equation describing radiative transfer along a specific direction is

$$\frac{dI(\nu)}{dl} = k(l, \nu)(B(l, \nu) - I(\nu)) \quad (6.51)$$



where  $I$  is the intensity per unit area,  $\nu$  the frequency,  $l$  the distance along the propagation path,  $k$  the total absorption coefficient (summed over all species and transitions) and  $B$  the Planck function. This differential equation can be solved:

$$I(\nu) = I_0(\nu)e^{-\int_0^h k(l', \nu) dl'} + \int_0^h k(l, \nu) B(T(l), \nu) e^{-\int_0^l k(l', \nu) dl'} dl \quad (6.52)$$

where the receiver is assumed to be placed at  $l = 0$  and  $h$  is the distance along the path to the limit of the media.  $I_0$  is the intensity at the point  $h$  which can represent thermal emission from the surface, solar radiation at top of the atmosphere or cosmic background radiation depending on the observation geometry. When discussing radiative transfer the quantity optical depth,  $\tau$ , is commonly used and it is defined as

$$\tau(l, \nu) = \int_0^l k(l', \nu) dl' \quad (6.53)$$

and Equation 6.52 can be written as

$$I(\nu) = I_0(\nu)e^{-\tau(h, \nu)} + \int_0^h k(l, \nu) B(T(l), \nu) e^{-\tau(l', \nu)} dl \quad (6.54)$$

The terms inside the integral found in this equation have a simple physical meaning, the radiation emitted at one point is  $kBdl$  and this quantity is attenuated by the factor  $e^{-\tau}$  before it reaches the observation point.

## 6.7 Clear sky simulations with sun like sources

In this section we describe the radiative transfer in clearsky with sun like sources. In this context clear sky means that there is no scattering by liquid or solid matter but scattering by atoms and molecules (gas scattering, see also Sect. 2.5). Fig. 6.3 shows the geometry for a receiver outside of the atmosphere. The incoming direct radiation (yellow rays) from the sun is attenuated by the atmosphere and scattered at the surface and in the atmosphere (black dots) towards the receiver.

The sun is assumed to be far away from the planet or to be more precise

$$r_{\odot} \ll d_{\odot p} \quad (6.55)$$

with  $r_{\odot}$  the sun radius, and  $d_{\odot p}$  the distance between sun and TOA of the planet. This means that the angular variability of the direction of the radiation from the sun can be neglected (parallel beam or collimated beam approximation) and the incoming radiation at top of the atmosphere (TOA) can be described as

$$I_{\odot, TOA}(\Omega) = F_{\odot} \delta(\Omega, \Omega') \quad (6.56)$$

with  $\Omega'$  the direction of the sun. We neglect polarization here and in the following part of this section for the sake of simplicity.

The flux of the incoming radiation from the sun at the top of the atmosphere  $F_{\odot}$  is

$$\begin{aligned} F_{\odot} &= \int_0^{2\pi} \int_0^{\alpha} I_{\odot} \cos \theta \sin \theta d\theta d\phi \\ &= \pi I_{\odot} \sin^2 \alpha \end{aligned} \quad (6.57)$$

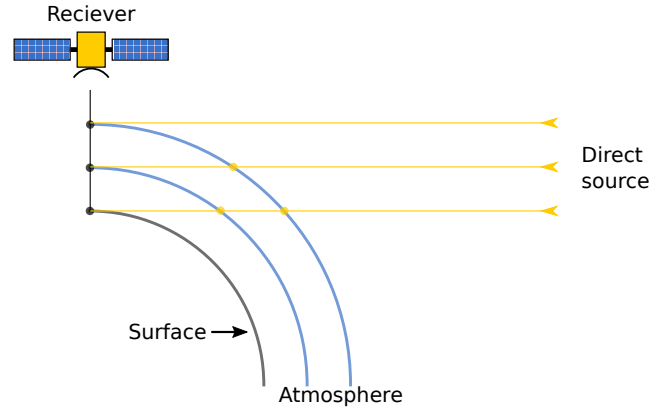


Figure 6.3: Radiative transfer of direct radiation form a sun to a nadir pointing receiver outside of the atmosphere assuming single scattering.

with  $I_{\odot}$  the sun spectral radiance, which is assumed to be isotropic, and  $\alpha$  the angular radius of the sun seen from TOA of the planet. This is

$$\alpha = \arctan \frac{r_{\odot}}{d_{\odot p}}. \quad (6.58)$$

As gas scattering is rather weak, multi scattering can be neglected and only single scattering of the incoming radiation from the sun needs to be considered. With this and Eq. 6.56, Eq. 6.36 neglecting polarization simplifies to

$$\begin{aligned} \frac{dI(s, \nu)}{ds} &= -kI(s, \nu) + aB(T(s)) + \\ &\quad \int_{4\pi} P(s, \nu, \Omega_i, \Omega_s) F_{\odot}^*(\nu, s) \delta(\Omega_i, \Omega') d\Omega_i \\ &= -kI(s, \nu) + aB(T(s)) + P(s, \nu, \Omega', \Omega_s) F_{\odot}^*(\nu, s) \end{aligned} \quad (6.59)$$

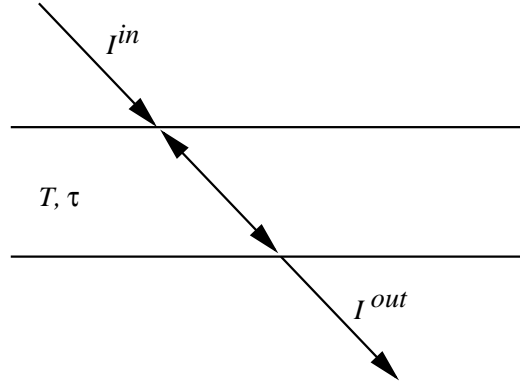
with  $s$  the position along the propagation path (black ray in Fig. 6.3),  $\nu$  the frequency,  $k$  and  $a$  the extinction and absorption coefficient,  $B$  the Planck function,  $\Omega_i$  the incoming and  $\Omega_s$  the direction of the propagation path.  $P$  is the phase function or if at the surface the bidirectional reflectance function. The incoming direct radiation  $F_{\odot}^*$  at along track position  $s$  is

$$F_{\odot}^*(\nu, s) = F_{\odot}(\nu, s) \exp \left( \int_0^{s'_{toa}} k(\nu, s') ds' \right) \quad (6.60)$$

with  $s'$  the position along the path from the position  $s$  to the top of the atmosphere in the direction of the sun (yellow rays in Fig. 6.3).

As in section ?? described the radius  $r_{\odot}$  of and distance  $d_{\odot}$  to the sun like object must be known. The position of this object in the sky of the planet is defined by the latitude and longitude where it stands at its zenith. The monochromatic irradiance spectra is define as the blackbody spectrum, which is calculated with the Plank function and the surface temperature of the object  $T_{astrosun}$ .

Figure 6.4: Schematic picture of the radiative transfer through a medium with constant temperature.



## 6.8 Special solutions

If the total emission along the propagation path can be neglected compared to the transmitted part of the incoming radiation, the radiative transfer equation is simplified to the well known Beer-Lambert law:

$$I(\nu) = I_0(\nu)e^{-\tau(h,\nu)} \quad (6.61)$$

This equation can for example be used when evaluating solar occultation observations.

If the temperature is constant through the medium studied (Fig. 6.4) the integral in Equation 6.52 can be solved analytically:

$$I^{out} = I^{in}e^{-\tau} + B(T, \nu)(1 - e^{-\tau}) \quad (6.62)$$

where  $\tau$  is the total optical thickness of the medium. Two special cases can be distinguished. If the layer is totally optically thick ( $\tau \rightarrow \infty$ ) then  $I^{in}$  is totally absorbed and  $I^{out} = B$ , the medium emits as a blackbody. If the layer has no absorption ( $\tau = 0$ ) then Equation 6.62 gives  $I^{out} = I^{in}$  as expected.

In microwave radiometry the measured intensity is normally presented by means of the brightness temperature,  $T_b$ . This quantity is derived from the Rayleigh-Jeans approximation of the Planck function:

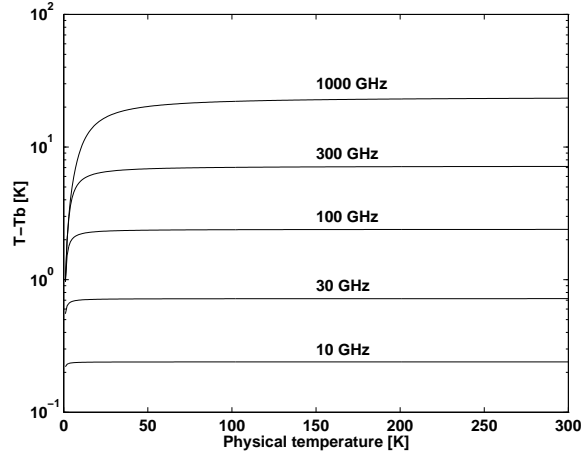
$$B(T, \nu) \approx \frac{2\nu^2 k_b T}{c^2} = \frac{2k_b T}{\lambda^2} \quad (6.63)$$

This equation is valid when  $h\nu \ll kT$  which is the case in the microwave region due to the relatively low frequencies. If the temperature is 50 K,  $h\nu$  equals  $kT$  at 1.04 THz. The important aspect of Equation 6.63 is the linear relationship between the intensity and the physical temperature. The natural definition of brightness temperature,  $T_b$ , is then

$$T_b(\nu) = \frac{\lambda^2}{2k_b T} I(\nu) \quad (6.64)$$

The difference between the brightness temperature and the physical temperature (corresponding to the actual intensity) increases with frequency which is exemplified in Figure

Figure 6.5: The difference between the physical temperature of a blackbody and the equivalent brightness temperature calculated using the Rayleigh-Jeans approximation.



6.5. The differences for higher frequencies are certainly not negligible and the brightness temperature shall not be mistaken for the physical temperature. The important fact is that the brightness temperature has a linear relationship to the intensity and gives a more intuitive understanding of the magnitude of the emission. In the Rayleigh-Jeans limit Equation 6.52 can be written as

$$T_b(\nu) = T_{b0}(\nu)e^{-\tau(h,\nu)} + \int_0^h k(l,\nu)T(l)e^{-\tau(l',\nu)}dl \quad (6.65)$$

## 6.9 Surface emission and reflection

### 6.9.1 The dielectric constant and the refractive index

The properties of a material can be reported either as the relative dielectric constant,  $\epsilon$ , or the refractive index,  $n$ . Both these quantities can be complex and are related as

$$n = \sqrt{\epsilon}. \quad (6.66)$$

### 6.9.2 Relating reflectivity and emissivity

Thermodynamic equilibrium can be assumed for natural surfaces, as long as there exist no strong temperature gradients. The Kirchoff law can then be used to relate the reflectivity and emissivity of a surface. For rough surfaces the scattering properties must be integrated to determine the emissivity (Equation 6.85). For specular reflections (defined below) and scalar radiative transfer calculations, the emissivity  $e$  is

$$e = 1 - r, \quad (6.67)$$

where  $r$  is the reflectivity (power reflection coefficient) of the surface. Equation 6.67 is valid for each polarisation state individually [Ulaby *et al.*, 1981, Eq. 4.190a].

We have then that

$$I^{\text{up}} = I^{\text{down}}r + (1 - r)B, \quad (6.68)$$

where  $I^{\text{up}}$  is upwelling radiation,  $I^{\text{down}}$  is downwelling radiation and  $B$  is the magnitude of blackbody radiation. As expected, if  $I^{\text{down}} = B$ , also  $I^{\text{up}}$  equals  $B$ . Expressing the last observation using vector nomenclature gives

$$\begin{bmatrix} B \\ 0 \\ 0 \\ 0 \end{bmatrix} = \mathbf{R} \begin{bmatrix} B \\ 0 \\ 0 \\ 0 \end{bmatrix} + \mathbf{b}, \quad (6.69)$$

where  $\mathbf{R}$  is the matrix (4 x 4) correspondence to the scalar reflectivity, describing the properties of the surface reflection. The vector  $\mathbf{b}$  is the surface emission, that can be expressed as

$$\mathbf{b} = (\mathbf{1} - \mathbf{R}) \begin{bmatrix} B \\ 0 \\ 0 \\ 0 \end{bmatrix}, \quad (6.70)$$

where  $\mathbf{1}$  is the identity matrix.

### 6.9.3 Specular reflections

If the surface is sufficiently smooth, radiation will be reflected/scattered only in the complementary angle, specular reflection. Required smoothness for assuming specular reflection is normally estimated by the Rayleigh criterion:

$$\Delta h < \frac{\lambda}{8 \cos \theta_1} \quad (6.71)$$

where  $\Delta h$  is the root mean square variation of the surface height,  $\lambda$  the wavelength and  $\theta_1$  the angle between the surface normal and the incident direction of the radiation. The criterion can also be defined with the factor 8 replaced with a higher number.

The complex reflection coefficient for the amplitude of the electromagnetic wave for vertical ( $R_v$ ) and horizontal ( $R_h$ ) polarisation is for a flat surface (if the relative magnetic permeability ( $\mu_r$ ) of both media is 1) given by the Fresnel equations:

$$R_v = \frac{n_2 \cos \theta_1 - n_1 \cos \theta_2}{n_2 \cos \theta_1 + n_1 \cos \theta_2} \quad (6.72)$$

$$R_h = \frac{n_1 \cos \theta_1 - n_2 \cos \theta_2}{n_1 \cos \theta_1 + n_2 \cos \theta_2} \quad (6.73)$$

where  $n_1$  is refractive index for the medium where the reflected radiation is propagating,  $\theta_1$  is the incident angle (measured from the local surface normal) and  $n_2$  is the refractive index of the reflecting medium. The angle  $\theta_2$  is the propagation direction for the transmitted part, and is (approximately) given by Snell's law:

$$\text{Re}(n_1) \sin \theta_1 = \text{Re}(n_2) \sin \theta_2, \quad (6.74)$$

where  $\text{Re}(\cdot)$  denotes the real part. Equation 6.74 is theoretically correct only if both  $n_1$  and  $n_2$  have no imaginary part. For cases where medium 1 is air,  $n_1$  can (in this context) be set to 1, and an expression allowing  $n_2$  to be complex is found in Section 5.4.1.3 of *Liou [2002]*. We are not aware of any expression for the case when both  $n_1$  and  $n_2$  are complex.

The power reflection coefficients are converted to an intensity reflection coefficient as

$$r = |R|^2, \quad (6.75)$$

where  $|\cdot|$  denotes the absolute value. Note that  $R$  can be complex, while  $r$  is always real.

The surface reflection can be seen as a scattering event and Section 5.5 can be used to derive the reflection matrix values. The scattering amplitude functions of Equation 5.95 are simply

$$S_2 = R_v, \quad (6.76)$$

$$S_1 = R_h, \quad (6.77)$$

$$S_3 = S_4 = 0. \quad (6.78)$$

This leads to that the transformation matrix for a specular surface reflection is (compare to *Liou* [2002, Sec. 5.4.3])

$$\mathbf{R} = \begin{bmatrix} \frac{r_v+r_h}{2} & \frac{r_v-r_h}{2} & 0 & 0 \\ \frac{r_v-r_h}{2} & \frac{r_v+r_h}{2} & 0 & 0 \\ 0 & 0 & \frac{R_h R_v^* + R_v R_h^*}{2} & i \frac{R_h R_v^* - R_v R_h^*}{2} \\ 0 & 0 & i \frac{R_v R_h^* - R_h R_v^*}{2} & \frac{R_h R_v^* + R_v R_h^*}{2} \end{bmatrix}. \quad (6.79)$$

In some cases just  $r_v$  and  $r_h$  are at hand (as assumed by `surfaceFlatRvRh`), the matrix  $\mathbf{R}$  is then set as:

$$\mathbf{R} = \begin{bmatrix} \frac{r_v+r_h}{2} & \frac{r_v-r_h}{2} & 0 & 0 \\ \frac{r_v-r_h}{2} & \frac{r_v+r_h}{2} & 0 & 0 \\ 0 & 0 & \frac{r_v+r_h}{2} & 0 \\ 0 & 0 & 0 & \frac{r_v+r_h}{2} \end{bmatrix}. \quad (6.80)$$

For example, the sea surface parameterization TESSEM provides the emissivity for vertical and horizontal polarisation ( $\epsilon_v$  and  $\epsilon_h$ ). The reflectivities are then set as  $r_v = 1 - \epsilon_v$  and  $r_h = 1 - \epsilon_h$ , respectively, and Eq. 6.80 is applied to set  $\mathbf{R}$  (WSM is `surfaceTessem`).

For the case of  $R_v = R_h$  (as assumed by `surfaceFlatScalarReflectivity`) the matrix in Equation 6.79 is strictly diagonal and all the diagonal elements have the same value,  $(r_v + r_h)/2 = r$ .

If the downwelling radiation is unpolarised, the reflected part of the upwelling radiation is

$$\mathbf{R} \begin{bmatrix} I \\ 0 \\ 0 \\ 0 \end{bmatrix} = \begin{bmatrix} I(r_v + r_h)/2 \\ I(r_v - r_h)/2 \\ 0 \\ 0 \end{bmatrix}. \quad (6.81)$$

as expected.

If  $\mathbf{R}$  is given by Equation 6.79, Equation 6.70 gives that the surface emission is

$$\mathbf{b} = \begin{bmatrix} B \left(1 - \frac{r_v+r_h}{2}\right) \\ B \frac{r_h-r_v}{2} \\ 0 \\ 0 \end{bmatrix}. \quad (6.82)$$

### 6.9.4 Rough surfaces

The scattering of rough surfaces is normally described by the bidirectional reflectance distribution function, BRDF. With the BRDF,  $f(\theta_0, \phi_0, \theta_1, \phi_1)$ , the scattered radiance in the direction  $(\theta_1, \phi_1)$  can be written as (see e.g. *Rees* [2001] or *Petty* [2006])

$$I'(\theta_1, \phi_1) = \int_0^{\pi/2} \int_0^{2\pi} I(\theta, \phi) \cos(\theta) f(\theta, \phi, \theta_1, \phi_1) \sin(\theta) d\phi d\theta, \quad (6.83)$$

where  $I(\theta, \phi)$  is the downwelling radiance for incidence angle  $\theta$  and azimuth angle  $\phi$ . One important property of the BRDF is

$$f(\theta_0, \phi_0, \theta_1, \phi_1) = f(\theta_1, \phi_1, \theta_0, \phi_0). \quad (6.84)$$

The reflectivity is the half-sphere integral of the BRDF

$$r(\theta_1, \phi_1) = \int_0^{\pi/2} \int_0^{2\pi} f(\theta_1, \phi_1, \theta, \phi) \cos(\theta) \sin(\theta) d\phi d\theta. \quad (6.85)$$

An ideally rough surface is denoted as Lambertian. The BRDF is for this case constant, and normally expressed using the diffuse reflectivity,  $r_d$  [e.g. *Petty*, 2006]:

$$f = \frac{r_d}{\pi}. \quad (6.86)$$

From Eq. 6.85 it follows that  $r = r_d$ .





## Chapter 7

# Propagation paths

### 7.1 Structure of implementation

The workspace method for calculating propagation paths is `ppathCalc`, but this is just a getaway function for `ppath_calc`. The main use of `ppathCalc` is to debug and test the path calculations, and that WSM should normally not be part of the control file.

#### 7.1.1 Main functions for clear sky paths

The master function to calculate full clear sky propagation paths is `ppath_calc`. This function is outlined in Algorithm 1. The function can be divided into three main parts, initialisation (handled by `ppath_start_stepping`), a repeated call of `ppath_step_agenda` and putting data into the return structure (`ppath`).

---

**Algorithm 1** Outline of the function `ppath_calc`.

---

```
check consistency of function input
call ppath_start_stepping to set ppath_step
while radiative background not reached do
  call ppath_step_agenda
  if path is at the highest pressure surface then
    radiative background is space
  else if path is at either end point of latitude or longitude grid then
    this is not allowed, issue an runtime error
  end if
  if cloud box is active then
    if path is at the surface of the cloud box then
      radiative background is the cloud box surface
    end if
  end if
end while
initialise the WSV ppath to hold found number of path points
```

---

---

#### History

120227 Created by splitting and revising the corresponding chapter in *ARTS User Guide* (Patrick Eriksson).

The main task of the function `ppath.start_stepping` is to set up `ppath.step` for the first call of `ppath.step_agenda`, which means that the practical starting point for the path calculations must be determined. As the propagation path is followed in the backward direction, the calculation starting points equals the end point of the path. If the sensor is placed inside the model atmosphere, the sensor position gives directly the starting point. For cases when the sensor is found outside the atmosphere, the point where the path exits the atmosphere must be determined. The exit point can be determined by pure geometrical calculations (see Sections 7.2 and 7.3) as the refractive index is assumed to have the constant value of 1 outside the atmosphere. The problem is accordingly to find the geometrical crossing between the limit of the atmosphere and the sensor line-of-sight (LOS). The function performs further some other tasks, which include:

- If the sensor is placed inside the model atmosphere
  - Checks that the sensor is placed above the surface level. If not, an error is issued.
  - If the sensor and surface altitudes are equal, and the sensor LOS is downward, the radiative background is set to be the surface. For 2D and 3D, the tilt of the surface radius is considered when determining if the LOS is downward.
  - If the cloud box is active and the sensor position is inside the cloud box, the radiative background is set to be “cloud box interior”.
- If the sensor is placed outside the model atmosphere
  - If it is found for 2D and 3D that the exit point of the path not is at the top of the atmosphere, but is either at a latitude or longitude end face of the atmosphere, an error is issued. This problem can not appear for 1D.

For further details, see the code.

### 7.1.2 Main functions for propagation path steps

Example on workspace methods to calculate propagation path steps are `ppath.stepGeometric` and `ppath.stepRefractionBasic`. All such methods adapt automatically to the atmospheric dimensionality, but the different dimensionalities are handled by separate internal functions. For example, the sub-functions to `ppath.stepGeometric` are `ppath.step_geom_1d`, `ppath.step_geom_2d` and `ppath.step_geom_3d`. See `m_ppath.cc` to get the names of the sub-functions for other propagation path step workspace methods.

Many tasks are independent of the algorithm for refraction that is used, or if refraction is considered at all. These tasks are solved by two functions for each atmospheric dimensionality. For 1D the functions are `ppath.start_1d` and `ppath.end_1d`, and the corresponding functions for 2D and 3D are named in the same way. The functions to calculate geometrical path steps are denoted as `do_gridrange_1d`, `do_gridcell_2d` and `do_gridcell_3d_byltest`. Paths steps passing a tangent point are handled by a recursive call of the step function. Algorithm 2 summarises this for geometrical 2D steps.

## 7.2 Some basic geometrical relationships for 1D and 2D

This section gives some expressions to determine positions along a propagation path when refraction is neglected. The expressions deal only with propagation path inside a plane,

**Algorithm 2** Outline of the function `ppath_step_geom_2d`.

---

```

call ppath_start_2d
if ppath_step.ppc < 1 then
    calculate the path constant (this is then first path step)
end if
call do_gridcell_2d
call ppath_end_2d
if calculated step ends with tangent point then
    call ppath_step_geom_2d with temporary Ppath structure
    append temporary Ppath structure to ppath_step
end if

```

---

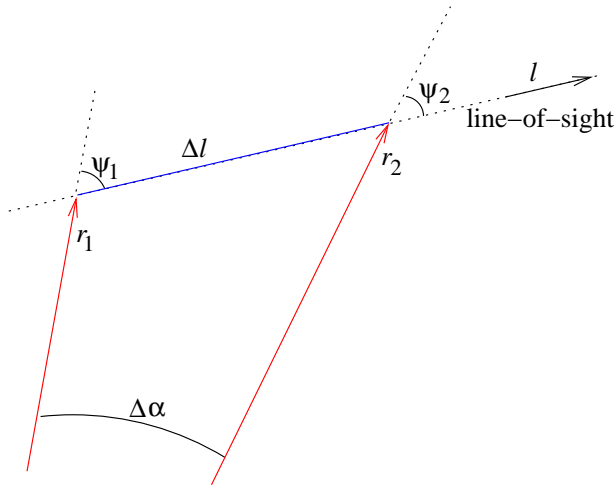


Figure 7.1: The radius ( $r$ ) and zenith angle ( $\psi$ ) for two points along the propagation path, and the distance along the path ( $\Delta l$ ) and the latitude difference ( $\Delta\alpha$ ) between these points.

where the latitude angle is the angular distance from an arbitrary point. This means that the expressions given here can be directly applied for 1D and 2D. Some of the expression are also of interest for 3D. The ARTS method for making the calculation of concern is given inside parenthesis above each equation, if not stated explicitly. A part of a geometrical propagation path is shown in Figure 7.1.

The law of sines gives that the product  $r \sin(\psi)$  must be constant along the propagation path:

$$p_c = r \sin(\psi), \quad (7.1)$$

where the absolute value is taken for 2D zenith angles as they can for such cases be negative. The propagation path constant,  $p_c$ , is determined by the position and line-of-sight of the sensor, a calculation done by the function `geometrical_ppc`. The constant equals also the radius of the tangent point of the path (that is found along an imaginary prolongation of the path behind the sensor if the viewing direction is upwards). The expressions below are based on  $p_c$  as the usage of a global constant for the path should decrease the sensitivity to numerical inaccuracies. If the calculations are based solely on the values for the neighbouring point, a numerical inaccuracy can accumulate when going from one point to next. The propagation path constant is stored in the field `constant` of `ppath` and `ppath_step`.

The relationship between the distance along the path for an infinitesimal change in radius is here denoted as the geometrical factor,  $g$ . If refraction is neglected, valid expressions

for the geometrical factor are

$$g = \frac{dl}{dr} = \frac{1}{\cos(\psi)} = \frac{1}{\sqrt{1 - \sin^2(\psi)}} = \frac{r}{\sqrt{r^2 - p_c^2}}. \quad (7.2)$$

For the radiative transfer calculations, only the distance between the points,  $\Delta l$ , is of interest, but for the internal propagation path calculations the length from the tangent point (real or imaginary),  $l$ , is used. By integrating Equation 7.2, we get that (geomppath\_l\_at\_r)

$$l(r) = \sqrt{r^2 - p_c^2}. \quad (7.3)$$

As refraction is here neglected, the tangent point, the point of concern and the centre of the coordinate system make up a right triangle and Equation 7.3 corresponds to the Pythagorean relation where  $p_c$  is the radius of the tangent point. The distance between two points ( $\Delta l$ ) is obtained by taking the difference of Equation 7.3 for the two radii.

The radius for a given  $l$  is simply (geomppath\_r\_at\_l)

$$r(l) = \sqrt{l^2 + p_c^2}. \quad (7.4)$$

The radius for a given zenith angle is simply obtained by rearranging Equation 7.1 (geomppath\_r\_at\_z)

$$r(\psi) = \frac{p_c}{\sin(\psi)}. \quad (7.5)$$

The zenith angle for a given radius is (geomppath\_z\_at\_r)

$$\psi(r) = \begin{cases} 180 - \sin^{-1}(p_c/r) & \text{for } 90^\circ < \psi_a \leq 180^\circ, \\ \sin^{-1}(p_c/r) & \text{for } 0^\circ \leq \psi_a \leq 90^\circ, \\ -\sin^{-1}(p_c/r) & \text{for } -90^\circ \leq \psi_a < 0^\circ, \\ \sin^{-1}(p_c/r) - 180 & \text{for } -180^\circ \leq \psi_a < -90^\circ, \end{cases} \quad (7.6)$$

where  $\psi_a$  is any zenith angle valid for the path on the same side of the tangent point. For example, for a 1D case, the part of the path between the tangent point and the sensor has zenith angles  $90^\circ < \psi_a \leq 180^\circ$ .

The latitude for a point (geomppath\_lat\_at\_z) is most easily determined by its zenith angle

$$\alpha(\psi) = \alpha_0 + \psi_0 - \psi \quad (7.7)$$

where  $\psi_0$  and  $\alpha_0$  are the zenith angle and latitude of some other point of the path. Equation 7.7 is based on the fact that the quantities  $\psi_1$ ,  $\psi_2$  and  $\Delta\alpha$  fulfil the relationship

$$\Delta\alpha = \psi_1 - \psi_2, \quad (7.8)$$

this independently of the sign of the zenith angles. The definitions used here result in that the absolute value of the zenith angle always decreases towards zero when following the path in the line-of-sight direction, that is, when going away from the sensor. It should then be remembered that the latitudes for 1D measures the angular distance to the sensor, and for 2D a positive zenith angle means observation towards higher latitudes.

The radius for a given latitude (geomppath\_r\_at\_lat) is obtained by combining Equations 7.7 and 7.5.

## 7.3 Calculation of geometrical propagation paths

This section describes the calculation of geometrical propagation paths for different atmospheric dimensionalities. That is, the effect of refraction is neglected. These calculations are performed by the workspace method `ppath_stepGeometric`. This method, as all methods for propagation path steps, adjust automatically to the atmospheric dimensionality, but the actual calculations are performed a sub-function for each dimensionality.

### 7.3.1 1D

The core function for this case is `do_gridrange_1d`. The lowest and highest radius value along the path step is first determined. If the line-of-sight is upwards ( $\psi \leq 90^\circ$ ), then the start point of the step gives the lowest radius, and the radius of the pressure surface above gives the highest value. In the case of a downwards line-of-sight, the lowest radius is either the tangent point, the pressure surface below or the surface. The needed quantities to describe the propagation path between the two found radii are calculated by the function `geompath_from_r1_to_r2`, that has the option to introduce more points to fulfil a length criterion between the path points. The mathematics of `geompath_from_r1_to_r2` are given by Equations 7.1–7.7.

### 7.3.2 2D

The definitions given in Chapter 3 of *ARTS User Guide* results in that for a 2D case the radius of a pressure surface varies linearly from one point of the latitude grid to next. Compared to the 1D case, this is the main additional problem to solve, handled by `plevel_crossing_2d`. A two step procedure is applied. In the first step the propagation path is moved towards the pressure level as far as exact expressions can be used. For example, if the level is approached from above the path is moved down to the maximum radius of the level inside the gridbox. An approximative solution is needed for the second step. Figure 7.2 gives a schematic description of the problem at hand, which is handled by the internal function `rslope_crossing`. The law of sine gives the following relationship for the crossing point:

$$\frac{\sin \Theta_p}{r_0 + c\alpha} = \frac{\sin(\pi - \alpha - \Theta_p)}{r_p}, \quad (7.9)$$

which can be re-written to

$$r_p \sin(\Theta_p) = (r_0 + c\alpha)(\sin \Theta_p \cos \alpha + \cos \Theta_p \sin \alpha). \quad (7.10)$$

This equation has no analytical solution. A first step to find an approximate solution is to note that  $\alpha$  is limited to relatively small values. For example, if it shall be possible for the angular distance  $\alpha$  to reach the value of  $3^\circ$ , the vertical distance between  $r_p$  and  $r$  must be about 8 km. For angles  $\alpha \leq 3^\circ$ , the sine and cosine terms can be replaced with the three first (non-constant) terms of their Taylor expansions maintaining a high accuracy. That is,

$$\begin{aligned} \cos \alpha &\approx 1 - \alpha^2/2 + \alpha^4/24 + \alpha^6/720 \\ \sin \alpha &\approx \alpha - \alpha^3/6 + \alpha^5/120 \end{aligned}$$

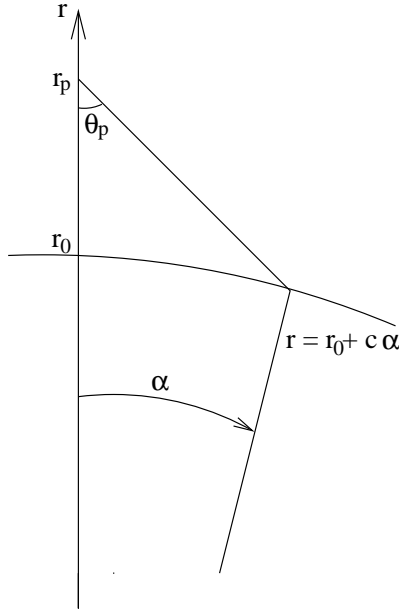


Figure 7.2: Quantities used to describe how to find the crossing between a geometrical propagation path and a tilted pressure surface. The angle  $\alpha$  is the angular distance from a reference point on the path. The problem at hand is to find  $\alpha$  for the crossing point. The radius of the pressure surface at  $\alpha = 0$  is denoted as  $r_0$ . The tilt of the pressure surface is  $c$ .

Equation 7.10 becomes with these replacements a polynomial equation of order 6:

$$\begin{aligned}
 0 &= p_0 + p_1\alpha + p_2\alpha^2 + p_3\alpha^3 + p_4\alpha^4 + p_5\alpha^5 + p_6\alpha^6, \\
 p_0 &= (r_0 - r_p) \sin(\Theta_p) \\
 p_1 &= r_0 \cos(\Theta_p) + c \sin(\Theta_p), \\
 p_2 &= -r_0 \sin(\Theta_p)/2 + c \cos(\Theta_p), \\
 p_3 &= -r_0 \cos(\Theta_p)/6 - c \sin(\Theta_p)/2, \\
 p_4 &= r_0 \sin(\Theta_p)/24 - c \cos(\Theta_p)/6, \\
 p_5 &= r_0 \cos(\Theta_p)/120 + c \sin(\Theta_p)/24, \\
 p_6 &= -r_0 \sin(\Theta_p)/720 + c \cos(\Theta_p)/120.
 \end{aligned} \tag{7.11}$$

This equation is solved numerically with the root finding algorithm implemented in the function `poly_root_solve`. Solutions of interest shall not be imaginary. Several issues associated with numerical accuracy must be considered, see the code (`rslope_crossing2d`) for details.

Geometrical 2D propagation path steps are determined by `do_gridcell_2d`. This function uses `plevel_crossing_2d` to calculate the latitude distance to a crossing of the pressure surface below and above the present path point, as well as the planets surface if it is found inside the grid box. If the closest crossing point with the pressure surfaces is outside the latitude range of the grid cell, it is the crossing of the path with the end latitude (in the viewing direction) that is of interest (Figure 7.3).

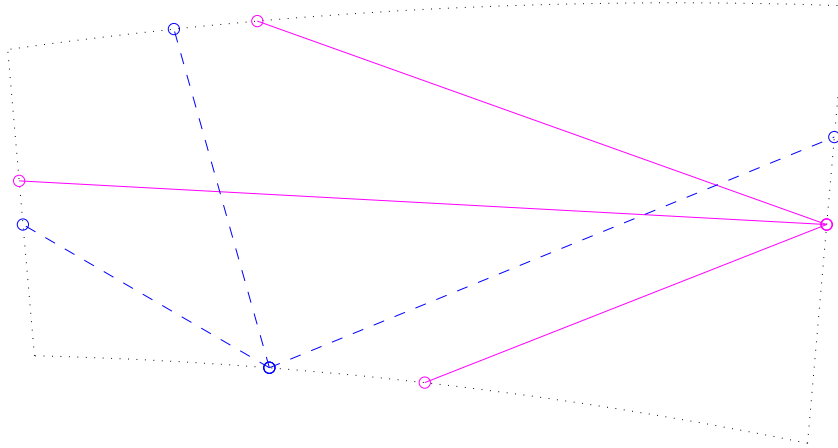


Figure 7.3: Example on propagation path steps starting from a latitude end face (solid lines), or the lower pressure surface (dashed lines), to all other grid cell faces. The distortion of the grid cell from cylinder segment is highly exaggerated compared to a real case. The relationship between vertical and horizontal size deviates also from normal real cases. Typical values for the vertical extension is around 500 m, while the horizontal length is normally  $>10$  km.

### 7.3.3 3D

#### Conversion between polar and Cartesian coordinates

The Cartesian coordinate system used follows the (standard?) Earth-centred earth-fixed (ECEF) system (<http://en.wikipedia.org/wiki/ECEF>), with the axes defined as:

**x-axis** is along latitude  $0^\circ$  and longitude  $0^\circ$

**y-axis** is along latitude  $0^\circ$  and longitude  $+90^\circ$

**z-axis** is along latitude  $+90^\circ$

This definition results in the following relationships between the spherical  $(r, \alpha, \beta)$  and Cartesian  $(x, y, z)$  coordinates

$$\begin{aligned} x &= r \cos(\alpha) \cos(\beta) \\ y &= r \cos(\alpha) \sin(\beta) \\ z &= r \sin(\alpha) \end{aligned} \tag{7.12}$$

and

$$\begin{aligned} r &= \sqrt{x^2 + y^2 + z^2} \\ \alpha &= \arcsin(z/r) \\ \beta &= \arctan(y/x) \quad (\text{implemented by the atan2 function}) \end{aligned} \tag{7.13}$$

The functions performing these transformations are `sph2cart` and `cart2sph`.

The first step to transform a line-of-sight, given by the zenith ( $\psi$ ) and the azimuth ( $\omega$ ) angle, to Cartesian coordinates is to determine the corresponding vector with unit length in the spherical coordinate system:

$$\begin{bmatrix} dr \\ d\alpha \\ d\beta \end{bmatrix} = \begin{bmatrix} \cos(\psi) \\ \sin(\psi) \cos(\omega)/r \\ \sin(\psi) \sin(\omega)/(r \cos(\alpha)) \end{bmatrix} \quad (7.14)$$

This vector is then translated to the Cartesian coordinate system as

$$\begin{bmatrix} dx \\ dy \\ dz \end{bmatrix} = \begin{bmatrix} \cos(\alpha) \cos(\beta) & -r \sin(\alpha) \cos(\beta) & -r \cos(\alpha) \sin(\beta) \\ \cos(\alpha) \sin(\beta) & -r \sin(\alpha) \sin(\beta) & r \cos(\alpha) \cos(\beta) \\ \sin(\alpha) & r \cos(\alpha) & 0 \end{bmatrix} \begin{bmatrix} dr \\ d\alpha \\ d\beta \end{bmatrix} \quad (7.15)$$

Note that the radial terms ( $r$ ) in Equations 7.14 and 7.15 cancel each other. These calculations are performed in `poslos2cart`. Special expressions must be used for positions at the north and south pole (see the code) as the azimuth angle has there a special definition (see Section 5.2.2 of *ARTS User Guide*).

The Cartesian position of a point along the geometrical path at a distance  $l$  is then simply

$$\begin{bmatrix} x_2 \\ y_2 \\ z_2 \end{bmatrix} = \begin{bmatrix} x_1 + l dx \\ y_1 + l dy \\ z_1 + l dz \end{bmatrix} \quad (7.16)$$

The Cartesian viewing vector  $[dx, dy, dz]^T$  is constant along a geometrical path. The new position is converted to spherical coordinates by Equation 7.13 and the new spherical viewing vector is calculated as

$$\begin{bmatrix} dr \\ d\alpha \\ d\beta \end{bmatrix} = \begin{bmatrix} \cos(\alpha) \cos(\beta) & \cos(\alpha) \sin(\beta) & \sin(\alpha) \\ -\sin(\alpha) \cos(\beta)/r & -\sin(\alpha) \sin(\beta)/r & \cos(\alpha)/r \\ -\sin(\beta)/(r \cos(\alpha)) & \cos(\beta)/(r \cos(\alpha)) & 0 \end{bmatrix} \begin{bmatrix} dx \\ dy \\ dz \end{bmatrix} \quad (7.17)$$

which is converted to a zenith and azimuth angle as

$$\begin{aligned} \psi &= \arccos(dr) \\ \omega &= \arccos(r d\alpha / \sin(\psi)), \quad \text{for } d\beta \geq 0 \\ \omega &= -\arccos(r d\alpha / \sin(\psi)), \quad \text{for } d\beta < 0 \end{aligned} \quad (7.18)$$

These calculations are performed in `cart2poslos`. Again special expressions must be used for positions at the north and south pole (see the code).

### Finding the crossing of a specified $r$ , $\alpha$ or $\beta$

The starting point in for all three cases is the following equation system:

$$\begin{aligned} r \cos(\alpha) \cos(\beta) &= x + l dx, \\ r \cos(\alpha) \sin(\beta) &= y + l dy, \\ r \sin(\alpha) &= z + l dz, \end{aligned} \quad (7.19)$$

where  $(x, y, z)$  is the position of the sensor,  $(dx, dy, dz)$  the sensor LOS, and either  $r$ ,  $\alpha$  or  $\beta$  is given.



The distance  $l$  to a given  $r$  is found by adding the square of all three equations:

$$r^2 = (x + ldx)^2 + (y + ldy)^2 + (z + ldz)^2. \quad (7.20)$$

Once  $l$  is determined, the latitude and longitude can easily be calculated by Equations 7.16 and 7.13. These calculations are implemented in the function `r_crossing_3d`.

If instead  $\alpha$  is given, the length to the point of interest can found by again squaring the three equations, but now summing the x- and y-terms and diving with the z-term:

$$\tan^2(\alpha) = \frac{(z + ldz)^2}{(x + ldx)^2 + (y + ldy)^2}. \quad (7.21)$$

The solution of this quadratic equation is implemented in the function `lat_crossing_3d`<sup>1</sup>. The solution for  $\alpha = 0^\circ$  is particularly simple ( $l = -z/dz$ ). The case of  $\alpha = 90^\circ$  is set to have no solution ( $\tan(90^\circ) = \infty$ ), and is instead assumed to be picked up as a crossing with one of the two longitudes defining the grid box. Another complication is that, as the  $\tan$ -term is squared, both  $\pm\alpha$  can show up as possible solutions, and it must be tested that the found length gives a  $\alpha$  with the correct sign.

For a given longitude, the x- and y-equations can be combined to give:

$$l = \frac{y - x \tan(\beta)}{dx \tan(\beta) - dy}. \quad (7.22)$$

This case is handled by `lon_crossing_3d`<sup>2</sup>. If the zenith or azimuth angle equals  $0^\circ$  or  $180^\circ$ , or if the start and target longitudes are equal, there is no valid solution.

### Finding the crossing with a pressure level

The same approach as for 2D is applied. The difference is that for 3D the additional dimension gives a more complex variation of the radius of the pressure level. For 2D, the variation can be expressed as a first order polynomial ( $r = r_0 + c\alpha$ ), while for 3D a second order polynomial must be used

$$r = r_0 + c_1\alpha + c_2\alpha^2. \quad (7.23)$$

The coefficients  $c_1$  and  $c_2$  are determined in a purely numerical way, by `p_level_slope_3d`. The change in radius,  $\Delta r_1$  and  $\Delta r_2$ , at a distance of  $\Delta\alpha$  and  $2\Delta\alpha$ , respectively, are determined. These values give

$$c_1 = \frac{4\Delta r_1 - \Delta r_2}{2\Delta\alpha} \quad (7.24)$$

and

$$c_2 = \frac{4\Delta r_1 - c_1\Delta\alpha}{(\Delta\alpha)^2}. \quad (7.25)$$

<sup>1</sup>This function is presently not used. The source code can be found in `p_path_NotUsed.cc`

<sup>2</sup>This function is presently not used. The source code can be found in `p_path_NotUsed.cc`

The polynomial to solve becomes (cf. Eq. 7.27)

$$\begin{aligned}
 0 &= p_0 + p_1\alpha + p_2\alpha^2 + p_3\alpha^3 + p_4\alpha^4 + p_5\alpha^5 + p_6\alpha^6, \\
 p_0 &= (r_0 - r_p) \sin(\Theta_p), \\
 p_1 &= r_0 \cos(\Theta_p) + c_1 \sin(\Theta_p), \\
 p_2 &= -r_0 \sin(\Theta_p)/2 + c_1 \cos(\Theta_p) + c_2 \sin(\Theta_p), \\
 p_3 &= -r_0 \cos(\Theta_p)/6 - c_1 \sin(\Theta_p)/2 + c_2 \cos(\Theta_p), \\
 p_4 &= r_0 \sin(\Theta_p)/24 - c_1 \cos(\Theta_p)/6 - c_2 \sin(\Theta_p)/2, \\
 p_5 &= r_0 \cos(\Theta_p)/120 + c_1 \sin(\Theta_p)/24 - c_2 \cos(\Theta_p)/6, \\
 p_6 &= -r_0 \sin(\Theta_p)/720 + c_1 \cos(\Theta_p)/120 + c_2 \sin(\Theta_p)/24.
 \end{aligned} \tag{7.26}$$

The solution of this polynomial is handled by `rslope_crossing3d`<sup>3</sup>.

### A robust 3D algorithm

Some of the expressions presented above, for finding the crossing of a specified  $r$ ,  $\alpha$  or  $\beta$ , were found to be sensitive to numerical inaccuracy and an algorithm that avoids those expressions have been devised. It applies a straightforward “length-search” algorithm (Algorithm 3 and Figure 7.4). The main advantage of the algorithm is that a correction for the shift in position caused by the transformations back and fourth to the Cartesian coordinate system can be applied. The correction term assures that the position is not changed for a step of zero length, and is not moved outside the grid cell due to the numerical problems. The algorithm was further found to be sufficiently fast to be accepted. A simple bisection search to find the length of the propagation path step is used. Both the position and the line-of-sight for the other end point of the path step are calculated using a transformation to Cartesian coordinates. This algorithm is implemented by the function `do_gridcell_3d_byltest`.

<sup>3</sup>This function is presently not used. The source code can be found in `p_path_NotUsed.cc`

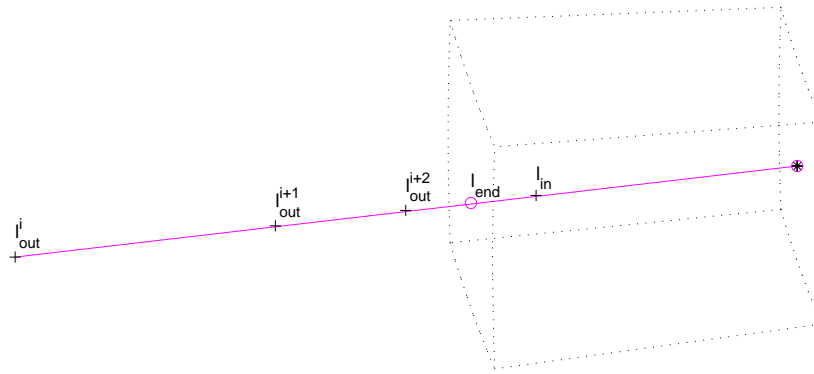


Figure 7.4: Schematic of Algorithm 3. The figure shows two iterations of the algorithm to search for the total length of the path step. The asterisk (\*) gives the start point for the calculations and the circles (o) are the final end points of the path step. The plus signs (+) shows the position of the different lengths tested during the iterations.

---

**Algorithm 3** The method applied in `do_gridcell_3d_byltest` to find the total length of the path step to be calculated. The symbol  $S$  signifies here conversion from Cartesian to spherical coordinates (Equation 7.13).

---

```

calculate the spherical position  $(x_0, y_0, z_0)$  and LOS vector  $(dx, dy, dz)$ 
calculate  $(r_c, \alpha_c, \beta_c) = S(x_0, y_0, z_0) - (r_0, \alpha_0, \beta_0)$ , the position correction term
set  $l_{in} = 0$ 
if  $l_s > 0$  then
     $l_{out} = l_s$  ( $l_s$  is a function input)
else
    set  $l_s$  to 3*vertical thickness of gid cell
end if
while  $S(x_0 + l_{out}dx, y_0 + l_{out}dy, z_0 + l_{out}dz) - (r_c, \alpha_c, \beta_c)$  is inside grid cell do
     $l_{out} \leftarrow 5 * l_{out}$ 
end while
set  $l_{end} = (l_{in} + l_{out})/2$ 
set accuracy flag to false
while accuracy flag is false do
    calculate  $(r, \alpha, \beta) = S(x_0 + l_{end}dx, y_0 + l_{end}dy, z_0 + l_{end}dz) - (r_c, \alpha_c, \beta_c)$ 
    if  $(r, \alpha, \beta)$  is inside grid cell then
         $l_{in} = l_{end}$ 
    else
         $l_{out} = l_{end}$ 
    end if
    if  $(l_{out} - l_{in})$  smaller than specified accuracy then
        set accuracy flag to true
    else
         $l_{end} = (l_{in} + l_{out})/2$ 
    end if
end while
 $(r, \alpha, \beta) \leftarrow (r, \alpha, \beta) + (r_c, \alpha_c, \beta_c)$ 
A recursive call can be needed, see the text.

```

---

The core task is to find the length of the path step. The search algorithm is safe with respect to all grid cell boundaries, except the lower pressure level where it can fail for zenith angles around 90°. In this case, the path can pass the lower pressure level and re-enter the grid cell after a short distance. For 1D cases, the part inside the lower cell would hold the tangent point, but for a non-spherical reference ellipsoid and “titled” pressure levels the tangent point can be found elsewhere.

The bisection algorithm can miss such excursions to the lower grid cell. Analytic approaches to handle this was rejected due to numerical problems. Instead, all final points of the path step are checked with respect to this issue and if any point is found to be below the lower pressure level, the function is called recursively with the distance to the problematic point as maximum search length ( $l_s$  in Algorithm 3).

## 7.4 Basic treatment of refraction

Refraction affects the radiative transfer in several ways. The distance through a layer of a fixed vertical thickness will be changed, and for a limb sounding observation the tangent point is moved both vertically and horizontally. If the atmosphere is assumed to be horizontally stratified (1D), a horizontal displacement is of no importance but for 2D and 3D calculations this effect must be considered. For limb sounding and a fixed zenith angle, the tangent point is moved downwards compared to the pure geometrical case (Figure 7.5), resulting in that inclusion of refraction in general gives higher intensities.

The refraction causes a bending of the path, which gives a deviation from the geometrical approximation of propagation along a straight line. The bending of the path is obtained by the relationship

$$\frac{dx}{dl} = \frac{1}{n} \left( \frac{\partial n}{\partial y} \right)_x \quad (7.27)$$

where  $x$  is the direction of propagation,  $l$  the distance along the path,  $n$  the refractive index<sup>4</sup>, and  $y$  is the coordinate perpendicular to the path. See further Section 9.4 in *Rodgers [2000]*.

The workspace method `ppath.stepRefractionBasic` takes refraction into consideration by probably the most simple (from the viewpoint of implementation) algorithm possible.

The approach taken in `ppath.stepRefractionBasic` is to take a geometrical ray tracing step from the present point of the path (and in the direction of present line-of-sight). Refraction is considered only when the line-of-sight at the new point is determined (Figure 7.6). The found line-of-sight is used to calculate the next ray tracing step etc. The main difference between handling 1D, 2D or 3D cases is how the line-of-sight for the new point is corrected to compensate for the bending due to refraction. The calculation of propagation paths including the effect of refraction is often denoted as ray tracing.

The length of the calculation steps is set by the generic input `lraytrace`. This length shall not be confused with the final distance between the points that define the path, which is controlled by `lmax`. The path is first determined in steps of `lraytrace`. The normal situation is that the ray tracing step length is considerably shorter than the final spacing between the path points. Suitable values for `lraytrace` have not yet been investigated in detail, but for limb sounding values in around 1–10 km should be appropriate. Shorter ray tracing steps (down to a level where rounding errors will start to have an impact) will

<sup>4</sup>The refractive index is here assumed to have no imaginary part

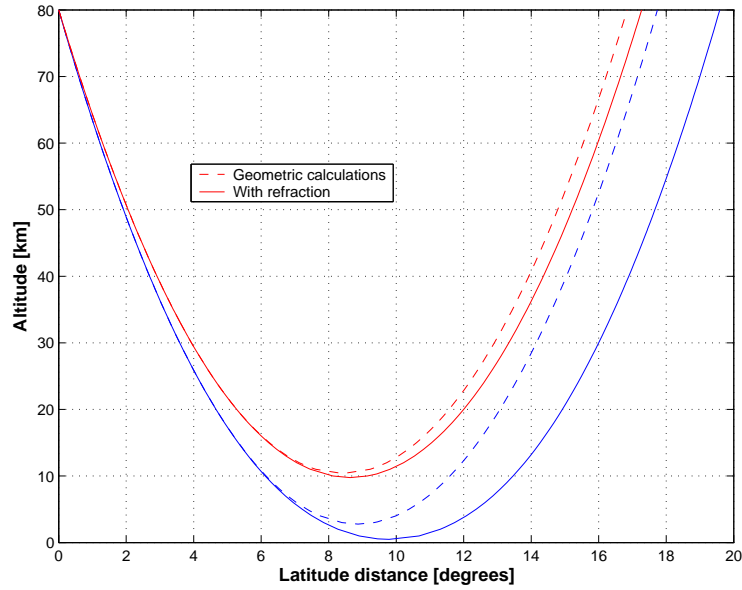


Figure 7.5: Comparison of propagation paths calculated geometrically and with refraction considered, for the same zenith angle of the sensor line-of-sight. The figure include two pair of paths, with refracted tangent altitude of about 0 and 10 km, respectively. The horizontal coordinate is the latitude distance from the point where the path exits the model atmosphere (at 80 km). The model atmosphere used had a spherical symmetry (that is, 1 D case, but the calculations were performed in 2D mode).

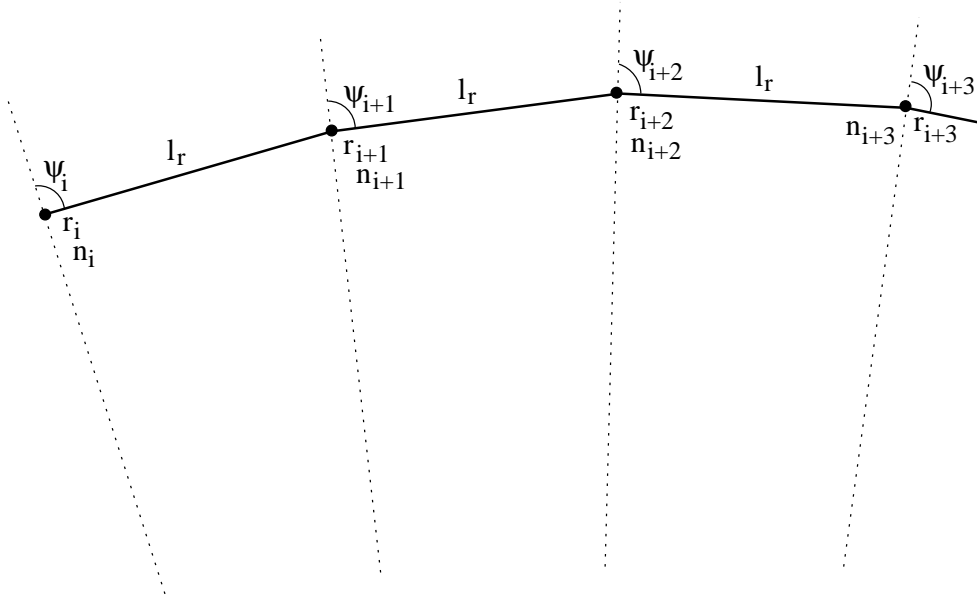


Figure 7.6: Schematic of the “basic” ray tracing scheme. The ray tracing step length is  $l_r$ .

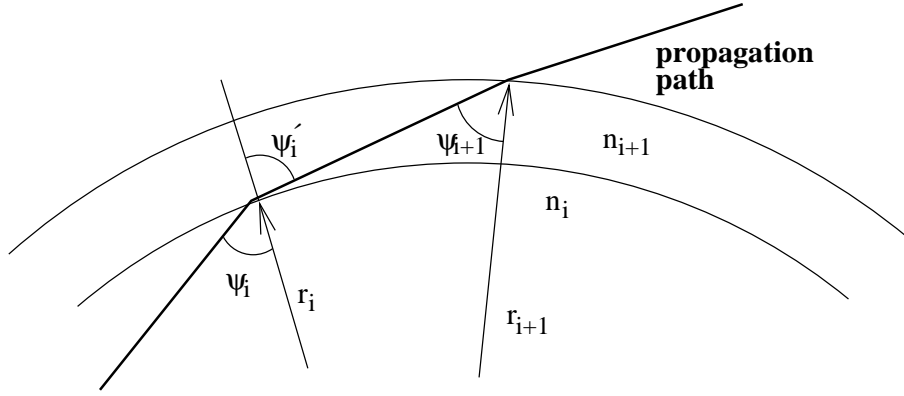


Figure 7.7: Geometry to derive Snell's law for a spherical atmosphere.

of course give a propagation path more accurately determined, but on the cost of more time consuming calculations.

#### 7.4.1 1D

When determining the propagation path through the atmosphere geometrical optics can be applied because the change of the refractive index over a wavelength can be neglected. Applying Snell's law to the geometry shown in Figure 7.7 gives

$$n_i \sin(\psi_i) = n_{i+1} \sin(\psi_{i'}) \quad (7.28)$$

Using the same figure, the law of sines gives the relationship

$$\frac{\sin(\psi_{i+1})}{r_i} = \frac{\sin(180^\circ - \psi_{i+1}')}{r_{i+1}} = \frac{\sin(\psi_{i'})}{r_{i+1}} \quad (7.29)$$

By combining the two equations above, the Snell's law for a spherical atmosphere (that is, 1D cases) is derived [e.g. *Kyle, 1991*; *Balluch and Lary, 1997*]:

$$p_c = r_i n_i \sin(\psi_i) = r_{i+1} n_{i+1} \sin(\psi_{i+1}) \quad (7.30)$$

where  $p_c$  is a constant. With other words, the Snell's law for spherical atmospheres states that the product of  $n$ ,  $r$  and  $\sin(\psi)$  is constant along the propagation path. It is noteworthy that with  $n = 1$ , Equations 7.1 and 7.30 are identical.

The Snell's law for a spherical atmosphere makes it very easy to determine the zenith angle of the path for a given radius. A rearrangement of Equation 7.30 gives

$$\psi = \arcsin(rn/p_c) \quad (7.31)$$

This relationship makes it possible to handle refraction for 1D without calculating any gradients of the refractive index, which is needed for 2D and 3D. These calculations are implemented in the function `raytrace.1d.linear.euler`. Figure 7.8 shows the vertical variation of the refractive index.

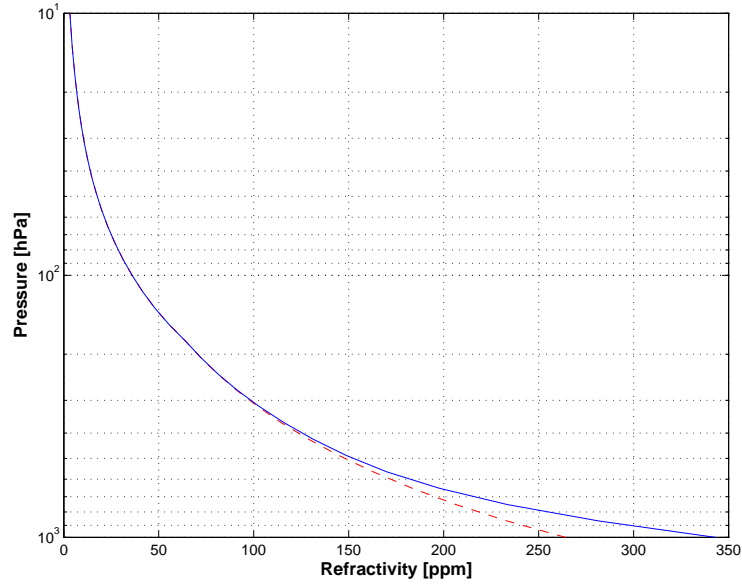


Figure 7.8: Vertical variation of refractivity  $(n-1) \cdot 10^6$ . Calculated for a mid-latitude summer climatology (FASCODE), where the dashed line is for a completely dry atmosphere, and the solid line includes also contribution from water vapour.

### 7.4.2 2D

Equation 7.27 expressed in polar coordinates is [Rodgers, 2000, Eq. 9.30]

$$\frac{d(\alpha + \psi)}{dl} = -\frac{\sin \psi}{n} \left( \frac{\partial n}{\partial r} \right)_\alpha + \frac{\cos \psi}{nr} \left( \frac{\partial n}{\partial \alpha} \right)_r \quad (7.32)$$

If the gradients are zero (corresponding to the geometrical case) we find that the sum of the zenith angle and the latitude is constant along a 2D geometrical path, which is also made clear by Equation 7.7. The geometrical zenith angle at ray tracing point  $i+1$  is accordingly  $\psi_{i+1} = \psi_i - (\alpha_{i+1} - \alpha_i)$ . If then also the refraction is considered, we get the following expression:

$$\psi_{i+1} = \psi_i - (\alpha_{i+1} - \alpha_i) + \frac{l_g}{n_i} \left[ -\sin \psi_i \left( \frac{\partial n}{\partial r} \right)_{\alpha_i} + \frac{\cos \psi_i}{r_i} \left( \frac{\partial n}{\partial \alpha} \right)_{r_i} \right] \quad (7.33)$$

These calculations are handled by `raytrace_2d_linear_euler`.

The gradients of the refractive index for 2D are calculated by the function `refr_gradients_2d`. The radial and latitudinal gradients of the refractive index are calculated in pure numerical way, by shifting the position slightly from the position of concern. Figures 7.9 and 7.10 show example on gradients of the refractive index. This function returns both gradients as the change of the refractive index over 1 m. The conversion for the latitude gradient, from  $\text{rad}^{-1}$  to  $\text{m}^{-1}$ , corresponds to the  $1/r$  term found in Equation 7.33, and this term is accordingly left out in `raytrace_2d_linear_euler`.

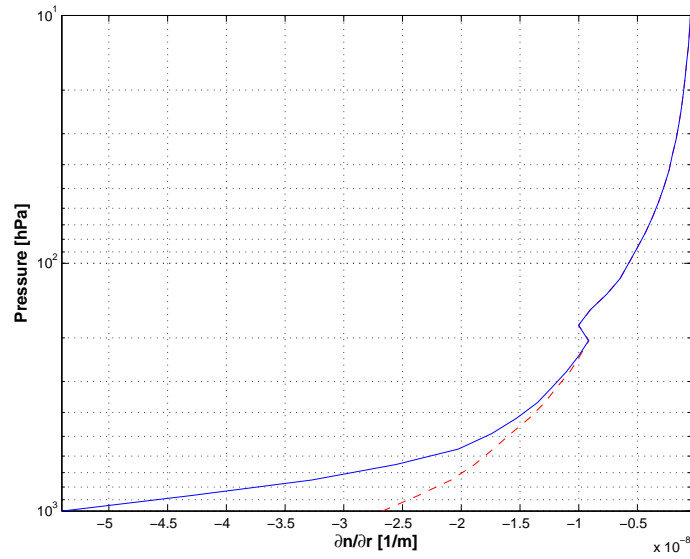


Figure 7.9: Vertical gradient of the refractive index. Calculated for a mid-latitude summer climatology (FASCODE), where the dashed line is for a completely dry atmosphere, and the solid line includes also contribution from water vapour.

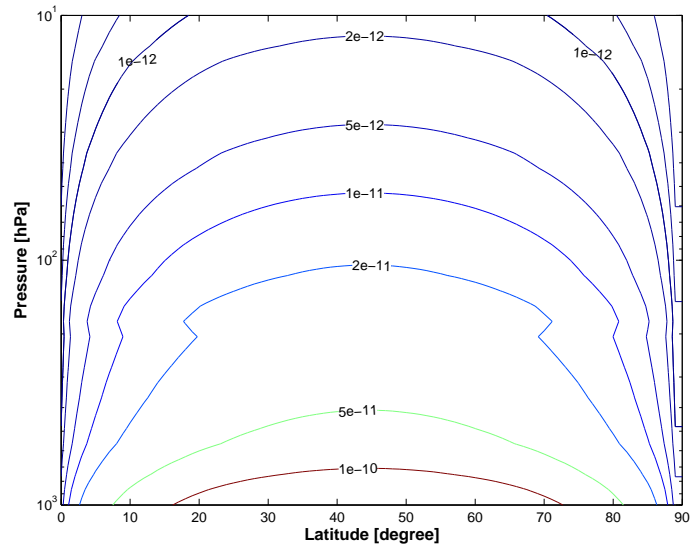


Figure 7.10: Latitude gradient of the refractive index due to varying radius of the geoid. The gradient is given as the change in refractive index over 1 m, which allows direct comparison with the values in Figure 7.9e. The wet atmosphere from Figure 7.9 was used for all latitudes, and the the plotted gradient is only caused by the fact that the radius of the geoid is not constant. The gradient is positive on the southern hemisphere (shown), and negative on the northern hemisphere.



### 7.4.3 3D

For 3D, the geometrical expressions are used to calculate the geometrical zenith and azimuth angles at the end of the ray tracing step. Following the methodology for 2D, the geometrical zenith and azimuth angles are then corrected to incorporate the influence of refraction. The zenith angle is calculated as

$$\begin{aligned} \psi_{i+1} = & \psi_g - \frac{l_g \sin \psi_i}{n_i} \left( \frac{\partial n}{\partial r} \right)_{(\alpha_i, \beta_i)} + \\ & + \frac{l_g \cos \psi_i}{r_i n_i} \left[ \cos \omega_i \left( \frac{\partial n}{\partial \alpha} \right)_{(r_i, \beta_i)} + \frac{\sin \omega_i}{\cos \alpha_i} \left( \frac{\partial n}{\partial \beta} \right)_{(r_i, \alpha_i)} \right] \end{aligned} \quad (7.34)$$

where  $\psi_g$  is the zenith angle obtained from the geometrical expressions. In similar manner, the geometrical azimuth angle,  $\omega_g$ , is corrected as

$$\omega_{i+1} = \omega_g + \frac{l_g \sin \psi_i}{r_i n_i} \left[ -\sin \omega_i \left( \frac{\partial n}{\partial \alpha} \right)_{(r_i, \beta_i)} + \frac{\cos \omega_i}{\cos \alpha_i} \left( \frac{\partial n}{\partial \beta} \right)_{(r_i, \alpha_i)} \right] \quad (7.35)$$

This expression, slightly modified, is found in `raytrace_3d_linear_euler`. The terms of Equation 7.35 missing in that function, are part of `refr_gradients_3d` to convert the gradients to the same unit. The longitude gradient is converted to the unit [1/m] by multiplication with the term  $1/(r \cos \alpha)$ .



## Chapter 8

# Particle size distributions

### 8.1 Handling of different size descriptors

Various quantities can be selected as size ( $x$ ), such as mass, maximum diameter and volume equivalent diameter. If size is selected to be some geometrical diameter,  $D_g$ , the mass of particles is normally assumed to follow a power-law (e.g. *Petty and Huang* [2011], Eq. 29):

$$m = aD_g^b.$$

However, this approach can in fact also be applied on all other standard size descriptors (including ones based on area). That is, the following expressions is applied generally:

$$m = ax^b. \tag{8.1}$$

For example, if  $x$  represents mass, both  $a$  and  $b$  are simply 1. If  $x$  is volume equivalent diameter (and the density is constant with size),  $b = 3$ . By this approach it can be avoided to have different equations for different size descriptors. For example,  $a$  and  $b$  are included generally in the expressions below for modified gamma distributions, and one set of equations suffices.

The workspace variables corresponding to  $a$  and  $b$  are `scat_species_a` and `scat_species_b`, respectively. These variables can be calculated with the `ScatSpeciesSizeMassInfo` workspace method.

### 8.2 Modified gamma particle size distributions

This section lists the expressions needed to handle particle size distributions (PSDs) of type modified gamma distribution (MGD). Expressions are needed for various derivatives, as well as for mapping from bulk properties to the native parameters of MGD. The general properties of MGD PSDs are discussed in detail in *Petty and Huang* [2011], below shortened to P&H11. However, derivatives are not discussed by P&H11 and to document those expressions is the main purpose of the section.

---

#### History

- 171101 Restarted the chapter, to instead deal with PSDs (Patrick).
- 161107 Created by Jana Mendrok. Moved parts from AUG clouds chapter here.

### 8.2.1 Native form

The MGD function has four parameters ( $N_0$ ,  $\mu$ ,  $\Lambda$  and  $\gamma$ ) and is here written as (P&H, Eq. 6):

$$n(N_0, \mu, \Lambda, \gamma) = N_0 x^\mu \exp(-\Lambda x^\gamma), \quad (8.2)$$

where  $x$  is “size” (Sec. 8.1). The derivatives of  $n$  with respect to the basic parameters are:

$$\frac{dn}{dN_0} = x^\mu \exp(-\Lambda x^\gamma) \quad (8.3)$$

$$\frac{dn}{d\mu} = N_0 \ln(x) x^\mu \exp(-\Lambda x^\gamma) = \ln(x) n \quad (8.4)$$

$$\frac{dn}{d\Lambda} = N_0 x^\mu (-x^\gamma) \exp(-\Lambda x^\gamma) = -x^\gamma n \quad (8.5)$$

$$\frac{dn}{d\gamma} = N_0 x^\mu (-\Lambda) \ln(x) x^\gamma \exp(-\Lambda x^\gamma) = -\Lambda \ln(x) x^\gamma n \quad (8.6)$$

The workspace method for the native form of MGD is `psdModifiedGamma`.

### 8.2.2 Moments and gamma function

It is common to express various properties of PSDs as “moments”. The  $k$ -th moment,  $M_k$  is defined as

$$M_k = \int_0^\infty x^k n(x) dx. \quad (8.7)$$

For MGD, the moments can be expressed analytically (P&H, Eq. 17):

$$M_k = \frac{N_0}{\gamma} \frac{\Gamma(\frac{\mu+k+1}{\gamma})}{\Lambda^{(\mu+k+1)/\gamma}}, \quad (8.8)$$

where  $\Gamma$  is the gamma function. One property of the gamma function used below is that for  $n \geq 0$ :

$$\frac{\Gamma(n+1)}{\Gamma(n)} = n. \quad (8.9)$$

### 8.2.3 Mass content

The mass content,  $w$  (i.e. kg/m<sup>3</sup>), for given  $N_0$ ,  $\mu$ ,  $\Lambda$ ,  $\gamma$ ,  $a$  and  $b$ , is the size-integrated mass (P&H, Eq. 22), that is proportional to the  $b$ -th moment:

$$w = \int_0^\infty m(x) n(x) dx = \int_0^\infty a x^b n(x) dx = a M_b. \quad (8.10)$$

If mass content is taken as an input to the PSD, one of the four MGD parameters must be selected as the dependent one. If  $N_0$  is selected as the dependent variable, i.e.  $n(w, \mu, \Lambda, \gamma)$ , the implied value of  $N_0$  is:

$$N_0 = \frac{w \gamma \Lambda^{(\mu+b+1)/\gamma}}{a \Gamma(\frac{\mu+b+1}{\gamma})}. \quad (8.11)$$

To simplify the expressions below, we define  $e$  as

$$e = \frac{\mu + b + 1}{\gamma}. \quad (8.12)$$

That is

$$w = \frac{aN_0}{\gamma} \frac{\Gamma(e)}{\Lambda^e}, \quad (8.13)$$

and

$$N_0 = \frac{w\gamma\Lambda^e}{a\Gamma(e)}. \quad (8.14)$$

The derivative of the PSD with respect to mass content is most easily handled by the chain rule:

$$\frac{dn}{dw} = \frac{dn}{dN_0} \frac{dN_0}{dw} = \frac{dn}{dN_0} \frac{\gamma\Lambda^e}{a\Gamma(e)}. \quad (8.15)$$

The code in ARTS is organised in such way that the derivatives to the native parameters are calculated as soon as they can be used (such as  $dn/dN_0$  in the equation just above). Accordingly, further simplifications of expressions involving terms from the chain-rule are not of practical interest.

Regarding the derivatives for remaining three native parameters, they are unchanged from the expressions given on Section 8.2.1. For example, Eqs. 8.4 and 8.6 give the derivative with respect to  $\mu$  and  $\gamma$  independently of if  $N_0$  or  $\Lambda$  is selected as dependent variable. The same is valid below, as long as  $\mu$  and  $\gamma$  are not dependent variables.

If instead  $\Lambda$  is the dependent parameter,  $n(w, N_0, \Lambda, \gamma)$ , these expressions apply:

$$\Lambda = \left( \frac{w\gamma}{aN_0\Gamma(e)} \right)^{-1/e} \quad (8.16)$$

and

$$\frac{dn}{dw} = \frac{dn}{d\Lambda} \frac{d\Lambda}{dw} = \frac{dn}{d\Lambda} \frac{(-1)}{e} w^{-(1/e+1)} \left( \frac{\gamma}{aN_0\Gamma(e)} \right)^{-1/e}. \quad (8.17)$$

The choices of having  $\mu$  and  $\gamma$  as dependent variables are not yet handled.

The workspace method for this form of MGD is `psdModifiedGammaMass`.

#### 8.2.4 Mass content and mean size

This section deals with the case when mass content and mean size replaces two of the native MGD parameters. There are six possible combinations of dependent parameters, but so far just a single one is handled, that  $N_0$  and  $\Lambda$  are the dependent ones.

Many definitions of mean and effective size exist. The definition of mean size,  $x_{\text{mean}}$ , selected here is:

$$x_{\text{mean}} = \frac{\int_0^\infty xm(x)n(x) dx}{\int_0^\infty m(x)n(x) dx}. \quad (8.18)$$

That is, a mass-weighted mean size is considered. This definition is fully consistent with e.g. Eq. 3 of *Delanoë et al.* [2014], just expressed in a more general manner. The equation above can be rewritten in several ways:

$$x_{\text{mean}} = \frac{\int_0^\infty x m(x) n(x) dx}{w} = \frac{M_{b+1}}{M_b} = \frac{\Gamma(e + 1/\gamma)}{\Gamma(e)} \Lambda^{-1/\gamma}. \quad (8.19)$$

As mentioned, so far only  $N_0$  and  $\Lambda$  are allowed to be the pair of dependent variables:  $n(w, x_{\text{mean}}, \mu, \gamma)$ . The implied value of  $\Lambda$  can be obtained by Eq. 8.19:

$$\Lambda = \left( \frac{x_{\text{mean}} \Gamma(e)}{\Gamma(e + 1/\gamma)} \right)^{-\gamma}. \quad (8.20)$$

With  $\Lambda$  at hand,  $N_0$  can be determined as for the mass-only case (Eq. 8.14).

As mass content only affects  $N_0$ , Eq. 8.15 is also valid here. The partial derivative with respect to  $x_{\text{mean}}$  is more complicated as both  $N_0$  and  $\Lambda$  are affected:

$$\begin{aligned} \frac{dn}{dx_{\text{mean}}} &= \left( \frac{dn}{dN_0} \frac{dN_0}{d\Lambda} + \frac{dn}{d\Lambda} \right) \frac{d\Lambda}{dx_{\text{mean}}} \\ &= \left( \frac{dn}{dN_0} \frac{w\gamma e \Lambda^{e-1}}{a\Gamma(e)} + \frac{dn}{d\Lambda} \right) \left( -\gamma \left( \frac{\Gamma(e)}{\Gamma(e + 1/\gamma)} \right)^{-\gamma} x_{\text{mean}}^{-(\gamma+1)} \right). \end{aligned} \quad (8.21)$$

The workspace method for this form of MGD is `psdModifiedGammaMassXmean`.

### 8.2.5 Mass content and median size

The median size,  $x_{\text{med}}$ , is defined as (P&H, Eq. 21)

$$\int_0^{x_{\text{med}}} m(x) n(x) dx = \int_{x_{\text{med}}}^\infty m(x) n(x) dx = \frac{W}{2}. \quad (8.22)$$

There is no exact analytic expression for  $x_{\text{med}}$  but an approximate one is (Eq. 33)

$$x_{\text{med}} = \left( \frac{\mu + 1 + b - 0.327\gamma}{\Lambda\gamma} \right)^{1/\gamma} \quad (8.23)$$

As for mean size, so far only  $N_0$  and  $\Lambda$  are allowed to be the pair of dependent variables:  $n(w, x_{\text{med}}, \mu, \gamma)$ . The implied value of  $\Lambda$  can be obtained by Eq. 8.23:

$$\Lambda = \frac{\mu + 1 + b - 0.327\gamma}{\gamma} x_{\text{med}}^{-\gamma}. \quad (8.24)$$

With  $\Lambda$  at hand,  $N_0$  can be determined as for the mass-only case (Eq. 8.14).

As mass content only affects  $N_0$ , Eq. 8.15 is also valid here. The partial derivative with respect to  $x_{\text{med}}$  is more complicated as both  $N_0$  and  $\Lambda$  are affected:

$$\begin{aligned} \frac{dn}{dx_{\text{med}}} &= \left( \frac{dn}{dN_0} \frac{dN_0}{d\Lambda} + \frac{dn}{d\Lambda} \right) \frac{d\Lambda}{dx_{\text{med}}} \\ &= \left( \frac{dn}{dN_0} \frac{w\gamma e \Lambda^{e-1}}{a\Gamma(e)} + \frac{dn}{d\Lambda} \right) (-1)(\mu + 1 + b - 0.327\gamma) x_{\text{med}}^{-(\gamma+1)} \end{aligned} \quad (8.25)$$

The workspace method for this form of MGD is `psdModifiedGammaMassXmedian`.

### 8.2.6 Mass content and mean particle mass

The mean particle mass is defined as

$$m_{\text{mean}} = \frac{w}{N_{\text{tot}}} \quad (8.26)$$

where  $N_{\text{tot}}$  is the total number density, that equals the 0:th moment:

$$N_{\text{tot}} = M_0. \quad (8.27)$$

That is

$$m_{\text{mean}} = \frac{aM_b}{M_0} = \frac{a}{\Lambda^{b/\gamma}} \frac{\Gamma(e)}{\Gamma(r)}, \quad (8.28)$$

where  $r$  is defined as

$$r = \frac{\mu + 1}{\gamma}. \quad (8.29)$$

As for mean and median size, so far only  $N_0$  and  $\Lambda$  are allowed to be the pair of dependent variables:  $n(w, m_{\text{mean}}, \mu, \gamma)$ . From Eq. 8.28 we get

$$\Lambda = \left( \frac{a}{m_{\text{mean}}} \frac{\Gamma(e)}{\Gamma(r)} \right)^{\gamma/b}. \quad (8.30)$$

With  $\Lambda$  at hand,  $N_0$  can be determined as for the mass-only case (Eq. 8.14).

As mass content only affects  $N_0$ , Eq. 8.15 is also valid here. The derivative with respect to mean particle mass is

$$\begin{aligned} \frac{dn}{dm_{\text{mean}}} &= \left( \frac{dn}{dN_0} \frac{dN_0}{d\Lambda} + \frac{dn}{d\Lambda} \right) \frac{d\Lambda}{dm_{\text{mean}}} \\ &= \left( \frac{dn}{dN_0} \frac{w\gamma e\Lambda^{e-1}}{a\Gamma(e)} + \frac{dn}{d\Lambda} \right) \left( a \frac{\Gamma(e)}{\Gamma(r)} \right)^{\gamma/b} \frac{(-\gamma)}{b} m_{\text{mean}}^{-(\gamma/b+1)}. \end{aligned} \quad (8.31)$$

The workspace method for this form of MGD is `psdModifiedGammaMassMeanParticleMass`.

### 8.2.7 Mass content and total number density

The total number density is defined above by Eq. 8.27. As for the combinations of mass and size above, so far only  $N_0$  and  $\Lambda$  are allowed to be the pair of dependent variables:  $n(w, N_{\text{tot}}, \mu, \gamma)$ . From Eqs. 8.28 and 8.30 we get

$$\Lambda = \left( \frac{aN_{\text{tot}}}{w} \frac{\Gamma(e)}{\Gamma(r)} \right)^{\gamma/b}. \quad (8.32)$$

With  $\Lambda$  at hand,  $N_0$  can be determined as for the mass-only case (Eq. 8.14).

As mass content is here affecting both  $N_0$  and  $\Lambda$ , Eq. 8.15 is not valid here. We have instead:

$$\begin{aligned} \frac{dn}{dw} &= \frac{dn}{dN_0} \left( \frac{dN_0}{dw} + \frac{dN_0}{d\Lambda} \frac{d\Lambda}{dw} \right) + \frac{dn}{d\Lambda} \frac{d\Lambda}{dw} \\ &= \frac{dn}{dN_0} \left( \frac{\gamma\Lambda^e}{a\Gamma(e)} + \frac{w\gamma e\Lambda^{e-1}}{a\Gamma(e)} \frac{d\Lambda}{dw} \right) + \frac{dn}{d\Lambda} \frac{d\Lambda}{dw}, \end{aligned} \quad (8.33)$$

where

$$\frac{d\Lambda}{dw} = \left( a N_{\text{tot}} \frac{\Gamma(e)}{\Gamma(r)} \right)^{\gamma/b} \frac{(-\gamma)}{b} w^{-(\gamma/b+1)}. \quad (8.34)$$

The derivative with respect to  $N_{\text{tot}}$  is:

$$\begin{aligned} \frac{dn}{dN_{\text{tot}}} &= \left( \frac{dn}{dN_0} \frac{dN_0}{d\Lambda} + \frac{dn}{d\Lambda} \right) \frac{d\Lambda}{dN_{\text{tot}}} \\ &= \left( \frac{dn}{dN_0} \frac{w\gamma e\Lambda^{e-1}}{a\Gamma(e)} + \frac{dn}{d\Lambda} \right) \left( \frac{a}{w} \frac{\Gamma(e)}{\Gamma(r)} \right)^{\gamma/b} \frac{\gamma}{b} N_{\text{tot}}^{\gamma/b-1}. \end{aligned} \quad (8.35)$$

The workspace method for this form of MGD is `psdModifiedGammaMassNtot`.

### 8.2.8 Avoiding numerical problems

For simplicity, all MGD methods demand that both  $\Lambda$  and  $\gamma$  are  $> 0$ . First of all, this ensures that  $\Lambda x^\gamma > 0$  as long as  $x > 0$ . It further avoids a number of possible “division with zero” cases, such as Eq. 8.8. It also demanded that  $a$  and  $b$  are  $> 0$ .

The gamma function is infinite at 0, and it also further demanded that argument given to the gamma function is  $> 0$ . When Eq. 8.12 is of concern, then  $\mu + b + 1 > 0$  is demanded. If Eq. 8.29 is of concern, the demand is harder:  $\mu + 1 > 0$ .

Negative mass is unphysical but it could still be beneficial to allow such values, to simplify performing. For this reason, negative mass contents are allowed as far as possible. It is possible as long as mass content sets  $N_0$  (then giving negative  $N_0$ ), but not when the mass content sets  $\Lambda$  (Eq. 8.16). On the other hand, all input mean or median sizes are required to be  $> 0$ , both for physical and numerical reasons.



## Chapter 9

# Scattering: The DOIT solver

The Discrete Ordinate Iterative (DOIT) method is one of the scattering algorithms in ARTS. The DOIT method is unique because a discrete ordinate iterative method is used to solve the scattering problem in a spherical atmosphere. Although the DOIT module is implemented for 1D and 3D atmospheres, it is strongly recommended to use it only for 1D, because the Monte Carlo module (Chapter 10) is much more appropriate for 3D calculations. More appropriate in the sense that it is much more efficient. A literature review about scattering models for the microwave region, which is presented in *Emde and Sreerekha [2004]*, shows that former implementations of discrete ordinate schemes are only applicable for (1D-)plane-parallel or 3D-cartesian atmospheres. All of these algorithms can not be used for the simulation of limb radiances. A description of the DOIT method, similar to what is presented in this chapter, has been published in *Emde et al. [2004]* and in *Emde [2005]*.

### 9.1 Radiation field

The Stokes vector depends on the position in the cloud box and on the propagation direction specified by the zenith angle ( $\psi$ ) and the azimuth angle ( $\omega$ ). All these dimensions are discretized inside the model; five numerical grids are required to represent the radiation field  $\mathcal{I}$ :

$$\begin{aligned}\vec{P} &= \{P_1, P_2, \dots, P_{N_P}\}, \\ \vec{\alpha} &= \{\alpha_1, \alpha_2, \dots, \alpha_{N_\alpha}\}, \\ \vec{\beta} &= \{\beta_1, \beta_2, \dots, \beta_{N_\beta}\}, \\ \vec{\psi} &= \{\psi_1, \psi_2, \dots, \psi_{N_\psi}\}, \\ \vec{\omega} &= \{\omega_1, \omega_2, \dots, \omega_{N_\omega}\}.\end{aligned}\tag{9.1}$$

Here  $\vec{P}$  is the pressure grid,  $\vec{\alpha}$  is the latitude grid and  $\vec{\beta}$  is the longitude grid. The radiation field is a set of Stokes vectors ( $N_P \times N_\alpha \times N_\beta \times N_\psi \times N_\omega$  elements) for all combinations

---

#### History

- 020601 Created and written by Claudia Emde
- 050223 Rewritten by Claudia Emde, mostly taken from Chapter 4 of Claudia Emde's PhD thesis
- 091014 Moved from user guide to theory document.

of positions and directions:

$$\begin{aligned} \mathcal{I} = \{ & \mathbf{s}_1(P_1, \alpha_1, \beta_1, \psi_1, \omega_1), \mathbf{s}_2(P_2, \alpha_1, \beta_1, \psi_1, \omega_1), \dots, \\ & \mathbf{s}_{N_P \times N_\alpha \times N_\beta \times N_\psi \times N_\omega}(P_{N_P}, \alpha_{N_\alpha}, \beta_{N_\beta}, \psi_{N_\psi}, \omega_{N_\omega}) \}. \end{aligned} \quad (9.2)$$

In the following we will use the notation

$$\begin{aligned} i &= 1 \dots N_P \\ j &= 1 \dots N_\alpha \\ \mathcal{I} = \{ & \mathbf{s}_{ijklm} \} & k &= 1 \dots N_\beta. \\ & & l &= 1 \dots N_\psi \\ & & m &= 1 \dots N_\omega \end{aligned} \quad (9.3)$$

## 9.2 Vector radiative transfer equation solution

Figure 9.1 shows a schematic of the iterative method, which is applied to solve the vector radiative transfer equation (compare Equation 6.36)

$$\frac{d\mathbf{s}(\hat{\mathbf{n}}, \nu, T)}{ds} = -\langle \mathbf{K}(\hat{\mathbf{n}}, \nu, T) \rangle \mathbf{s}(\hat{\mathbf{n}}, \nu, T) + \langle \mathbf{a}(\hat{\mathbf{n}}, \nu, T) \rangle B(\nu, T) \quad (9.4)$$

$$+ \int_{4\pi} d\hat{\mathbf{n}}' \langle \mathbf{Z}(\hat{\mathbf{n}}, \hat{\mathbf{n}}', \nu, T) \rangle \mathbf{s}(\hat{\mathbf{n}}', \nu, T), \quad (9.5)$$

where  $\mathbf{s}$  is the specific intensity vector,  $\langle \mathbf{K} \rangle$  is the ensemble-averaged extinction matrix,  $\langle \mathbf{a} \rangle$  is the ensemble-averaged absorption vector,  $B$  is the Planck function and  $\langle \mathbf{Z} \rangle$  is the ensemble-averaged phase matrix. Furthermore  $\nu$  is the frequency of the radiation,  $T$  is the temperature,  $ds$  is a path-length-element of the propagation path and  $\hat{\mathbf{n}}$  the propagation direction. The vector radiative transfer equation is explained in more detail in Section 6.4.

The *first guess field*

$$\mathcal{I}^{(0)} = \left\{ \mathbf{s}_{ijklm}^{(0)} \right\}, \quad (9.6)$$

is partly determined by the boundary condition given by the radiation coming from the clear sky part of the atmosphere traveling into the cloud box. Inside the cloud box an arbitrary field can be chosen as a first guess. In order to minimize the number of iterations it should be as close as possible to the solution field.

The next step is to solve the scattering integrals

$$\left\langle \mathbf{S}_{ijklm}^{(0)} \right\rangle = \int_{4\pi} d\hat{\mathbf{n}}' \langle \mathbf{Z}_{ijklm} \rangle \mathbf{s}_{ijklm}^{(0)}, \quad (9.7)$$

using the first guess field, which is now stored in a variable reserved for the *old radiation field*. For the integration we use equidistant angular grids in order to save computation time (cf. Section 9.6.1). The radiation field, which is generally defined on finer angular grids  $(\vec{\omega}, \vec{\psi})$ , is interpolated on the equidistant angular grids. The integration is performed over all incident directions  $\hat{\mathbf{n}}'$  for each propagation direction  $\hat{\mathbf{n}}$ . The evaluation of the scattering integral is done for all grid points inside the cloud box. The obtained integrals are interpolated on  $\vec{\omega}$  and  $\vec{\psi}$ . The result is the first guess *scattering integral field*  $\mathcal{S}^0$ :

$$\mathcal{S}^{(0)} = \left\{ \left\langle \mathbf{s}_{ijklm}^{(0)} \right\rangle \right\}. \quad (9.8)$$

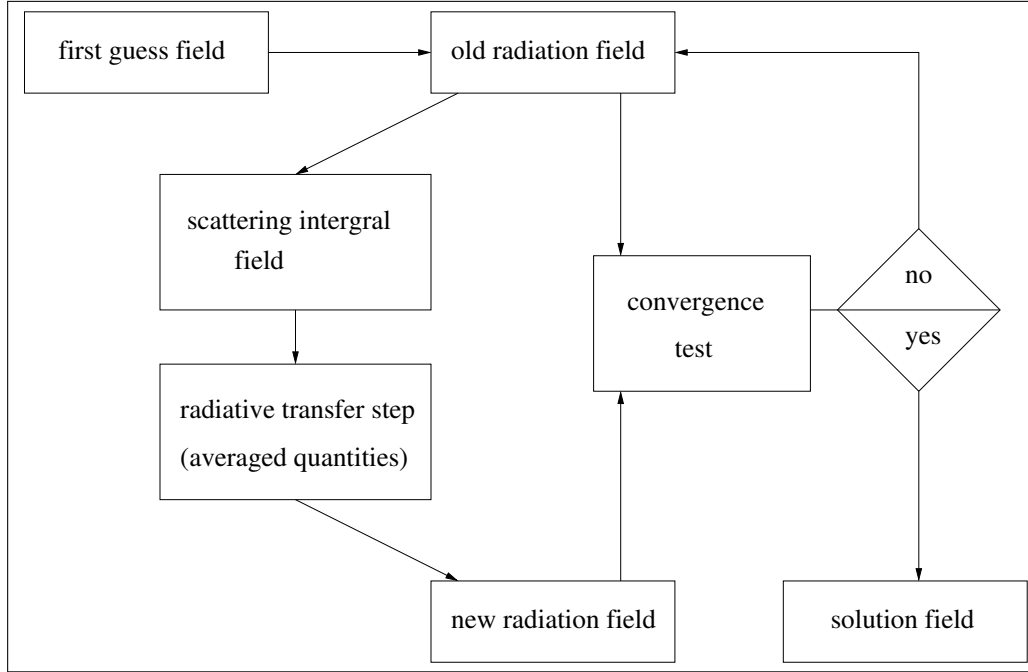


Figure 9.1: Schematic of the iterative method to solve the VRTE in the cloud box.

Figure 9.2 shows a propagation path step from a grid point  $\mathbf{P} = (P_i, \alpha_j, \beta_k)$  into direction  $\hat{\mathbf{n}} = (\psi_l, \omega_m)$ . The radiation arriving at  $\mathbf{P}$  from the direction  $\hat{\mathbf{n}}'$  is obtained by solving the linear differential equation:

$$\frac{d\mathbf{s}^{(1)}}{ds} = -\overline{\langle \mathbf{K} \rangle} \mathbf{s}^{(1)} + \overline{\langle \mathbf{a} \rangle} \bar{B} + \overline{\langle \mathbf{s}^{(0)} \rangle}, \quad (9.9)$$

where  $\overline{\langle \mathbf{K} \rangle}$ ,  $\overline{\langle \mathbf{a} \rangle}$ ,  $\bar{B}$  and  $\overline{\langle \mathbf{s}^{(0)} \rangle}$  are *averaged quantities*. This equation can be solved analytically for constant coefficients. Multi-linear interpolation gives the quantities  $\mathbf{K}'$ ,  $\mathbf{a}'$ ,  $\mathbf{s}'$  and  $T'$  at the intersection point  $\mathbf{P}'$ . To calculate the radiative transfer from  $\mathbf{P}'$  towards  $\mathbf{P}$  all quantities are approximated by taking the averages between the values at  $\mathbf{P}'$  and  $\mathbf{P}$ . The average value of the temperature is used to get the averaged Planck function  $\bar{B}$ .

The solution of Equation 9.9 is found analytically using a matrix exponential approach:

$$\mathbf{s}^{(1)} = e^{-\overline{\langle \mathbf{K} \rangle} s} \mathbf{s}^{(0)} + \left( \mathbf{1} - e^{-\overline{\langle \mathbf{K} \rangle} s} \right) \overline{\langle \mathbf{K} \rangle}^{-1} \left( \overline{\langle \mathbf{a} \rangle} \bar{B} + \overline{\langle \mathbf{s}^{(0)} \rangle} \right), \quad (9.10)$$

where  $\mathbf{1}$  denotes the identity matrix and  $\mathbf{s}^{(0)}$  the initial Stokes vector. The *radiative transfer step* from  $\mathbf{P}'$  to  $\mathbf{P}$  is calculated, therefore  $\mathbf{s}^{(0)}$  is the incoming radiation at  $\mathbf{P}'$  into direction  $(\psi'_l, \omega'_m)$ , which is the first guess field interpolated on  $\mathbf{P}'$ . This radiative transfer step calculation is done for all points inside the cloud box in all directions. The resulting set of Stokes vectors ( $\mathbf{s}^{(1)}$  for all points in all directions) is the first order iteration field  $\mathcal{I}^{(1)}$ :

$$\mathcal{I}^{(1)} = \left\{ \mathbf{s}_{ijklm}^{(1)} \right\}. \quad (9.11)$$

The first order iteration field is stored in a variable reserved for the *new radiation field*.

In the *convergence test* the *new radiation field* is compared to the *old radiation field*. For the difference field, the absolute values of all Stokes vector elements for all cloud box

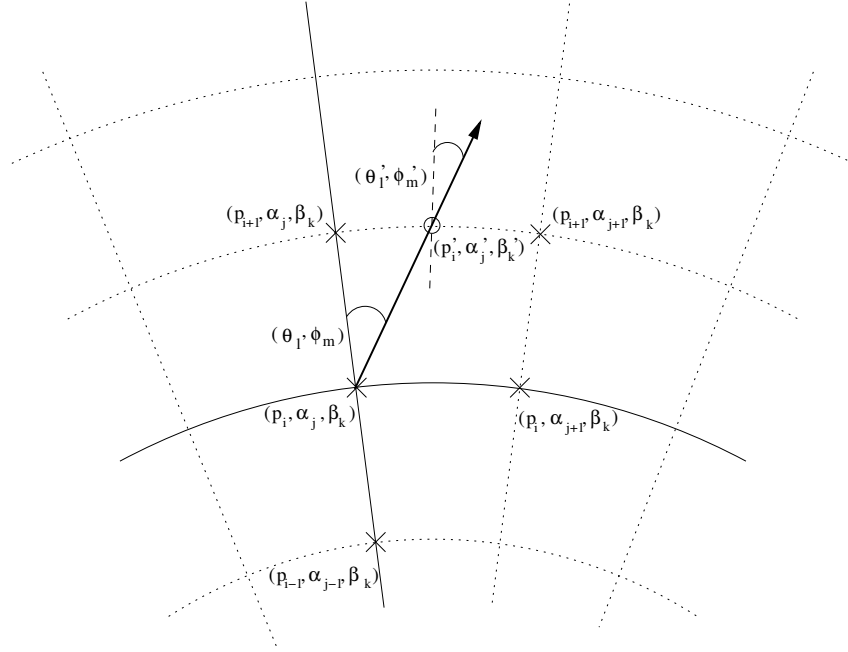


Figure 9.2: Path from a grid point  $((P_i, \alpha_j, \beta_k) - (\times))$  to the intersection point  $((P'_i, \alpha'_j, \beta'_k) - (\circ))$  with the next grid cell boundary. Viewing direction is specified by  $(\psi_l, \omega_m)$  at  $(\times)$  or  $(\psi'_l, \omega'_m)$  at  $(\circ)$ .

positions are calculated. If one of the differences is larger than a requested accuracy limit, the convergence test is not fulfilled. The user can define different convergence limits for the different Stokes components.

If the convergence test is not fulfilled, the first order iteration field is copied to the variable holding the *old radiation field*, and is then used to evaluate again the scattering integral at all cloud box points:

$$\langle \mathbf{s}_{ijklm}^{(1)} \rangle = \int_{4\pi} d\hat{\mathbf{n}}' \langle \mathbf{Z} \rangle \mathbf{s}_{ijklm}^{(1)}. \quad (9.12)$$

The second order iteration field

$$\mathcal{I}^{(2)} = \{ \mathbf{s}_{ijklm}^{(2)} \}, \quad (9.13)$$

is obtained by solving

$$\frac{d\mathbf{s}^{(2)}}{ds} = -\langle \mathbf{K} \rangle \mathbf{s}^{(2)} + \langle \mathbf{a} \rangle \bar{B} + \langle \mathbf{s}^{(1)} \rangle, \quad (9.14)$$

for all cloud box points in all directions. This equation contains already the averaged values and is valid for specified positions and directions.

As long as the convergence test is not fulfilled the scattering integral fields and higher order iteration fields are calculated alternately.

We can formulate a differential equation for the  $n$ -th order iteration field. The scattering integrals are given by

$$\langle \mathbf{s}_{ijklm}^{(n-1)} \rangle = \int_{4\pi} d\hat{\mathbf{n}}' \langle \mathbf{Z} \rangle \mathbf{s}_{ijklm}^{(n-1)}, \quad (9.15)$$

and the differential equation for a specified grid point into a specified direction is

$$\frac{ds^{(n)}}{ds} = -\overline{\langle \mathbf{K} \rangle} s^{(n)} + \overline{\langle \mathbf{a} \rangle} \bar{B} + \overline{\langle s^{(n-1)} \rangle}. \quad (9.16)$$

Thus the  $n$ -th order iteration field

$$\mathcal{I}^{(n)} = \left\{ s_{ijklm}^{(n)} \right\}, \quad (9.17)$$

is given by

$$s^{(n)} = e^{-\overline{\langle \mathbf{K} \rangle} s} + s^{(n-1)} (1 - e^{-\overline{\langle \mathbf{K} \rangle} s}) \overline{\langle \mathbf{K} \rangle}^{-1} (\overline{\langle \mathbf{a} \rangle} \bar{B} + \overline{\langle s^{(n-1)} \rangle}), \quad (9.18)$$

for all cloud box points and all directions defined in the numerical grids.

If the convergence test

$$\left| s_{ijklm}^{(N)}(P_i, \alpha_j, \beta_k, \psi_l, \omega_m) - s_{ijklm}^{(N-1)}(P_i, \alpha_j, \beta_k, \psi_l, \omega_m) \right| < \epsilon, \quad (9.19)$$

is fulfilled, a solution to the vector radiative transfer equation has been found:

$$\mathcal{I}^{(N)} = \left\{ s_{ijklm}^{(N)} \right\}. \quad (9.20)$$

### 9.3 Scalar radiative transfer equation solution

In analogy to the *scattering integral* vector field the scalar scattering integral field is obtained:

$$\left\langle S_{ijklm}^{(0)} \right\rangle = \int_{4\pi} d\hat{\mathbf{n}}' \langle Z_{11} \rangle I_{ijklm}^{(0)}. \quad (9.21)$$

The *scalar radiative transfer* equation (compare Equation 6.45) with a fixed scattering integral is

$$\frac{dI^{(1)}}{ds} = -\langle K_{11} \rangle I^{(1)} + \langle a_1 \rangle B + \left\langle S^{(0)} \right\rangle. \quad (9.22)$$

Assuming constant coefficients this equation is solved analytically after averaging extinction coefficients, absorption coefficients, scattering vectors and the temperature. The averaging procedure is done analogously to the procedure described for solving the VRTE. The solution of the averaged differential equation is

$$I^{(1)} = I^{(0)} e^{-\overline{\langle K_{11} \rangle} s} + \frac{\overline{\langle a_1 \rangle} \bar{B} + \overline{\langle S^{(0)} \rangle}}{\overline{\langle K_{11} \rangle}} \left( 1 - e^{-\overline{\langle K_{11} \rangle} s} \right), \quad (9.23)$$

where  $I^{(0)}$  is obtained by interpolating the initial field, and  $\overline{\langle K_{11} \rangle}$ ,  $\overline{\langle a_1 \rangle}$ ,  $\bar{B}$  and  $\overline{\langle S^{(0)} \rangle}$  are the averaged values for the extinction coefficient, the absorption coefficient, the Planck function and the scattering integral respectively. Applying this equation leads to the first iteration scalar intensity field, consisting of the intensities  $I^{(1)}$  at all points in the cloud box for all directions.

As the solution to the vector radiative transfer equation, the solution to the scalar radiative transfer equation is found numerically by the same iterative method. The convergence test for the scalar equation compares the values of the calculated intensities of two successive iteration fields.

## 9.4 Single scattering approximation

The DOIT method uses the single scattering approximation, which means that for one propagation path step the optical depth is assumed to be much less than one so that multiple-scattering can be neglected along this propagation path step. It is possible to choose a rather coarse grid inside the cloud box. The user can define a limit for the maximum propagation path step length. If a propagation path step from one grid cell to the intersection point with the next grid cell boundary is greater than this value, the path step is divided in several steps such that all steps are less than the maximum value. The user has to make sure that the optical depth due to particles for one propagation path sub-step is sufficiently small to assume single scattering. The maximum optical depth due to particles along such a propagation path sub-step is

$$\tau_{max} = \langle \mathbf{K}^P \rangle \cdot \Delta s_{max}, \quad (9.24)$$

where  $\Delta s_{max}$  is the maximum length of a propagation path sub-step. In all simulations presented in *Emde* [2005],  $\tau_{max} \ll 0.01$  is assumed. This threshold value is also used in *Czekala* [1999]. The radiative transfer calculation is done along the propagation path through one grid cell. All coefficients of the VRTE are interpolated linearly on the propagation path points.

## 9.5 Sequential update

In the previous Sections, the iterative solution method for the VRTE has been described. For each grid point inside the cloud box the intersection point with the next grid cell boundary is determined in each viewing direction. After that, all the quantities involved in the VRTE are interpolated onto this intersection point. As described in the sections above, the intensity field of the previous iteration is taken to obtain the Stokes vector at the intersection point. Suppose that there are  $N$  pressure levels inside the cloud box. If the radiation field is updated taking into account for each grid point only the adjacent grid cells, at least  $N-1$  iterations are required until the scattering effect from the lower-most pressure level has propagated throughout the cloud box up to the uppermost pressure level. From these considerations, it follows, that the number of iterations depends on the number of grid points inside the cloud box. This means that the original method is very ineffective where a fine resolution inside the cloud box is required to resolve the cloud inhomogeneities.

A solution to this problem is the “sequential update of the radiation field”, which is shown schematically in Figure 9.3. For simplicity it will be explained in detail for a 1D cloud box. We divide the update of the radiation field, i.e., the radiative transfer step calculations for all positions and directions inside the cloud box, into three parts: Update for “up-looking” zenith angles ( $0^\circ \leq \psi_{up} \leq 90^\circ$ ), for “down-looking” angles ( $\psi_{limit} \leq \psi_{down} \leq 180^\circ$ ) and for “limb-looking” angles ( $90^\circ < \psi_{limb} < \psi_{limit}$ ). The “limb-looking” case is needed, because for angles between  $90^\circ$  and  $\psi_{limit}$  the intersection point is at the same pressure level as the observation point. The limiting angle  $\psi_{limit}$  is calculated geometrically. Note that the propagation direction of the radiation is opposite to the viewing direction or the direction of the line of sight, which is indicated by the arrows. In the 1D case the radiation field is a set of Stokes vectors each of which depend upon the position and direction:

$$\mathcal{I} = \{ \mathbf{s}(P_i, \psi_l) \}. \quad (9.25)$$

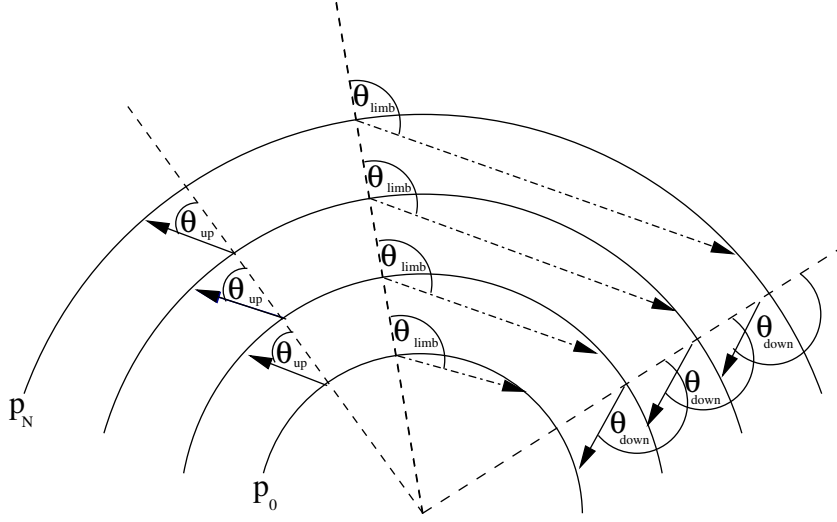


Figure 9.3: Schematic of the sequential update (1D) showing the three different parts: “up-looking” corresponds to zenith angles  $\psi_{\text{up}}$ , “limb-looking” corresponds to  $\psi_{\text{limb}}$  “down-looking” corresponds to  $\psi_{\text{down}}$ .

The *boundary condition* for the calculation is the incoming radiation field on the cloud box boundary  $\mathcal{I}^{bd}$ :

$$\mathcal{I}^{bd} = \{s(P_i, \psi_l)\} \text{ where } \begin{aligned} P_i &= P_N \forall \psi_l \in [0, \psi_{\text{limit}}] \\ P_i &= P_0 \forall \psi_l \in (\psi_{\text{limit}}, 180^\circ], \end{aligned} \quad (9.26)$$

where  $P_0$  and  $P_N$  are the pressure coordinates of the lower and upper cloud box boundaries respectively. For down-looking directions, the intensity field at the lower-most cloud box boundary and for up- and limb-looking directions the intensity field at the uppermost cloud box boundary are the required boundary conditions respectively.

### 9.5.1 Up-looking directions

The first step of the sequential update is to calculate the intensity field for the pressure coordinate  $P_{N-1}$ , the pressure level below the uppermost boundary, for all up-looking directions. Radiative transfer steps are calculated for paths starting at the uppermost boundary and propagating to the  $(N - 1)$  pressure level. The required input for this radiative transfer step are the averaged coefficients of the uppermost cloud box layer and the Stokes vectors at the uppermost boundary for all up-looking directions. These are obtained by interpolating the boundary condition  $\mathcal{I}^{bd}$  on the appropriate zenith angles. Note that the zenith angle of the propagation path for the observing direction  $\psi_l$  does not equal  $\psi'_l$  at the intersection point due to the spherical geometry. If  $\psi_l$  is close to  $90^\circ$  this difference is most significant.

To calculate the intensity field for the pressure coordinate  $P_{N-2}$ , we repeat the calculation above. We have to calculate a radiative transfer step from the  $(N - 1)$  to the  $(N - 2)$  pressure level. As input we need the interpolated intensity field at the  $(N - 1)$  pressure level, which has been calculated in the last step.

For each pressure level  $(m - 1)$  we take the interpolated field of the layer above ( $\mathcal{I}(P_m)^{(1)}$ ). Using this method, the scattering influence from particles in the upper-most cloud box layer can propagate during one iteration down to the lower-most layer. This

means that the number of iterations does not scale with the number of pressure levels, which would be the case without sequential update.

The radiation field at a specific point in the cloud box is obtained by solving Equation 9.10. For up-looking directions at position  $P_{m-1}$  we may write:

$$\begin{aligned} \mathbf{s}(P_{m-1}, \psi_{\text{up}})^{(1)} &= e^{-\overline{\mathbf{K}(\psi_{\text{up}})}s} \mathbf{s}(P_m, \psi_{\text{up}})^{(1)} \\ &+ \left( \mathbf{1} - e^{-\overline{\mathbf{K}(\psi_{\text{up}})}s} \right) \overline{\mathbf{K}(\psi_{\text{up}})}^{-1} \left( \overline{\mathbf{a}(\psi_{\text{up}})} \bar{B} + \overline{\mathbf{s}(\psi_{\text{up}})^{(0)}} \right). \end{aligned} \quad (9.27)$$

For simplification we write

$$\mathbf{s}(P_{m-1}, \psi_{\text{up}})^{(1)} = \mathbf{A}(\psi_{\text{up}}) \mathbf{s}(P_m, \psi_{\text{up}})^{(1)} + \mathbf{B}(\psi_{\text{up}}). \quad (9.28)$$

Solving this equation sequentially, starting at the top of the cloud and finishing at the bottom, we get the updated radiation field for all up-looking angles.

$$\mathcal{I}(P_i, \psi_{\text{up}})^{(1)} = \left\{ \mathbf{s}^{(1)}(P_i, \psi_l) \right\} \quad \forall \psi_l \in [0, 90^\circ]. \quad (9.29)$$

### 9.5.2 Down-looking directions

The same procedure is done for down-looking directions. The only difference is that the starting point is the lower-most pressure level  $P_1$  and the incoming clear sky field at the lower cloud box boundary, which is interpolated on the required zenith angles, is taken as boundary condition. The following equation is solved sequentially, starting at the bottom of the cloud box and finishing at the top:

$$\mathbf{s}(P_m, \psi_{\text{down}})^{(1)} = \mathbf{A}(\psi_{\text{down}}) \mathbf{s}(P_{m-1}, \psi_{\text{down}})^{(1)} + \mathbf{B}(\psi_{\text{down}}). \quad (9.30)$$

This yields the updated radiation field for all down-looking angles.

$$\mathcal{I}(P_i, \psi_{\text{down}})^{(1)} = \left\{ \mathbf{s}^{(1)}(P_i, \psi_l) \right\} \quad \forall \psi_l \in [\psi_{\text{limit}}, 180^\circ]. \quad (9.31)$$

### 9.5.3 Limb directions

A special case for limb directions, which correspond to angles slightly above  $90^\circ$  had to be implemented. If the tangent point is part of the propagation path step, the intersection point is exactly at the same pressure level as the starting point. In this case the linearly interpolated clear sky field is taken as input for the radiative transfer calculation, because we do not have an already updated field for this pressure level:

$$\mathbf{s}(P_m, \psi_{\text{limb}})^{(1)} = \mathbf{A}(\psi_{\text{limb}}) \mathbf{s}(P_m, \psi_{\text{limb}})^{(0)} + \mathbf{B}(\psi_{\text{limb}}) \quad (9.32)$$

By solving this equation the missing part of the updated radiation field is obtained

$$\mathcal{I}(P_i, \psi_{\text{limb}})^{(1)} = \left\{ \mathbf{s}(P_i, \psi_l) \right\} \quad \forall \psi_l \in ]90^\circ, \psi_{\text{limit}}[ \quad (9.33)$$

For all iterations the sequential update is applied. Using this method the number of iterations depends only on the optical thickness of the cloud or on the number of multiple-scattering events, not on the number of pressure levels.



## 9.6 Numerical Issues

### 9.6.1 Grid optimization and interpolation

The accuracy of the DOIT method depends very much on the discretization of the zenith angle. The reason is that the intensity field strongly increases at about  $\psi = 90^\circ$ . For angles below  $90^\circ$  (“up-looking” directions) the intensity is very small compared to angles above  $90^\circ$  (“down-looking” directions), because the thermal emission from the lower atmosphere and from the ground is much larger than thermal emission from trace gases in the upper atmosphere. Figure 9.4 shows an example intensity field as a function of zenith angle for different pressure levels inside a cloud box, which is placed from 7.3 to 12.7 km altitude, corresponding to pressure limits of 411 hPa and 188 hPa respectively. The cloud box includes 27 pressure levels. The frequency of the sample calculation was 318 GHz. A midlatitude-summer scenario including water vapor, ozone, nitrogen and oxygen was used. The atmospheric data was taken from the FASCOD [Anderson *et al.*, 1986] and the spectroscopic data was obtained from the HITRAN database [Rothman *et al.*, 1998]. For simplicity this 1D set-up was chosen for all sample calculations in this section. As the intensity (or the Stokes vector) at the intersection point of a propagation path is obtained by interpolation, large interpolation errors can occur for zenith angles of about  $90^\circ$  if the zenith angle grid discretization is too coarse. Taking a very fine equidistant zenith angle grid leads to very long computation times. Therefore a zenith angle grid optimization method is required.

For the computation of the scattering integral it is possible to take a much coarser zenith angle resolution without losing accuracy. It does not make sense to use the zenith angle grid, which is optimized to represent the radiation field with a certain accuracy. The integrand is the product of the phase matrix and the radiation field. The peaks of the phase matrices can be at any zenith angle, depending on the incoming and the scattered directions. The multiplication smooths out both the radiation field increase at  $90^\circ$  and the peaks of the phase matrices. Test calculations have shown that an increment of  $10^\circ$  is sufficient. Taking the equidistant grid saves the computation time of the scattering integral to a very large extent, because much less grid points are required.

### 9.6.2 Zenith angle grid optimization

As a reference field for the grid optimization the DOIT method is applied for an empty cloud box using a very fine zenith angle grid. The grid optimization routine finds a reduced zenith angle grid which can represent the intensity field with the desired accuracy. It first takes the radiation at  $0^\circ$  and  $180^\circ$  and interpolates between these two points on all grid points contained in the fine zenith angle grid for all pressure levels. Then the differences between the reference radiation field and the interpolated field are calculated. The zenith angle grid point, where the difference is maximal is added to  $0^\circ$  and  $180^\circ$ . After that the radiation field is interpolated between these three points forming part of the reduced grid and again the grid point with the maximum difference is added. Using this method more and more grid points are added to the reduced grid until the maximum difference is below a requested accuracy limit.

The top panel of Figure 9.5 shows the clear sky radiation in all viewing directions for a sensor located at 13 km altitude. This result was obtained with a switched-off cloud box. The difference between the clear sky part of the ARTS model and the scattering part is that in the clear sky part the radiative transfer calculations are done along the line of sight of the instrument whereas inside the cloud box the RT calculations are done as described in

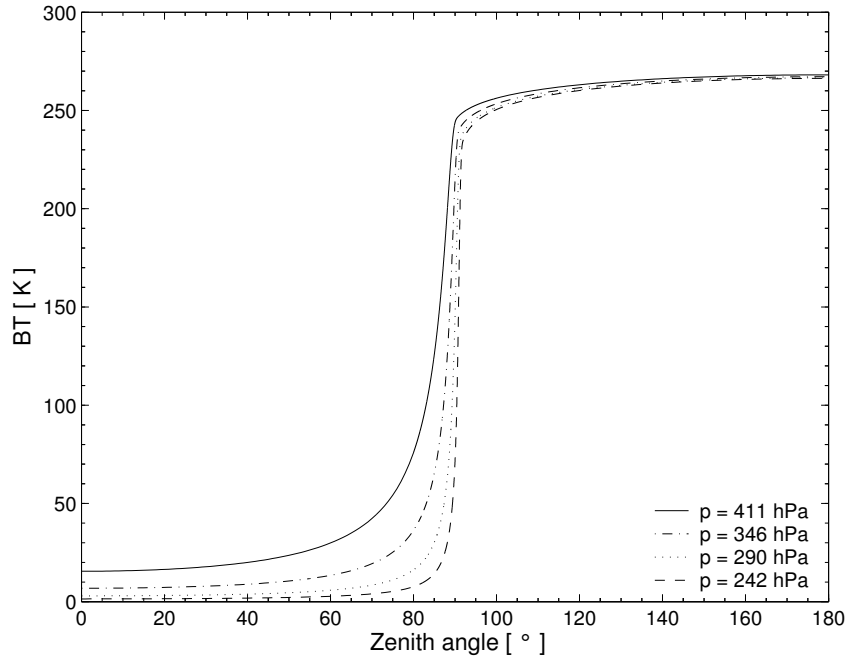


Figure 9.4: Intensity field for different pressure levels.

the previous section to obtain the full radiation field inside the cloud box. In the clear sky part the radiation field is not interpolated, therefore we can take the clear sky solution as the exact solution.

The interpolation error is the relative difference between the exact clear sky calculation (cloud box switched off) and the clear sky calculation with empty cloud box. The bottom panels of Figure 9.5 show the interpolation errors for zenith angle grids optimized with three different accuracy limits (0.1%, 0.2% and 0.5%). The left plot shows the critical region close to 90°. For a grid optimization accuracy of 0.5% the interpolation error becomes very large, the maximum error is about 8%. For grid accuracies of 0.2% and 0.1% the maximum interpolation errors are about 0.4% and 0.2% respectively. However for most angles it is below 0.2%, for all three cases. For down-looking directions from 100° to 180° the interpolation error is at most 0.14% for grid accuracies of 0.2% and 0.5% and for a grid accuracy of 0.1% it is below 0.02%.

### 9.6.3 Interpolation methods

Two different interpolation methods can be chosen in ARTS for the interpolation of the radiation field in the zenith angle dimension: linear interpolation or three-point polynomial interpolation. The polynomial interpolation method produces more accurate results provided that the zenith angle grid is optimized appropriately. The linear interpolation method on the other hand is safer. If the zenith angle grid is not optimized for polynomial interpolation one should use the simpler linear interpolation method. Apart from the interpolation of the radiation field in the zenith angle dimension linear interpolation is used everywhere in the model. Figure 9.6 shows the interpolation errors for the different interpolation methods. Both calculations are performed on optimized zenith angle grids, for polynomial interpolation 65 grid points were required to achieve an accuracy of 0.1% and for linear interpolation

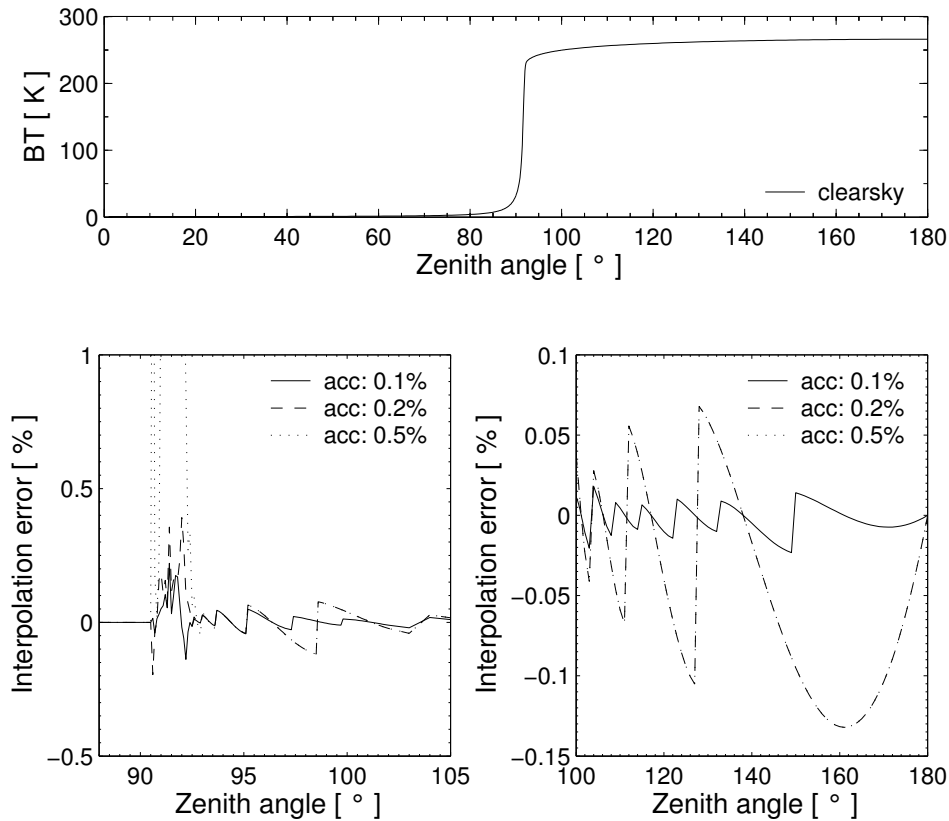


Figure 9.5: Interpolation errors for different grid accuracies. Top panel: Clear sky radiation simulated for a sensor at an altitude of 13 km for all viewing directions. Bottom left: Grid optimization accuracy for limb directions. Bottom right: Grid optimization accuracy for down-looking directions.

101 points were necessary to achieve the same accuracy. In the region of about  $90^\circ$  the interpolation errors are below 1.2% for linear interpolation and below 0.2% for polynomial interpolation. For the other down-looking directions the differences are below 0.08% for linear and below 0.02% for polynomial interpolation. It is obvious that polynomial interpolation gives more accurate results. Another advantage is that the calculation is faster because less grid points are required, although the polynomial interpolation method itself is slower than the linear interpolation method. Nevertheless, we have implemented the polynomial interpolation method so far only in the 1D model. In the 3D model, the grid optimization needs to be done over the whole cloud box, where it is not obvious that one can save grid points. Applying the polynomial interpolation method using non-optimized grids can yield much larger interpolation errors than the linear interpolation method.

#### 9.6.4 Error estimates

The interpolation error for scattering calculations can be estimated by comparison of a scattering calculation performed on a very fine zenith angle grid (resolution  $0.001^\circ$  from  $80^\circ$  to  $100^\circ$ ) with a scattering calculation performed on an optimized zenith angle grid with 0.1% accuracy. The cloud box used in previous test calculations is filled with spheroidal particles with an aspect ratio of 0.5 from 10 to 12 km altitude. The ice mass content is assumed to be

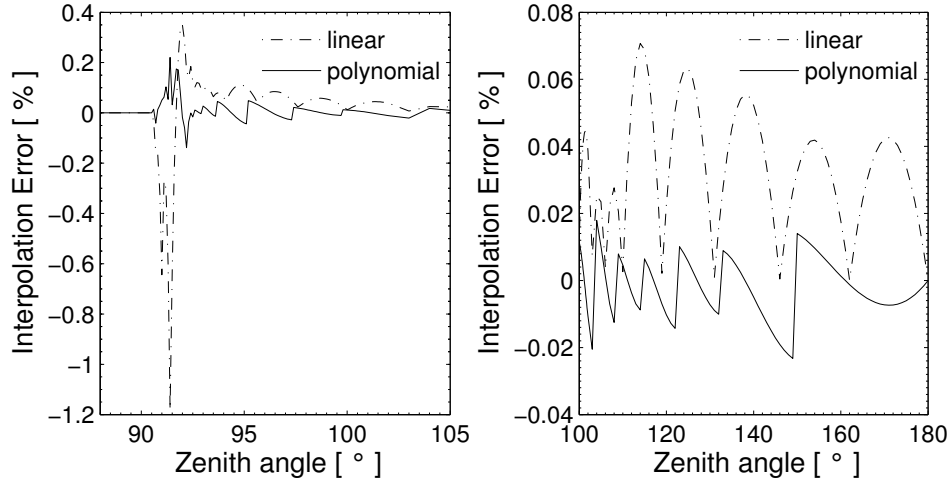


Figure 9.6: Interpolation errors for polynomial and linear interpolation.

$4.3 \cdot 10^{-3} \text{ g/m}^3$  at all pressure levels. An equal volume sphere radius of  $75 \mu\text{m}$  is assumed. The particles are either completely randomly oriented ("totally\_random") or horizontally aligned (a special case of "azimuthally\_random" oriented particles) (cf. *ARTS User Guide*, Section 8.2.2). The top panels of Figure 9.7 show the interpolation errors of the intensity. For both particle orientations the interpolation error is in the same range as the error for the clear sky calculation, below 0.2 K. The bottom panels show the interpolation errors for  $Q$ . For the randomly oriented particles the error is below 0.5%. For the horizontally aligned particles with random azimuthal orientation it goes up to 2.5% for a zenith angle of about  $91.5^\circ$ . It is obvious that the interpolation error for  $Q$  must be larger than that for  $I$  because the grid optimization is accomplished using only the clear-sky field, where the polarization is zero. Only the limb directions about  $90^\circ$  are problematic, for other down-looking directions the interpolation error is below 0.2%.

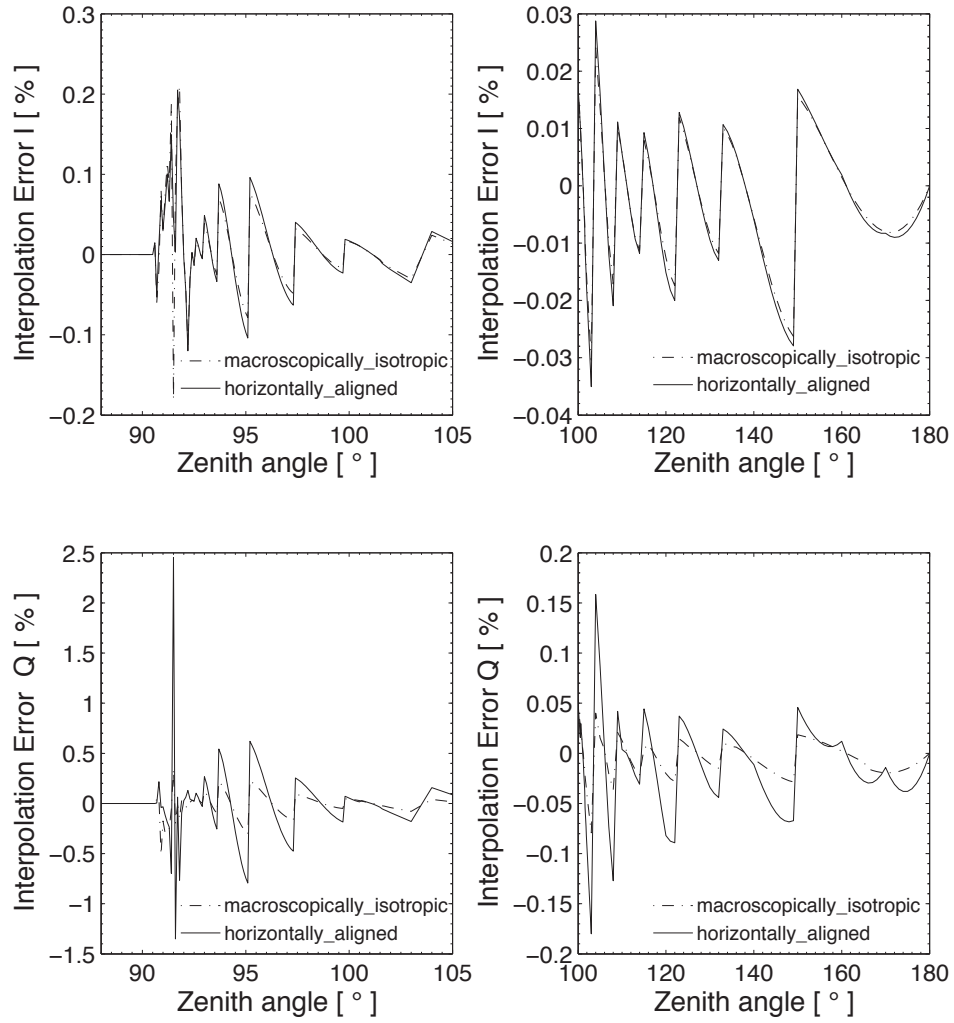


Figure 9.7: Interpolation errors for a scattering calculation. Left panels: Interpolation errors for limb directions. Right panels: Interpolation errors for down-looking directions. Top: Intensity  $I$ , Bottom: Polarization difference  $Q$



## Chapter 10

# Scattering: The Reversed Monte Carlo solver ARTS-MC

### 10.1 Introduction

The ARTS Monte Carlo scattering module (ARTS-MC) offers an efficient method for polarized radiative transfer calculations in arbitrarily complex 3D cloudy cases. The algorithm solves the integral form of the Vector Radiative Transfer Equation (VRTE), by applying Monte Carlo integration with importance sampling (MCI) (e.g. [*Press et al.*, 1997]). As described in [*Battaglia et al.*, 2007], when compared to other techniques for solving the VRTE in 3D domains the ARTS-MC algorithm has the following advantages:

- All computational effort is dedicated to calculating the Stokes vector at the location of interest and in the direction of interest. This is in contrast to forward Monte Carlo and discrete ordinate methods where the whole radiation field is calculated.
- CPU and memory cost scale more slowly than discrete ordinate methods with grid size, so that large or detailed 3D scenarios are not a problem.
- Only parts of the atmosphere that significantly contribute to the observed radiance are considered in the computation. Where the medium is optically thick, only the parts of the atmosphere closest to the sensor are visited by the algorithm. This contrasts with DOM methods, where the whole radiation field is computed, and in particular with forward Monte Carlo methods, where added optical thickness further restricts the number of photons reaching the sensor.

The Monte Carlo integration of the VRTE is over infinite dimensions, where for each scattering order there is a dimension representing: path-lengths, the choice between emission and scattering, and the choice between reflection or emission at the earth's surface. In practice the integrand is always calculated for a finite scattering order, as the dimensionality of the integral is truncated by photon emission or the boundary of the domain. Thus, the algorithm can be pictured as tracing a large number of photons backwards from sensor, in

---

#### History

- 120410 Moved from user guide to theory document.
- 300504 Created and written by Cory Davis.

randomly selected multiply scattered propagation paths to either their point of emission, or entry into the scattering domain. This physical picture is identical to the Backward-Forward Monte Carlo algorithm described by [Liu *et al.*, 1996]. However, BFMC did not account for dichroism, which is correctly accounted for in ARTS-MC by importance sampling.

The description of reversed Monte Carlo as tracing photon paths backwards from the sensor gives a useful first-order physical picture for understanding the algorithm, but can lead to difficulty understanding the veracity of the method with regard to polarization. These difficulties are not apparent in the scalar radiative transfer case<sup>1</sup>. Specifically, questions I have been asked that highlight the difficulty have included:

- how can you sample a single reversed pathlength when the medium is dichroic? (i.e. different extinction for the different polarized components)
- when reverse tracing, how can you decide on a scattering or emission event when the single scattering albedo depends on the polarization state of the incoming photon?
- How can you sample a single reverse scattered (i.e. incoming) direction when the scattered polarization state depends on the polarization state of the incoming photon?

The answer in each case is to forget the physical picture, focus on the mathematical solution to the VRTE, and realise that MCI permits some freedom in the choice of probability density functions (PDFs), provided the sampled integrand is properly weighted. In the model presented here we choose PDFs that aim to minimise the variance in the 1st element of the Stokes vector. This issue does not arise in the scalar case because it is possible to perfectly sample the phase function to choose new incoming directions, and perfectly sample the transmission function to choose pathlengths, so no weighting terms appear. With the above difficulties in mind, in comparison with [Davis *et al.*, 2005], the algorithm description presented here is more in the context of MCI and with less reference to reversed traced photons. What were referred to as photons in [Davis *et al.*, 2005] we now call Stokes Vector Evaluations (SVE).

The current implementation of the algorithm differs slightly from the description in [Davis *et al.*, 2005]; changes include:

- the initial line of sight is no longer treated differently than the scattered paths
- the algorithm is no longer confined to the ‘cloudbox’,
- MCI is now used for convolving the simulated Stokes vector with a 2D antenna response ([Davis *et al.*, 2005] discusses only pencil beam calculations)
- MCI is now used to treat emission or reflection from the earth’s surface.

These changes make the algorithm simpler and more general.

---

<sup>1</sup> Although this physical picture of reversed Monte Carlo radiative transfer in the scalar case makes intuitive sense, the mathematical demonstration of how this method solves the Schwarzschild equation is often neglected



## 10.2 Model

The radiative transfer model solves the vector radiative transfer equation (VRTE), here written as (cf. Eq. 6.36)

$$\frac{d\mathbf{I}(\mathbf{n})}{ds} = -\mathbf{K}(\mathbf{n})\mathbf{I}(\mathbf{n}) + \mathbf{K}_a(\mathbf{n})I_b(T) + \int_{4\pi} \mathbf{Z}(\mathbf{n}, \mathbf{n}')\mathbf{I}(\mathbf{n}')d\mathbf{n}' \quad (10.1)$$

where  $\mathbf{I}$  is the 4 element column vector of radiances  $\mathbf{I} = [I, Q, U, V]^T$  with units ( $\text{Wm}^{-2}\mu\text{m}^{-1}\text{sr}^{-1}$ ). This will be referred to as the Stokes vector, although normally the Stokes vector is expressed in units of intensity.  $s$  is distance along direction  $\mathbf{n}$  and  $I_b$  is the Planck radiance.  $\mathbf{K}(\mathbf{n})$ ,  $\mathbf{K}_a(\mathbf{n})$ , and  $\mathbf{Z}(\mathbf{n}, \mathbf{n}')$  are the bulk extinction matrix, absorption coefficient vector and phase matrix of the medium respectively. For brevity these have been expressed as bulk optical properties, where individual single scattering properties have been multiplied by particle number density and averaged over all orientations and scattering elements. The argument  $\mathbf{n}$  has been retained to signify that in general these properties depend on the direction of propagation.

To apply Monte Carlo integration to the problem, the VRTE needs to be expressed in integral form. (e.g. *Hochstadt* [1964])

$$\mathbf{I}(\mathbf{n}, \mathbf{s}_0) = \mathbf{O}(\mathbf{u}_0, \mathbf{s}_0)\mathbf{I}(\mathbf{n}, \mathbf{u}_0) + \int_{\mathbf{u}_0}^{\mathbf{s}_0} \mathbf{O}(\mathbf{s}', \mathbf{s}_0) (\mathbf{K}_a(\mathbf{n})I_b(T) + \int_{4\pi} \mathbf{Z}(\mathbf{n}, \mathbf{n}')\mathbf{I}(\mathbf{n}')d\mathbf{n}') ds' \quad (10.2)$$

, where  $\mathbf{O}(\mathbf{s}', \mathbf{s})$  is the evolution operator defined by *Degl'Innocenti and Degl'Innocenti* [1985].  $\mathbf{u}_0$  is the point where the line of sight intersects the far boundary of the scattering domain, and  $\mathbf{s}_0$  is the exit point where the outgoing Stokes vector is calculated.

### 10.2.1 Integration over the antenna response function

If we consider a scalar antenna response function,  $\psi = \psi(\theta, \phi) = \psi(\mathbf{n})$ , where  $\psi(\mathbf{n})$  is normalised such that  $\int_{4\pi} \psi(\mathbf{n})d\mathbf{n} = 1$ , then the observed Stokes vector  $\mathbf{I}_{\text{ant.}}(\mathbf{n}, \mathbf{s}_0)$  will be

$$\mathbf{I}_{\psi}(\mathbf{n}, \mathbf{s}_0) = \int_{4\pi} \psi(\mathbf{n}')\mathbf{I}(\mathbf{n}', \mathbf{s}_0)d\mathbf{n}' \quad (10.3)$$

If we apply Monte Carlo integration with importance sampling to Eq. 10.3 and sample  $\mathbf{n}'$  according to a probability density function (PDF) equal to  $\psi(\mathbf{n}')$ , an unbiased estimate of Eq. 10.3 is given by (e.g. *Press et al.* [1992])

$$\mathbf{I}_{\psi}(\mathbf{n}, \mathbf{s}_0) = \int_{4\pi} \mathbf{I}(\mathbf{n}', \mathbf{s}_0)\psi(\mathbf{n}')d\mathbf{n}' \quad (10.4)$$

$$\approx \langle \mathbf{I}(\mathbf{n}', \mathbf{s}_0) \rangle_{\psi}, \quad (10.5)$$

where the angled brackets indicate the arithmetic mean, and the  $\psi$  subscript indicates the sampled PDF. Eq. 10.5 has an estimated error for each Stokes index,  $j$ , of

$$\delta I_j = \sqrt{\frac{\langle I_j^2 \rangle - \langle I_j \rangle^2}{N}}. \quad (10.6)$$

### 10.2.2 The path integral

We now require a Monte Carlo estimate of the integrand in Eq. 10.5, which is given by Eq. 10.2. First, we re-express 10.2 as a single integral, for simplicity dropping the prime on  $\mathbf{n}'$ ,

$$\mathbf{I}(\mathbf{n}, \mathbf{s}_0) = \int_{-\infty}^{s_0} \begin{cases} \mathbf{O}(\mathbf{s}', \mathbf{s}_0) (\mathbf{K}_a(\mathbf{n}) I_b(T) + \int_{4\pi} \mathbf{Z}(\mathbf{n}, \mathbf{n}') \mathbf{I}(\mathbf{n}') d\mathbf{n}') & s' < s'_{\text{boundary}} \\ \frac{\mathbf{O}(\mathbf{u}_0, \mathbf{s}_0) \mathbf{I}(\mathbf{n}, \mathbf{u}_0) g}{\int_{u_0}^{\infty} g ds} & s' \geq s'_{\text{boundary}} \end{cases} ds' \quad (10.7)$$

, where  $g$  is the PDF we will eventually use to sample pathlength,  $\Delta s$ .  $s'_{\text{boundary}}$  represents the pathlength corresponding to the boundary of the domain opposite the line of sight. The integrand Eq. 10.7 is a piecewise function of the path distance, where path distances corresponding to positions outside the modelled domain give a boundary radiance attenuated by the evolution operator over the length of the path within the model domain, and path distances corresponding to points within the modelled atmosphere give a sum of emission and scattering attenuated by the evolution operator over the distance between the point and the atmosphere exit. The reader could easily verify that evaluating Eq. 10.7 is equivalent Eq. 10.2.

The aim in importance sampling is to choose probability density functions (PDFs) for the independent variables that are as close as possible to being proportional to the integrand Liu [2001]. This concentrates computational effort on regions where the integrand is most significant and also reduces the variance in the Stokes Vector evaluations (SVE), thus reducing the number of SVEs and hence CPU time required to give a prescribed accuracy. Eq. 10.2 suggests that the PDF for sampling path length, where path length is the distance traced backwards from the sensor,  $\Delta s = |\mathbf{s} - \mathbf{s}'|$ , should be proportional in some way to the evolution operator  $\mathbf{O}(\mathbf{s}', \mathbf{s})$ .

In general there is no closed form expression for  $\mathbf{O}(\mathbf{s}', \mathbf{s})$ . However, in cases where the extinction matrix is constant along a propagation path

$$\mathbf{O}(\mathbf{s}', \mathbf{s}) = \exp(-\mathbf{K} \Delta s) \quad (10.8)$$

In ARTS a propagation path consists of a set of coordinates indicating where the path intersects with grid surfaces. If the extinction matrix in the path segment between two such points is considered constant,  $\mathbf{K} = (\mathbf{K}_j + \mathbf{K}_{j+1})/2$ , the evolution operator between two arbitrary points  $\mathbf{s}_0$  and  $\mathbf{s}_N$  is

$$\mathbf{O}(\mathbf{s}_0, \mathbf{s}_N) = \mathbf{O}(\mathbf{s}_{N-1}, \mathbf{s}_N) \mathbf{O}(\mathbf{s}_{N-2}, \mathbf{s}_{N-1}) \dots \mathbf{O}(\mathbf{s}_1, \mathbf{s}_2) \mathbf{O}(\mathbf{s}_0, \mathbf{s}_1), \quad (10.9)$$

, where  $\mathbf{O}(\mathbf{s}_i, \mathbf{s}_{i+1})$  is given by Eq. 10.8.

Since PDFs are scalar functions, and that we consider the first element of the Stokes vector most important, we choose the pathlength PDF to be proportional to the (1,1) element of  $\mathbf{O}(\mathbf{s}', \mathbf{s})$ ,

$$g(\Delta s) = \tilde{k} \tilde{O}_{11}(\Delta s) \quad (10.10)$$

, where  $\tilde{O}_{11}(\Delta s)$ , is the piecewise exponential function that includes  $O_{11}(\mathbf{s}', \mathbf{s})$  values at points where the line of sight intersects with grid surfaces. Between two such adjacent

intersections,  $A$  and  $B$ , the function  $\tilde{O}_{11}(\Delta s)$  is given by

$$\tilde{O}_{11}(\Delta s) = O_{11}(\Delta s_A) \exp \left( -\tilde{k} (\Delta s - \Delta s_A) \right) \quad (10.11)$$

, and

$$\tilde{k} = \frac{1}{(\Delta s_B - \Delta s_A)} \ln \left( \frac{O_{11}^A}{O_{11}^B} \right), \quad (10.12)$$

which, for cases where the extinction matrix is diagonal, is equal to  $K_{11} = (K_{11}^A + K_{11}^B)/2$ . Eq. 10.10 is sampled by drawing a random number (from the uniform distribution  $[0,1]$ ),  $r$ , and solving

$$\tilde{O}_{11}(\Delta s) = r. \quad (10.13)$$

for  $\Delta s$ . In practise this is done by stepping backwards over grid boundaries until  $O_{11} \leq r$ , and solving Eqs. 10.11 and 10.13 within the final grid step,

$$\Delta s = \Delta s_A + \frac{1}{\tilde{k}} \ln \left( \frac{O_{11}^A}{r} \right) \quad (10.14)$$

With pathlength sampled according to Eq. 10.13, the Monte Carlo estimate for Eq. 10.7 becomes

$$\begin{aligned} \mathbf{I}(\mathbf{n}, \mathbf{s}_0) &= \int_{\infty}^{s_0} \left\{ \begin{array}{ll} \frac{\mathbf{O}(\mathbf{s}', \mathbf{s}_0)}{g(\Delta s)} (\mathbf{K}_a(\mathbf{n}) I_b(T) + \int_{4\pi} \mathbf{Z}(\mathbf{n}, \mathbf{n}') \mathbf{I}(\mathbf{n}') d\mathbf{n}') & s' < s'_{boundary} \\ \frac{\mathbf{O}(\mathbf{u}_0, \mathbf{s}_0) \mathbf{I}(\mathbf{n}, \mathbf{u}_0)}{1 - O_{11}(\Delta s)} & s' \geq s'_{boundary} \end{array} \right\} g(\Delta s) ds' \\ &\approx \left\langle \left\{ \begin{array}{ll} \frac{\mathbf{O}(\mathbf{s}', \mathbf{s}_0)}{g(\Delta s)} (\mathbf{K}_a(\mathbf{n}) I_b(T) + \int_{4\pi} \mathbf{Z}(\mathbf{n}, \mathbf{n}') \mathbf{I}(\mathbf{n}') d\mathbf{n}') & s' < s'_{boundary} \\ \frac{\mathbf{O}(\mathbf{u}_0, \mathbf{s}_0) \mathbf{I}(\mathbf{n}, \mathbf{u}_0)}{1 - O_{11}(\Delta s)} & s' \geq s'_{boundary} \end{array} \right\} \right\rangle_{g(\Delta s)} \quad (10.15) \end{aligned}$$

So if the sampled pathlength corresponds to a point outside the atmosphere, or below the earth's surface, the SVE is given by  $\frac{\mathbf{O}(\mathbf{u}_0, \mathbf{s}_0) \mathbf{I}(\mathbf{n}, \mathbf{u}_0)}{1 - O_{11}(\Delta s)}$ . In the top of atmosphere cases, this can be immediately calculated:  $\mathbf{O}(\mathbf{u}_0, \mathbf{s}_0)$  from Eq. 10.9, and  $\mathbf{I}(\mathbf{n}, \mathbf{u}_0)$  from the background radiation from space. As shown in Figure 10.2.8, in this event, we have our SVE and we can begin the calculation for the next one. If however the reversed traced path passes the earth's surface, the calculation of  $\mathbf{I}(\mathbf{n}, \mathbf{u}_0)$  requires more steps.

### 10.2.3 Emission and scattering

If the sampled pathlength corresponds to a point within the atmosphere then the emission and scattering terms in the top term in Eq. 10.15, must be calculated. We also treat this as Monte Carlo integration:

$$\begin{aligned} \mathbf{K}_a(\mathbf{n}) I_b(T) + \int_{4\pi} \mathbf{Z}(\mathbf{n}, \mathbf{n}') \mathbf{I}(\mathbf{n}') d\mathbf{n}' &= \int_0^1 \left\{ \begin{array}{ll} \frac{1}{\tilde{\omega}} \int_{4\pi} \mathbf{Z}(\mathbf{n}, \mathbf{n}') \mathbf{I}(\mathbf{n}') d\mathbf{n}' & r \leq \tilde{\omega} \\ \frac{\mathbf{K}_a(\mathbf{n}) I_b(T)}{1 - \tilde{\omega}} & r > \tilde{\omega} \end{array} \right\} dr \\ &\approx \left\langle \left\{ \begin{array}{ll} \frac{1}{\tilde{\omega}} \int_{4\pi} \mathbf{Z}(\mathbf{n}, \mathbf{n}') \mathbf{I}(\mathbf{n}') d\mathbf{n}' & r \leq \tilde{\omega} \\ \frac{\mathbf{K}_a(\mathbf{n}) I_b(T)}{1 - \tilde{\omega}} & r > \tilde{\omega} \end{array} \right\} \right\rangle \quad (10.16) \end{aligned}$$

. Here we are using a uniform random deviate  $r$ , and an albedo-like quantity,

$$\tilde{\omega} = 1 - \frac{K_{a1}(\mathbf{n}_0, \mathbf{s}_1)}{K_{11}(\mathbf{n}_0, \mathbf{s}_1)} \quad (10.17)$$

, to choose between emission and scattering contributions. Note: we can't use the actual single-scattering albedo as this depends on the polarization state of the incident radiation. If  $r > \tilde{\omega}$ , then the event is considered to be emission. In this case we have all the information required to calculate the SVE,

$$\mathbf{I}^i(\mathbf{n}, \mathbf{s}_0) = \frac{\mathbf{Q}_k \mathbf{O}(\mathbf{s}_{k+1}, \mathbf{s}_k) \mathbf{K}_a(\mathbf{n}_k, \mathbf{s}_{k+1}) I_b(T, \mathbf{s}_{k+1})}{g(\Delta s)(1 - \tilde{\omega})} \quad (10.18)$$

, where  $\mathbf{O}(\mathbf{s}_{k+1}, \mathbf{s}_k)$  is the evolution operator pertaining to the preceding pathlength sample, and  $g(\Delta s)$ , the corresponding importance sampling weight, as indicated in Eq. 10.15. The matrix  $\mathbf{Q}_k$ , whose calculation will be described below, holds the multiplicative effect of previous evolution operators, phase matrices, surface reflection matrices, and importance sampling weighting factors, acting on the reversed traced multiply scattered propagation path.

#### 10.2.4 The scattering integral

If, in Eq. 10.16 our sampled  $r \leq \tilde{\omega}$ , we have sampled a scattering event. In this case we need to evaluate the scattering integral  $\int_{4\pi} \mathbf{Z}(\mathbf{n}, \mathbf{n}') \mathbf{I}(\mathbf{n}') d\mathbf{n}'$ . Again we apply Monte Carlo integration with importance sampling to this integral.

$$\begin{aligned} \int_{4\pi} \mathbf{Z}(\mathbf{n}, \mathbf{n}') \mathbf{I}(\mathbf{n}') d\mathbf{n}' &= \int_0^{2\pi} \int_0^\pi \frac{\mathbf{Z}(\mathbf{n}, \mathbf{n}') \mathbf{I}(\mathbf{n}')}{g(\theta_{inc}, \phi_{inc})} g(\theta_{inc}, \phi_{inc}) \sin \theta_{inc} d\theta_{inc} d\phi_{inc} \\ &\approx \left\langle \frac{\sin \theta_{inc} \mathbf{Z}(\mathbf{n}, \mathbf{n}') \mathbf{I}(\mathbf{n}')}{g(\theta_{inc}, \phi_{inc})} \right\rangle_{g(\theta_{inc}, \phi_{inc})} \end{aligned} \quad (10.20)$$

Given the desire to use a PDF proportional to the integrand, we choose to sample incoming directions,  $\mathbf{n}' = (\theta_{inc}, \phi_{inc})$  from a PDF proportional to  $\sin \theta_{inc} \mathbf{Z}(\theta_{scat}, \phi_{scat}, \theta_{inc}, \phi_{inc})$ . At the scattering point sample a new incident direction  $(\theta_{inc}, \phi_{inc})$  according to

$$g(\theta_{inc}, \phi_{inc}) = \frac{Z_{11}(\theta_{scat}, \phi_{scat}, \theta_{inc}, \phi_{inc}) \sin(\theta_{inc})}{K_{11}(\theta_{scat}, \phi_{scat}) - K_{a1}(\theta_{scat}, \phi_{scat})}, \quad (10.21)$$

which is sampled by the rejection method as described in *Liu* [2001]. This sampling of the new incoming direction for the evaluation of Eq. 10.20 leads to the calculation of the incoming stokes vector  $\mathbf{I}(\mathbf{n}', \mathbf{s})$  at the point of scattering  $\mathbf{s}$  in the new incident direction  $\mathbf{n}'$ . We thus return to pathlength sampling and evaluation of Eq. 10.15.

#### 10.2.5 Applying the Mueller matrices

The influence of the phase matrix and the preceding evolution operator, along with the importance sampling weights, are stored by calculating the matrix

$$\mathbf{Q}_k = \mathbf{Q}_{k-1} \mathbf{q}_k \quad (10.22)$$

, where

$$\mathbf{q}_k = \frac{\sin(\theta_{inc})_k \mathbf{O}(\mathbf{s}_k, \mathbf{s}_{k-1}) \mathbf{Z}(\mathbf{n}_{k-1}, \mathbf{n}_k)}{g(\Delta s) g(\theta_{inc}, \phi_{inc}) \tilde{\omega}}, \quad (10.23)$$

and  $\mathbf{Q}_0 = 1$ . The index  $k$  represents the scattering order. The  $\mathbf{Q}_k$  is updated through precedent scattering events and finally applied to an emission contribution (Eq. 10.18) if an emission event is sampled in Eq. 10.16.

### 10.2.6 Boundary contributions

If the  $k^{\text{th}}$  pathlength sampled in Eq. 10.15 is beyond the top of the atmosphere or below the earth surface,  $\mathbf{Q}_k$  is applied in

$$\mathbf{I}^i(\mathbf{n}, \mathbf{s}_0) = \frac{\mathbf{Q}_k \mathbf{O}(\mathbf{u}_k, \mathbf{s}_k) \mathbf{I}(\mathbf{n}_k, \mathbf{u}_k)}{O_{11}(\mathbf{u}_k, \mathbf{s}_k)}, \quad (10.24)$$

where  $\mathbf{I}(\mathbf{n}_k, \mathbf{u}_k)$  is the incoming radiance at boundary point  $\mathbf{u}_k$ . For the top of atmosphere case,  $\mathbf{I}(\mathbf{n}_k, \mathbf{u}_k) = I_{space}$ . In ARTS it is possible to set  $I_{space}$  to any value, but in most cases this is set to the cosmic background radiance associated with a Planck temperature of 2.735K.

For the surface case, if we choose to treat the surface as a blackbody, i.e. there is no reflection, in Eq. 10.24 we set  $\mathbf{I}(\mathbf{n}_k, \mathbf{u}_k) = I_{surf}$ , where  $I_{surf}$  is the Planck radiance associated with the surface temperature,  $I_{surf} = I_b(T_{surf})$ .

### 10.2.7 Surface reflection

Currently ARTS-MC can only consider specular reflection. Mostly ARTS-MC has been applied where surface reflections have a small or negligible effect on simulated remote sensing observations. *It would be a straightforward development to handle more complicated reflections. In the same way that the phase matrix is sampled to choose new incoming directions for scattering events, we could sample the Bidirectional reflection distribution (BDRF) for surface reflection events.* In analogy with scattering and emission in Eq. 10.16,  $\mathbf{I}_{surf}$  is given by the sum of reflected and emitted radiation:

$$\begin{aligned} \mathbf{I}_{surf}(\mathbf{n}_k, \mathbf{u}_k) &= \mathbf{B}(\mathbf{n}_k, \mathbf{u}_k) + \mathbf{R}(\mathbf{n}_k, \mathbf{n}_{k+1}, \mathbf{u}_k) \mathbf{I}(\mathbf{n}_{k+1}, \mathbf{u}_k) \\ &= \int_0^1 \begin{cases} \frac{1}{R_{11}} \mathbf{R}(\mathbf{n}_k, \mathbf{n}_{k+1}, \mathbf{u}_k) \mathbf{I}(\mathbf{n}_{k+1}, \mathbf{u}_k) & r \leq R_{11} \\ \frac{\mathbf{B}(\mathbf{n}_k, \mathbf{u}_k)}{1-R_{11}} & r > R_{11} \end{cases} dr \\ &\approx \left\langle \begin{cases} \frac{1}{R_{11}} \mathbf{R}(\mathbf{n}_k, \mathbf{n}_{k+1}, \mathbf{u}_k) \mathbf{I}(\mathbf{n}_{k+1}, \mathbf{u}_k) & r \leq R_{11} \\ \frac{\mathbf{B}(\mathbf{n}_k, \mathbf{u}_k)}{1-R_{11}} & r > R_{11} \end{cases} \right\rangle_r \end{aligned} \quad (10.25)$$

The reflection matrix  $\mathbf{R}(\mathbf{n}_k, \mathbf{n}_{k+1}, \mathbf{u}_k)$  and related surface emission,  $\mathbf{B}(\mathbf{n}_k, \mathbf{u}_k)$  are calculated in one of several ways, as described in section [FIXME: that stuff should be in this document but it isn't yet]. As in Eq. 10.16, we use a uniform random deviate  $r$ ; if  $r > R_{11}$ , where  $R_{11}$  is the (1,1) element of  $\mathbf{R}(\mathbf{n}_k, \mathbf{n}_{k+1}, \mathbf{u}_k)$ , then the event is considered to be surface emission. In this case we have all the information required to calculate the SVE in Eq. 10.24 becomes,

$$\mathbf{I}^i(\mathbf{n}, \mathbf{s}_0) = \frac{\mathbf{Q}_k \mathbf{O}(\mathbf{u}_k, \mathbf{s}_k) \mathbf{B}(\mathbf{n}_k, \mathbf{u}_k)}{O_{11}(\mathbf{u}_k, \mathbf{s}_k)(1 - R_{11})}. \quad (10.26)$$

If our sampled  $r \leq R_{11}$  in Eq. 10.25, then we have a surface reflection contribution, and the incoming (downward) stokes vector  $\mathbf{I}(\mathbf{n}_{k+1}, \mathbf{u}_k)$  remains unknown. As in the scattering case we record the effect the evolution and reflection operators in the matrix  $\mathbf{Q}_k = \mathbf{Q}_{k-1} \mathbf{q}_k$ , where

$$\mathbf{q}_k = \frac{\mathbf{O}(\mathbf{s}_k, \mathbf{s}_{k-1}) \mathbf{R}(\mathbf{n}_{k-1}, \mathbf{n}_k)}{O_{11}(\mathbf{u}_k, \mathbf{s}_k) R_{11}}, \quad (10.27)$$

and continue with another path integral (Eq. 10.15) in the direction  $\mathbf{n}_{k+1}$ . Since the reflection is specular,  $\mathbf{n}_{k+1}$  is described by zenith and azimuthal angles  $\theta_{k+1} = \pi - \theta_k$  and  $\phi_{k+1} = \phi_k$ . With regard to the scattering order  $k$ , surface reflection is considered the same as scattering.

### 10.2.8 Summary

Summarizing sections 10.2.2 to 10.2.7 we see that successively nested Monte Carlo integrals are calculated until atmospheric emission, surface emission, or top of atmosphere contributions are sampled. Mueller matrices encountered in each nested integral (evolution operators, phase matrices, reflection matrices), along with Monte Carlo weights, are recorded in the matrix  $\mathbf{Q}_k$ . This matrix applies the Mueller matrices in the correct ‘forward’ order to each emission or top of atmosphere contribution (Eq.s 10.18, 10.26, and 10.24). The algorithm summarized graphically in Figure 10.2.8.

## 10.3 Practical considerations regarding optical properties

### 10.3.1 Particle orientation and the evolution operator

The calculation of the evolution operator in Eqs. 10.8 and 10.9 requires evaluation of the matrix exponential. If the scattering elements are spheres or randomly orientated (“totally\_random”), as described in *ARTS User Guide*, Section 8.2.2, then Eq. 10.8 is simply

$$O_{jj}(s', s) = \exp(-K_{jj}\Delta s) \quad (10.28)$$

If scattering elements have rotational symmetry, and the axis of symmetry is oriented vertically, or if the scattering elements have random azimuthal orientation (“azimuthally\_random”) then the extinction matrix has a block diagonal form with 3 independent elements,  $K_{jj}$ ,  $K_{12}$ , and  $K_{34}$ .

### 10.3.2 Particle orientation and the phase matrix

## 10.4 Variations on the ARTS-MC algorithm

### 10.4.1 The original ARTS-MC and forcing the original pathlength sample to be within the 3D box

### 10.4.2 1D clear sky variables and clear sky radiance look up

### 10.4.3 MCIPA

### 10.4.4 optical path and ice water path calculations

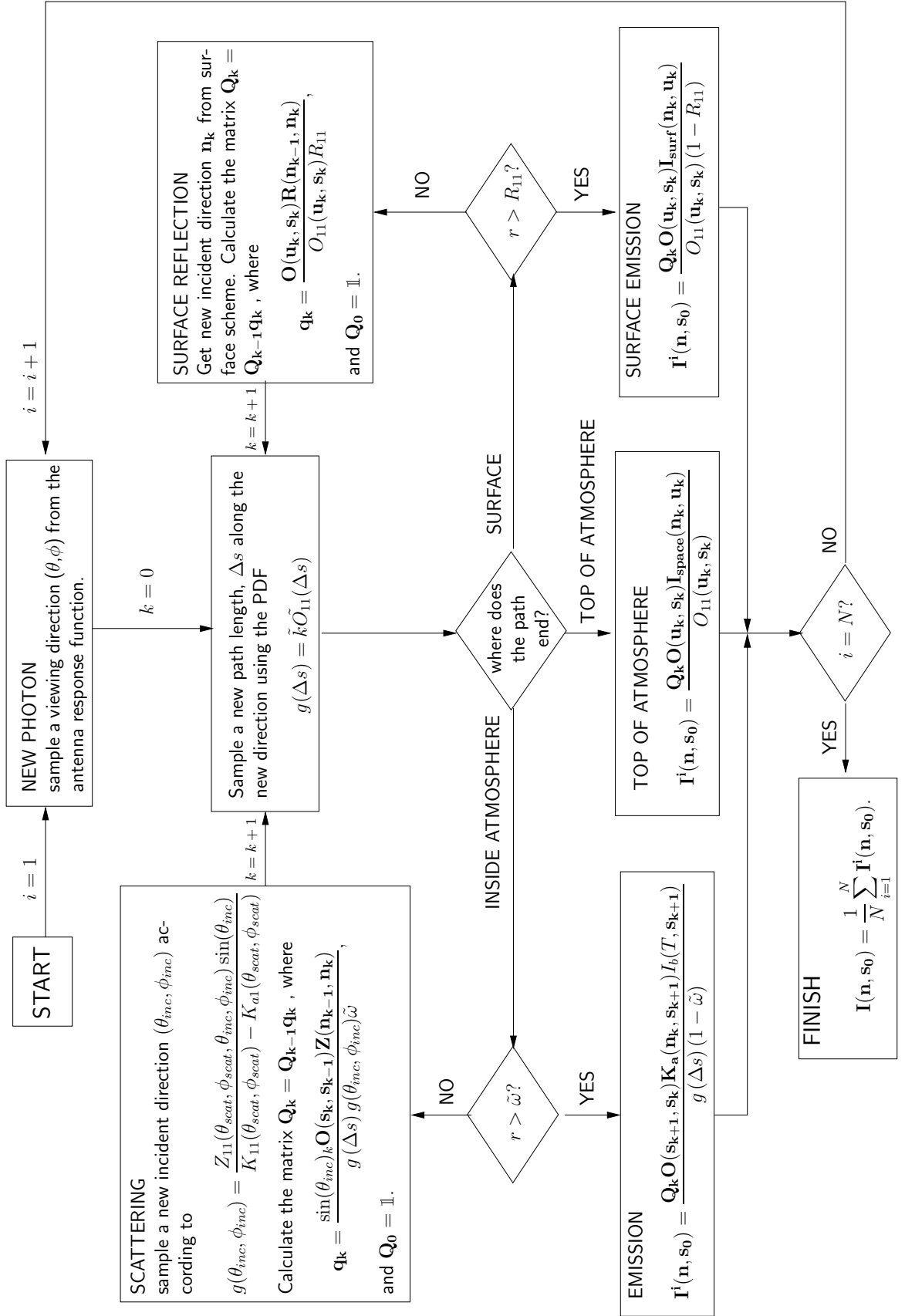


Figure 10.1: Flowchart illustrating MCGeneral algorithm





## **Part I**

# **Bibliography and Appendices**



# Bibliography

- Anderson, G. P., S. A. Clough, F. X. Kneizys, J. H. Chetwynd, and E. P. Shettle, AFGL atmospheric constituent profiles (0–120 km), *Tech. Rep. TR-86-0110*, AFGL, 1986.
- Balluch, M., and D. Lary, Refraction and atmospheric photochemistry, *Journal of Geophysical Research*, 102, 8845–8854, 1997.
- Bates, D., Rayleigh scattering by air, *Planetary and Space Science*, 32, 785–790, 1984.
- Battaglia, A., C. P. Davis, C. Emde, and C. Simmer, Microwave radiative transfer intercomparison study for 3-D dichroic media, *Journal of Quantitative Spectroscopy and Radiative Transfer*, 105, 55–67, 2007.
- Bauer, A., M. Godon, M. Kheddari, and J. M. Hartmann, Temperature and perturber dependence of water vapor line broadening: Experiments at 183 GHz; calculations below 1000 GHz, *Journal of Quantitative Spectroscopy and Radiative Transfer*, 41, 49–54, 1989.
- Bauer, A., M. Godon, J. Carlier, Q. Ma, and R. H. Tipping, Absorption by H<sub>2</sub>O and H<sub>2</sub>O-N<sub>2</sub> mixtures at 153 GHz, *Journal of Quantitative Spectroscopy and Radiative Transfer*, 50, 463–475, 1993.
- Bauer, A., M. Godon, J. Carlier, and Q. Ma, Water vapor absorption in the atmospheric window at 239 GHz, *Journal of Quantitative Spectroscopy and Radiative Transfer*, 53, 411–423, 1995.
- Becker, G. E., and S. H. Autler, Water vapor absorption of electromagnetic radiation in the centimeter wavelength range, *Physical Review*, 70, 300–307, 1946.
- Bernath, P., *Spectra of Atoms and Molecules*, Oxford University Press, 1995, ISBN 0-195-07598-6.
- Berton, R. P. H., Statistical distribution of water content and sizes for clouds above Europe, *Ann. Geophys.*, 18, 385–397, 2000.
- Bevis, M., S. Businger, S. Chiswell, T. A. Herring, R. A. Anthes, C. Rocken, and R. H. Ware, GPS meteorology: Mapping zenith wet delays onto precipitable water, *Journal of Applied Meteorology*, 33, 379–386, 1994.
- Bodhaine, B. A., N. B. Wood, E. G. Dutton, and J. R. Slusser, On Rayleigh Optical Depth Calculations, *Journal of Atmosphere and Ocean Technology*, 16, 1854–1861, 1999.
- Bohren, C., and D. R. Huffman, *Absorption and Scattering of Light by Small Particles*, Wiley Science Paperback Series, 1998.

- Borysow, A., and L. Frommhold, Collision induced rototranslational absorption spectra of  $N_2$ - $N_2$  pairs for temperatures from 50 to 300 K, *Astrophysical Journal*, 311, 1043–1057, 1986.
- Brussaard, G., and P. A. Watson, *Atmospheric Modelling and Millimetre Wave Propagation*, Chapman & Hall, 1995, ISBN 0-412-56230-8.
- Buehler, S. A., P. Eriksson, T. Kuhn, A. von Engeln, and C. Verdes, ARTS, the Atmospheric Radiative Transfer Simulator, *Journal of Quantitative Spectroscopy and Radiative Transfer*, 91, 65–93, 2005.
- Chandrasekhar, S., *Radiative Transfer*, Dover Publications, New York, 1960.
- Clough, S. A., F. X. Kneizys, and R. W. Davis, Line shape and water vapor continuum, *Atmospheric Research*, 23, 229–241, 1989.
- Costa, A. A., G. P. Almeida, and A. J. C. Sampaio, A bin-microphysics cloud model with high-order, positive-definite advection, *Atmospheric Research*, 55, 225–255, 2000.
- Cruz Pol, S. L., C. S. Ruf, and S. J. Keihm, Improved 20– to 32–GHz atmospheric absorption model, *Radio Science*, 33, 1319–1333, 1998, updated version can be downloaded from <http://ece.uprm.edu/~pol/Atmosphere.html>.
- Czekala, H., Microwave radiative transfer calculations with multiple scattering by non-spherical hydrometeors, Ph.D. thesis, Rheinische Friedrich-Wilhelms-Universität Bonn, Auf dem Hügel 20, 53121 Bonn, 1999.
- Dagg, I. R., G. E. Reesor, and J. L. Urbaniak, Collision induced absorption in  $N_2$ ,  $CO_2$ , and  $H_2$  at  $2\text{ cm}^{-1}$ , *Canadian Journal of Physics*, 53, 1764–1776, 1975.
- Dagg, I. R., G. E. Reesor, and M. Wong, A microwave cavity measurement of collision-induced absorption in  $N_2$  and  $CO_2$  at  $4.6\text{ cm}^{-1}$ , *Can. J. Phys.*, 56, 1037–1045, 1978.
- Davis, C., C. Emde, and R. Harwood, A 3D polarized reversed monte carlo radiative transfer model for mm and sub-mm passive remote sensing in cloudy atmospheres, *IEEE Transactions on Geoscience and Remote Sensing*, 43, 1096–1101, 2005.
- Degl’Innocenti, E. L., and M. L. Degl’Innocenti, On the solution of the radiative-transfer equations for polarized radiation, *Solar Physics*, 97, 239–250, 1985.
- Delanoë, J., A. J. Heymsfield, A. Protat, A. Bansemer, and R. Hogan, Normalized particle size distribution for remote sensing application, *Journal of Geophysical Research*, 119, 4204–4227, 2014.
- Drayson, S. R., Rapid computation of the Voigt profile, *Journal of Quantitative Spectroscopy and Radiative Transfer*, 16, 611, 1976.
- Eberhard, W. L., Correct equations and common approximations for calculating rayleigh scatter in pure gases and mixtures and evaluation of differences, *Appl. Opt.*, 49, 1116–1130, 2010.
- Emde, C., A polarized discrete ordinate scatterig model for radiative transfer simulations in spherical atmospheres with thermal source, Ph.D. thesis, University of Bremen, 2005.

- Emde, C., and T. R. Sreerekha, Development of a RT model for frequencies between 200 and 1000 GHz, WP1.2 Model Review, *Tech. rep.*, ESTEC Contract No AO/1-4320/03/NL/FF, 2004.
- Emde, C., S. A. Buehler, C. Davis, P. Eriksson, T. R. Sreerekha, and C. Teichmann, A polarized discrete ordinate scattering model for simulations of limb and nadir longwave measurements in 1D/3D spherical atmospheres, *Journal of Geophysical Research*, 109, 2004.
- English, S. J., C. Guillou, C. Prigent, and D. C. Jones, Aircraft measurements of water vapor continuum absorption at millimeter wavelengths, *Quarterly Journal of the Royal Meteorological Society*, 120, 603–625, 1994.
- Eriksson, P., Microwave radiometric observations of the middle atmosphere: Simulations and inversions, Ph.D. thesis, School of Electrical and Computer Engineering, Chalmers University of Technology, Sweden, 1999.
- Eriksson, P., F. Merino, D. Murtagh, P. Baron, P. Ricaud, and J. de La Noë, Studies for the Odin sub-millimetre radiometer: 1. Radiative transfer and instrument simulation, *Canadian Journal of Physics*, 80, 321–340, 2002.
- Eriksson, P., M. Ekström, S. Bühler, and C. Melzheimer, Efficient forward modelling by matrix representation of sensor responses, *International Journal of Remote Sensing*, 27, 1793–1808, 2006.
- Fisák, J., Krticka, J., Munzar, D., and Kubát, J., Rayleigh scattering in the atmospheres of hot stars, *AA*, 590, A95, 2016.
- Gamache, R. R., B. Vispoel, M. Rey, A. Nikitin, V. Tyuterev, O. Egorov, I. E. Gordon, and V. Boudon, Total internal partition sums for the hitran2020 database, *Journal of Quantitative Spectroscopy and Radiative Transfer*, 271, 107713, 2021.
- Godon, M., J. Carlier, and A. Bauer, Laboratory studies of water vapor absorption in the atmospheric window at 213 GHz, *Journal of Quantitative Spectroscopy and Radiative Transfer*, 47, 275–285, 1992.
- Goody, R. M., *Principles of atmospheric physics and chemistry*, Oxford University Press, 1995.
- Goody, R. M., and Y. L. Yung, *Atmospheric radiation, theoretical basis*, Oxford University Press, 1989, second edition.
- Gordon, I. E., et al., The HITRAN2016 molecular spectroscopic database, *Journal of Quantitative Spectroscopy and Radiative Transfer*, 203, 3–69, 2017.
- Gordy, W., and R. Cook, *Microwave Molecular Spectra*, Interscience Publishers, 1970, SBN 471 93161 6.
- Herzberg, G., *Infrared and Raman Spectra of Polyatomic Molecules*, Van Nostrand Reinhold Company, 1945, ISBN 0-442-03386-9.
- Hess, M., P. Koepke, and I. Schult, Optical properties of aerosols and clouds: The software package OPAC, *Bulletin of the American Meteorological Society*, 79, 831–844, 1998.

- Ho, W., I. A. Kaufman, and P. Thaddeus, Laboratory measurement of microwave absorption in models of the atmosphere of Venus, *Journal of Geophysical Research*, 71, 5091–5108, 1966.
- Hochstadt, H., *Differential Equations: A Modern Approach*, Holt, Rinehart, and Winston, 1964.
- Hufford, G. A., A model for the complex permittivity of ice at frequencies below 1 thz, *Internatl. J. Infrared & Millimeter Waves*, 12, 677–682, 1991.
- Hui, A. K., B. H. Armstrong, and A. A. Wray, Rapid computation of the voigt and complex error functions, *Journal of Quantitative Spectroscopy and Radiative Transfer*, 19, 509–516, 1978.
- Jackson, J. D., *Classical electrodynamics*, John Wiley & Sons, New York, 1998.
- Kneizys, F. X., et al., The MODTRAN2/3 report and LOWTRAN7 model laboratory studies and propagation modelling, *Tech. Rep. 1/11/96*, Phillips Laboratory, Geophysical Directorate, PL/GPOS, 1996, editors: L. W. Abreu and G. P. Anderson.
- Kochanov, R. V., et al., Infrared absorption cross-sections in hitran2016 and beyond: Expansion for climate, environment, and atmospheric applications, *Journal of Quantitative Spectroscopy and Radiative Transfer*, 230, 172–221, 2019.
- Kuntz, M., and M. Höpfner, Efficient line-by-line calculation of absorption coefficients, *Journal of Quantitative Spectroscopy and Radiative Transfer*, 63, 97–114, 1999.
- Kyle, T., *Atmospheric transmission, emission and scattering*, Pergamon Press, 1991.
- Larsen, H., J.-F. Gayet, G. Febvre, H. Chepfer, and G. Brogniez, Measurement errors in cirrus cloud microphysical properties, *Ann. Geophys.*, 16, 266–276, 1998.
- Li, L., J. Vivekanandan, C. H. Chan, and L. Tsang, Microwave radiometric technique to retrieve vapor; liquid and ice; part I – developement of a neural network-based inversion method, *IEEE Transactions on Geoscience and Remote Sensing*, 35, 224–235, 1997.
- Liebe, H. J., Modelling attenuation and phase of radio waves in air at frequencies below 1000 ghz, *Radio Science*, 16, 1183–1199, 1981.
- Liebe, H. J., The atmospheric water vapor continuum below 300 GHz, *Internatl. J. Infrared & Millimeter Waves*, 5(2), 207–227, 1984.
- Liebe, H. J., MPM – an atmospheric millimeter-wave propagation model, *Internatl. J. Infrared & Millimeter Waves*, 10, 631–650, 1989.
- Liebe, H. J., and D. H. Layton, Millimeter-wave properties of the atmosphere: Laboratory studies and propagation modelling, *Tech. Rep. 87224*, U.S. Dept. of Commerce, National Telecommunications and Information Administration, Institute for Communication Sciences, 1987, 80p.
- Liebe, H. J., T. Manabe, and G. A. Hufford, Millimeter-wave attenuation and delay rates due to fog/cloud conditions, *IEEE Trans. Antennas Propag.*, 37, 1617–1623, 1989.

- Liebe, H. J., G. A. Hufford, and T. Manabe, A model for the complex permittivity of water at frequencies below 1 thz, *Internatl. J. Infrared & Millimeter Waves*, 12, 659–675, 1991.
- Liebe, H. J., P. W. Rosenkranz, and G. A. Hufford, Atmospheric 60-GHz oxygen spectrum: new laboratory measurements and line parameters, *Journal of Quantitative Spectroscopy and Radiative Transfer*, 48, 629–643, 1992.
- Liebe, H. J., G. A. Hufford, and M. G. Cotton, Propagation modeling of moist air and suspended water/ice particles at frequencies below 1000 GHz., in *AGARD 52nd Specialists Meeting of the Electromagnetic Wave Propagation Panel, Palma de Mallorca, Spain*, 1993, <ftp://ftp.its.bldrdoc.gov/pub/mpm93/>.
- Liou, K. N., *An introduction to atmospheric radiation*, 2nd ed., Academic Press, 2002.
- Lipton, A. E., M. K. Griffin, and A. G. Ling, Microwave transfer model differences in remote sensing of cloud liquid water at low temperatures, *IEEE Transactions on Geoscience and Remote Sensing*, 37, 620–623, 1999.
- Liu, J. S., *Monte Carlo Strategies in Scientific Computing*, Springer-Verlag, 2001.
- Liu, Q., C. Simmer, and E. Ruprecht, Three-dimensional radiative transfer effects of clouds in the microwave spectral range, *Journal of Geophysical Research*, 101, 4289–4298, 1996.
- Long, D. A., *The Raman Effect: A Unified Treatment of the Theory of Raman Scattering by Molecules*, John Wiley & Sons Ltd., 2002.
- Ludlam, F. H., and B. J. Mason, The physics of clouds, in *Encyclopedia of Physics*, edited by S. Flügge, vol. 48, Springer, Berlin, 1957.
- Ma, Q., and R. H. Tipping, Water vapor continuum in the millimeter spectral region, *Journal of Chemical Physics*, 93, 6127–6139, 1990.
- Mätzler, C., and C. Melsheimer, Radiative transfer and microwave radiometry, in *Thermal microwave radiation: applications for remote sensing*, edited by C. Mätzler, The institution of engineering and technology, UK, 2006.
- Mishchenko, M. I., Vector radiative transfer equation for arbitrarily shaped and arbitrarily oriented particles: a microphysical derivation from statistical electromagnetics, *Applied Optics*, 41, 7114–7134, 2002.
- Mishchenko, M. I., J. W. Hovenier, and L. D. Travis, eds., *Light Scattering by Nonspherical Particles*, Academic Press, 2000, ISBN 0-12-498660-9.
- Mishchenko, M. I., L. D. Travis, and A. A. Lacis, *Scattering, Absorption and Emission of Light by Small Particles*, Cambridge University Press, 2002, ISBN 0-521-78252.
- Mobley, C. D., *Light and water: radiative transfer in natural waters*, chap. Across the surface, Academic Press, USA, 1994.
- Newell, A. C., and R. C. Baird, Absolute determination of refractive indices of gases at 47.7 Gigahertz, *J. Appl. Phys.*, 36, 1965.

- Oliveiro, J. J., and R. L. Longbothum, Empirical fits to voight line width: A brief review, *Journal of Quantitative Spectroscopy and Radiative Transfer*, 17, 233–236, 1977.
- Pawlowska, H., J. L. Brenguier, and F. Burnet, Microphysical properties of stratocumulus clouds, *Atmospheric Research*, 55, 15–33, 2000.
- Petty, G. W., *A first course in atmospheric radiation*, Sundog Publishing, 2006.
- Petty, G. W., and W. Huang, The modified gamma size distribution applied to inhomogeneous and nonspherical particles: Key relationships and conversions, *Journal of the Atmospheric Sciences*, 68, 1460–1473, 2011.
- Press, W., S. Teukolsky, W. Vetterling, and B. Flannery, *Numerical recipes in FORTRAN*, 2nd ed., Cambridge University Press, 1992.
- Press, W., S. Teukolsky, W. Vetterling, and B. Flannery, *Numerical recipes in C*, 2nd ed., Cambridge University Press, 1997.
- Ray, P., Broadband complex refractive indices of ice and water, *Appl. Opt.*, 11, 1836–1844, 1972.
- Rees, W. G., *Physical principles of remote sensing*, 2nd ed., Cambridge University Press, 2001.
- Rodgers, C., *Inverse methods for atmospheric sounding: Theory and practise*, 1st ed., World Scientific Publishing, 2000.
- Rodgers, C. D., Characterization and error analysis of profiles retrieved from remote sounding measurements, *Journal of Geophysical Research*, 95, 5587–5595, 1990.
- Rosenkranz, P. W., Absorption of microwaves by atmospheric gases, in *Atmospheric remote sensing by microwave radiometry*, edited by M. A. Janssen, pp. 37–90, John Wiley & Sons, Inc., 1993, [ftp://mesa.mit.edu/phil/lbl\\_rt](ftp://mesa.mit.edu/phil/lbl_rt).
- Rosenkranz, P. W., Water vapor microwave continuum absorption: A comparison of measurements and models, *Radio Science*, 33, 919–928, 1998, (correction in 34, 1025, 1999), [ftp://mesa.mit.edu/phil/lbl\\_rt](ftp://mesa.mit.edu/phil/lbl_rt).
- Rothman, L. S., et al., The HITRAN molecular database: editions of 1991 and 1992, *Journal of Quantitative Spectroscopy and Radiative Transfer*, 48, 469–507, 1992.
- Rothman, L. S., et al., The HITRAN molecular spectroscopic database and HAWKS (HITRAN atmospheric workstation): 1996 edition, *Journal of Quantitative Spectroscopy and Radiative Transfer*, 60, 665–710, 1998.
- Rybicki, G. B., and A. P. Lightman, *Radiative processes in astrophysics*, chap. Plasma effects, John Wiley and Sons, Inc., USA, 1979.
- Salby, M. L., *Fundamentals of Atmospheric Physics*, vol. 61 of *International Geophysics Series*, Academic Press, 1996, ISBN 0-12-615160-1.
- Seinfeld, J. H., and S. N. Pandis, *Atmospheric Chemistry and Physics : from Air Pollution to Climate Change*, Wiley, 1998, ISBN 0-471-17816-0.



- Shupe, M. D., T. Uttal, S. Y. Matrosov, and A. S. Frisch, Cloud water content and hydrometeor sizes during the FIRE-Arctic Clouds Experiment, *Journal of Geophysical Research*, 106, 15015–15028, 2000.
- Stamnes, K., G. E. Thomas, and J. J. Stamnes, *Radiative Transfer in the Atmosphere and Ocean (2nd edition)*, chap. Chapter 3.3, p. 79, Cambridge University Press, 2017.
- Stankevich, K. S., Absorption of sub-millimeter-range radio waves in a dry atmosphere, *Radiophys. Quantum Electron. (Engl. Transl.)*, 17, 579–581, 1974.
- Stone, N. W., W. G. Read, A. Anderson, I. R. Dagg, and W. Smith, Temperature-dependent collision-induced absorption in nitrogen, *Can. J. Phys.*, 62, 338–347, 1984.
- Stratton, A. J., Optical and radio refraction on Venus, *Journal of the Atmospheric Sciences*, 25, 666–667, 1968.
- Thomas, G., and K. Stamnes, *Radiative Transfer in the Atmosphere and Ocean*, Cambridge Atmospheric and Space Science Series, Cambridge University Press, 2002.
- Thorne, A., U. Litzen, and S. Johansson, *Spectrophysics : principles and applications*, Springer, 1999, 1999, ISBN 3-540-65117-9.
- Tomasi, C., V. Vitale, B. Petkov, A. Lupi, and A. Cacciari, Improved algorithm for calculations of rayleigh-scattering optical depth in standard atmospheres, *Applied Optics*, 44, 3320–3341, 2005.
- Townes, C. H., and A. L. Schawlow, *Microwave Spectroscopy*, Mc Graw-Hill, 1955.
- Tran, H., N. Ngo, and J.-M. Hartmann, Efficient computation of some speed-dependent isolated line profiles, *Journal of Quantitative Spectroscopy and Radiative Transfer*, 129, 199 – 203, 2013.
- Ulaby, F., R. Moore, and A. Fung, *Microwave remote sensing: Active and passive, Volume I: Microwave remote sensing fundamentals and radiometry*, Addison-Wesley Publishing Company, 1981, ISBN 0-201-10759-7 (v. 1).
- van de Hulst, H., *Light Scattering by Small particles*, Dover Publications, New York, 1957, corrected republication 1981.
- Van Vleck, J. H., The relation between absorption and dispersion, in *Propagation of Short Radio Waves*, edited by D. E. Kerr, pp. 641–664, Peter Peregrinus Ltd, 1987, first published in 1951 by McGraw-Hill Book Comp. Inc.
- Van Vleck, J. H., and D. L. Huber, Absorption, emission, and linebreadths: a semihistorical perspective, *Reviews of Modern Physics*, 49, 939–959, 1977.
- Van Vleck, J. H., and V. F. Weisskopf, On the shape of collision-broadening lines, *Reviews of Modern Physics*, 17, 227—236, 1945.
- Verdes, C., A. von Engeln, and S. A. Buehler, Partition function data and impact on retrieval quality for a mm/sub-mm limb sounder, *Journal of Quantitative Spectroscopy and Radiative Transfer*, 90, 217–238, 2005.

- Vinogradov, A. P., V. Y. Shishkov, I. V. Doronin, E. S. Andrianov, A. A. Pukhov, and A. A. Lisyansky, Quantum theory of rayleigh scattering, *Opt. Express*, 29, 2501–2520, 2021.
- Westwater, E. R., J. B. Snider, and M. J. Falls, Ground-based microwave radiometric retrieval of precipitable water vapor in the presence of clouds with high liquid content, *Radio Science*, 15, 947–957, 1980.
- Zaghloul, M. R., and A. N. Ali, Algorithm 916: Computing the faddeyeva and voigt functions, *ACM Trans. Math. Softw.*, 38, 15:1–15:22, 2012.

## **Part II**

## **Index**



# Index

- ARTS files
  - hitran\_species.cc, 29
  - isotopolgues.h, 29
  - jpl\_species.cc, 29
- Coordinate systems, 90
- data reduction, 3
- data reduction matrix, 3
- Discrete Ordinate ITERative (DOIT) method, 129
- dispersion, 63
- forward model, 1
- geometrical factor, 107
- internal ARTS functions
  - cart2poslos, 112
  - cart2sph, 111
  - do\_gridcell\_2d, 106, 107, 110
  - do\_gridcell\_3d\_bytest, 106, 114
  - do\_gridrange\_1d, 106, 109
  - geometrical\_ppc, 107
  - geompath\_from\_r1\_to\_r2, 109
  - geomppath\_l\_at\_r, 108
  - geomppath\_lat\_at\_za, 108
  - geomppath\_r\_at\_l, 108
  - geomppath\_r\_at\_lat, 108
  - geomppath\_r\_at\_za, 108
  - geomppath\_za\_at\_r, 108
  - lat\_crossing\_3d, 113
  - lon\_crossing\_3d, 113
  - plevel\_crossing\_2d, 109
  - plevel\_slope\_3d, 113
  - poly\_root\_solve, 110
  - poslos2cart, 112
  - ppath\_calc, 105
  - ppath\_end\_1d, 106
  - ppath\_end\_2d, 107
  - ppath\_start\_1d, 106
  - ppath\_start\_2d, 107
  - ppath\_start\_stepping, 105, 106
  - ppath\_step\_geom\_1d, 106
  - ppath\_step\_geom\_2d, 106, 107
  - ppath\_step\_geom\_3d, 106
  - r\_crossing\_3d, 113
  - raytrace\_1d\_linear\_euler, 118
  - raytrace\_2d\_linear\_euler, 119
  - raytrace\_3d\_linear\_euler, 121
  - refr\_gradients\_2d, 119
  - refr\_gradients\_3d, 121
  - rslope\_crossing, 109
  - rslope\_crossing2d, 110
  - rslope\_crossing3d, 114
  - sph2cart, 111
- laboratory frame, 90
- measurement errors, 1
- model parameter vector, 1
- monochromatic, 2
- pencil beam, 2
- radiation field, 129
- ray tracing, 116
- refractive index, 63
- scalar radiative transfer, 133
- scattering frame, 90
- sensor transfer matrix, 2
- Sequential update, 134
- single scattering approximation, 134
- state vector, 1
- vector radiative transfer equation, 130
- vector space, 3
- weighting function, 3
- workspace agendas
  - ppath\_step\_agenda, 105
- workspace methods
  - isotopologue\_ratiosInitFromBuiltin, 29

---

- ppath\_stepGeometric, 106
- ppath\_stepRefractionBasic, 106, 116
- ppathCalc, 105
- psdModifiedGamma, 124
- psdModifiedGammaMass, 125
- psdModifiedGammaMassMeanParticleMass, 127
- psdModifiedGammaMassNtot, 128
- psdModifiedGammaMassXmean, 126
- psdModifiedGammaMassXmedian, 126
- refr\_index\_airFreeElectrons, 65
- refr\_index\_airMicrowavesEarth, 64
- ScatSpeciesSizeMassInfo, 123
- surfaceFlatRvRh, 102
- surfaceFlatScalarReflectivity, 102
- surfaceTessem, 102
- workspace variables
  - ppath, 107
  - ppath\_step, 106, 107
  - scat\_species\_a, 123
  - scat\_species\_b, 123